Nanoscale Structure and Single Molecule Diffusion in Smart Polymeric Systems

Ateyyah AL-Baradi

A Thesis Submitted for the Degree of Doctor of Philosophy

The University Of Sheffield.

The Department of Physics and Astronomy

November 2011

To my parents

Abstract

Soft nanotechnology requires the development and understanding of smart polymeric systems that respond to small changes in the surrounding environment. This thesis reports on the structure and dynamics in poly(methacrylic acid) (PMAA) hydrogels and hyperbranched poly(N-isopropyl acrylamide) (HB-PNIPAM) in response to physical and chemical stimuli.

Fluorescence correlation spectroscopy (FCS) has been utilized to study the diffusion of single dextran molecules labelled with fluorescein isothiocyanate within a PMAA hydrogel. Diffusion in pure water shows a temperature dependence described by Zimm dynamics, whereas the diffusion coefficient decreases with temperature in the hydrogel for which a model has been developed. Diffusion in PMAA hydrogel has revealed the mesh size dependence on temperature. The effect of pH and salt on the diffusion in PMAA hydrogel has also been considered. Introducing magnetic nanoparticles to hydrogels forms ferrogels the mesh of which is controlled by applied magnetic fields. The swelling, diffusion and release in PMAA ferrogel has been found to follow the same scaling theory developed in this work.

Small angle neutron scattering (SANS) has revealed the structural behaviour of HB-PNIPAM as a function of temperature compared to its linear counterpart. These experiments have shown that water is a good solvent for HB-PNIPAM at low temperatures, while increasing the temperature leads to a gradual collapse of these polymers until they form spherical particles with sharp boundaries of the order of 24-40 nm in diameter, depending on the branching degree. This indicates that HB-PNIPAM shows no entanglements either as a function of temperature or branching degree. In contrast, linear PNIPAM showed a network-like behaviour above its collapsing temperature. Neutron spin echo experiments on HB-PNIPAM are described well by the Rouse model for unentangled chains and the self-diffusion of HB-PNIPAM by FCS follows Zimm behaviour, which is in agreement with SANS results.

These studies have given a better understanding of the nanostructure and dynamics in the investigated polymeric systems, showing their usefulness as delivery systems for many biological and medical applications.

Acknowledgments

The work in this thesis would not have been possible without the support from many people, who I would like to thank.

First of all, I would like to deeply thank my supervisor Professor Mark Geoghegan for his trust in me and for giving me the opportunity to do this PhD. Mark's help was not limited to his guidance of the work in this thesis, but rather he supported and encouraged me to know where the good science is.

Thanks go to my polymer physics group past and present: Dr Rita La Spina, Dr Zhenyu Zhang, Dr Andrew Parnell, Dr Mike Weir, Dr Muneer Jalloh, Ana Morales, Maryam Raftari, Amy Hall, Dr Warren Taylor and Youmna Mouhamad, for the friendly environment in the group. My special thanks go to my colleague Dr Matthew Mears for his help to develop a model to describe the temperature dependence of diffusion in PMAA hydrogel.

Performing the SQUID measurements would not have been possible without help from people in the magnetic oxides group, especially, I thank Dr Harry J. Blythe and Mohamed Al-Qahtani.

In chemistry, I would like to thank Dr Steven Rimmer and his student Kathryn for giving me the opportunity to use their laboratory to synthesize highly branched PNIPAMs. I also thank Dr Steve Carter, who is working at BP now, for helping me to synthesize highly branched PNIPAMs. I also thank Dr Oleksandr Mykhaylyk for his help with SAXS measurements and analysis.

I also thank those people who have helped me with the neutron experiments. At ISIS (UK), Dr Stephen King and Dr R. K. Heenan, at Saclay (France), Dr Laurence Noirez and at Grenoble (France), Dr Marco Maccarini and Dr Peter Falus.

I would also like to thank my sponsor, Taif University, represented by the Saudi Arabian Cultural Bureau in London for funding me in the last six years to complete my studies in the UK.

Last but not least, I would like to thank my parents for their encouragement and support during my studies. I am also thankful to my wife and

children for their patience and emotional support throughout my studies. As well, I thank the rest of my family, my brothers and sisters.

Declaration

The work described in this thesis was undertaken at the University of Sheffield between January 2008 and January 2011, under the supervision of Professor Mark Geoghegan. Unless otherwise stated, it is the work of the author and has not been submitted in whole or part for any other degree at this or any other institute.

Ateyyah AL-Baradi
November 2011

Publicly Presented Work

1. "Magnetic field dependence of the diffusion of single dextran molecules within a hydrogel containing magnetite nanoparticles"; Ateyyah M. AL-Baradi, Oleksandr O. Mykhaylyk, Harry J. Blythe, and Mark Geoghegan; Journal of chemical physics, 2011.

2. Advanced Nanomaterials Conference, Agadir, 2010. Talk tittled "Single molecule diffusion in magnetic fields".

3. 43rd IUPAC World Polymer Congress, Glassgow, 2010. Poster presentation tittled "Nanocomposite Ferrogel Behaviour Under an Applied Magnetic Field: A Single Molecule Diffusion Study".

4. IOP Polymer Physics Group Biennial Conference, Bristol University, 2009. Poster presentation tittled "Single Molecule Diffusion in Polymer Hydrogels: Physical and Chemical Stimuli Effects".

Manuscripts in Preparation:

1. "The effect of structural changes of poly(methacrylic acid) hydrogels on the diffusion of dextran"; Ateyyah M. AL-Baradi, Matthew Mears, Richard A. L. Jones and Mark Geoghegan.

2. "Structural behaviour and dynamics of highly branched PNIPAm as a function of temperature"; Ateyyah M. AL-Baradi, Stephen Rimmer, Steven Carter, Johann P. de Silva and Mark Geoghegan.

Symbols and Abreviations

AIBN	Azobis(isobutyronitrile)
AMPA	2,2'-azobis (2-methylpropionamidine) dihydrochloride
CLSM	Confocal Laser Scanning Microscopy
D_7-HB-PNIPAM	Deuterated hyperbranched Poly(N-isopropyl acrylamide)
FC	Field cooled
FCS	Fluorescence correlation spectroscopy
FITC	Fluorescein isothiocyanate
GPC	Gel permeation chromatography
HB-PNIPAM	Hyperbranched Poly(N-isopropyl acrylamide)
LCST	Lower critical solution temperature
MAA	Methacrylic acid
MBA	Methyl-bisacrylamide
NMR	Nuclear magnetic resonance
NSE	Neutron spin echo
PMAA	Poly(methacrylic acid)
PNIPAM	Poly(N-isopropyl acrylamide)
RAFT	Reversible Addition-Fragmentation chain Transfer
SALS	Small-angle light scattering
SANS	Small-angle neutron scattering
SAXS	Small-angle X-ray scattering
SEC	Size exclusion chromatography
SQUID	Superconducting quantum interference device
ZFC	Zero field cooled
B	Magnetic field induction
b	Monomer size
b	Scattering length
c	Concentration
c_s	Ion concentration in the gel
c_s^*	Ion concentration in the solution
$C(r,t)$	Local concentration of the fluorescent particles
D	Diffusion coefficient

D_{R}	Rouse diffusion coefficient
D_{Z}	Zimm diffusion coefficient
D_0	Diffusion coefficient in pure solvent
D_{eff}	Effective diffusion coefficient
D_{f}	Fractal dimension
d	Molecule size (diameter)
E	Neutron energy
E_{a}	Activation energy
$\overrightarrow{f}$	Force applied on a particle
f_{m}	Magnetic force
G	Modulus
$G(\tau)$	Autocorrelation function
H	Magnetic field strength
H^+	Hydrogen ion
$[H^+]$	Concentration of hydrogen ions
h	Planck's constant
$\hbar$	Reduced Plank's constant
i	Ionisation degree
$I(q)$, $I(Q)$	Scatering intensity
J	Flux
K	Magnetic anisotropy
K_{a}	Acid disociation constant
K_{b}	Base disociation constant
K_{P}	Porod's constant
k_B	Boltzmann constant
k_{H}	Huggins coefficient
l	C-C bond length
M_{n}	Molecular weight
m	Neutron mass
m_{s}	Mass of swollen gel
m_{d}	Mass of dry gel
M_{c}	Molecular weight of the chain between two cross-links
M_{f}	Magnetization of pure ferromagnetic material

M	Magnetization
M_{s}	Saturation magnetization
N	Polymerisation (number of units per chain)
N	Number of beads in Rouse diffusion model
N	Number of fluorescent molecules
n	Number of lattice points
n	Number of cross-links per chain
N_{A}	Number of lattice sites occupied by molecules of species A
N_{B}	Number of lattice sites occupied by molecules of species A
OH^-	Hydroxide
$P(Q)$	Form factor
P_t	Triplet fraction
$P(r)$	Pair distance distribution function
P	Neutron momentum
Q	Swelling ratio
Q_{m}	Equilibrium swelling ratio
Q, q	Momentum transfer or Scattering vector
R	Particle radius
$\bar{R}$	The gas constant
R_{H}	Hydrodynamic radius
$R = \omega_{xy}/\omega_z$	The elongation parameter
$R_n^i(t)$	Quantum mechanical operator
r_0	Particle radius
r	The distance between two scattering centres
S	System entropy
S^*	Ionic strength
$S(Q)$	Structure factor
$S(r)$	Optical transfer function
$S(Q,\omega)$	Scattering function
$S(Q,t)$	Intermediate scattering function
T	Absolute Temperature
T_0	Vogel-Fulcher temperature
T_{g}	Glass transition temperature

T_B	Blocking temperature
V	Particle volume
V	Swollen volume
V	Volume of one scattering centre
V_0	Unswollen volume
V_A	Volume of species A
V_B	Volume of species B
v_1	Molar volume of the solvent
V_{eff}	Effective confocal volume
$\bar{v}$	Polymer specific volume
ϕ_A	Volume fraction of species A
ϕ_B	Volume fraction of species B
Ω	Number of arrangements of the molecules on the lattice
$\triangle S_\mathrm{mix}$	Change in entropy of a mixture
$\triangle U_\mathrm{mix}$	Change in enthalpy of a mixture
χ	Flory interaction parameter
$\triangle F_\mathrm{mix}$	Free energy of mixing
$\triangle F_\mathrm{el}$	Change in the elastic force
ν_e	Effective number of polymer chains
α_s	Linear deformation factor
μ_0, μ_1^0	Chemical potential inside and outside polymer network
ϕ_m	Maximum polymer volume fraction at equilibrium
$\triangle F_\mathrm{ion}$	Change in ionic energy in the network
$\triangle F_\mathrm{dis}$	Change in dissociation energy of the ionisable groups
$\triangle F_\mathrm{Coul}$	Change in Coulombic interactions in the network
Π_ion	Ionic osmotic pressure
ϑ	Valency factor
z_-	Valency of electrolyte ions
Π_total	Total osmotic pressure
Π_mix	Mixing osmotic pressure
Π_el	Elastic osmotic pressure
ϕ_r	Polymer volume fraction in the network after cross-linking
$\frac{\partial c}{\partial x}$	Concentration gradient

$\overrightarrow{v}$	Particle velocity
ζ	Friction coefficient
η	Viscosity
η_0	Viscosity of pure solvent
ζ_{R}	Friction coefficient in Rouse diffusion model
ν	Reciprocal of fractal dimention
η_{s}	Solvent viscosity
ζ_{Z}	Friction coefficient in Zimm diffusion model
τ	Relaxation time
ρ	Mass density
ρ	Neutron scattering length density of the solute
ρ_{m}	Neutron scattering length density of the medium
ω_{xy}	The radial size of the beam waist
ω_z	The axial size of the beam waist
κ	Overall detection efficiency
$\delta\sigma$	The fluctuations in the molecular absorption cross-section
δq	The fluctuations in the quantum yield
τ_D	Translational diffusion time
τ_t	Triplet time
λ	Wavelength
2θ	Scatteing angle
ρ	constant electron density in the particle
ρ_0	constant electron density in the solvent
v	Neutron speed
$\mathrm{d}\sigma(\theta)/\mathrm{d}\Omega\mathrm{d}E$	Differential cross section
Φ	Incident neutron flux
$\mathrm{d}\Omega$	Solid angle
ξ	Mesh size (or correlation length)
ϕ	Equilibrium swelling ratio
ϕ_0	Initial equilibrium swelling ratio
μ_0	Magnetic permeability of vacuum
χ_{m}	Magnetic susceptibility
Σ	The total area of interface

τ_N	Néel relaxation time
τ_0	Attempt time
τ_m	Measurement time
ϕ_p	Volume fraction of particles
$\frac{S(Q,t)}{S(Q,0)}$	Dynamic structure factor
β	Stretching parameter
Γ	Relaxation rate

Contents

Chapter 1

Introduction

Over the past two decades there has been a dramatic increase in the attention given to water-based heterogeneous polymeric systems due to their wide range of applications in nanotechnology in areas such as medicine, biotechnology, membrane technology and environment. For example, soft nanomachines that can be formed from these heterogeneous systems are useful for tissue engineering, biosensors and drug delivery and release [1, 2. 3, 4]. The smartness of such materials comes from their high response to external physical and chemical stimuli, such as temperature [5, 6], magnetic field [7, 8], electric field [9, 10], pH and salt [11, 12].

The ongoing studies on these materials are mainly attempting to control the responsiveness of such materials and a major area of interest is to find structures that can be used effectively in a human body. For instance, a material that is to be used as an artificial muscle must function as quickly as a real one; this property has been seen in hydrogels, which will be described below, but their response time is yet to be improved [13]. For the use of such smart materials in medicine, one must consider the diverse conditions in a human body such as the different pH in different areas of the body. These features of the human tissues could be utilized for drug delivery and release. For example, the difference in pH in the human stomach (pH 1-3) and in the small intestine (pH 8) could be utilized for a targeted delivery system [14]. A polymer material that swells at high pH and collapses at

low pH will not deliver or release a drug in the stomach but rather in the small intestine. The body temperature is another example where a polymer that collapses at low temperatures and swells around the body temperature could be used for a drug injection. Other materials, such as poly(N-isopropyl acrylamide) (PNIPAM) are swollen at low temperatures and collapsed around the body temperature, which makes them useful for cell penetration and drug delivery. The above mentioned examples are just a simple utilization of heterogeneous water-based responsive systems which are among many other more complicated applications.

An important class of polymers are polylectrolytes, which have ionisable groups that, in polar solvents (such as water) can, dissociate into charged polymer chains releasing counterions in solution (see Chapter 2). The wide range of applications of polyelectrolytes is mainly due to their water solubility and responsiveness in pH and salt solutions. Therefore, polyelectrolytes have been a subject of interest for many decades [12, 15]. A well-known example of a polyelectrolyte is poly(methacrylic acid) (PMAA). When these polyelectolytes are cross-linked, a polymer network of charged polymers is obtained which is called a polymer hydrogel when swollen with water.

Hydrogels are chemically or physically cross-linked polymer networks which are swollen with water but do not dissolve in it. Polymer hydrogels are a unique state of matter as they simultaneously have solid and liquid-like properties once the cross-linking takes place, the process by which the polymer chains become part of a three-dimensional cluster (see Chapter 5). Although these complex materials have been investigated for many decades, a complete understanding of their behaviour is still lacking, especially as there are many discrepancies between the predicted theories and the experimental results [16].

Although these conventional hydrogels are useful for many tasks, materials that can respond to other stimuli, such as electric and magnetic fields, are required for some other applications. Composite hydrogels are examples of such systems where the addition of inorganic substances to the gels gives them different characteristics in terms of their responsiveness to the surrounding environments. In this work, the focus will be on magnetic nanocomposite

hydrogels.

Polymer hydrogels are originally paramagnetic materials with a weak response to magnetic fields that is hardly detected. A way to make gels responsive to magnetic fields is by introducing magnetic nanoparticles ($\sim$ 10 nm) either before or after cross-linking to form so-called "ferrogels". These magnetic nanoparticles are bound to the polymer network and are fixed in place, with no translational diffusion within the gel medium (see Chapter 6). Since Zrínyi *et al.* [17] introduced the concept of ferrogels in 1995, useful applications in biotechnology, membrane technology, artificial muscles, and drug delivery and release have been suggested [18, 19].

Another example of an important type of polymer is poly(N-isopropyl acrylamide) (PNIPAM), which was first synthesized in the 1950s and has received considerable attention in the last few decades due to its biocompatibility and transition temperature, which is close to the body temperature (32°C for linear PNIPAM) [20, 21]. This transition temperature is a lower critical solution temperature (LCST), which is the temperature at which the polymer exhibits a coil to globule transition caused by hydrophobic and hydrophilic interactions [22]. Therefore, PNIPAM, as a neutral polymer, is water soluble below its LCST via strong hydrogen bonding; whereas these water-polymer hydrogen bonds are disrupted above the LCST and the polymer chain preferentially makes hydrogen bonds with neighboring chains.

PNIPAM has been produced in different ways resulting in varied polymer architectures. These architectures include linear, microgels [23] and micelles [24]. It has been a challenge to increase the LCST of these PNIPAM to that of the body and many attempts have been reported using different synthetic methods, such as copolymerizing PNIPAM with hydrophilic chain-end functionalized polymers. For example, Rimmer *et al.* [25, 26, 27] have been able to synthesize highly branched HB-PNIPAM with no cyclization or microgelation. They have utilized the self-considering vinyl polymerization (SCVP) principles [28] by using the Reversible Addition Chain Transfer Polymerization (RAFT) method to produce HB-PNIPAM with imidazole-chain ends. These end groups can be replaced with COOH acid groups, which can be then used for binding with other polymers or biological species. Therefore, a

number of biotechnological and medical applications have been reported in this way, for example, protein purification for breast cancer therapy [29, 30], DNA binding [31], cell penetration [5] and drug delivery [32].

The structure of the above mentioned water-based polymeric systems is important, but the transport and diffusion of macromolecules within these systems is also of great importance for molecular delivery and release. Diffusion in polymeric systems, especially in hydrogels, has received a lot of attention and the reason behind this is that most biological processes follow the same principle, for example, the transport of proteins and drug molecules through the cell membrane [33]. The complexity of polymer networks results in a complicated diffusion process with a coefficient that lies between that in viscoelastic and Newtonian fluids. Moreover, the dependence of diffusion on the polymer concentration when making the network and the degree of swelling of these networks makes it a challenge to understand the diffusion of large molecules or even small particles in such systems. Polymer gels are normally characterised by their pore size (mesh size, also called the correlation length, ξ) which can be determined from the diffusion of a probe in this network, and therefore, the effect of external stimuli can be detected from the diffusion results. There have been many techniques used to study the diffusion in polymer solutions and gels, such as gravimetry, dynamic light scattering and neutron reflectometry [34, 35]. The results of these studies have led to a better understanding of the diffusion concepts with the help of the physical models based on the hydrodynamic interactions, obstruction and the free volume theories [36]. In addition, the development of powerful techniques, for instance, fluorescence correlation spectroscopy (FCS), makes it much easier to study diffusion in more complex systems [37].

1.1 Aims and Objectives

The previous section introduced the importance of water-based polymeric systems and the lack of a complete understanding of such systems which is needed in order to utilize them as predicted theoretically. In this section, the main objectives of the study presented in this thesis will be discussed. The

first goal was to investigate the stimuli responsive polyelectrolyte hydrogels (namely PMAA) in different physical and chemical environments (temperature, pH and salt). The volume phase transition of such hydrogels has been extensively studied with strong agreements with the available theories. However, the correlation between the effect of these external stimuli on the characteristic length scale (mesh size ξ) is still unknown. With the help of a powerful technique such as FCS, one can easily study the diffusion process in hydrogels in different conditions. The aim in this part of the study was to explore the correlation between temperature and mesh size, despite there being a little theory in the literature in this regard. In this case, a fluorescently labeled-dextran (FITC-dextran) was used as a probe diffusing within the polymer matrix. The results showed no agreement with the available theories, which was overcome by modifying and developing the appropriate models. Likewise, the effect of pH and salt solutions on the diffusion of FITC-dextran was investigated by FCS.

In addition, to introduce more physical stimuli on hydrogels, magnetite nanoparticles were embedded within the PMAA networks during polymerisation (to make ferrogels). As for the temperature effect mentioned above, the effect of applied magnetic fields on the mesh size was investigated by utilizing the diffusion measurements of FITC-dextran. To the knowledge of the author, there is no existing theory that describes the effect of magnetic fields on the diffusion of single molecules within ferrogels. In this study, this effect of magnetic fields on diffusion of macromolecules has been modeled in terms of the change in mesh size as a function of the magnetic field induction. It has also been correlated to the macroscopic swelling measurements and the release of FITC-dextran from PMAA ferrogels to the surrounding solution using the same scaling law. These ferrogels were also characterised by small angle x-ray scattering (SAXS) and superconducting quantum interference device (SQUID) magnetometry.

The other half of this study was looking at another class of water-based polymeric systems, hyperbranched PNIPAM. In this part, an investigation of the structural behaviour of HB-PNIPAMs in water with different branching degrees (different LCST) was done using small-angle neutron scattering

(SANS). This study revealed the shape and size changes at temperatures below and above their LCST compared to their linear analogues. Furthermore, These HB-PNIPAMs were also studied by neutron spin echo (NSE) which revealed the local dynamics of the backbone between branches as a function of temperature (below and close to the collapse transition of the polymers) and degree of branching. As a complementary study, HB-PNIPAMs and their linear analogues were labeled with fluorescein to be able to study their dynamics using FCS. FCS results showed an agreement with that seen by NSE in terms of the dynamic behaviour of PNIPAMs as a function of temperature confirming that HB-PNIPAMs do not entangle. FCS also revealed the concentration dependence of self-diffusion of HB-PNIPAMs and the linear PNIPAMs in their own solutions.

1.2 Scope of Study

While this Chapter introduces the plan of this work, in Chapter 2, I discuss some of the basic principles of of polymer physics regarding the thermodynamics of polymer networks and diffusion in polymeric systems. Chapter 3 introduces the background and basic concepts of water-based systems with a review on the previous studies in this field. In Chapter 4, the experimental techniques used throughout this work are described including fluorescence correlation spectroscopy (FCS), small-angle X-ray scattering (SAXS), small-angle neutron scattering (SANS), neutron spin echo (NSE) and superconducting quantum interference device (SQUID) magnetometry. The results of this work are divided into two parts. The first part is related to polymer gels and networks (chapters 5 and 6) , while the second part is the study of HB-PNIPAMs (chapters 7 and 8). The work in Chapter 5 is related to the study of single molecule diffusion in PMAA hydrogels in different environments such as temperature, pH and salt using FCS. Chapter 6 introduces the study of the structural behaviour and single molecule diffusion in PMAA ferrogels in magnetic fields, including molecular release from these materials. The investigation of the structural behaviour of linear and HB-PNIPAMs as a function of temperature, using SANS, is shown in Chapter 7, while the

dynamics of these polymers, using NSE and FCS, is introduced in Chapter 8. Finally, Chapter 9 summarizes the work introduced in this thesis with some suggestions for future work.

Chapter 2

Basic Principles of Polymer Physics

2.1 Introduction

A polymer can be defined as a large molecule (macromolecule) made up of many repeat segments (monomers) connected together by covalent bonds. Since the beginning of polymer science during the 1920s, there has been significant progress in the synthesis and understanding of polymers. Most of the physical principles of polymers were introduced in the first 30 years (1930-1960). For example, in his major study, Flory [38] investigated the swelling behaviour of polymer gels. Furthermore, the work of Huggins and Flory highlighted the principles of thermodynamics of polymeric systems. The study of gelation was also carried out by Flory and Stockmayer in that period. Polymer dynamics of single molecules was developed during this period by Rouse and Zimm [39, 40].

During the following 20 years (1960-1980), many scientists contributed to the development of modern polymer physics. This includes the work of Edwards, de Gennes and Doi, especially in the area of polymer dynamics. Nevertheless, despite the above-mentioned progress in polymer science, a complete understanding of polymer behaviour is still lacking. This history of the progress in polymer physics can be found in more detail in many useful

texts [38, 39, 41, 42, 40, 43, 44].

In this chapter, the polymer physics principles relevant to the work in this thesis will be discussed, including the different polymer architectures, thermodynamics of mixing and the dynamics of polymer chains.

2.2 Polymer Architecture

As noted in the previous section, a polymer is a large molecule containing many segments connected together. These segments commonly form what is known as a carbon backbone in which carbon atoms form the 'spine' of the polymer while other elements dangle from these carbon atoms. These segments are connected together in a process called polymerization. The nature and structure of these segments and the polymerization method used to form the polymer may result in different polymer architectures [39, 40, 38]. For instance, if the monomers are connected continuously through the carbon atoms, then a linear polymer chain can be formed (Figure 2.1(a)). If the first and last monomers of the polymer are connected, then a polymer ring would be achieved (Figure 2.1(b)). It is also possible for a polymer chain to have some segments branching out of the main backbone. Again, depending on the polymerization method and the nature of the segments, different branched polymers can be obtained, such as star-branched, H-branched, comb, ladder, dendrimer, or randomly branched shown in Figure 2.1 (c), (d), (e), (f), (g) and (h), respectively. Introducing cross-links between linear or branched polymer chains results in a macroscopic molecule called a polymer network, sketched in Figure 2.1(i).

In this work, chapters 5 and 6 will investigate chemically cross-linked polymer networks (hydrogels and ferrogels of poly(methacrylic acid) [PMAA]), including their physical properties and the dynamics of single linear polymers within these networks. In addition, Chapters 7 and 8 will study randomly branched polymers (poly(N-isopropyl acrylamide) [PNIPAm]) compared to their linear counterpart, including their structures and dynamics.

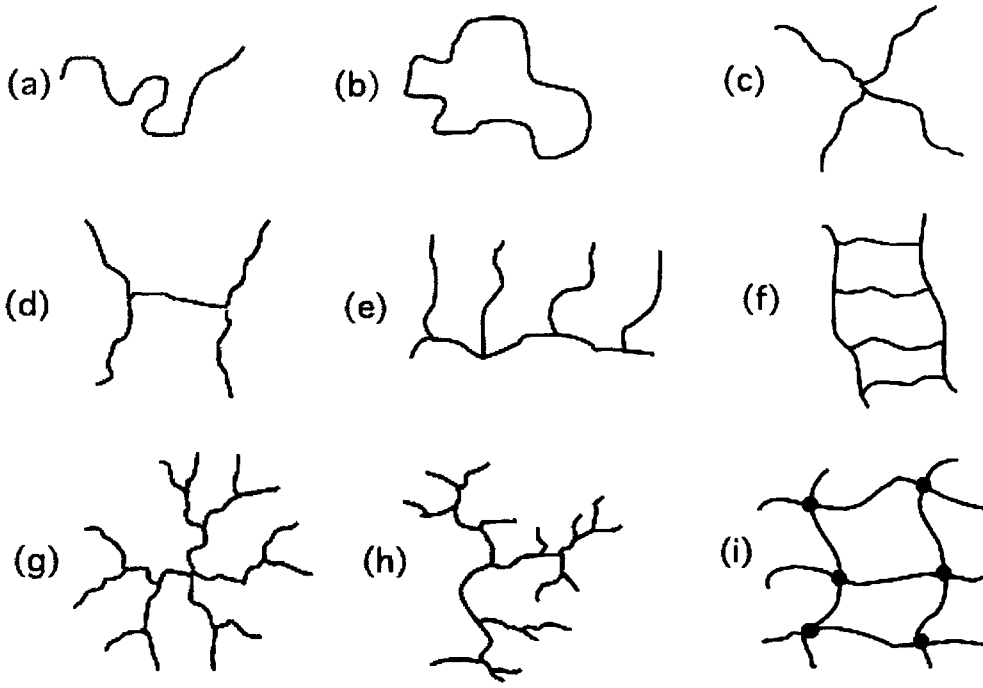

Figure 2.1: Examples of different polymer architectures: (a) linear, (b) ring, (c) star, (d) H-polymer, (e) comb, (f) ladder, (g) dendrimer, (h) randomly branched and (i) network, with the filled circles in (i) indicating the cross-links.

2.3 Polymer Conformations

Polymer chains are made of atoms connected by covalent bonds, which are able to rotate creating different conformations. These conformations and therefore the shape of the polymer chain are difficult to define. The simplest model to describe a polymer chain is the Freely Jointed Chain model (FJC). This model, as shown in Figure 2.2, considers a chain made of N links or bonds defined by vectors $\overrightarrow{r_i}$. These bond vectors have a fixed length $|\overrightarrow{r_i}| = b$ that is known as the Kuhn length, and can rotate freely in space with an angle θ. The free rotation of each vector leads to a different orientation from its neighbour creating a random walk for the polymer chain. The end-to-end vector R is introduced to give the characteristic size of a FJC. This end-to-end distance is expressed as the mean square displacement $\langle R^2 \rangle$, since it is possible for this vector to be $-R$ or $+R$ leading to an average of zero. The mean square displacement $\langle R^2 \rangle$ is proportional to N and can be given as:

$$\langle R^2 \rangle = b^2 N = Lb, \tag{2.1}$$

where L is the contour length given by $L = Nb$. The end-to-end distance can easily be calculated for linear polymers but it is difficult to obtaine for branched polymer chains. Therefore, an alternative approach to estimate the size of polymer chains is the radius of gyration, R_g, which is defined as the root-mean-square distance of the segments from the centre of mass. For a linear polymer chain, R_g can be given as [40]:

$$\langle R_g^2 \rangle = \frac{1}{6} b^2 N = \frac{1}{6} \langle R^2 \rangle . \tag{2.2}$$

For a branched polymer, Kramers theorem is used to obtain the radius of gyration, R_g. In general R_g for a branched polymer is given by:

$$\langle R_g^2 \rangle = g \frac{1}{6} b^2 N, \tag{2.3}$$

where g, which depends on the specific details of the branching, is less than 1.

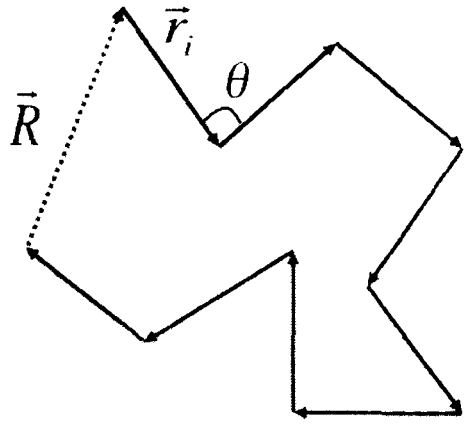

Figure 2.2: Conformation of a felxible polymer chain according to the freely jointed chain model.

2.4 Thermodynamics of Mixing

If two or more different chemical species are mixed, then the properties of this mixture is governed by the amount of each component and their thermodynamic interactions. Here, only binary mixtrues are considered, for example, two species A and B with volumes V_{A} and V_{B}, respectively. If the total volume of this mixture is $V_{\mathrm{A}}+V_{\mathrm{B}}$, then the volume fractions of these components are:

$$\phi_{\mathrm{A}} = \frac{V_{\mathrm{A}}}{V_{\mathrm{A}} + V_{\mathrm{B}}}, \phi_{\mathrm{B}} = \frac{V_{\mathrm{B}}}{V_{\mathrm{A}} + V_{\mathrm{B}}} \tag{2.4}$$

Using a lattice theory allows to determine the entropy, S, in terms of the number of arrangements, Ω, of the molecules on the lattice

$$S = k_B \ln \Omega, \tag{2.5}$$

where k_{B} is the Boltzmann constant. The entropy change of one component (e.g. A) on mixing is

$$\triangle S_{\mathrm{A}} = k_{\mathrm{B}} \ln(\frac{1}{\phi_{\mathrm{A}}}) = -k_{\mathrm{B}} \ln \phi_{\mathrm{A}}. \tag{2.6}$$

The total energy of mixing can be given as [40]:

$$\triangle \bar{S}_{\text{mix}} = -k_{\text{B}} \left[\frac{\phi_{\text{A}}}{N_{\text{A}}} \ln \phi_{\text{A}} + \frac{\phi_{\text{B}}}{N_{\text{B}}} \ln \phi_{\text{B}} \right]. \tag{2.7}$$

where N_{A} and N_{B} are the number of lattice sites occupied by molecules of species A and B, respectively. Note that a lattice site can either be occupied by a solvent molecule or a monomer. For a regular solution where $N_{\text{A}} = N_{\text{B}} = 1$, equation 2.7 can be rewritten as:

$$\triangle \bar{S}_{\text{mix}} = -k_{\text{B}} \left[\phi_{\text{A}} \ln \phi_{\text{A}} + \phi_{\text{B}} \ln \phi_{\text{B}} \right]. \tag{2.8}$$

Whereas, for a polymer solution ($N_{\text{A}} = N$ and $N_{\text{B}} = 1$) equation 2.7 reads:

$$\triangle \bar{S}_{\text{mix}} = -k_{\text{B}} \left[\frac{\phi_{\text{A}}}{N} \ln \phi_{\text{A}} + \phi_{\text{B}} \ln \phi_{\text{B}} \right]. \tag{2.9}$$

Using the same lattice theory above, the energy of mixing (enthalpy) per lattice site is given as [40]:

$$\triangle \bar{U}_{\text{mix}} = \phi_{\text{A}} \phi_{\text{B}} \chi k_{\text{B}} T, \tag{2.10}$$

where χ is the Flory interaction parameter and T is the absolute temperature.

The free energy of mixing (Gibbs free energy $\triangle \bar{F}_{\text{mix}}$) is the combination of the entropy and enthalpy equations given by [40]:

$$\triangle \bar{F}_{\text{mix}} = \triangle \bar{U}_{\text{mix}} - T \triangle \bar{S}_{\text{mix}}, \tag{2.11}$$

and so,

$$\triangle \bar{F}_{\text{mix}} = k_{\text{B}} T \left[\frac{\phi_{\text{A}}}{N_{\text{A}}} \ln \phi_{\text{A}} + \frac{\phi_{\text{B}}}{N_{\text{B}}} \ln \phi_{\text{B}} + \chi \phi_{\text{A}} \phi_{\text{B}} \right]. \tag{2.12}$$

The Flory-Huggins equation (equation 2.12) can be simplified by taking $\phi_{\text{A}} = \phi$ and $\phi_{\text{B}} = 1 - \phi$. Therefore, for polymeric solutions, where $N_{\text{A}} = N$ and $N_{\text{B}} = 1$, equation 2.12 can be rewritten as:

$$\triangle \bar{F}_{\text{mix}} = k_{\text{B}} T \left[\frac{\phi}{N} \ln \phi + (1 - \phi) \ln(1 - \phi) + \chi \phi (1 - \phi) \right]. \tag{2.13}$$

Equation 2.13 will be exploited in the next section for a mixtue of a polymer network and a solvent.

2.5 Swelling Behaviour of Polymer Networks

When a solvent is introduced to a polymer network, it swells the network until an equlibrium is reached. The driving force of this swelling process is the change in the entropy of the system. The swelling process is also governed by the elastic force that arises from stretching the chains, which usually results in a decrease in the entropy of the system. When the osmotic pressure due to polymer-solvent interactions balances the elastic effect on the polymer network, then the system is in equilibrium. At this point, the total free energy of the system can be given as [38, 45, 40]:

$$\triangle F = \triangle F_{\text{el}} + \triangle F_{\text{mix}}, \tag{2.14}$$

where $\triangle F_{\text{el}}$ is the elastic force contribution to the swelling and $\triangle F_{\text{mix}}$ is the thermodynamics of mixing described in section 2.3. Using the classical Flory-Huggins lattice theory for polymer networks [38], the energy of mixing is expressed as:

$$\triangle F_{\text{mix}} = nk_{\text{B}}T\left[\phi \ln \phi + \chi\phi(1-\phi)\right], \tag{2.15}$$

where n is the number of lattice points. One should note the difference between equation 2.15 for the energy of mixing in polymer networks and that for polymer solutions in section 2.3 (equation 2.13); the term related to the contribution of the polymer chains in the lattice is missing in the case of polymer networks because of the absence of single molecules in the network structure [38].

The elastic term in the total free energy (equation 2.14) can be obtained based on the rubber elasticity with a solvent taken in consideration:

$$\triangle F_{\text{el}} = (k_{\text{B}}T\nu_{\text{e}}/2)(3\alpha_{\text{s}}^2 - 3 - \ln \alpha_{\text{s}}^3), \tag{2.16}$$

where ν_e is the effective number of polymer chains in the network and α_s is the linear deformation factor which is considered to be equal in all directions ($\alpha_s = \alpha_x = \alpha_y = \alpha_z$) assuming the network is streched to the same degree in all directions.

The total free energy can be obtained by adding equations 2.15 and 2.16. By differentiating this total free energy with respect to the number of lattice points, one can obtain the chemical potential [38],

$$\mu_1 - \mu_1^0 = \bar{R}T \left[\ln(1-\phi) + \phi + \chi\phi^2 + v_1(\frac{\nu_e}{V_0})(\phi^{1/3} - \frac{\phi}{2}) \right], \qquad (2.17)$$

where $\bar{R}$ is the gas constant, V_0 is the total volume of the polymer network before swelling and v_1 is the molar volume of the solvent. At equilibrium, the chemical potential inside and outside the gel can be set equal to zero, and therefore the elastic and mixing terms in the total free energy must balance each other [38, 45, 40] giving:

$$0 = \mu_1 - \mu_1^0 = RT \left[\ln(1-\phi_m) + \phi_m + \chi\phi_m^2 + v_1(\frac{\nu_e}{V_0})(\phi_m^{1/3} - \frac{\phi_m}{2}) \right], \qquad (2.18)$$

and

$$-\left[\ln(1-\phi_m) + \phi_m + \chi\phi_m^2\right] = \frac{v_1\nu_e}{V_0}(\phi_m^{1/3} - \frac{\phi_m}{2}), \qquad (2.19)$$

where ϕ_m refers to the maximum polymer volume fraction at equilibrium. Equation 2.19 can be given in another form in terms of the molecular weight of the chain between two cross-links, M_c, and the specific volume of the polymer, $\bar{v}$, as:

$$-\left[\ln(1-\phi_m) + \phi_m + \chi\phi_m^2\right] = \frac{v_1}{\bar{v}M_c}(\phi_m^{1/3} - \frac{\phi_m}{2}), \qquad (2.20)$$

Equation 2.20 describes the swelling of an ideal polymer network and one must multiply the right side of this equation by the factor $(1 - 2M_c/M_n)$, where M_n is the molecular weight of an identical uncross-linked (linear) poly-

mer chain, as a correction for problems arising from unreacted chain ends. For ideal networks, where $M_n = \infty$, this factor tends to be 1.

The left side of equation 2.20 suggests that the chemical potential decreases due to the thermodynamic interactions between the polymer and the solvent; while the right side indicates an increase in the chemical potential given by the elastic force of the network.

If the swelling ratio, Q, is defined as the ratio between the swollen volume, V, and the unswollen volume, V_0, then the equilibrium swelling ratio, Q_m, can be obtained from equation 2.19 as [46, 38]:

$$Q_m^{5/3} \cong \frac{V_0}{\nu_0 v_1 (2 - \chi)}. \tag{2.21}$$

Equation 2.21 indicates the dependence of the swelling ratio on the quality of the solvent, χ, and the cross-link density in the polymer network.

2.5.1 Swelling of Ionic Networks

The swelling forces of polymer networks may be increased if they contain ionisable groups; these are polyelectrolyte networks. One of the most studied polyelectrolyte gels by Katchalsky *et al.* is poly(methacrylic acid) [PMAA] [47, 38], which carries carboxylic acid as ionisable groups.

In a solvent, for any charge located on a monomer there should be a counterion to balance the neutrality of the hydrogel. These counterions are confined within the gel to maintain the electroneutrality; this creates a significant osmotic pressure. An illustration is shown in Figure 2.3 for a polymer network with fixed negatively charged ions (for example PMAA) surrounded by their counterions and some other cations and anions diffusing in and out of the gel.

Weakly charged polymer networks have been studied extensively because of their unique swelling behaviour in salt and salt-free solutions. For example, Katchalsky *et al.* [47] studied the effect of the degree of ionisation on the swelling of PMAA networks; while Flory and Rehner developed the earliest theory to describe the swelling of ionic networks [38, 12]. In salt free solutions, the osmotic pressure is mainly due to the confined counterions interacting

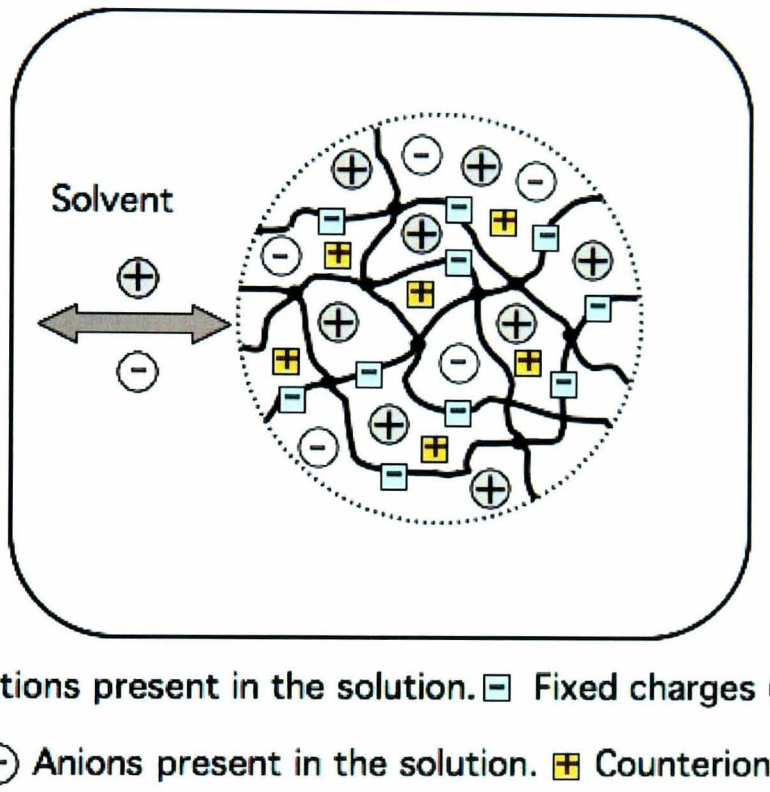

Figure 2.3: Schematic diagram showing the equilibrium swelling of a polyelectrolyte network (e.g. PMAA) similar to Donnan membrane equilibrium. The arrows indicate the free ions in the solution diffusing in and out of the polymer network through the outer part of the network (similar to a membrane), while the counterions are trapped inside the network, causing the osmotic pressure.

with their surroundings. However, when salt ions are present the system resembles Donnan membrane equilibria (Figure 2.3) where the polymer outer part acts as a membrane controlling the diffusion of ions in and out of the polymer network [38, 45]. The driving force for salt ions to move into the membrane is the electric interaction between the oppositely charged ions, while ions move out of the membrane because of the concentration gradient. These ions keep moving into and out of the membrane until an equilibrium is reached, this is called Donnan equilibrium.

In PMAA, for example, in the simplest case there is only one type of ion that can be considered to chemically bind to the network-fixed carboxylate (counterion); in this case the hydrogen ion (H^+). The electrostatic repulsions between the fixed ions are reduced (screened) when other ions are present in the solution (H^+ and OH^- in water solutions and other cations and anions in salt solutions). The equilibrium swelling of polyelectrolyte networks is described by the Flory theory of non-ionic gels (section 3.4) plus the osmotic pressure due to Donnan equilibrium [38]. This ionic effect can be added to the total free energy of the swollen gel, which can be given as [48]:

$$\triangle F = \triangle F_{\text{el}} + \triangle F_{\text{mix}} + \triangle F_{\text{ion}}, \tag{2.22}$$

where the added term to the non-ionic free energy equation, $\triangle F_{\text{ion}}$, is related to the ionic nature of the network and can be expressed as [49]:

$$\triangle F_{\text{ion}} = \triangle F_{\text{dis}} + \triangle F_{\text{Coul}}, \tag{2.23}$$

The term $\triangle F_{\text{dis}}$ represents the energy associated with the dissociation of the ionisable groups, which for a weakly charged polymer can be negligible, assuming no interactions between these charged groups as they are far apart in the chains; while the term $\triangle F_{\text{Coul}}$ is the energy associated with Coulombic interactions in the system.

Equation 2.22 can be given in terms of the chemical potential by:

$$\mu_1 - \mu_1^0 = \triangle \mu_{\text{el}} + \triangle \mu_{\text{mix}} + \triangle \mu_{\text{ion}}. \tag{2.24}$$

The first two terms of equation 2.24 were described in section 2.4 for non-ionic networks, which can be similar for weakly charged polyelectrolyte networks. However, it has been found that the ionisation of highly charged polymers affects the mixing and elastic terms in the total free energy [45]. Flory [38] used an osmotic pressure approach to determine the ionic term in equation 2.24. The osmotic pressure associated with the difference in ionic concentrations inside and outside the gel can be given by the following relation (the reader is directed to reference [38] for a full derivation):

$$\Pi_{\text{ion}} = RT \left[\frac{ic_2}{z_-} - \vartheta \left(c_{\text{s}}^* - c_{\text{s}} \right) \right], \tag{2.25}$$

where c_{s} and c_{s}^* are the total ion concentrations in the gel and in the solution, respectively; and ϑ is the valency factor of the ions in the solution. The term ic_2/z_- is the contribution from the ionisable groups in the polymer with ic_2 being the concentration of the fixed charges, where i is the degree of ionisation and z_- is the valency of these charged groups.

The total osmotic pressure for an ionic network is the sum of that of the mixing, elasticity and ions:

$$\Pi_{\text{total}} = \Pi_{\text{mix}} + \Pi_{\text{el}} + \Pi_{\text{ion}}. \tag{2.26}$$

The relationship between the total osmotic pressure and the equilibrium chemical potential is expressed by the following equation:

$$\Pi_{\text{total}} = - \left(\frac{\mu_1 - \mu_1^0}{\text{v}_1} \right). \tag{2.27}$$

When $\mu_1 - \mu_1^0 = 0$, at equilibrium, then equation 2.26 becomes:

$$\Pi_{\text{ion}} = - \left(\Pi_{\text{mix}} + \Pi_{\text{el}} \right). \tag{2.28}$$

The two terms on the right hand side of equation 2.28 can be calculated from equation 2.18, as for non-ionic networks. Hence, from equations 2.25 and 2.18 one can obtain the following relation for an ionic network at equilibrium:

$$\frac{ic_{2m}}{z_-} - \vartheta\left(c_s^* - c_s\right) = \frac{1}{v_1}\left[\ln(1-\phi_m) + \phi_m + \chi\phi_m^2\right] + \left(\frac{\nu_e}{V_0}\right)\left(\phi_m^{1/3} - \frac{\phi_m}{2}\right). \tag{2.29}$$

A special case of this equation is considered when $c_s^* > ic_2$ and the difference $c_s^* - c_s$ is comparable inside and outside the gel. The ionic osmotic pressure in this case can be given by the following relation [38]:

$$\Pi_{ion} \cong RT\frac{(ic_2)^2}{4S^*}, \tag{2.30}$$

where $S^* = \vartheta w c_s^*/2$ is the ionic strength with w being the valency of the fixed ions on the polymer network (the electrolyte). By substituting equation 2.30 into equation 2.29 one can obtain:

$$\frac{(ic_{2m})^2}{4S^*} \cong \frac{1}{v_1}\left[\ln(1-\phi_m) + \phi_m + \chi\phi_m^2\right] + \left(\frac{\nu_e}{V_0}\right)\left(\phi_m^{1/3} - \frac{\phi_m}{2}\right). \tag{2.31}$$

As for the non-ionic network in section 2.4, the swelling ratio of an ionic gel can be obtained from equation 2.31 as:

$$Q_{m,\,ion}^{5/3} \cong Q_{m,\,neut}^{5/3} + \frac{V_0}{4\nu_e v_u^2}\frac{i^2}{S^*} \tag{2.32}$$

where $Q_{m,\,neut}^{5/3}$ is the maximum equilibrium swelling ratio of a neutral polymer network (equation 2.21).

The Flory-Rehner theory for swelling of ionic networks, described above in this section, does not account for the solvent used during the polymerisation of the polymer network. Nonetheless, a similar theory was introduced by Peppas and Merrill [50, 48] who added a volume fraction term, ϕ_r, of the polymer after cross-linking but before swelling to the Flory-Rehner model (equation 2.29) which then reads:

$$\frac{ic_{2m}}{z_-} - \vartheta\left(c_s^* - c_s\right) = \frac{1}{v_1}\left[\ln(1-\phi_m) + \phi_m + \chi\phi_m^2\right] +$$

$$(\phi_r)\left(\frac{\nu_e}{V_0}\right)\left(\left(\frac{\phi_m}{\phi_r}\right)^{1/3}-\frac{\phi_m}{2\phi_r}\right). \tag{2.33}$$

Furthermore, neither Flory-Rehner theory nor the Peppas-Merrill model above takes into account the effect of the solvent on the degree of ionisation, i, which was considered later by Brannon-Peppas and Peppas [48, 45, 2] in their model to describe the pH effect on the swelling of anionic and cationic networks. Brannon-Peppas and Peppas introduced the degree of ionisation in terms of other variables of the polymer-solvent system,

$$i=\frac{K_a/[H^+]}{1+K_a/[H^+]}=\frac{K_a}{[H^+]+K_a}=\frac{K_a}{10^{-pH}+K_a}, \tag{2.34}$$

with some modification to the right hand side of equation 2.33, which gave for anionic network the following relation [48]:

$$\frac{1}{4S^*}\left(\frac{\phi_m^2}{\bar{v}}\right)\left(\frac{K_a}{10^{-pH}+K_a}\right)^2=\frac{1}{v_1}\left[\ln(1-\phi_m)+\phi_m+\chi\phi_m^2\right]+$$

$$(\phi_r)\left(\frac{\nu_e}{V_0}\right)\left(\left(\frac{\phi_m}{\phi_r}\right)^{1/3}-\frac{\phi_m}{2\phi_r}\right). \tag{2.35}$$

Similarly for a cationic network they obtained [45, 48]:

$$\frac{1}{4S^*}\left(\frac{\phi_m^2}{\bar{v}}\right)\left(\frac{K_b}{10^{pH-14}+K_a}\right)^2=\frac{1}{v_1}\left[\ln(1-\phi_m)+\phi_m+\chi\phi_m^2\right]+$$

$$(\phi_r)\left(\frac{\nu_e}{V_0}\right)\left(\left(\frac{\phi_m}{\phi_r}\right)^{1/3}-\frac{\phi_m}{2\phi_r}\right), \tag{2.36}$$

where K_a and K_b are the dissociation constants for acid and base, respectively, at equilibrium (see appendix B.1 for more details about these dissociation constants).

2.6 Diffusion

The basic form of any molecular motion is Brownian motion whereby molecules surrounding a colloidal particle, for example, hit it constantly in all directions making it jiggle and move in a random walk (diffusion). Therefore, diffusion is a process by which molecules are transported from one region of a system to another as a result of the random motions of these molecules [51]. This motion is well understood in the case of gases and uniform particles in solutions by considering Fick's and Einstein's laws. However, modifications are required in the case of macromolecules in solutions and in their melts, despite many theoretical and experimental successes in the past sixty years. This is because the molecular motion is dependent on viscosity, temperature and polymer conformations due to the interactions between the molecule and the surrounding environment [52, 53, 51, 40, 44]. Diffusion is only one process among others which is happening in electrolytic environments; for instance, acid-base reactions and many biological processes in the human body. Therefore, if the rate of the diffusion is low, it affects the overall process [52]. In the following sections, diffusion phenomena will be discussed starting from the basics with Fick's laws to those models that describe diffusion in polymeric systems.

2.6.1 Basic Concepts

If one assumes a gradient of a solute concentration in a solution, $\partial c/\partial x$, then according to the second law of thermodynamics and as mentioned above, this gradient is not stable but rather the molecules will diffuse throughout the system until a constant concentration is reached, assuming the system is thermodynamically stable in the mixed phase. If one imagines a flow across a cross section of area perpendicular to the concentration gradient, the flux (the rate of flow per unit area), J, is directly proportional to $\partial c/\partial x$ [54, 52]:

$$J = -D\frac{\partial c}{\partial x}, \tag{2.37}$$

where the proportionality constant D is the diffusion coefficient or the diffusivity with dimensions of (length)^2(time)$^{-1}$, c is the concentration and x is the distance in the direction of the diffusion. Equation 2.37 is called Fick's first law named after Adolf Fick who developed the first theory for diffusion in 1855 [52].

By applying the mass conservation law (the mass balance), one should obtain:

$$\frac{\partial c}{\partial t} = -\frac{\partial J}{\partial x}. \tag{2.38}$$

From Fick's first law and equation 2.38 one can obtain Fick's second law for diffusion, which describes the change in concentration with time, t, as:

$$\frac{\partial c}{\partial t} = -\frac{\partial}{\partial x}\left(-D\frac{\partial c}{\partial x}\right) = D\frac{\partial^2 c}{\partial x^2}. \tag{2.39}$$

Equation 2.39 normally describes diffusion in one dimension and can be given in three dimensions by:

$$\frac{\partial c}{\partial t} = D\left(\frac{\partial^2 c}{\partial x^2} + \frac{\partial^2 c}{\partial y^2} + \frac{\partial^2 c}{\partial z^2}\right) = D\nabla^2 c. \tag{2.40}$$

Based on Fick's laws, diffusion can be classified into two types: Fickian (Case 1) and non-Fickian (Case 2). In polymer systems there are a few examples that have been reported in the literature to obey Fick's laws. For instance, solvent diffusion in polymer networks was found to be Fickian at temperatures above the glass temperature (T_g) of the polymer. This was explained by the polymer network above T_g being in the rubbery state in which the polymer chains have a higher mobility that could allow solvent penetration [35]. In this case the solvent diffusion rate is slower than the relaxation rate of the polymer chains. On the other hand, when the mobility of the polymer chains is not high enough to allow immediate or rapid penetration of the solvent into the core of the polymer, the diffusion process is described as non-Fickian. This case of diffusion is normally observed at temperatures below T_g. Non-Fickian diffusion can be divided into Case 2 and anomalous diffusion; the only difference between them is the relaxation

rate of the polymer compared to the solvent diffusion rate. For Case 2, the solvent diffusion rate is faster than the relaxation rate of the polymer chains, while these rates are equal in anomalous diffusion [35].

2.6.2 Diffusion in Polymer Systems

Diffusion is of great importance in polymer dynamics, especially when scaled with other physical quantities such as molecular weight, concentration and temperature. In polymer systems, diffusion is normally characterised in terms of the lateral (translational) and rotational processes. Rotational diffusion, which can be characterised by the time it takes the molecules to reorientate themselves [55], is not the subject of this study. Translational diffusion may be divided into intra-diffusion and inter-diffusion (or mutual diffusion). Intra-diffusion can be subdivided into self-diffusion, when a molecule diffuses in an uniform system of identical molecules (see Chapter 8 for PNIPAM molecules diffusing in PNIPAM solutions), and probe tracer diffusion, when a molecule diffuses in a system that consists of different molecules (see chapters 5 and 6 for a probe diffusing in hydrogels and ferrogels) [56, 57, 58]. Inter-diffusion occurs in a two-component system due to the change in concentration gradient, i.e. an equal amount of each component diffuses within the other one in a fixed-volume. An example of inter-diffusion is the swelling of a polymer network by linear chains [59]. Again, the latter diffusion process in not the subject of this study.

Diffusion in polymer solutions and gels has been extensively studied in the last 50 years with some successful experimental and theoretical work. In the following sections the most successful theories for diffusion of macromolecules in dilute and semi-dilute solutions will be discussed.

2.6.2.1 Stokes-Einstein Relation

If a particle experiences a constant force, $\vec{f}$, pulling it through a liquid, it will move in the direction of the force at a constant velocity, $\vec{v}$. Therefore, this force can be correlated to the velocity by:

$$\vec{f} = \zeta \vec{v}, \tag{2.41}$$

where ζ is a quantity known as the friction coefficient. Because of the viscosity of the liquid there will be an equal and opposite force applied on the particle. Einstein introduced the relationship between the diffusion coefficient and the friction coefficient in terms of the absolute temperature, T and Boltzmann constant, k_{B} as [40]:

$$D = \frac{k_{\mathrm{B}}T}{\zeta}. \tag{2.42}$$

By assuming a spherical particle in a Newtonian liquid, one can obtain Stokes' law,

$$\zeta = 6\pi\eta R, \tag{2.43}$$

where R is the particle size and η is the viscosity of the liquid. By combining equations 2.42 and 2.43, one can obtain the Stokes-Einstein relation [40]:

$$D = \frac{k_{\mathrm{B}}T}{6\pi\eta R}. \tag{2.44}$$

The Stokes-Einstein equation can describe self-diffusion of macromolecules in dilute solutions, which can be utilized in this case to obtain the hydrodynamic radius of a polymer coil as:

$$R_{\mathrm{H}} = \frac{k_{\mathrm{B}}T}{6\pi\eta D}. \tag{2.45}$$

The relationship between the hydrodynamic radius, R_{H}, and the radius of gyration, R_{g}, is highly dependent on the shape of the polymer chain and can be given by:

$$R_{\mathrm{g}} = \rho R_{\mathrm{H}}, \tag{2.46}$$

where ρ is a constant that is predicted for spherical molecules to be $\sqrt{3/5}$ [40].

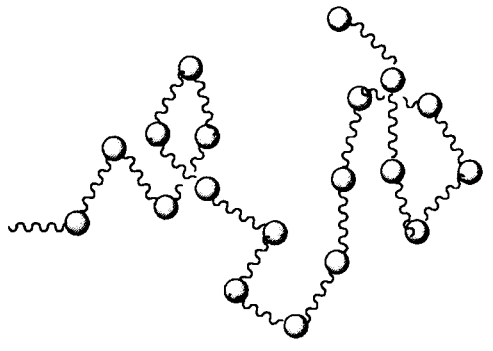

Figure 2.4: A polymer chain in Rouse model consists of N beads connected by springs.

2.6.2.2 Rouse Model

The earliest model to describe the diffusion of macromolecules was introduced by Rouse who assumed the polymer chain consists of N beads connected by springs, as shown in Figure 2.4. In a Rouse chain, there are only interactions between the beads through the springs connecting them and each bead has its own friction coefficient, ζ_b. Under the assumption that there is no interactions between the solvent and these beads, the total friction can be given as the sum of the friction from the N beads [40, 60, 61]:

$$\zeta_R = N\zeta_b. \tag{2.47}$$

By substituting equation 2.47 into Einstein's relation (equation 2.42), one can obtain the Rouse diffusion coefficient as [40]:

$$D_R = \frac{k_B T}{\zeta_R} = \frac{k_B T}{N\zeta_b}. \tag{2.48}$$

2.6.2.3 Zimm Model

If a particle moves through a liquid, the viscosity of the liquid must resist this movement and the diffusing particle has to drag some of the surrounding solvent with it. This results in a force applied on the diffusing molecules which is the hydrodynamic interaction. The Rouse model did not take these interactions between the solvent and the beads into account; this can be

easily corrected for a polymer melt but not for a dilute solution [40, 44, 39].

In a dilute solution, hydrodynamic interactions between the monomers themselves and between them and the solvent within the pervaded volume are strong. Therefore, the molecule drags the solvent with its movement within the pervaded volume. The Zimm model considers the polymer chain as a solid object diffusing in the surrounding solvent with a size of $R \approx bN^{\nu}$. where, b is the monomer size and ν is the reciprocal of the fractal dimension of the polymer (for a linear polymer in its melt $\nu = 1/2$, otherwise it depends on the quality of the solvent). The friction coefficient of this chain can be given in terms of solvent viscosity, η_{s} , by Stokes' law [40]:

$$\zeta_{\mathrm{Z}} \approx \eta_{\mathrm{s}} R. \tag{2.49}$$

As polymer chains are not spherical, the numerical coefficient in Stokes' law, 6π, has been discarded. By substituting the Zimm friction coefficient into the Einstein relation (equation 2.42), one can obtain the Zimm model for diffusion:

$$D_{\mathrm{Z}} = \frac{k_{\mathrm{B}}T}{\zeta_{\mathrm{Z}}} \approx \frac{k_{\mathrm{B}}T}{\eta_{\mathrm{s}}R} \approx \frac{k_{\mathrm{B}}T}{\eta_{\mathrm{s}}bN^{\nu}}. \tag{2.50}$$

For an ideal chain, Zimm calculated the hydrodynamic interactions and added an extra coefficient of $8/(3\sqrt{6\pi^3})$ as [40]:

$$D_{\mathrm{Z}} = \frac{8}{3\sqrt{6\pi^3}} \frac{k_{\mathrm{B}}T}{\eta_{\mathrm{s}}bN^{\nu}} \cong 0.196 \frac{k_{\mathrm{B}}T}{\eta_{\mathrm{s}}R}. \tag{2.51}$$

2.6.3 Temperature Dependence of Polymer Diffusion

Studying the temperature dependence of diffusion in polymeric systems leads to a greater understanding of the behaviour of these systems in response to changes in temperature, which might be of great importance for many applications in biology and medicine. By considering Stokes-Einstein diffusion (equation 2.44), one realizes that the diffusion coefficient depends strongly on temperature. The size of the molecule does not depend on temperature in this case and therefore it is constant (only in the Stokes-Einstein relation).

Thus, the diffusion is mainly controlled by the temperature dependence of viscosity, $\eta(T)$.

The viscosity of a polymer solution is generally proportional to the product of the relaxation time, τ, and modulus at this time, G [53, 40]:

$$\eta \approx G\tau. \tag{2.52}$$

The relationship between any relaxation time (Zimm or Rouse) and the temperature is given in terms of the friction coefficient as [40]:

$$\tau \sim \frac{\zeta}{T}. \tag{2.53}$$

The dependence of the modulus at any relaxation time is generally expressed by

$$G \sim \rho T, \tag{2.54}$$

where ρ is the mass density. Because an understanding of the dependence of the friction coefficient on temperature is still lacking, the temperature dependence of viscosity can be expressed in the simplest form, the Arrhenius equation, as [40]:

$$\eta(T) \sim \exp\left(\frac{E_\mathrm{a}}{k_\mathrm{B}T}\right), \tag{2.55}$$

where E_a is the activation energy, which is a constant at high temperatures.

One can use equation 2.55 in the Stokes-Einstein equation which results in an Arrhenius relation between the diffusion coefficient and temperature [62]:

$$D = \left(\frac{k_\mathrm{B}}{6\pi\eta R}\right)\exp\left(-\frac{E_\mathrm{a}}{k_\mathrm{B}T}\right). \tag{2.56}$$

This diffusion model is valid if the diffusion is controlled soley by the dynamics of solvent molecules; therefore, the activation energy of the diffusion is close to that of the viscosity. To examine this Arrhenius model, one can plot $\ln D$ against the reciprocal of temperature, $1/T$, and obtain a linear

relationship [35]. The disadvantage of this theory is that it can be applied only at high temperatures where the viscosity and relaxation times depend strongly on temperature. Another disadvantage is that this theory does not provide any correlation between the diffusing molecules and the medium in which they are diffusing.

The first problem with the Arrhenius theory, the requirement of high temperatures, can be solved by using another form of viscosity relation with temperature called the Vogel-Fulcher relationship [53, 40]:

$$\eta = \eta_0 \exp\left(\frac{E_a}{T - T_0}\right), \tag{2.57}$$

where T_0 is the Vogel-Fulcher temperature at which the relaxation time appears to diverge. Again, by using the Vogel-Fulcher viscosity equation (equation 2.57) in the Stokes-Einstein relation (equation 2.44), one obtains a diffusion coefficient dependence on temperature as:

$$D = D_0 \exp\left(-\frac{E_a}{T - T_0}\right). \tag{2.58}$$

Chapter 3

Responsive Water-based Systems

3.1 Introduction

Smart or responsive water-based polymeric systems are water-soluble polymers that show interesting shape transition behaviours. These materials are generally environmentally friendly and of great importance for many medical and industrial applications. The behaviour of polymeric systems in water is controlled by many factors including polymer architecture, concentration, and the external stimulus applied to the system. In this chapter, two different water-soluble polymeric materials will be discussed including their theory and applications: polymer networks and highly branched polymers. Cross-linked polymers (polymer networks) can be swollen by water to form so-called hydrogels. These hydrogels show interesting volume transitions between swollen and collapsed states in response to small changes in the physical or chemical properties of the system. Hydrogels that are responsive to pH, temperature and ionic strength will be considered in this work. Other physical stimuli, such as magnetic fields, can be also applied to hydrogels if they have the appropriate functionality. Hydrogels can be made magnetically responsive (ferrogels) by introducing magnetic nanoparticles to them before or after polymerisation. Temperature-responsive polymers, such as poly(*N*-isoporopylacrylamide) (PNIPAM), are examples of smart polymers that can be tuned by a small change in temperature around their critical transition

points. Modifying the architecture of such polymers results in changing their temperature response. In this chapter, the effect of PNIPAM branching on its response to temperature will be considered. Diffusion of single molecules within the above mentioned polymeric systems is a powerful means of exploring the internal structure of such materials. The control of the inter- and intra-diffusion of macromolecules in these systems is also of great interest for biomedical and drug delivery and release applications.

3.2 Polymer Gels and Networks

3.2.1 Hydrogels

As described in Chapter 2, polymer architecture plays a significant role in controlling the properties of polymer systems. For instance, polymer networks, which are physically or chemically cross-linked chains, have different physical and mechanical properties from (uncross-linked) linear chains. These networks are formed by connecting polymer chains by strong bonds (chemical or physical) resulting in a three-dimensional macroscopic molecule in a process called gelation. Gelation is a very complicated transformation of matter from a liquid (a sol) to a solid-like (a gel) at a critical gelation point, at which all polymer chains are connected together. The main property of polymer networks is their capability to resist the solvent introduced to them, as they cannot be dissolved in solvents but rather they swell in good solvents. This swelling process can be characterized by the swelling ratio which may be the ratio between the volume or the mass in the swollen state to that in the deswollen or dry state (Figure 3.1). Swollen networks are called gels and if the solvent is water then they are known as hydrogels. In other words, a hydrogel is obtained when a hydrophilic polymer network uptakes a large amount of water by expanding the polymer chains between cross-links. Once the solvent is removed, these networks retain their original form, which makes them good candidates for many industrial and medical applications. Surface coating, paper, photographic and food industries as well as tissue engineering and drug delivery and release are good examples which illustrate

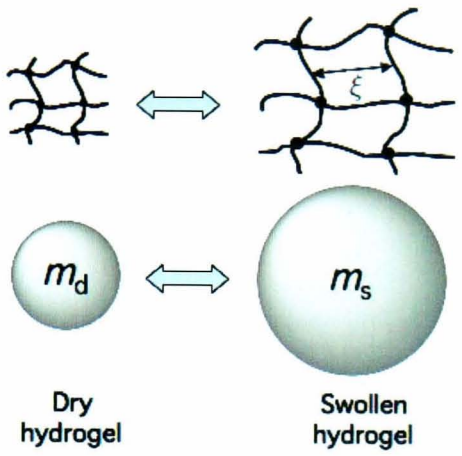

Figure 3.1: Hydrogel swelling measurements, where the swelling ratio can be determined by the ratio of the swollen mass (m_s) and dry mass (m_d). The characteristic length scale in hydrogels is the average mesh size, ξ.

the importance of such materials [63, 64, 40, 4, 53].

In addition to the classification of polymer networks based on the charged nature of the chains forming the networks, which was described in Chapter 2, they can also be classified according to the type of the bonds connecting the polymer chains. For example, monomers may have a multi-functionality that can form covalent bonds connecting these monomers in a three-dimensional network. An alternative way is to covalently cross-link polymer chains to form the network; rubber is an example of this latter process. Both of these gels are known as a "chemical gels", which are permanent and irreversible. However, they can undergo volume phase transition when exposed to a solvent. In contrast, the physical interactions between linear polymer chains, including hydrogen bonding and Van der Waals forces, enable a thermoreversible "physical gel" to take place. The following sections will discuss physical and chemical hydrogels and their response to the surrounding environments.

3.2.1.1 Chemical Hydrogels

Chemical hydrogels are stable and permanent gels due to the covalent bonds introduced by the cross-links. This type of gel can be formed by polymerising monomers in the presence of a cross-linker and an initiator to start the poly-

merisation. Microgels (gel molecules with a size smaller than 100 μm) and nanogels (small hydrogels with size smaller than 100 nm) have been reported in the literature which can be distinguished from three-dimensional bulk hydrogels [57]. There are many ways to polymerise chemical gels, such as radical polymerisation, UV polymerisation, gamma rays and X-ray polymerisation [65, 66]. The mechanical and physical properties of chemical hydrogels depend strongly on the density of cross-linker in the gel medium. For example, the characteristic length scale (mesh size, ξ, Figure 3.1) can be controlled by the amount of cross-linker added during the polymerisation. However, chemical gels are usually heterogeneous due to the cross-linkers not being homogeneously distributed in the medium during polymerisation. This can form clusters and defects in the hydrogel. Defects in chemical hydrogels also arise from non-reacted parts of the chains which can form dangling ends or chain loops [40].

There are three processes to prepare chemical hydrogels: condensation, vulcanization and addition polymerisation. The condensation process usually starts with a monomer solution or melt in which the monomers can react with each other if they have a functionality of three or more, while the vulcanization reaction starts with long polymer chains that can be cross-linked by covalent bonds through a cross-linker. An example of the vulcanization process is cross-linking natural rubber with sulfur, which was introduced by Goodyear in 1839 [40]. In the addition polymerisation process, a free radical transfers from one monomer to another resulting in the formation of a chemical bond. Since some monomers have two double bonds, they can react twice with free radicals to form cross-links. This latter process has been utilized to make the chemical hydrogels used in this study (see Chapter 5, section 5.2.1.1).

3.2.1.2 Physical Hydrogels

In physical gels, the cross-linking is due to weak or strong physical interactions which results in either weak or strong physical gels. Glassy and microcrystalline or double and triple helixes are examples of strong physi-

cal gels. Such systems are generally known as thermoreversible gels as the bonds break at high temperatures and reform at lower temperatures. At a given set of experimental conditions, strong physical gels are analogous to the chemical gels described above. In contrast, weak physical interactions, such as hydrogen bonds and ionic associations, form physical gels that have temporary cross-links with a finite lifetime as they can break and reform continuously. This lifetime is important to distinguish between strong and weak physical gels. If the lifetime is sufficient enough for a gel to appear like a solid, it can then be considered as a strong physical gel. Microphase separation in block copolymers to form micelles is an example of weak physical gels [53, 40, 57, 67].

3.2.1.3 pH and Salt Effects on Chemical Hydrogels

The swelling behaviour of ionic networks was introduced in Chapter 2, section 2.4.1. pH-sensitive hydrogels are weak polyelectrolytes having acidic or basic groups which can accept or donate protons in response to the pH environment. Altering the ionization of these groups results in a net charge giving rise to more repulsion or attraction forces. These forces in turn cause the swelling and collapse of polymer gels which is always explained by an osmotic pressure effect. In general, polymers can be classified into neutral and charged (see Chapter 2). However, charged linear polymers as well as cross-linked polymer gels can be subdivided on the basis of functional groups into polyacids and polybases. Polyacids, such as poly(methacrylic acid) (PMAA), have carboxylic acid groups that accept protons at low pH and donate protons at high pH. However, at high pH it is argued that the swelling degree decreases at some point due to charge shielding [68, 3]. On the other hand, polybases, such as poly(N,N'-diethylaminoethyl methacrylate) (PDEAEMA), show the opposite effect as they become ionized at low pH due to the release of protons, which is indicated by high swelling degrees at low pH.

The oscillation between swollen and collapsed states by changing the pH of the solution has been observed and reported many times in the literature

mimicking biological muscles. For instance, Crook and co-workers [68] observed the ability of PMAA hydrogels to change their size periodically with an oscillating pH between 3 and 7. Similar results were reported by Deen *et al.* [69], showing the ability of hydrogels synthesized by copolymerizing N-acryloyl-N'-ethyl piperazine (AcrNEP) and methyl methacrylate (MMA) to oscillate periodically when alternating the pH between 2.6 and 7.

Various microscopic (e.g. scanning electron microscopy SEM and atomic force microscopy AFM) and spectroscopic (e.g. SANS and SAXS) techniques have been used to explore the internal structure of hydrogels in response to external stimuli. For example, He *et al.* [70] used SEM amongst other techniques to study the morphology of PMAA hydrogels swollen by water and a solvent mixture of water and ethanol. There results (Figure 3.2) showed that it is not only the pore size that is dependent on the quality of the solvent but the morphology of the walls between these pores; solvent containing higher amount of water gave a hydrogel with smaller pores and thicker walls.

The presence of simple salts like NaCl and $CaCl_2$ has been observed to affect the swelling behaviour of hydrogels and some other physical properties, such as shear modulus [71, 72, 73, 74]. For almost all polyelectrolytes in solution, it is known that at very low salt concentrations the electrostatic repulsive forces increase, leading to an increase in the swelling degree until a critical point is reached at which charge screening takes place. Beyond this point, a dramatic volume transition takes place depending on the nature of the charges in the solution. The discussion in Chapter 2 showed the dependence of the swelling of ionic hydrogels on ion valency. This explains the reported results in the literature in which $CaCl_2$ was found to introduce a stronger effect on the gel structure than NaCl [74, 75, 76].

3.2.2 Nanocomposite Hydrogels

Conventional hydrogels described in section 3.2.1 are reasonable materials for certain tasks. However, some applications require materials with improved properties, which can be fulfilled by introducing other organic or inorganic materials into the hydrogels. The resulting multiphase solid materials are

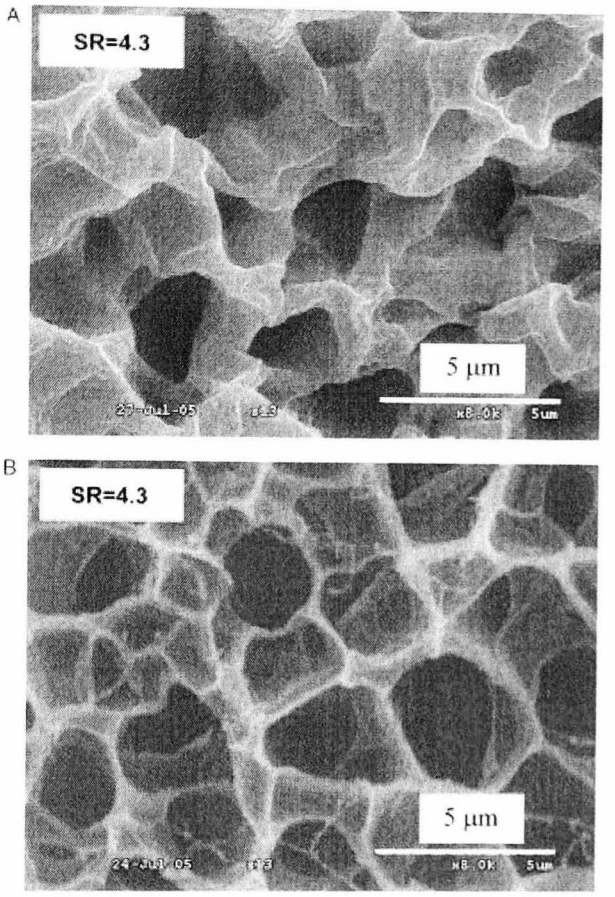

Figure 3.2: SEM images of swollen PMAA hydrogels with swelling ratio SR= 4.3 in different pH solutions: (A) pH= 6.2 and (B) pH= 3.0. The solvent is a mixture of (A) 9:1 and (B) 1:4 water and ethanol. (Taken from H. He and co-workers, Photopolymerization and structure formation of methacrylic acid based hydrogels in water/ethanol mixture, *Polymer*, **47**, p1612, Copyright (2006) with permission from Elsevier Science)[70], see appendix A.1.

known as composite hydrogels. If at least one phase has one, two or three dimensions at the nanoscale (1-100 nm), a nanocomposite hydrogel will be obtained [10, 77, 78, 79]. The presence of these nanostructured materials in the gel composite exhibits significant improvements in the properties of the system including mechanical behaviour, molecular permeability and the control of drug delivery and release. In some situations, the introduced nanostructured materials yield new properties that cannot be found in the original polymer matrix. For example, introducing magnetic nanoparticles to polymer networks results in nanocomposite gels with magnetic properties which would not be achieved with traditional hydrogels. This type of nanocomposite hydrogels is known as a "ferrogel", which will be discussed in the following section.

3.2.2.1 Ferrogels

Ferrogels are magnetic hydrogels which are fabricated by introducing magnetic nanoparticles ($\sim$ 10 nm) into polymer networks during or after polymerisation. The presence of these magnetic nanoparticles enhances the influence of external magnetic fields on hydrogels. The concept of "ferrogels" was first introduced in 1995 by Zrínyi and co-workers, who synthesised magnetic gels by introducing Fe_3O_4 nanoparticles into poly(N-isopropylacrylamide) (PNIPAm) and poly(vinyl alcohol) (PVA) networks [7, 17, 16]. The authors first studied the mechanical properties of such materials in uniform and nonuniform magnetic and electric fields [80]. Their results showed that uniform magnetic fields align ferrogel beads in the direction of the applied magnetic field, whereas nonuniform fields form aggregates of ferrogel beads. This was explained by, in the case of nonuniform magnetic fields, the field-particle interactions being dominant, causing the particles to experience a dielectrophoretic or magnetophoretic force, resulting in the particles being attracted to the regions of stronger magnetic field intensities. In contrast, in uniform magnetic fields there is no field gradient and therefore there are no field-particle interactions. In this case, particle-particle interactions are dominant and the attractive forces between these particles influence the gel

structure. These results suggested many potential applications in which these ferrogels can work as magnetic actuators.

Several researchers have used different techniques to investigate the mobility of magnetic nanoparticles within the ferrogel matrix. For example, works by Török and co-workers involving neutron spin echo (NSE) and small-angle neutron scattering (SANS) confirmed that there is no translational diffusion of Fe_3O_4 nanoparticles within PVA ferrogels [81, 82]. X-ray photoelectron spectroscopy (XPS), which can measure the binding energy, was used by Hu *et al.* [83] who found that magnetic nanoparticles were chemically attached to polymer chains in the ferrogel.

The last decade has seen an increase in the number of studies of ferrogels in terms of their synthesis and characterisation. For instance, Chatterjee and co-workers [84] synthesized a biodegradable magnetic gel by cross-linking hydroxypropyl cellulose and maghemite. Their study showed a uniform distribution of magnetic particles as a result of using a surfactant, cetyldimethylethylammonium bromide (CTAB), to modify the surface of the ion oxide nanoparticles. The magnetic properties of the ferrogels in this study showed a broad range of blocking temperatures below room temperature. Therefore, a superparamagnetic behaviour of these materials was reported.

A novel type of ferrogel was obtained by Qin *et al.* [85] who used Pluronic F127 copolymer (a copolymer of poly(ethylene oxide) and poly(propylene oxide)) and superparamagnetic iron oxide nanoparticles to synthesize an injectable ferrogel. This type of ferrogel has the advantage of being temperature and magnetic field-sensitive. Thus, below its temperature transition point, it is in the form of a "sol" (or liquid) that can be injected into the body, for example, with drug or biological cells incorporated with it [86]. The release of the drug from these ferrogels after the injection can be controlled by the applied magnetic field.

Another approach to prepare ferrogels was demonstrated by Reséndiz-Hernández and co-workers [87], which involved the use of freezing-thawing technique to form a ferrogel of PVA and magnetite nanoparticles ($\sim$ 12 nm) without the need for cross-linkers. However, the disadvantage of this technique is that magnetic nanoparticles form large agglomerates ($\sim$ 58 nm)

inside a PVA matrix resulting in a superparamagnetic behaviour of the ferrogel.

In another study by Czaun *et al.* [88], it was found that it is possible to employ magnetic nanoparticles as nano cross-linkers to replace the conventional cross-linking agents that might be toxic. The authors used the "grafting from" method, in which an initiator is used to grow polymer chains from inorganic surfaces, to functionalize iron nanoparticles via atom transfer radical polymerisation (ATRP). Although this novel approach to prepare ferrogels might help to reduce the risk of toxicity, the mechanical and swelling properties of the resulting ferrogels have not been tested.

The type of magnetic particles used to prepare ferrogels plays a significant role in determining the magnetic and mechanical properties of the ferrogel. The most reported materials for this purpose in the literature are magnetite and maghemite. However, other magnetic compounds can be used to obtain ferrogels. For example, cobalt-ferrite ($CoFe_2O_4$) was utilized in a study by Monz *et al.* [89]. In this study, the authors investigated the magnetic properties of ferrogels containing $CoFe_2O_4$ and their analogy, ferrofluids. The transformation from a superparamagnetic behaviour in the ferrofluids to a ferromagnetic behaviour was observed. This was explained by $CoFe_2O_4$ nanoparticles showing Néel relaxation when in the gel matrix which is responsible for the magnetization hysteresis, whereas Brownian rotational relaxation is restricted due to particle-polymer mechanical interactions. In contrast, Brownian rotational relaxation is dominant in ferrofluids leading to a superparamagnetic behaviour.

3.2.2.2 Applications of Ferrogels

The magnetic properties of ferrogels, mentioned in the previous section, have made them useful materials for many possible applications including bio-separation, artificial mussels and molecular delivery and release. However, the focus of this section will be on the use of ferrogels for molecular delivery and release under applied magnetic fields. In fact, there are two mechanisms for the use of ferrogels as delivery carriers, depending on the size of the

molecules (solute) required to be delivered; these are illustrated in Figure 3.3. In the first case, the solute molecule size is small compared to the mesh size of the ferrogel and therefore, under applied magnetic fields, when the ferrogel contracts, solute molecules can be expelled out of the gel medium depending on the magnetic field strength. In the second case, the solute molecule size is comparable to or larger than the mesh size of the ferrogel. As the mesh size becomes smaller in the applied magnetic field, solute molecules get trapped inside the polymer network, restricting their release to the surrounding environment. When the magnetic field is removed, the ferrogel swells again and releases the trapped molecules.

There are a few examples in the literature in which drug release (the first case described above) from ferrogels has been described. For instance, Liu *et al.* [90, 83] showed that drug release rate can be controlled by an on-off magnetic field switch and the time duration between two alternating on-off operations. This study also showed that the size of Fe_3O_4 nanoparticles in the PVA and gelatin ferrogel affects the performance of the system, as larger Fe_3O_4 nanoparticles result in more sensitivity due to their stronger saturation magnetisation and smaller coercive force (see Figure 3.4). Another study by the same authors exhibited a similar behaviour of gelatin-Fe_3O_4 ferrogels in which the release rate of vitamin B_{12} was found to decrease by almost 10% in a magnetic field [91].

In another study, Satarkar and Hilt [92] found that the application of a high frequency (300 kHz) alternating magnetic field (AMF) to ferrogels made of temperature-sensitive polymers, such as PNIPAm, can control their transition temperature given that magnetic nanoparticles generate heat in AMF due to Néel and Brownian relaxations. This can be used to enhance the rate of drug release by a pulse application of AMF. These authors also reported the use of these ferrogels as valves in microfluidic devices [93].

3.3 Temperature-responsive Polymers

In addition to the polymeric systems that are responsive to pH, ionic strength and magnetic fields, described previously in this chapter, there are some poly-

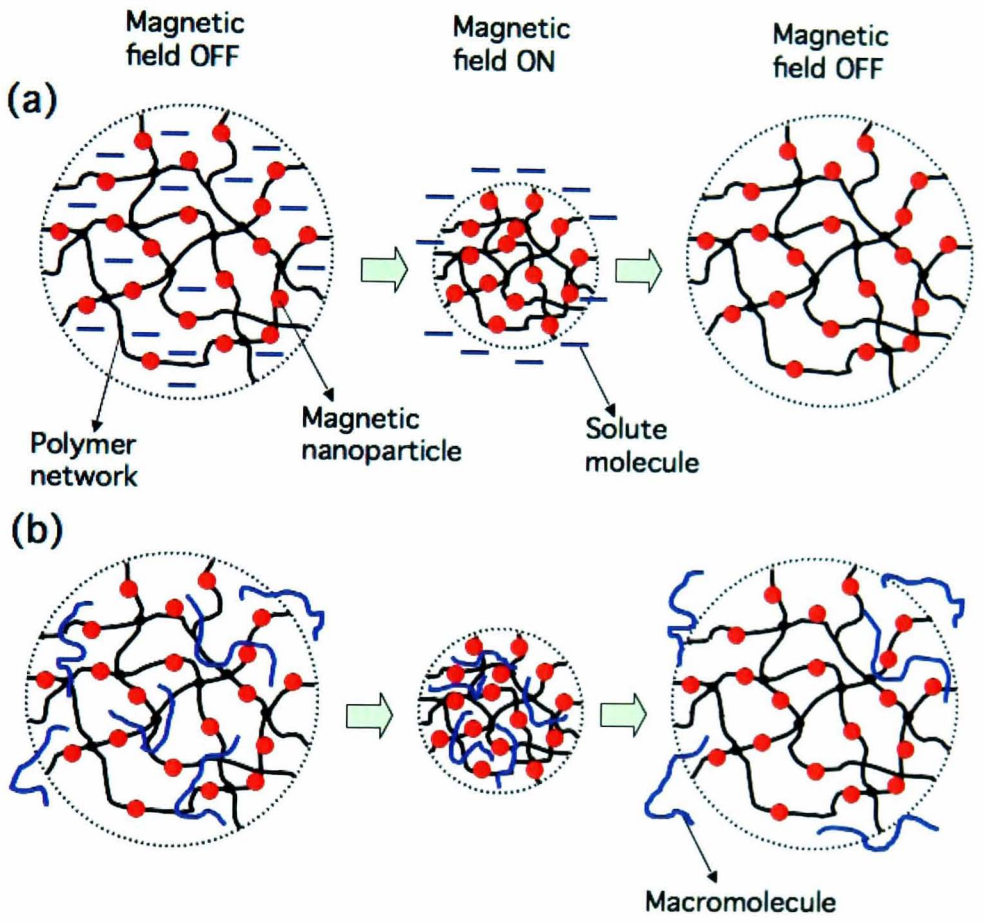

Figure 3.3: Schematic diagram showing the mechanism by which a ferrogel responds to an external magnetic field. In zero magnetic field, the ferrogel can be swollen and drug molecules, for example, can penetrate the network. When an external magnetic field is applied, the ferrogel contracts and releases drug molecules to the surrounding environment. Once the magnetic field is removed the ferrogel retains its original state. In diagram (a), small drug molecules are released once the ferrogel contracts. On the other hand, diagram (b) shows large molecules which are trapped under the applied magnetic filed but can be released by removing the magnetic field.

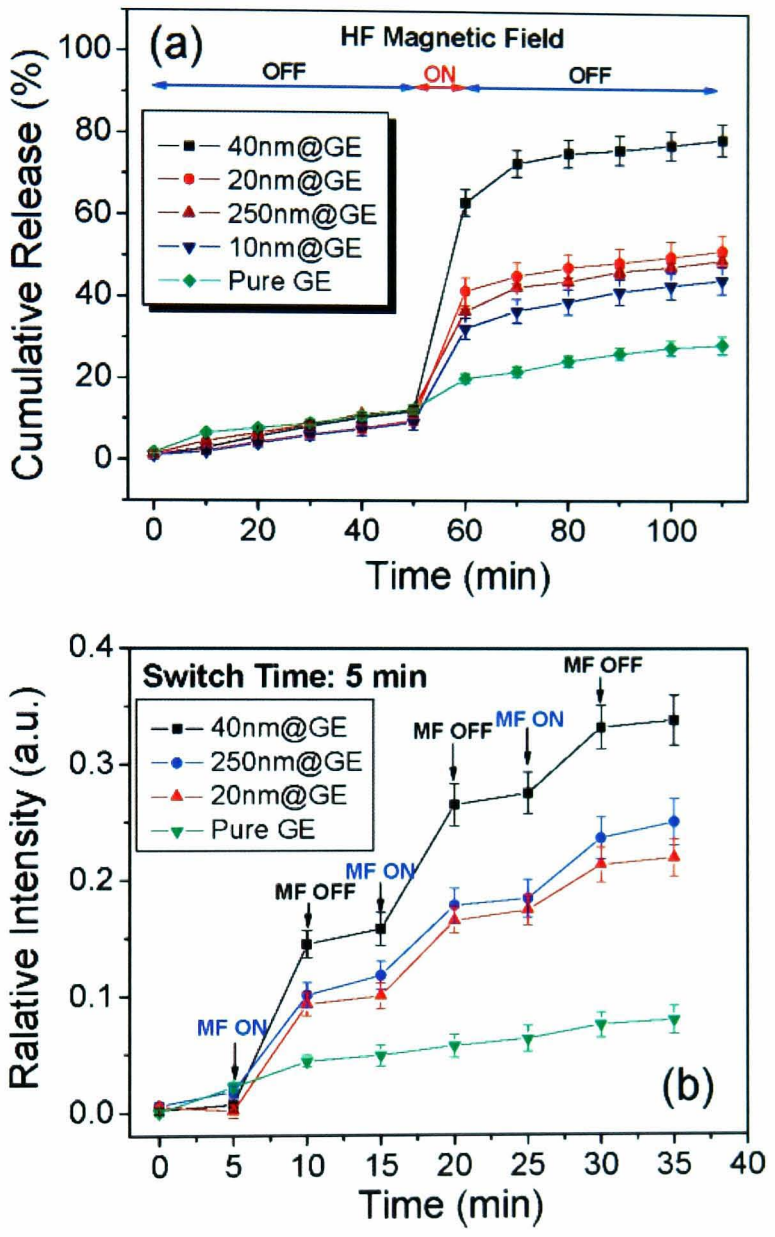

Figure 3.4: Drug release behaviour of gelatin ferrogels under a high-frequency magnetic field. Plot (a) shows the behaviour of the ferrogels when exposed to the magnetic field for 10 min; whereas plot (b) illustrates the effect of on-off operation of magnetic field on the drug release from gelatin ferrogels. In both cases there is an effect of the size of magnetic nanoparticles on the performance of the system. (Taken from S.H. Hu and co-workers, Controlled Pulsatile Drug Release from a Ferrogel by a High-Frequency Magnetic Field, *Macromolecules*, **40**, p6786, Copyright (2007) with permission from the American Chemical Society [83], see appendix A.1).

mers which are highly responsive to temperature. The most widely investigated responsive systems are those stimulated by temperature and pH due to their ease of modification under laboratory conditions and their potential use in biomedical applications, both *in vivo* and *in vitro*. For example, temperature-responsive polymers have been considered as candidate smart materials for tissue engineering applications [94] and delivery vehicles for therapeutic agents [95, 6].

In general, the thermoresponsive nature of these polymers exists because they possess a critical solution temperature. The solubility of a polymer in water is changed dramatically at this temperature which leads to a transition between swelling and collapsing. A well known example is gelatin, in which the solubility decreases with decreasing temperature and at an upper critical solution temperature (UCST) this polymer undergoes a phase transition from a solution to a gel. However, many other temperature responsive polymers display reversed solubility. In other words, these polymers have been observed to undergo a sudden decrease in solubility as the temperature of the system increases. The temperature at which this reverse phase transition occurs is the lower critical solution temperature (LCST), as shown in Figure 3.5. The LCST here indicates a transition from hydrophilic to hydrophobic structures. This phenomenon is thermodynamically described as a result of a small change in entropy which leads to a transition from a random polymer coil to a collapsed polymer (or globule). However, this globule structure is a highly disordered system.

The most widely studied thermoresponsive polymers are poly(*N*-alkylacrylamide)s due to their ease of synthesis via free radical polymerisations. Moreover, the LCST of this class of materials can be controlled by using various alkyl groups, which in turn change the balance between hydrophobicity and hydrophilicity. It is also possible to copolymerize these polymers with some other desired materials to control their LCST. One of the most widely used polymers of this class is poly(*N*-isopropylacrylamide) (PNIPAM) which has a sharp phase transition around its LCST of 32°C. Because the LCST of PNIPAM is close to the body temperature, it is a popular polymer for use in many proposed applications [96, 20]; for these reasons there have been

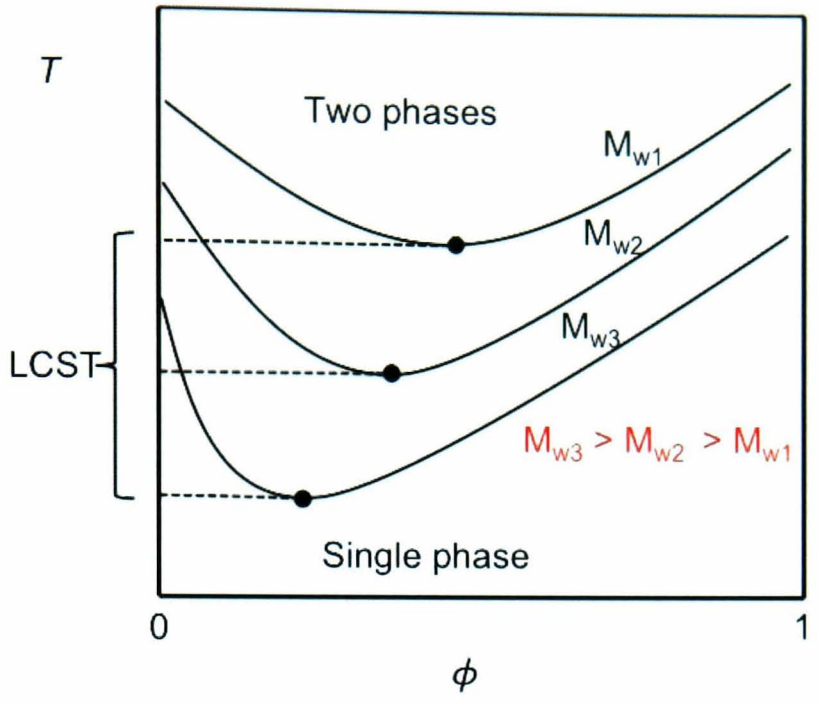

Figure 3.5: Schematic diagram showing the phase diagram of a polymer binary mixture indicating the change of LCST with molecular weight.

many attempts to increase this transition temperature to be closer to 37°C. The following sections will discuss the thermodynamics of PNIPAM and the possibility of controlling its LCST.

3.3.1 Thermodynamics of PNIPAM

The reversible solubility of PNIPAM was first reported by Scarpa *et al.* in 1967 [97]; however, a full understanding of the mechanism of this phase transition is still lacking. The scope of this section is only concerned with the basic mechanism by which the LCST of PNIPAM is controlled including some factors that affect this LCST. For more details about the historical and current discussions about the LCST of PNIPAM, the interested reader is referred to some reviews in the literature [20].

A remarkable change in solubility of linear PNIPAM chains in aqueous solution is observed at 32°C. Below this temperature, linear PNIPAM chains are in the form of individual extended coils which is a characteristic of a polymer dissolved in a good solvent. Above this temperature, PNIPAM coils

collapse and form aggregated globular structures which precipitate out of solution. This can also be observed at the macroscopic level, at high polymer concentration, as a change from a clear to a cloudy solution.

As described in Chapter 2, section 2.3, any solubility process or mixing can be explained by the second law of thermodynamics (equation 2.11). Below the LCST of the polymer, Gibbs free energy is dominated by the enthalpy term which is favourable for interactions such as hydrogen bonding between water molecules and the amide moiety of PNIPAMs. Once the temperature increases, hydrogen bonds formed earlier will break, increasing the entropy of the system until it overcomes the enthalpy and the Gibbs free energy becomes positive which leads to the collapse of the polymer.

The phase transition behaviour of PNIPAM can be explained by two distinct polymer-solvent interactions. First is the hydrophobic effect, which is a result of water molecules orienting themselves around non-polar regions of the polymer (i.e. the isopropyl groups), forcing the isopropyl groups to associate with the polymer backbone to form aggregates. The second effect is the hydrogen bonding effect, which is a result of water molecules orienting themselves around amide moieties [20, 98]. These two effects were first suggested by Heskins and co-workers in 1968 [99] when they introduced the "ice like" behaviour of water molecules around amide and isopropyl groups. However, different research groups have reported, with evidence, each effect independently as the driving force for the phase transition [100, 101, 102, 103, 104]. Soon after these arguments, Winnick [105] suggested that both effects are important in the phase transition behaviour of PNIPAM, which is the conclusion that was drawn in Schild's review in 1992 [20].

The Flory-Huggins theory of solubility and mixing of polymer solutions (see Chapter 2) included a characteristic parameter (the interaction parameter, χ) that describes the strength of the interactions between the solvent molecules and the monomer units within a polymer. The quality of solvents can be classified based on this interaction parameter. In conditions where $\chi = \frac{1}{2}$ (the θ point), the polymer-solvent interactions are balanced by monomer-monomer interactions and the polymer is said to be an ideal random coil. When $\chi < \frac{1}{2}$, the solvent is described as "good", in which

monomers effectively repel each other and monomer-solvent interactions are energetically favourable for mixing. Therefore, the polymer is in a swollen random coil conformation. By contrast, when $\chi > \frac{1}{2}$, the solvent is "poor", in which the solvent-monomer interactions are weak and the polymer exists in a collapsed conformation [40, 106].

According to the second law of thermodynamics, mixing and solubility are dependent on temperature. Thus, ideal θ conditions occur only at a specific temperature which is called the θ temperature. For example, the transition temperature of linear PNIPAM is observed rapidly over the θ temperature, which is equivalent to the LCST, 32°C. In the case of PNIPAM, water is a good solvent below 32°C, whereas it is a poor solvent above it where PNIPAM linear chains change their structures from swollen to a collapsed conformation.

The LCST of PNIPAM is affected by various factors including polymer design and additives to the solution like salts and surfactants. The focus of this work is on the effect of polymer architecture on the LCST of PNIPAMs. PNIPAM has been rarely used as a homopolymer and normally it is copolymerized with other monomers in order to control its physical properties and to be able to functionalize it with biochemical materials. This copolymerisation has been used to modify the LCST of PNIPAM depending on the architecture of the obtained copolymers. For example, when PNIPAM is copolymerised with a more hydrophobic monomer, such as styrene [107], the LCST will decrease. Whereas, if it is copolymerised with a more hydrophilic monomer, such as acrylic acid [108, 109], the LCST will increase. Block or graft copolymerisations [110, 111, 112] are particularly popular, but these have a little effect on the LCST. This was explained by PNIPAM chains behaving as independent homopolymers in these systems.

Chain end groups also have a significant effect on the LCST of PNIPAMs. Chung *et al.* [113] were the first to introduce the idea that the transition from a soluble to an insoluble phase starts from chain ends. These authors showed that the LCST is dramatically enhanced when the end groups were attached to one end of the polymer chain rather than along the backbone.

Other polymer architectures of PNIPAM, such as microgels [23] and

highly branched PNIPAM [114, 21] have also been reported with an LCST different from their linear PNIPAM counterparts. For example, in highly branched PNIPAM, it has been found that the LCST depends on the number of branch points per backbone and the end groups of these branches [115, 21].

3.3.2 Highly Branched PNIPAMs

The wide range of applications of branched polymers is due to the large number of chain ends per molecule and their controlled architecture. Whilst polymer architecture affects the rheology and solubility of branched polymers, the large number of chain ends is useful for functionlization with different chemicals from those along the main chain. Branched polymers can be synthesized by chain growth polymerisation in which branching units are used acting as transfer agents or initiators. Addition-fragmentation and reversible addition-fragmentation chain transfer (RAFT) methods are examples of the approaches that can form branched polymers. RAFT method has the advantage of giving the opportunity to modify the end groups [21]. This method has been used throughout this work and the mechanism of such approach will be discussed in Chapter 7, section 7.2.1.

Using RAFT polymerisation, Rimmer *et al.* [21, 26, 29, 114, 5] were able to prepare various highly branched PNIPAMs with different functionalities for different applications. For example, they used a polymerizable chain transfer agent that contains an imidazole thioacarbonylthio RAFT group to prepare highly branched PNIPAM with imidazole groups at the chain ends. These polymers were found to be useful for protein purification and temperature controlled entry and delivery into cells [29, 5]. A similar approach was used by Vogt and Sumerlin [116] to prepare branched PNIPAM in which they used RAFT polymerization with acryloyl trithiocarbonate.

It was found that an increase in the branching degree of PNIPAM leads to a reduction in the LCST by several degrees compared to the equivalent linear PNIPAM [21, 114]. This was attributed to the aggregation of chain end groups. Another study by Rimmer *et al.* [115] showed that converting

the chain end groups from N-pyrrole into more polar acids, such as COOH, improves the stability of the solution above the LCST by forming a dispersion of sub-micron particles. The LCST was also found to increase in the case of COOH end groups to be above that of N-pyrrole end groups.

Although many studies showed that the phase transition behaviour is independent of PNIPAM concentration, at least below 1% [103, 20], more recent studies on PNIPAM hydrogels [117] and highly branched PNIPAM [118] revealed a dependence of the LCST on concentrations above 1%. In the latter study, Tao *et al.* used laser light scatting (LLS) to measure the hydrodynamic radius of highly branched PNIPAM and found that the particle size (or molecular weight) and the polymer concentration play a significant role in controlling the phase behaviour of PNIPAM.

3.4 Diffusion in Water-based Systems

The basic principles of diffusion of macromolecules in polymeric systems were introduced in Chapter 2. The main purpose of this section is to review some of the most advanced studies on molecular transport in polymer solutions and gels. Diffusion in polymer solutions and gels is of great importance for biological and industrial applications, such as drug delivery and release in living tissue, and chromatographic separation. Thus, a thorough understanding of diffusion in polymeric systems is required to explore the structure and the mechanism of molecular transport in these systems. For instance, the diffusion coefficient of single polymer chains was found to be dependent on the structural behaviour of hydrogels including the change of mesh size, ξ, with response to the change in the surrounding environment. This gives the opportunity to sense the entrant structure of these materials which is difficult to obtain by conventional techniques. Various experimental techniques have been utilized to study diffusion in gels and solutions. Among these techniques are gravimetry, ion scattering, dynamic light scattering, neutron reflectometry and neutron spin echo [34, 35, 119, 120, 59]. Fluorescence spectroscopy techniques, such as fluorescence correlation spectroscopy (FCS) and fluorescence recovery after photobleaching (FRAP) are also powerful tools for

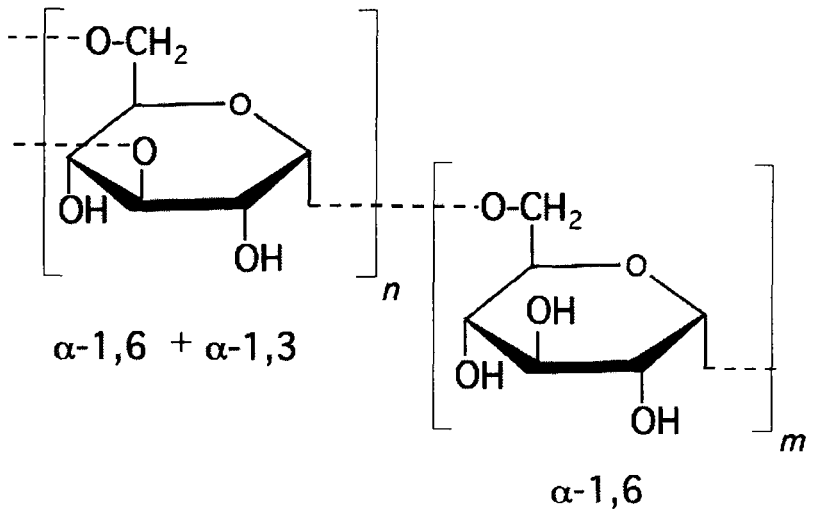

Figure 3.6: Chemical structure of fragment of dextran molecule showing α-1,6 glycosidic linkage between glucose molecules. The branching begins from α-1,3 linkages.

studying diffusion.

Fluorescently labeled dextran is the most widely used probe to study diffusion in living and polymeric systems. Dextran is a neutral homopolysaccharide that has many glucose units connected by α-1,6 linkeages to form the molecular backbone. Dextran is a branched biopolymer with the side-chains being formed by α-1,3 linkeages of glucose units (Figure 3.6). Water is a good solvent for dextran in which it forms a clear and stable solution. However, as a neutral polymer, the pH of the solvent and the addition of salt do not affect the solubility and viscosity of dextran. In many studies and for several biological applications dextran has been labeled with fluorescent materials, such as fluorescein isothiocyanate (FITC). It is debatable whether FITC-dextran is a neutral or charged polymer, although in many cases in the litreatue it is considered as a negatively charged biopolymer due to the negatively charged FITC that is attached to it [121, 122]. FITC-dextran has been used many times as a probe to study diffusion and release in various polymeric systems. For example, FCS has been utilized to investigate the effect of polymer concentration, temperature, pH and salt on the diffusion of FITC-dextran in polymer solutions and gels [123, 124, 125, 126, 127, 128, 129]. This method will be used throughout this work to study the diffusion of FITC-dextran

in PMAA hydrogels and ferrogels (Chapters 5 and 6) and highly branched PNIPAM solutions (Chapter 8). The choice of the molecular weight of FITC-dextran (70 kDa in this study) was based on the possibility of penetrating the polymer networks in the collapsed state. Smaller molecular weights of this tracer will minimize the interactions between the probe molecules and the mesh of the polymer network. However, these interactions were not taken into account in this study. Previous studies [130] showed a strong dependence of diffusion coefficient on the probe molecular weight. This can be explained by considering Phillies diffusion model:

$$D = D_0 \exp\left(-\alpha c^{\nu}\right), \tag{3.1}$$

where α is a scaling prefactor that is a function of the probe size and its interactions with the polymer matrix. It has been found that α depends strongly on the molecular weight as ($\alpha \sim M_w^{0.8}$) for macromolecular probes. c in equation 3.1 refers to the concentration of the polymer matrix and ν is a stretching exponent that is related to the properties of the polymer solution and has a value between 0.5 and 1.

Chapter 4

Experimental Techniques

4.1 Introduction

Progress in nanotechnology has brought with it the need to describe and understand the processes and interactions on a molecular basis. Therefore, powerful techniques have been developed or improved, incorporating lasers, X-rays and neutrons. In this chapter, the experimental techniques used throughout this work will be discussed. However, some techniques were used only for basic characterisations, such as NMR, GPC and UV-visible spectroscopy, and these will only be briefly mentioned in the subsequent chapters. All of the techniques described in this chapter are considered to be analytical techniques that provide information about the examined materials at the nanoscale. These methods use primary probes (light, X-rays, neutrons) to excite secondary effects (electrons, photons, ions) in the regions of interest in the sample under study. These secondary effects can be recorded as a function of different variables including energy, temperature, intensity, angle and phase.

The work in this thesis involved the use of fluorescence correlation spectroscopy (FCS) and neutron spin echo (NSE) to investigate the dynamics in different polymeric systems; small-angle (X-ray and neutron) scattering (SAXS and SANS) to study the structural behaviour of different organic and inorganic materials. In addition, a superconducting quantum interference

device magnetometer (SQUID) was used to measure magnetization and particle size. The theoretical background and the principles of these techniques will be discussed in this chapter, but the operation of these techniques is beyond the scope of this work.

4.2 Fluorescence Correlation Spectroscopy

One of the most powerful techniques with a temporal resolution for investigations at the molecular level is fluorescence correlation spectroscopy (FCS) which has been extensively used in physics, chemistry and biology. The most obvious examples are the study of molecular mobility, photophysics and photochemistry. There is a considerable number of FCS studies, developments and reviews in the literature [131, 132, 133, 134, 135, 136, 137, 138], and the aim of this section is to give an overview of the principles of the technique. FCS was first introduced by Magde and co-workers in 1970 as a dynamic light scattering technique [139]. The early work done using FCS was the study of biological systems including DNA kinetics and interactions [131]. After that, FCS was used for measuring concentrations and molecular mobilities [134]. In 1993, Rigler and co-workers demonstrated the importance of the confocal volume for FCS measurements. Following this, in 1995, the multiphoton technique was introduced in order to decrease and improve the sampling volume in a similar way to the confocal technique but without the need of emission pinholes [140, 141, 133]. Another advantage of using two-photon FCS is that only the part of the sample at the focal spot is excited by the used laser which prevents damage of other parts of the sample. This was a great development especially for living cells [141]. In addition to its usefulness in three-dimensional systems, FCS has been adopted for two-dimensional diffusion (on surfaces) [142, 143].

4.2.1 Principles of FCS

FCS is a single molecule technique that uses a very tightly focused laser beam to observe the random Brownian motion of fluorescently labelled molecules

within a very small detection volume ($\sim$ 1 femtolitre). Earlier confocal systems like the one used by Ricka and Binkert (1989) [144] suffered from poor signal-to-noise ratio due to many reasons including the large number of detected molecules, unstable laser sources and low-efficiency detectors. The widespread use of confocal systems started after the work of Rigler and coworkers in the early 1990s [138]. The use of confocal illumination was the main key for pushing the sensitivity of FCS to the single molecule level. The setup used in the Rigler confocal system contains an epi-illuminated microscope configuration, a strong and focused laser beam, a small pinhole and an avalanche photodiode (APD) detector. This focused laser beam is reflected by a dichroic mirror into a high numerical aperture (NA) objective, which projects a more focused laser beam into the sample. The emitted light from the sample is collected by the same objective which then passes through a pinhole to be filtered by cutting off the out-of-focus light. This results in the formation of a typical observation volume (confocal volume) for FCS of about 1 femtolitre. This small detection volume allows the fluctuations generated by single molcules to be accurately recorded. As a result, the signal-to-noise ratio is large compared to that at high number of molecules. Thus, FCS has been found to perform best when the number of fluorophores in the detection volume is <10 [145]. In typical experiments, the concentration of the fluorescent probes should be around 1 nM, which gives an average of 0.7 molecules in the detection volume (for the setup used in this work with a detection volume of 1.2 femtolitre). The diffusion or transport into and out of the detection volume can be easily measured for the average number of molecules passing through this volume. Therefore, FCS is an ideal technique to measure diffusion coefficients, fluorophore concentrations, particle sizes, chemical reactions, conformational changes, binding/unbinding processes and some others.

4.2.2 Fluorescence Phenomena

The emission of light from electronically excited states in any substance is called luminescence. There are two types of luminescence, fluorescence and

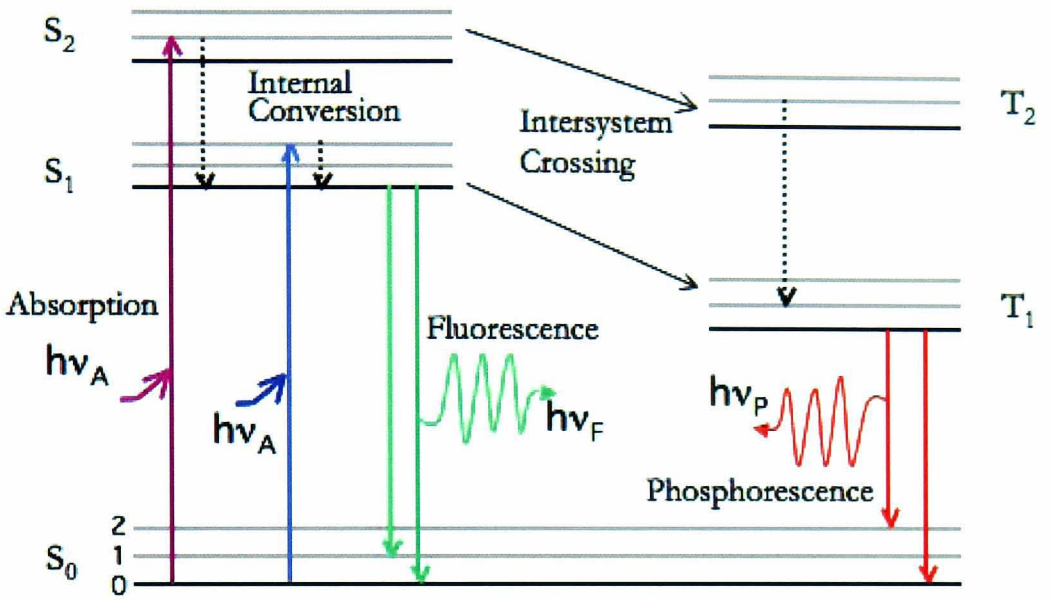

Figure 4.1: A schematic of a typical Jablonski diagram showing the radiative process (solid arrows) and non-radiative processes (dashed arrows) from the singlet states (ground, S_0, and excited, S_1 and S_2, states) and triplet states T_1 and T_2. Each of these electronic energy levels has a number of vibrational levels (0, 1, 2, etc) in which the fluorophores can exist. This diagram also shows the two different photophysical processes: fluorescence and phosphorescence.

phosphorescence, depending on the excited states from which the emission occurs. A Jablonski diagram (Figure 4.1) shows the electronic states of a substance and the transition between them. Acording to the Pauli exclusion principle, the ground state is usually occupied by two electrons. The absorption of a photon (with energy $h\nu_A$) results in an excitation of an electron from the ground state, S_0, to an excited state, S_n, $(n = 1, 2, 3, ...)$ with many vibrational levels. The excited electrons can return to the ground state via a number of routes including radiative and non-radiative transitions.

The radiative transitions include the absorption of energy $(h\nu_A)$, when the excited electron moves from the ground state to a higher energy level, and the photon emission energy $(h\nu_{em})$. Fluorescence emission occurs when an electron transfers between the same spin states $(S_n - S_0)$. On the other hand, the phosphorescence emission occurs when the transition is between states with different spin multiplicity $(T_n - S_0)$. The fluorescence emission

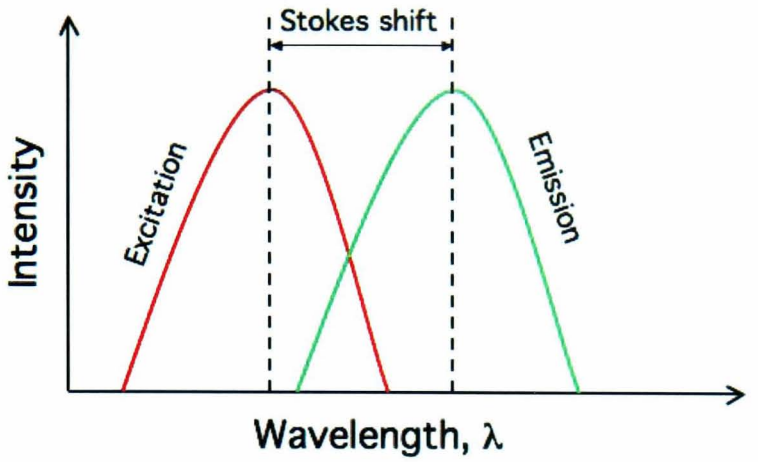

Figure 4.2: A Schematic graph showing the Stokes shift between excitation and emission light.

has a lower energy (longer wavelength) compared to the excitation energy. This phenomenon is called the Stokes Shift (figure 4.2).

In contrast, the non-radiative transitions can take place in three different ways. First, the vibrational relaxation of the excited state to its lowest vibrational level, which occurs quickly (< 1 ps) and can be enhanced by physical contact of the excited molecule with other molecules. The energy lost in this process dissipates in the form of heat. Second, the internal conversion which is a result of the transition from an excited state to a lower electronic state of the same spin multiplicity. Third, the intersystem crossing which is the transition between the electronic states with different spin multiplicity.

There are a number of processes that occur during the excited state, such as photobleaching, collisional quenching and fluorescence energy transfer, which can cause a loss of some fluorescence photons. For example, photobleaching, which occurs when a fluorophore irreversibly loses the ability to emit light due to chemical damage and covalent modification, is found to arise after the transition from an excited singlet state to the excited triplet state in many fluorescent molecules, because the triplet state is a long-lived state that allows excited molecules to interact with the surrounding environment for longer times [146]. Although this phenomenon can be destructive to microscopy measurements, it has been exploited for studying diffusion of molecules in a technique called fluorescence recovery after photobleaching

(FRAP) [147, 146]. Therefore, not all of the excited fluorophore molecules will go back to the ground state, and the ratio between the emitted and absorbed photons is called the quantum yield, which can be between 0, for non-fluorescent materials, and 1 for highly fluorescent fluorophores in the ideal case assuming no triplet state excitations. However, even highly fluorescent materials do not emit as many photons as they absorb due to the above mentioned non-radiative transitions which compete with fluorescence. This quantum efficiency can be affected by the surrounding environment, such as temperature, pH and ionic strength [148].

Fluorophore molecules can be repeatedly excited, unless they are damaged by photobleaching, resulting in a cyclical process of fluorescence. The distribution of the excitation spectrum of a given fluorophore is due to the fact that an electron can be excited from different energy levels in the ground state and can move to any energy level of the excitation state. Fluorescence techniques are highly sensitive and this sensitivity is determined by the shift in the wavelength between the excitation and emission spectra (Stokes Shift, Figure 4.2). The emitted photons can be detected against low background by using bandpass filters to separate them from the excitation ones (see the setup in the next section). In dilute solutions, there is a linear relationship between the fluorescence intensity and the molar excitation coefficient, the optical path length, the fluorophore concentration, the fluorescence quantum yield, the excitation intensity and the detector efficiency in the instrument. If one used a laser light source, then the illumination wavelength (energy) and the excitation intensity can be constant and the fluorescence intensity would be only a linear function of the fluorophore concentration. However, at high fluorophore concentrations, this relationship is not linear due to some other processes, such as self-absorption, which interfere with the measurement [148].

4.2.3 FCS Instrumentation and Setup

A typical confocal microscope setup is shown in figure 4.3. The incident laser beam is collected by an objective and a lens. The resulting parallel beam

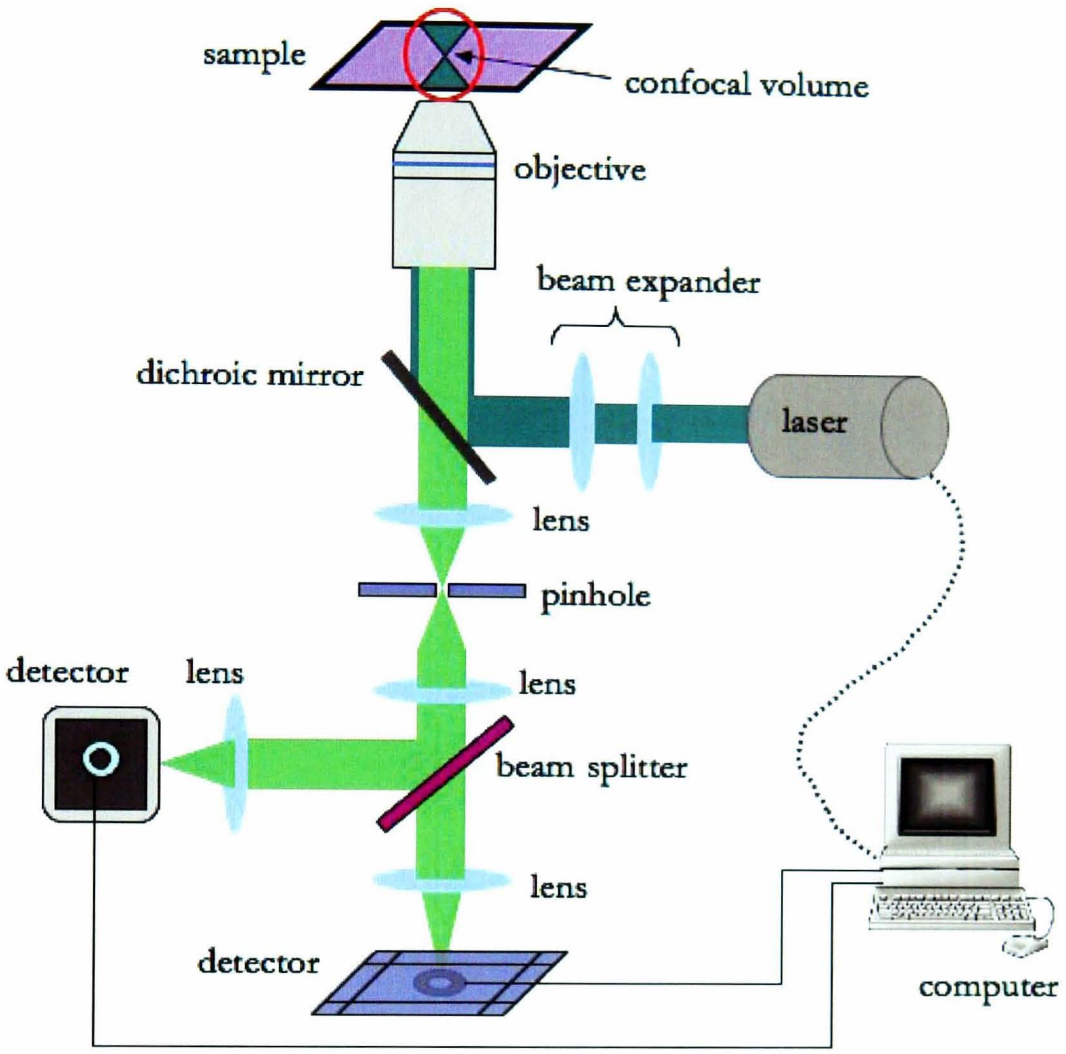

Figure 4.3: Schematic diagram showing the main principles of FCS and the optics of the inverted confocal microscope.

is then deflected by a main dichroic mirror to an objective lens placed in the focal plane of this objective, which focuses the beam into a diffraction limited volume in the sample, forming a double cone of excitation light (called confocal volume). It has been found that the highest intensity is between these two cones, although it is possible for the excitation and fluorescence to take place anywhere in the volume outlined by the two cones.

Once the fluorophores are excited, the fluorescence emission is collected through the same objective and focused onto a pinhole. Hence, the waist of the laser beam in the sample can be imaged onto the pinhole aperture. The main idea of the confocal approach is spatial filtering which is used to

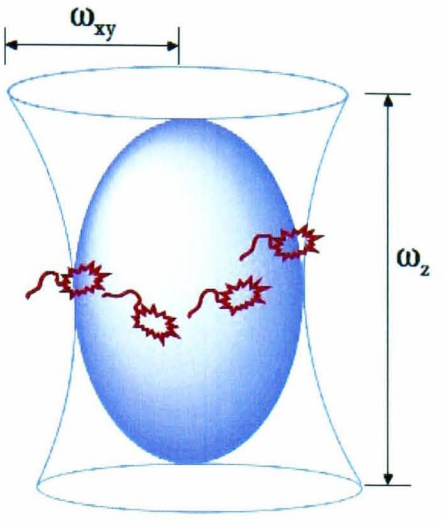

Figure 4.4: Schematic diagram showing the confocal volume with ω_{xy} and ω_z being the confocal waist in xy-plane and z-axis, respectively.

eliminate the out-of-focus light in the sample that is thicker than the plane of the focus. The coupling of the objective and the pinhole results in a spatial filter, which controls the size of the sampling volume. If the pinhole is relatively small ($30 - 50$ μm), only fluorescent light from the focal plane of the objective can go through this pinhole. This passing light is collected by a photon counting detector and then transformed into an autocorrelation function. However, this autocorrelation function can be affected by some of the properties of the detector such as "afterpulsing". Afterpulsing phenomenon is the detector pulse that follow the genuine output. In photomultipliers, afterpulsing is usually caused by ionized atoms of the residual gas resulting in delayed photoelectrons or by the effect of the fluorescence and luminescence of the residual gas. In avalanche photodiode (APD), some of the charge carriers are trapped in the junction depletion layer which can be thermally released at a later time leading to afterpulsing [149]. In order to overcome the afterpulsing problem resulting from the collected light on the detector, a beam splitter is used to split the fluorescent light between two photodetectors. The collected lights on both detectors are then cross-correlated to give a similar function to the autocorrelation function but without the afterpulsing noise [134]. This way of collecting the fluorescent light on two detectors is also useful in the case of two photon and two colour FCS setups [150].

The sampling volume (confocal volume), shown in Figure 4.4. does not have sharp boundaries due to the diffraction of the light in the sample but forms an elliptical shape. Hence, this sampling volume can be considered as a 3D image of a point source for which the point spread function of a lens system can be applied. This means that there are more excited fluorescent particles than those detected. By using a small pinhole, one can approximate the point spread function by the Gaussian function. Therefore, the Gaussian distribution of the detected intensity can be given as:

$$I(x, y, z) = I_o \exp\left(-\frac{2(x^2 + y^2)}{\omega_{xy}^2} - \frac{2z^2}{\omega_z^2}\right), \tag{4.1}$$

where I_0 is the peak intensity, (x, y) and z are the radial and axial coordinates of the fluorescent particle in the confocal volume, respectively, and ω_{xy} and ω_z are the radial and axial sizes of the beam waist, respectively, where $\omega_z > \omega_{xy}$.

4.2.4 FCS Autocorrelation Functions

As mentioned in the previous section, each emitted photon from a single molecule in the detection volume is recorded by highly sensitive single-photon counting modules in a time-resolved way. The probability of detecting this photon determines the shape of the correlation function. This detection probability is the probability that a molecule emits a photon and that this photon is detected. Therefore, this probability depends on the excitation laser intensity distribution and the detection efficiency function. However, the number of the detected photons fluctuates with time due to the change of the number of fluorescent molecules in the confocal volume (diffusion) and the fluctuation in the number of emitted photons per molecule. The diffusion of fluorophores in the confocal volume contributes to the signal and the noise, while the number of emitted photons per molecule affects the noise only. In addition, the background noise and the correlated laser noise contribute to the limitation of the signal-to-noise. Although increasing the concentration of fluorescent molecules reduces the background in the signal, the amplitude of the correlation decreases with the number of fluorescent molecules, N.

The probability of the molecular detection can be given as:

$$P = \frac{k \cdot I(r,t)}{I_0} = k \cdot \exp\left(-\frac{2(x^2+y^2)}{\omega_{xy}^2} - \frac{2z^2}{\omega_z^2}\right), \tag{4.2}$$

where k is the collection efficiency function. The total fluorescence intensity can be written as:

$$F(t) = \alpha \int I^2(r,t) C(r,t) \mathrm{d}r, \tag{4.3}$$

where $C(r,t)$ is the local concentration of the fluorescent particles. The diffusion of these particles into and out of the confocal volume changes the particle concentration within this volume which, according to equation 4.3, affects the fluorescence intensity.

If the excitation power is constant, then the fluctuations of the fluorescence signal are characterized by the deviations from the temporal average of this signal:

$$\delta F(t) = F(t) - \langle F(t) \rangle, \tag{4.4}$$

where

$$\langle F(t) \rangle = \frac{1}{T} \int_0^T F(t) \mathrm{d}t. \tag{4.5}$$

If the signal fluctuations are only due to changes in the particle concentration within the effective confocal volume, V_{eff}, then the fluctuation of the fluorescence intensity is given as:

$$\delta F(t) = \kappa \int_V I(r) \cdot S(r) \cdot \delta(\sigma \cdot q \cdot C(r,t)) \cdot \mathrm{d}V, \tag{4.6}$$

where κ is the overall detection efficiency and $S(r)$ is the optical transfer function of the objective-pinhole combination. The parameter $\delta(\sigma \cdot q \cdot C(r,t))$ is the dynamics of a single probe, where $\delta\sigma$ is the fluctuation in the molecular absorption cross-section, δq is the fluctuation in the quantum yield and

$\delta C(r,t)$ is the fluctuation in the concentration (Brownian motion) of the particles at time t.

Because it is difficult to obtain the parameters in equation 4.6, it is simplified as follows:

$$\delta F(t) = \kappa \int_V W(r)\delta(\eta C(r,t)) \cdot \mathrm{d}V, \tag{4.7}$$

where $W(r)$ is a combination of the two dimensionless spatial optical transfer functions, which are related to the spatial distribution of the emitted light by:

$$W(r) = \frac{I(r)}{I_0} \cdot S(r) = \exp\left(-\frac{2(x^2+y^2)}{\omega_{xy}^2} - \frac{2z^2}{\omega_z^2}\right). \tag{4.8}$$

The parameter η in equation 4.7 defines the photon count rate per detected molecule per second and can be given in terms of the excitation intensity amplitude, I_0, as:

$$\eta = I_0 \cdot \kappa \cdot \sigma \cdot q. \tag{4.9}$$

This parameter is important as a measure of the signal-to-noise ratio which is therefore used for measurement quality and setup.

The autocorrelation function, $G(\tau)$, which is used to describe the fluctuation of the flurescence intensity, compares the fluorescence intensity at time t, $F(t)$, with that after a lag time, τ, $F(t+\tau)$. Mathematically, the normalized form of $G(\tau)$ can be written as [151]:

$$G(\tau) = \frac{\langle \delta F(t)\delta F(t+\tau)\rangle}{\langle F(t)\rangle^2}. \tag{4.10}$$

Depending on the diffusing probe, there have been a number of correlation models. For example, these models depends on wether the probe is diffusing freely or anomalously, or if it is affected by photodynamical properties of the dyes (triplet state kinetics and photobleaching). However, the anomalous diffusion will not be discussed in this work, as all of the studied systems showed no such process. In all of these models, the autocorrelation function

is taken as the product of the different involved processes as:

$$G(\tau) = 1 + (\text{Amplitude}) \cdot (\text{Flickering}) \cdot (\text{Diffusion})$$

$$G(\tau) = 1 + \frac{1}{\langle N \rangle} \cdot (G_{\text{F}}(\tau) - 1) \cdot (G_{\text{diff}}(\tau) - 1), \tag{4.11}$$

where $G_{\text{F}}(\tau)$ and $G_{\text{diff}}(\tau)$ are the correlation of flickering and diffusion, respectively.

Assuming a freely diffusing fluorophore through a 3D sampling volume without any changes in its fluorescence properties (i.e. $\delta\eta = 0$), then the autocorrelation in this case can be given by [134, 131, 136]:

$$G(\tau) = \frac{1}{V_{\text{eff}} \langle C \rangle} \left(1 + \frac{\tau}{\tau_D}\right) \left(1 + \frac{\tau}{R^2 \tau_D}\right)^{-\frac{1}{2}}, \tag{4.12}$$

where $R = \omega_{xy}/\omega_z$ is the elongation parameter and the effective confocal volume can be calculated as follows:

$$V_{\text{eff}} = \frac{\left(\int W(r) dV\right)^2}{\int W^2(r) dV} = \pi^{3/2} \cdot \omega_{xy}^2 \cdot \omega_z. \tag{4.13}$$

The amplitude of the correlation curve, shown in Figure 4.5, is related to the mean number of particles by:

$$G(0) = \frac{1}{\langle N \rangle} = \frac{1}{V_{\text{eff}} \cdot \langle C \rangle} \tag{4.14}$$

The autocorrelation function (4.12) is useful for determining the concentration of the diffusing fluorophores (as will be seen in chapter 5) and their translational diffusion time, τ_{D}. From this diffusion time, and for particles with hydrodynamic radius less than $\omega_{xy}/10$, the diffusion coefficient can be obtained using a relationship described by Varma and co-workers [152, 131]:

$$D = \frac{\omega_{xy}^2}{4\tau_{\text{D}}}. \tag{4.15}$$

The above-mentioned assumption, however, cannot be true for real dyes at high excitation powers (i.e. fluorescence properties change and $\delta\eta \neq 0$).

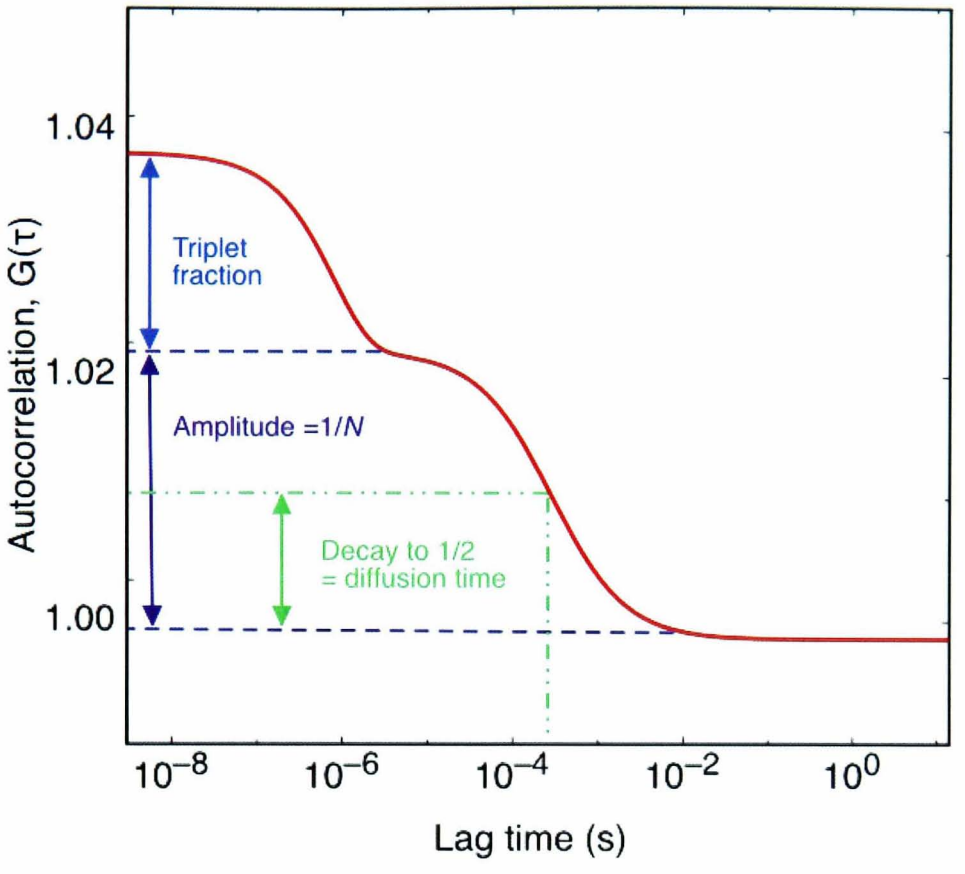

Figure 4.5: A typical autocorrelation curve showing the triplet contribution at short time scales (first shoulder) and the diffusion contribution at longer time scales (second shoulder). This curve was achieved by plotting the autocorrelation function described by Equation 4.19.

Flickering phenomena (intersystem crossing process in Figure 4.1) are caused by the transition of the dye to triplet states. According to quantum mechanics, this transition is forbidden and the fluorophore needs extra time to relax back to its ground state. The dye at this "flickering" stage cannot emit any photons and can accordingly be called a dark stage, which interrupts the continuous fluorescence emission of the excited molecule.

If the fluorescence fluctuations which arise from intra- or intermolecular reactions are much faster than those caused by the movement of the particle itself, then the autocorrelation function can be written in terms of these dynamics in a general form as:

$$G_{\text{total}}(\tau) = G_{\text{motion}}(\tau) \cdot X_{\text{kinetics}}(\tau). \tag{4.16}$$

This assumption can only be true if the diffusion coefficient is not affected by this reaction [153, 154]. The triplet blinking is described as:

$$X_{\text{triplet}}(\tau) = 1 - P_{\text{t}} + P_{\text{t}} \cdot \exp(-\frac{\tau}{\tau_{\text{t}}}), \tag{4.17}$$

where P_{t} is the triplet fraction and τ_{t} is the triplet time. The addition of this term to the autocorrelation function adds another shoulder in the correlation curve at shorter time scales (see Figure 4.5). Equation 4.17 can also be normalized by dividing by $(1 - P_{\text{t}})$ [155, 136] to give:

$$X_{\text{triplet}}(\tau) = 1 + \frac{P_{\text{t}}}{1 - P_{\text{t}}} \cdot \exp(-\frac{\tau}{\tau_{\text{t}}}). \tag{4.18}$$

The overall autocorrelation function, including diffusion and flickering, for a freely diffusing fluorophore in 3D can be written as:

$$G(\tau) = 1 + \frac{1}{N}\left[\left(1 + \frac{\tau}{\tau_{\text{D}}}\right)^{-1}\left(1 + \frac{\tau}{R^2\tau_{\text{D}}}\right)^{-\frac{1}{2}}\left(1 + \frac{P_{\text{t}}}{1 - P_{\text{t}}} \cdot \exp(-\frac{\tau}{\tau_{\text{t}}})\right)\right]. \tag{4.19}$$

It can be noticed from equation 4.19 that the flickering is independent of the size of the confocal volume. One requirment for equation 4.19 to be used is that the confocal volume must be Gaussian and therefore the detector aperture should be relatively small.

4.3 Small-Angle Scattering

Small-angle scattering generally encompasses small-angle neutron (SANS), X-ray (SAXS) and light (SALS) scattering [156, 157, 158, 159]. All of these techniques use the elastically scattered radiation from a sample to obtain a scattering pattern that is used to give information about the size, shape, orientation and surface-to-volume ratio of the sample under investigation. SANS and SAXS, for example, are able to probe nanostructures ranging from 1 nm to more than 100 nm (see Figure 4.6). Therefore, they have a wide range of applications such as in the investigation of polymer and

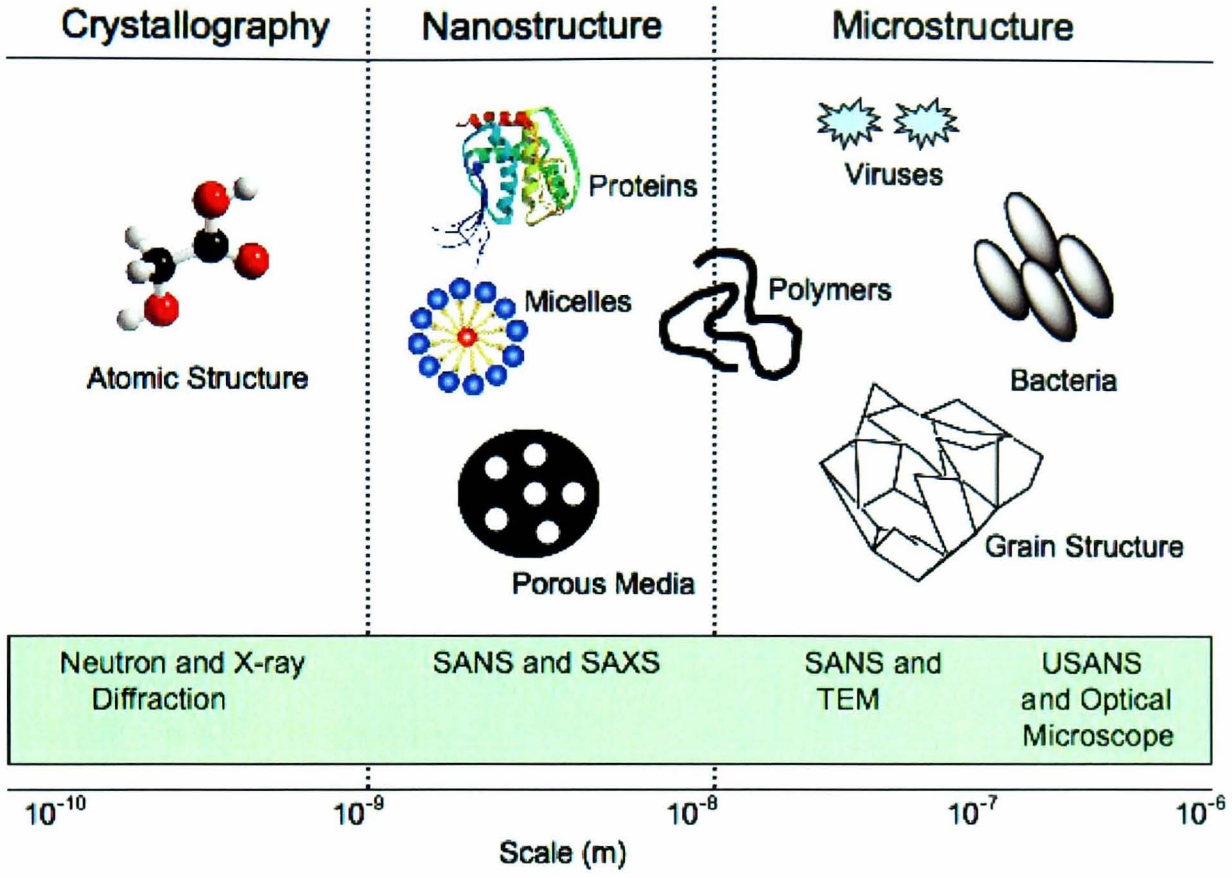

Figure 4.6: A scale diagram of some condensed matters with respective characterisation techniques.

biological molecules and nanoparticles. The type of radiation one can use depends on many factors including the nature of the sample, the sample environment, the length scale to be probed and the information that can be obtained. For example, SALS cannot be employed to study optically opaque samples and SAXS would not be a useful tool to study thick samples, whereas SANS can be used in most cases to probe different length scales. Despite the difference in radiation, basic laws (Guinier, Zimm, Kratky and Porod) can be employed to analyze the data obtained from these three techniques, making them complementary to each other with some differences in the experimental details.

4.3.1 Small-Angle X-ray Scattering (SAXS)

Small-angle X-ray scattering (SAXS) is a reliable and economic analytical technique that allows one to study the structure and interactions of organic and inorganic systems with no need to crystallize the sample under investigation [160, 161]. Therefore, SAXS has been utilized to probe complex systems (from 1 nm up to several hundred of nanometres), such as proteins, nucleic acids and a variety of synthetic polymer structures [161, 162, 77, 163, 164, 165, 166]. The materials that one can study by SAXS could be solid, liquid or a combination of solid, liquid or gaseous domains. Particles as well as ordered systems and fractal-like materials can be studied using SAXS. Applications of SAXS include colloids of all types, metals, cement, oil, polymers, plastics, proteins, foods and pharmaceuticals. Despite being mostly used for research purposes, SAXS could also be used for quality control.

4.3.1.1 SAXS Principles

Scattering processes are generally described by the inverse relationship between particle size and scattering angle. For example, a particle with size between 1 nm and 100 nm, which is larger than the wavelength of X-rays (0.15 nm for the frequently used CuK_{α}-line), requires a small range of scattering angles (typically 0.1-10°). X-rays are scattered by electrons; therefore, there must be electron density inhomogeneities in the sample under study. These electrons oscillate with the same frequency as the X-rays used, then emit coherent secondary X-ray waves. If the scattered X-rays have the same wavelength as the incident beam, it is called elastic (coherent) scattering. In contrast, if the scattered radiation has a different wavelength from the incident beam, it is inelastic (incoherent) scattering. However, incoherent scattering is insignificant at small angles [160].

The diffraction of X-rays (Figure 4.7) produced by the interference between the waves scattered by the electrons in the sample is used to study the different structures in the sample. X-rays with wavelength, λ, reflected from the planes of the sample interfere with each other. This interference is destructive unless the path difference between the interfered rays is equal to

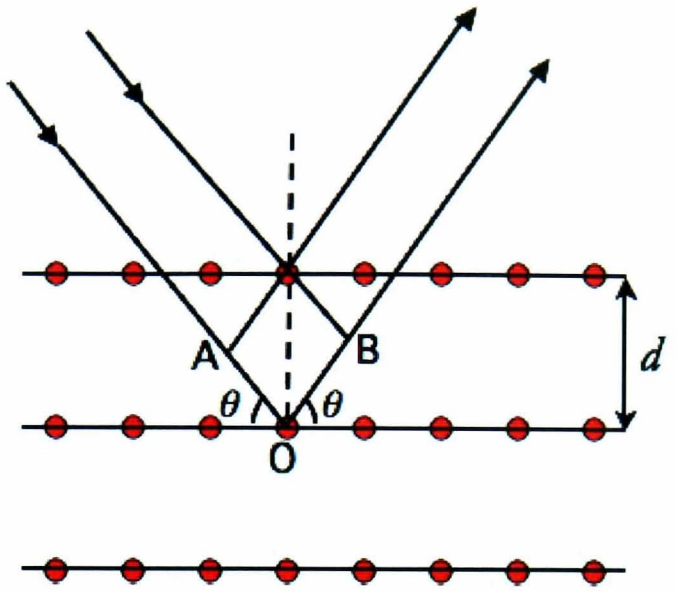

Figure 4.7: Bragg reflection of two X-rays from two adjacent planes, separated by a distance d, having a path difference $(\mathrm{OA} + \mathrm{OB}) = 2d\sin\theta$.

an integer number of the wavelengths ($n = 1, 2, 3, ...$). Therefore, according to Bragg's law, the path difference for a constructive interference of reflected waves from any two planes separated by a distance, d, is given by [167, 160]

$$2d\sin\theta = n\lambda. \tag{4.20}$$

In a typical experiment, the collimated X-rays are scattered by a sample through an angle 2θ (Figure 4.8). The intensity of the scattered radiation is recorded as a function of the scattering angle, from which the structure information can be obtained. As mentioned previously, the scattering of X-rays occurs when there is a difference in the electron density and the scattering pattern, on the detector, occurs because of the interference of the secondary waves that are emitted from the various irradiated electrons. Hence, the small-angle scattering of X-rays can be observed if and only if there is an inhomogeneity in the electron density in the sample and when these electrons resonate with the frequency of the applied X-rays, emitting coherent secondary waves which interfere with each other.

The obtained pattern (Figure 4.8) does not show directly the structural and morphological information in the sample, but rather it is related to the

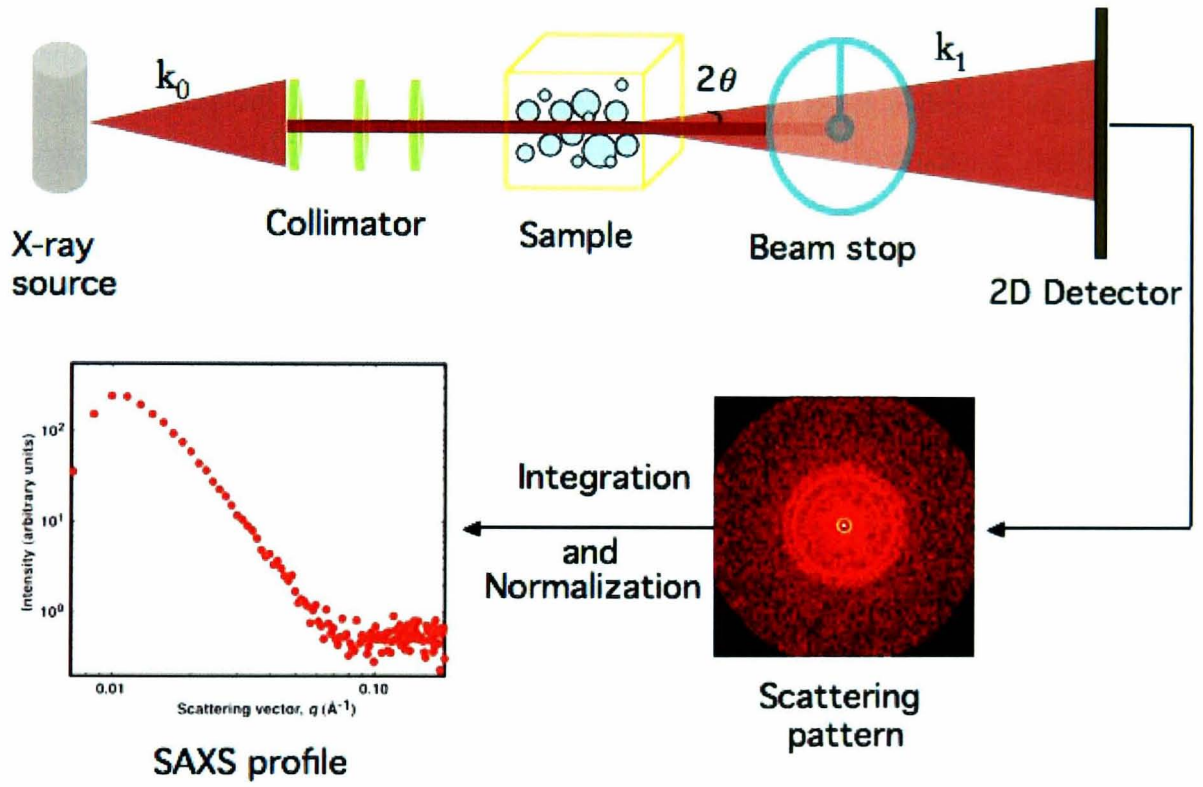

Figure 4.8: A schematic diagram showing 2D SAXS setup and the process of scattering data.

intensity of the Fourier transformation of the electron density, which can be interpreted to obtain the required information about the structure and size and morphology. The scattering of X-rays of a wavelength, λ, through an angle 2θ is represented by the scattering vector, $\overrightarrow{q}$, the modulus of which is given by

$$\left|\overrightarrow{q}\right| = (\frac{4\pi}{\lambda})\sin\theta. \tag{4.21}$$

Since incoherent and Compton scatterings can be neglected at small scattering angles, the scattered waves are assumed to be coherent. Hence, the resulting amplitude is the sum of all the secondary waves, and the intensity is the absolute square of this amplitude. However, the resulting amplitude is usually given in terms of the electron density, $\rho(r)$, because of the large number of electrons given that single electrons cannot be localized.

If one takes a solution, for example, the particles in the solution are not oriented. However, the physical scattering process is the contribution from a large number of randomly oriented particles. Therefore, the 3-dimensional electron density distribution, $\rho(r)$, which represents the structure of the particle, is reduced to a one-dimensional distance distribution function, $P(r)$. The Fourier transformation of this function, $P(r)$, is the mathematical expression of the physical scattering process. Practically, the scattering intensity is affected by the polychromatic radiation, the length and width of the slit of the collimator and the detector. Thus, this scattering intensity must be corrected according to these effects. However, these effects can be neglected if one uses a monochromatic primary beam with a point collimator of very high intensity and an infinitesimal detector.

The focus of the SAXS experiments in this work is on dilute systems, in which the inter-particle interactions are negligible and the scattering from these systems is mainly due to the particle scattering (form factor) [168]. In this case, SAXS data can be obtained using the indirect Fourier transformation method. Hence, the scattering intensity from one scattering particle (the form factor), $I(q)$, is the Fourier transformation of the pair distance distribution function, $P(r)$, given by [160]:

$$I(q) = 4\pi \int_0^\infty P(r)\frac{\sin(qr)}{qr}\mathrm{d}r, \tag{4.22}$$

where $P(r)$ is related to the characteristic function, $\gamma(r)$, of the particle by

$$P(r) = r^{d-1}\gamma(r), \tag{4.23}$$

where r is the distance between two scattering centres in the particle and d is the dimension which determines the symmetry type (e.g. $d = 3$ for spherical symmetry). This pair distance distribution function provides information about the particle size, shape and internal structure.

The simplest case of particle scattering is that of spherical particles because they show equivalent orientations all over the scattering volume. This allows a direct calculation of the scattering intensity. Assuming a spherical particle in a dilute solution with a radius, R, and volume, V; and if the difference between the constant electron density in the particle, ρ, and in the solvent, ρ_0, is $\Delta\rho = (\rho - \rho_0)$, then the scattering intensity can be given by the Rayleigh equation [160]:

$$I(q) = (\Delta\rho)^2 V^2 \left[\frac{3(\sin qR - qR\cos qR)}{(qR)^3}\right]^2. \tag{4.24}$$

4.3.1.2 SAXS Instrumentation

In this work, SAXS measurements were carried out using the Bruker NanoStar pictured in Figure 4.9. This technique has an optical system, which contains an active crossed multi-layer monochromatic system and a passive pinhole collimator, to adjust the X-ray beam (as illustrated in Figure 4.8). The X-ray radiation is monochromatised by the muti-layer monochromator, so the divergent 2-dimensional beam is adjusted to a 2-dimensional beam with a single wavelength from a distribution of λ. The use of the pinhole collimator system helps to obtain a direct and controlable beam size by which SAXS achieves the highest resolution with an extremely low background. A

spatial resolution can be obtained by using many pinhole collimators combined with a "cross-coupled Göbel Mirror" (ccGM).

An X-ray generator, operated at 40 kV and 35 mA, is used to generate X-ray radiation through a water cooled ceramic diffraction (KF type) X-ray tube which focuses an electron beam on a copper anode and allows the generated X-rays to exit via a Beryllium window. The X-ray beam passes through the ccGM system making four parallel beams. These beams are then controlled by a four pinhole system. The unwanted radiation is removed at the first pinhole and the rest of the X-rays continue to the second pinhole which controls the size of the beam with to a 750 μm diameter. The beam is defined at the third pinhole that has a diameter of 400 μm. The first three pinholes are mounted on XY translational stages and positioned between beam path tubes made of steel. The fourth pinhole is mounted on the chamber itself and the function of this pinhole is to remove the edge scattering of the third pinhole, which is why it is called an anti-scatter pinhole.

The (xy) position of the scattered X-rays entering the imaging area of the detector is determined by xenon gas atoms in the detector which are ionised by X-rays. These xenon ions move towards an electrode generating electrical signals that are transferred to a preamplifier in the detector. These signals are represented by the real time colour display building up the scattering pattern as shown in Figure 4.8. The built-in SAXS software is used to integrate intensity profiles and to transfer the 2-dimensional scattering patterns into a one-dimensional intensity $I(q)$, as a function of the scattering angle or the scattering vector (q).

4.3.2 Small-Angle neutron Scattering (SANS)

Small-angle neutron scattering (SANS) was developed in the 1960s, i.e. 30 years after the discovery of small-angle scattering by Guinier during X-ray diffraction experiments on metallic materials [169]. Since its development, SANS has become a powerful technique for probing different structures and materials. At the beginning, the technique was mainly used for studying crystalline materials, which improved the understanding of structural infor-

Figure 4.9: A typical setup of NanoStar SAXS, The University of Sheffield.

mation of many important materials. However, the last two decades have seen increasing intrest in using SANS for other disciplines, including soft matter (organic polymers and biological macromolecules). These materials contain many hydrogen atoms which makes them suitable for labeling with deuterium. Using this labeling method enhances the contrast between different regions in the sample or between the sample and the surrounding solvent [157].

The following sections will consider the principles and theory behind SANS with some description of its instrumentation and setup. However, the theories used to deal with the data obtained from SANS will be given in detail in Chapter 7.

4.3.2.1 Neutron Sources and Properties

Generally, there are two different ways to produce neutrons: by using a nuclear reactor or a spallation process. In the first approach, neutrons are obtained by the fission of uranium-235. Each fission process results in 2-3 neutrons. The most powerful research reactor in the world is the 57 MW HFR at ILL, France. The second approach employs particle accelerators and synchrotrons to acquire intense, high-energy protons. These protons are

directed at a target containing heavy nuclei (usually tantalum) to obtain 20 to 30 neutrons after each impact. The most powerful spallation neutron source in the world is currently the ISIS facility at Rutherford Appleton Laboratory (RAL), UK [156, 170].

The neutrons produced have wavelengths of between 0.01 and 3 nm by cooling them, for example, down to 20 K in liquid H_2. The energy of these neutrons can be calculated using the following equation,

$$E = \frac{3}{2} k_B T, \tag{4.25}$$

where k_B is Boltzmann constant and T is the absolute temperature (e.g. 20 K). According to the Maxwell-Boltzmann distribution, the most probable speed (v) can be calculated from:

$$\frac{3}{2} k_B T = \frac{1}{2} m v^2, \tag{4.26}$$

which gives

$$v = \sqrt{\frac{3 k_B T}{m}}, \tag{4.27}$$

where m is the neutron mass. The momentum of the neutron is given by

$$P = mv = \frac{h}{\lambda}. \tag{4.28}$$

Therefore,

$$\lambda = \frac{h}{mv} = \frac{h}{\sqrt{3 k_B T m}}, \tag{4.29}$$

where h is Planck's constant. Neutrons travel a distance L from the chopper to the detector in a time t (i.e. $v = L/t$). Intensity is measured as a function of time (number of neutrons arrived to the detector in time t), so the intensity can be obtained as a function of wavelength (λ).

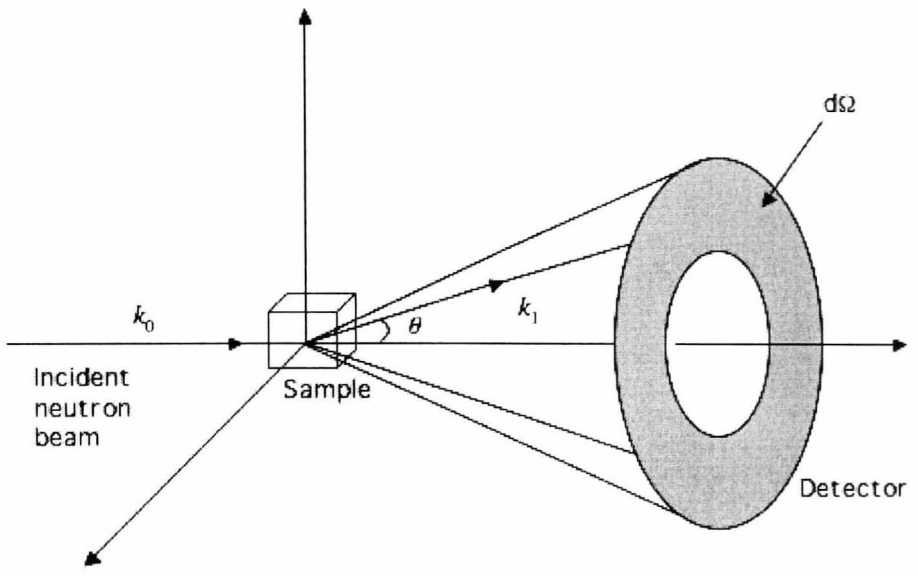

Figure 4.10: A schematic diagram showing the basic scattering principles (k_0, k_1 are the initial and final wave vectors) and including the solid angle of scattering, dΩ.

4.3.2.2 SANS Principles

A detailed theory of SANS can be found in many books and reviews in the literature [158, 171, 172, 173]. As for any small angle scattering method, the scattered momentum transfer Q is the difference between the incident wavevector k_0 and the scattered wavevector k_1 ($Q = k_1 - k_0$) in a given direction θ (see Figure 4.10).

When neutrons are scattered by a sample, they exchange energy and momentum with this sample. Therefore, the change in energy of the scattered neutrons is given by

$$\Delta E = E_1 - E_0 = \frac{1}{2}m(v_1^2 - v_0^2), \tag{4.30}$$

where ω is the neutron frequency and $\hbar$ is the reduced Plank's constant ($\hbar = h/2\pi$) . The momentum transfer Q can be written as:

$$\hbar Q = \hbar(k_1^2 + k_0^2 - 2k_1k_0\cos\theta)^{1/2}. \tag{4.31}$$

For elastic scattering, $k_1 = k_0$ and

$$Q = |Q| = \frac{4\pi}{\lambda} \sin \frac{\theta}{2}. \tag{4.32}$$

A SANS detector usually records the scattering intensity as a function of the energy and the scattering angle in terms of the differential cross section $\mathrm{d}\sigma(\theta)/\mathrm{d}\Omega\mathrm{d}E$, where $\sigma(\theta)$ is the cross section in barns ($10^{-28}\mathrm{m}^2$) and $\mathrm{d}\Omega$ is the solid angle (see Figure 4.10). This differential cross section is [173, 156]:

$$\frac{\mathrm{d}\sigma(\theta)}{\mathrm{d}\Omega\mathrm{d}E} = \frac{\text{number of neutrons scattered per second into } \mathrm{d}\Omega}{\Phi \mathrm{d}\Omega}, \tag{4.33}$$

where Φ is the incident neutron flux. In other words, $\mathrm{d}\sigma(\theta)/\mathrm{d}\Omega\mathrm{d}E$ is the probability that neutrons will be scattered by the sample with energy $\mathrm{d}E$ in an element of solid angle $\mathrm{d}\Omega$. From this differential cross section one can obtain the so-called scattering function (or Van Hove scattering law) [173]:

$$S(Q,\omega) = \frac{k_0}{k_1} \frac{1}{Nb^2} \frac{\mathrm{d}\sigma(\theta)}{\mathrm{d}\Omega\mathrm{d}E}, \tag{4.34}$$

where b is the scattering length, which is the probability that a neutron will be scattered by a nucleus, and N is the number of incident neutrons. The differential scattering cross section $\mathrm{d}\sigma(\theta)/\mathrm{d}\Omega\mathrm{d}E$ is referred to as the microscopic differential cross section to distinguish it from the macroscopic cross section that can be given by:

$$\frac{\mathrm{d}\Sigma(\theta)}{\mathrm{d}\Omega} = n \times \frac{\mathrm{d}\sigma(\theta)}{\mathrm{d}\Omega\mathrm{d}E}, \tag{4.35}$$

where n is the number concentration of scattering centres in the sample. The macroscopic differential cross section (which is often referred to in the literature as the scattering intensity $I(Q)$) can be written as [156]:

$$\frac{\mathrm{d}\Sigma(\theta)}{\mathrm{d}\Omega} = nV^2(\Delta\rho)^2 P(Q)S(Q) + B, \tag{4.36}$$

where V is the volume of one scattering centre, $(\Delta\rho)^2$ is the contrast between the solute and the surrounding medium, given by $(\Delta\rho)^2 = (\rho - \rho_\mathrm{m})^2$ with ρ and ρ_m being the neutron scattering length densities of the solute and the

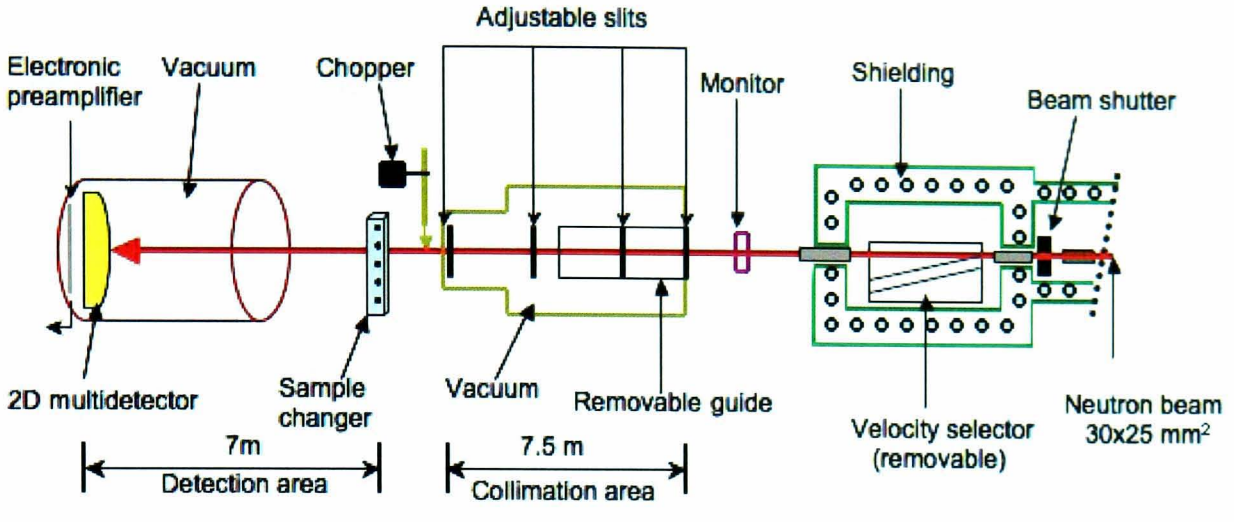

Figure 4.11: A schematic diagram showing a typical setup of small-angle neutron scattering based on the PAXY spectrometer at LLB, Saclay.

medium, respectively, and B is the background scattering signal. Equation 4.36 is a generalized form of the macroscopic differential cross section with $P(Q)$ and $S(Q)$ being the form factor and structure factor, respectively.

4.3.2.3 SANS Instrumentation

A typical setup of SANS based on the PAXY spectrometer used at LLB, Saclay (France) is shown in Figure 4.11, although other instruments have been used such as the one at the ISIS facility at Rutherford Appleton Laboratory (RAL), UK [156, 172, 171]. The incoming neutrons are monochromatized by a velocity selector to achieve wavelengths from 0.4 nm to 2 nm. The neutrons are then collimated using two collimation guides under vacuum. A sample holder is placed in the neutron beam path equipped with various sample environments, such as an automated temperature controller, magnetic field and shearing cells (e.g. Couette cell). The scattered neutrons arrive at a two dimensional detector in a vacuum tube at a distance between 1 and 7 m from the sample.

4.4 Neutron Spin Echo (NSE)

Relaxation and transport properties of polymer systems play a significant role in controlling the processing and applications of these systems [120, 174, 175, 176]. Therefore, characterizing these dynamic properties at the molecular level is necessary. However, understanding such dynamics is very complicated due to the fact that different molecular motions take place on different length scales governed by the general chain properties and the chemical structure of monomers [39, 44]. The first and simplest theoretical approach to address such dynamics was started by Langevin as an alternative to Brownian theory. However, the first successful model to describe molecular motions was developed by Rouse, who introduced the entropic effect between monomers (beads). This was followed by Zimm theory, which takes into account the hydrodynamic interactions between monomers and the surrounding solvent. For dense polymer systems, e.g. polymer melts, reptation (tube) theory was introduced by de Gennes and Edwards [40, 39, 61].

Testing these theories involves microscopic and mesoscopic techniques with high temporal resolution. For instance, quasi-elastic scattering techniques, such as neutron spin echo (NSE) spectroscopy play a significant role in the study of long-range relaxation processes of soft polymers and local dynamics of solid matters in space ($\leq$ 15 nm) and time (0.005 ns to 40 ns). The following sections will highlight the principles and instrumentation of NSE.

4.4.1 NSE Principles

Generally, as mentioned in section 3.3.2.3, the information obtained from neutron scattering is in terms of the differential cross section, which can be used to obtain the scattering function $S(Q,\omega)$ (equation 4.34). The intermediate scattering function $S(Q,t)$ can be written as the Fourier transform of $S(Q,\omega)$ [119, 177, 178]:

$$S(Q,t) = \int_{-\infty}^{\infty} S(Q,\omega)e^{i\omega t}\mathrm{d}\omega. \tag{4.37}$$

This intermediate scattering function depends on the atomic displacement (time) by:

$$S_{ij}(\underline{Q},t) = \left\langle \sum_{n,m} e^{i\underline{Q}\cdot[\underline{R}_n^i(t)-\underline{R}_m^j(0)]} \right\rangle, \tag{4.38}$$

where $\underline{R}_n^i(t)$ is the position of an atom (n) of a type (i) at time t. NSE measures the change in neutron velocity (Δv), i.e. the energy transfer between the scattered neutrons and the sample. The frequency (ω) is proportional to this energy transfer

$$\frac{\omega}{2\pi} = \frac{m}{2h}\left[v^2 - (v+\Delta v)^2\right]. \tag{4.39}$$

The analyzer of the NSE instrument allows the determination of the cosine transform of the scattering function $S(Q,\omega)$. Therefore, the output data of NSE is in the following form:

$$I_{det}\alpha\frac{1}{2}\left[S(Q) \pm \int \cos(J\lambda^3\gamma\frac{m^2}{2\pi h^2}\omega)S(Q,\omega)\mathrm{d}\omega\right], \tag{4.40}$$

where $J = \int_{path} |\underline{B}|\,\mathrm{d}l$ is the integral of the magnetic field induction, $|\underline{B}|$, along the distance between the first $\pi/2$ flipper and the sample, and $\gamma = 1.83033 \times 10^8$ rad/sT is the gyromagnetic ratio of the neutron. The type of the analyzer and the sign of the second $\pi/2$ flipper determine the sign of the integral in equation 4.40. The term $(J\lambda^3\gamma\frac{m^2}{2\pi h^2})$ is the time parameter, t.

4.4.2 NSE Instrumentation

Figure 4.12 illustrates the typical setup of an NSE spectrometer which was invented by F. Mezei [120, 174, 119, 179, 178, 180]. Neutrons first pass through a velocity selector to select the required velocity (wavelength) of the neutron beam. The neutron beam is then polarized and the resulting neutrons are

aligned in the velocity direction, e.g. x-axis. A $\pi/2$ flipper is used to change the spin direction of neutrons from x to z direction (i.e. perpendicular to the coil's magnetic field). The polarized flipped neutron beam travels through the first precession coils that produce a homogenous magnetic field in the direction of the beam path. Each neutron spin will make a Larmor precession around the magnetic field direction. Faster neutrons travel through the magnetic field rapidly and hence their angle of precession will be smaller. The neutron beam at the end of these precession coils is completely depolarized. A π flipper is used to rotate the spin of the neutrons 180° around the z-axis. When the neutron beam meets the sample, neutrons exchange momentum and energy with the sample resulting in changes in their velocity and directions but not the spin direction unless the sample is magnetic. The scattered neutrons then travel through the second precession coils. These precession coils produce the same value of magnetic field as the first coils but with an opposite direction. The elastically scattered neutrons will be fully polarized at the end of these coils, whereas the inelastically scattered neutrons will not experience a full repolarization. The resulting neutron beam will have spin direction distributed around the z-axis. Another $\pi/2$ flipper is employed to adjust the spin direction to a direction in the xy plane. A supermirror analyzer transmits the passing neutrons with a probability proportional to the cosine of the angle between the final neutron beam direction and z-axis. Finally, the transmitted neutrons are then collected on an area detector.

4.5 Magnetometry (SQUID)

A superconducting quantum interference device magnetometer (SQUID) is a very sensitive technique used to measure magnetisation [181]. Due to the extremely weak magnetic fields ($\approx 5 \times 10^{-18}$ T) that can be detected by the SQUID with a very low noise level (≈ 3 fT.Hz$^{-1/2}$), it has been used for many applications including biomagnetism and material characterisation [182]. SQUID may be classfied into direct current (DC) SQUID and radio frequency (RF) SQUID. These two types of SQUID use superconducting loops containing Josephson junctions. However, RF SQUIDs use only one

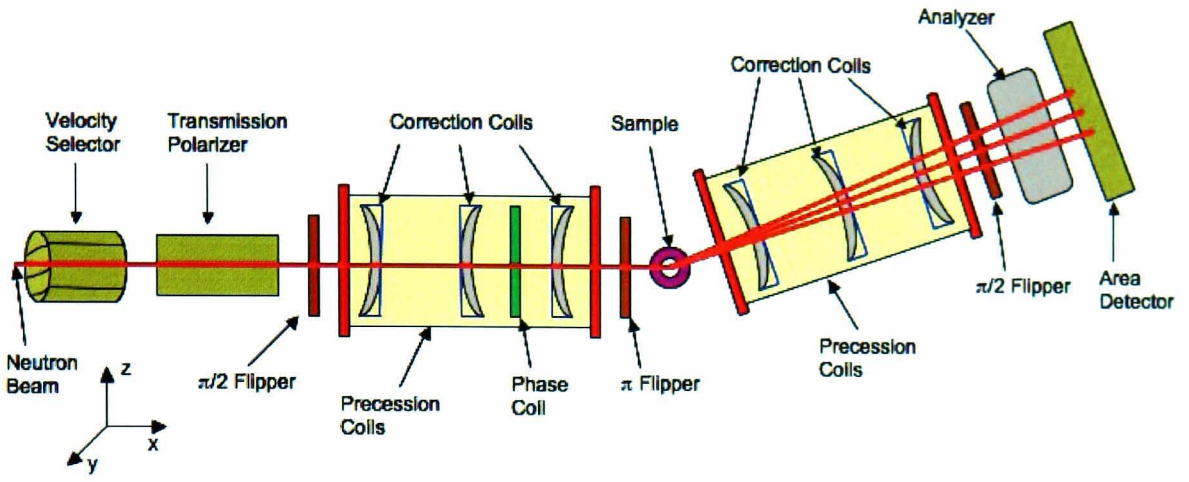

Figure 4.12: A schematic diagram showing a typical setup of NSE spectrometer.

Josephson junction, which makes them cheaper but less sensitive compared to DC SQUIDs [183, 184]. In this work, an RF SQUID was used for all magnetisation measurements (see section 6.2.3).

4.5.1 SQUID Principles

The main principle behind the SQUID is the measurement of the voltage induced by the magnetic field originating from a sample in a field-sensitive coil. RF SQUID, for example, consists of an Nb-superconducting ring and RF circuit (tank circuit), which are inductively coupled to each other by superconducting transformers (Figure 4.13). The superconducting ring is fed with an oscillating external flux. The tank circuit is used to detect changes in the internal flux which has a typical resonance of 20-30 MHz [183]. The entire system must be operated at low temperatures using liquid helium.

After removing the magnetic field, the superconducting ring will retain some discrete levels of magnetic flux due to induced surface currents. This in turn generates a supercurrent in the superconducting ring which will remain indefinitely. However, this supercurrent must remain at the same level for superconduction to continue. The presence of a Josephson junction "weak-link" has the advantage of lowering the supercurrent significantly to about 50 μA because electron pairs can tunnel through the weak-link [185]. A

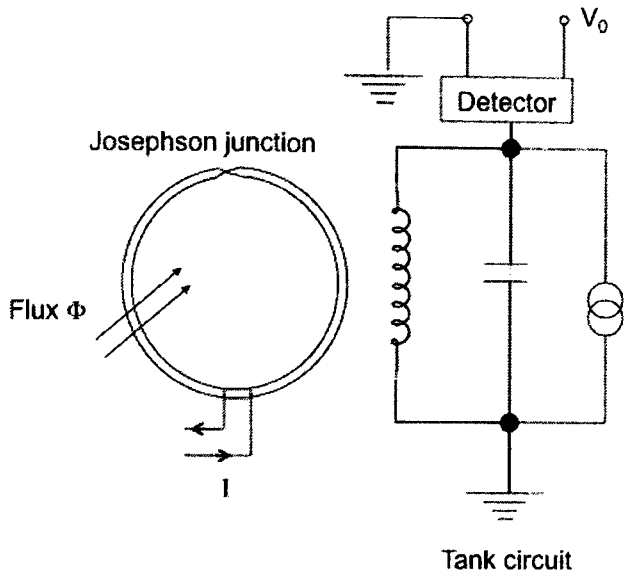

Figure 4.13: A schematic diagram showing the principles of RF SQUID.

magnetic flux will be generated from the oscillation of the supercurrent with a period of one fluxon (one fluxon = 2×10^{-15} Tm^2) [186].

The supercurrent through the weak-link can be changed by the magnetic field originating from a system placed near the sensing coils, which in turn can change the total flux (the total flux is a combination of the external flux and that from the oscillating current in the weak-link). This change in the flux inductively changes the resonance of the tank circuit which can be recorded by a controlling system. The recorded variation in flux can then be converted to magnetisation values using some theoretical models.

Part I

Gels and Networks

Chapter 5

Single Molecule Diffusion in Hydrogels

5.1 Introduction

The development of smart polymer systems has gained attention in the last decade because of their many possible applications for drug delivery and tissue engineering [71, 63]. Smart polymers have the ability to change their physicochemical properties in response to the surrounding environments. Different polymer systems are responsive to different physical and chemical stimuli, such as temperature, magnetic field (see chapter 6), pressure, pH and ions. Hydrogels are an example of responsive polymer systems that can be stimulated by changes in temperature, pH and ionic strength.

The theory of diffusion of linear polymers in a fixed network was introduced by Doi and Edwards [44]. In this theory, the controlling factor of the diffusion coefficient is the network mesh size, which is the distance between cross-link points, and the size of the linear polymer chain. This diffusion process is very complicated and there is no simple theory to describe and explain many observed behaviours. However, some work in the literature can be considered as progress in combining the above theory with the responsiveness of hydrogels for useful applications [187, 15]. Studying diffusion through polymer networks is key to understanding their properties and to explore the

possibility of modifying their behaviour for certain tasks [188, 189]. There have been many techniques used to study diffusion in polymer solutions and gels, such as gravimetry, dynamic light scattering, neutron reflectometry and fluorescence correlation spectroscopy (FCS) [34, 35]. Furthermore, understanding diffusion in heterogeneous media is of special importance in many processes in biological systems, such as the transport of proteins and drug molecules through the cell membrane [190].

In this chapter, the diffusion of FITC-dextran in poly(methacrylic acid) (PMAA) hydrogels will be investigated as a function of different physical and chemical stimuli including temperature, pH and salt using fluorescence correlation spectroscopy (FCS). The macroscopic swelling behaviour of the PMAA hydrogel in the above conditions will be considered to support the understaning of the diffusion behaviour in the system.

5.2 Experimental

5.2.1 Materials and Synthesis

5.2.1.1 Free Radical Polymerisation

Free radical polymerisation [191] is a type of polymerisation by which a polymer is formed in three steps: initiation, propagation and termination, as shown in Figure 5.1. The free radicals (atoms or molecules with unpaired electrons), which are responsible for starting the polymerisation, are formed in the initiation step under conditions of heat or electromagnetic radiation. These free radicals must remain active and stable enough until reacting with monomers to create other active centres out of these monomers in a step called propagation. The new active centres can react with other species to form active chain ends in a process called chain transfer. In principle, the chain can propagate until consuming all the monomers but these radicals are very reactive and bind to other species very rapidly, forming inactive covalent bonds which terminate the polymerisation process. Termination of chains can be formed through two ways: (1) combination, in which two radical chain ends are bound together to form one long chain; (2) disproportionation, in

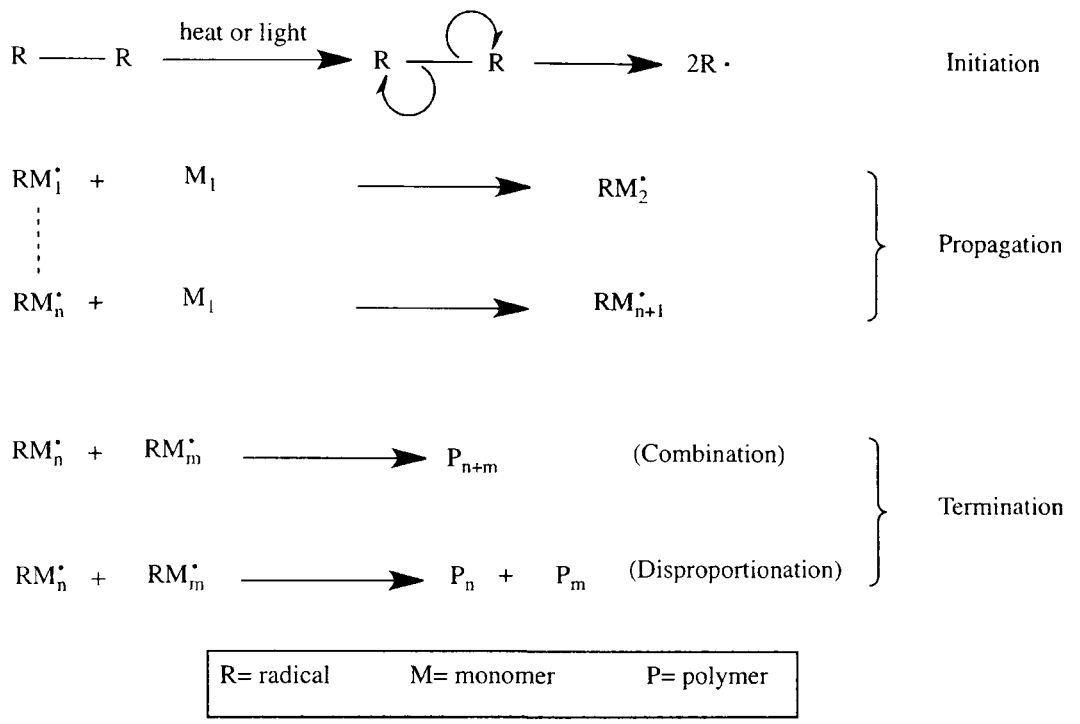

Figure 5.1: Free radical polymerisation mechanism.

which two separate polymer chains are formed by moving a hydrogen atom from one active end to another to prevent chain growth on both sides. Due to the fact that termination steps cannot be controlled, the reactions generate very heterogeneous systems.

5.2.1.2 Hydrogel Synthesis

PMAA hydrogels [68] were synthesized via a free radical polymerisation. An initiator, 2,2'-azobis (2-methylpropionamidine) dihydrochloride (AMPA) (Aldrich, 98%) and a cross-linker, methyl-bisacrylamide (MBA) (Aldrich, 98%), were dissolved in distiled water and added to the monomer methacrylic acid (MAA) (Aldrich, 98%) in a sealed container and then exposed to a nitrogen flow for 30 min. The chemical structures of the used reagents are shown in Figure 5.2 and the quantities used for this preparation are listed in table 5.1. However, the amount of water and cross-linker were varied resulting in different structural behaviour of the hydrogel (this will be discussed in more detail in the corresponding sections). The polymerisation of MAA

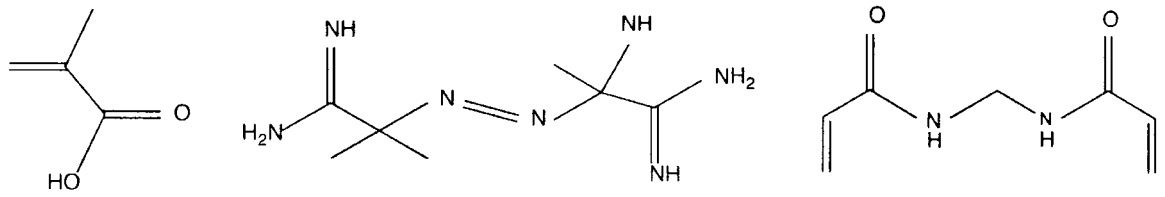

MAA AMPA MBA

Figure 5.2: Chemical structures of the reagents used to prepare PMAA hydrogels.

Reagents	Quantities	
H_2O	10 ml	0.555 mol
MAA	2 ml	0.024 mol
AMPA	0.002 g	7.347×10^{-6} mol
MBA	0.006 g	3.892×10^{-5} mol

Table 5.1: Quantities used to prepare the hydrogels.

took place by placing the sealed solution in an oven at 65 °C for 8 h. After the polymerisation was completed, the hydrogels were washed many times with distilled water to remove unreacted materials.

5.2.1.3 FITC-dextran Solution Preparation

In order to study diffusion in PMAA hydrogels, FITC-dextran was used as a fluorescent probe since it can be detected by FCS. FITC-dextran solutions were prepared by dissolving the required amount of FITC-dextran in 5 ml of distilled water (HCl, NaOH and salt solutions were used as well depending upon the experiment required) to obtain a concentration of 10^{-5} M depending on the molecular mass of FITC-dextran (in this case 70 kDa). The obtained solution was then diluted to 1 nM to meet FCS requirements, which will be discussed in the following section. A small piece of the hydrogel was placed in these probe solutions for sufficient time to allow penetration of FITC-dextran chains and to reach the equilibrium of the hydrogel.

5.2.2 FCS Measurements

FCS measurements were conducted using a ConfoCor2 FCS Module fitted to an LSM510 inverted confocal microscope (Zeiss), which is pictured in Figure 5.3. The temperature of the sample was controlled using a Linkam heating stage (Linkam Scientific Instruments Ltd, Surrey, UK) with TMS94 heat controller and LNP-1 nitrogen flow control. The required excitation wavelength for FITC-dextran is 492 nm which then emits light with a wavelength of 518 nm. Thus, this excitation radiation was obtained using an argon laser beam (488 nm), which was directed into the microscope objective (water immersion objective 40× /1.2NA), via a dichroic mirror and focused on the sample. The resulting fluorescence light from the sample was collected by the same objective and passed through the dichroic mirror and the Long Pass 505 (LP505) emission filter. The spatial resolution was obtained by a pinhole (70 μm) in the image plane, which cuts off any fluorescence light not coming from the focal plane. The light was then detected using an avalanche photodiode (SPCM-200PQ), which is a single photon sensitive detector. The translational diffusion of the fluorescence molecules within the confocal volume leads to fluctuations in the fluorescence intensity of the emitted light that are recorded by the detector. These fluctuations, and hence the autocorrelation function, are quantified from the changes in the local concentration of the fluorophore within the confocal volume. The power of the excitation laser beam was kept at 5% in order to to keep the fluorescence emission linear with the excitation and to reduce the distortion of the correlation function originating from triplet state formation.

The confocal waist radius, ω_{xy}, was ascertained by evaluating the diffusion time of Rhodamine (Rh6G), which has a known diffusion coefficient ($D = 281$ $\mu m^2/s$) in water. From the fitting to the autocorrelation function (equation 4.19), the diffusion time of Rhodamine in water was $\tau = 80$ μs. Using this value in equation 4.15 yielded a confocal waist radius $\omega_{xy} = 150$ nm. This value has been used throughout this work to calculate the diffusion coefficients from the respective diffusion times using equation 4.15.

The obtained FCS autocorrelation function for each sample is the accu-

Figure 5.3: A photograph of the inverted confocal microscope, including FCS, used for diffusion measurements.

mulation of at least 100 short runs, with 10 s measuring time in each run. This measuring time was found to be of sufficient duration in this work, for single fluorescent molecules to be detected while passing the confocal volume. However, a longer measuring time would be required if large aggregates were expected in the confocal volume, in order to minimize the distortion they might cause in the autocorrelation function. The average value of the runs is taken as the normalized autocorrelation data. Diffusion times were obtained from the fit of these autocorrelation data to the model described by equation 4.19, from which the diffusion coefficients were determined using equation 4.15. An example of the obtained FCS data is shown in Figure 5.4 in which the autocorrelation curves for FITC-dextran in water at different selected temperatures are fitted to the autocorrelation model (equation 4.19). For the reason that PMAA hydrogels are heterogenous [192], five measurements in different areas of each sample were taken from which averages of the diffusion times and coefficients were obtained.

The work in this chapter involved two different diffusion measurements:

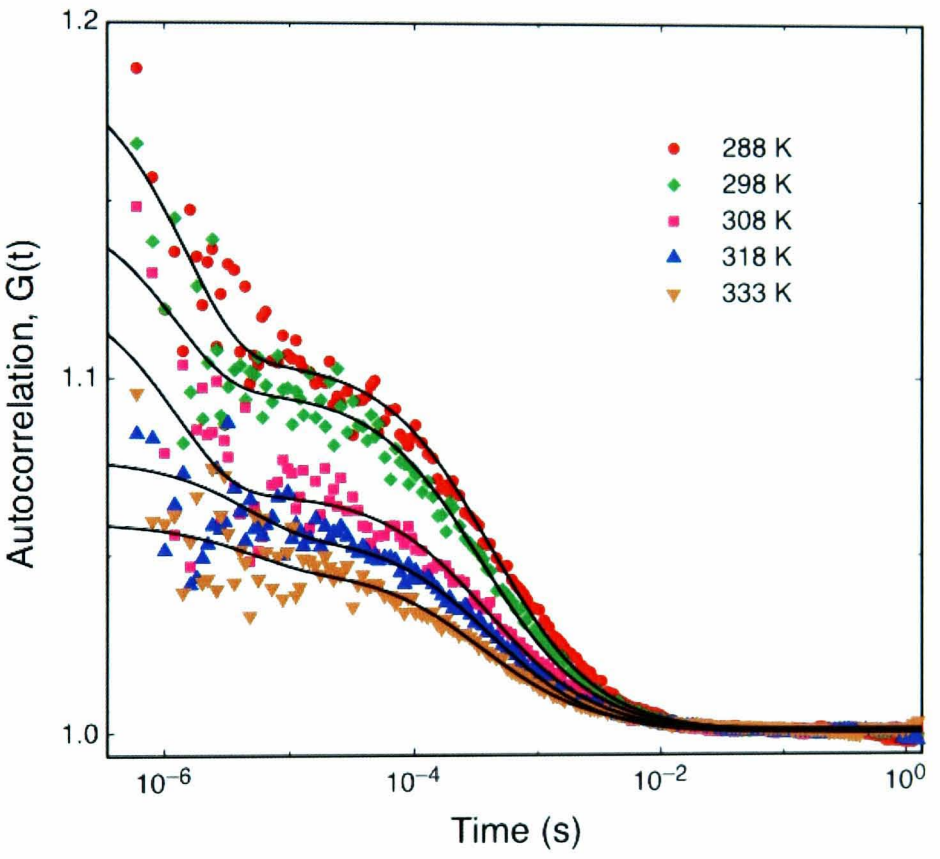

Figure 5.4: An example of FCS data for diffusion of FITC-dextran in water at selected temperatures, showing the decrease of diffusion time with temperature. The solid lines are the best fit to equation 4.19.

the self-diffusion of FITC-dextran chains in solutions and the diffusion of FITC-dextran within PMAA hydrogels. For self-diffusion, 1 nM of FITC-dextran in water (at different pH and ionic strength) was used and it was assumed to be in an infinite dilution of non-interacting spherical molecules. Using these assumptions, the hydrodynamic radius of FITC-dextran, R_{H} . can be calculated from the Stokes-Einstein equation for diffusion which is given by:

$$D_0 = \frac{k_{\mathrm{B}}T}{6\pi\eta_{\mathrm{s}}R_{\mathrm{H}}}, \tag{5.1}$$

where η_{s} is the viscosity of the solvent.

The diffusion coefficient of FITC-dextran in PMAA hydrogel can be correlated to the molecule size (diameter), d, and its diffusion coefficient in pure solvent, D_0, (equation 5.1) to obtain the average mesh size (also known as the correlation length) of the PMAA hydrogel, ξ, using a relationship introduced by de Gennes and co-workers [193, 194]:

$$D = D_0 \exp\left(-\beta\left(\frac{d}{\xi}\right)^{\delta}\right), \tag{5.2}$$

where $\delta = 2.5$ for cross-linked networks and β can be considered to be of the order of one [193].

5.2.3 Swelling Measurements

The PMAA hydrogel, synthesized as described in section 5.2.1.2, was immersed in distilled water to ensure complete swelling and when equilibrium was reached (constant mass), small pieces of hydrogel were taken for examination. For measurements of the swelling of PMAA hydrogels, the hydrogel pieces were first dried under vacuum at 40 °C for 5 h before being immersed in water and allowed to reach an equilibrium swelling as a function of temperature, ionic strength and pH. The equilibrium swelling ratio, Q, is defined as:

$$Q = \frac{m_s - m_d}{m_d}, \tag{5.3}$$

where m_s and m_d are the mass of the swollen and dry hydrogel, respectively.

5.2.4 Titration and NMR

H_2O was boiled vigorously for 10 min to remove any dissolved CO_2 then put in a sealed airtight container to cool. 500 μl of 1.0 M HCl was added to 30 ml of the previously degassed water which gave a pH of 2. 0.013 g of FITC-dextran was added to the water. The pH changed immediately from 2 to 2.4 upon the addition of FITC-dextran. 1 M NaOH was added drop-wise to the solution while the pH was recorded as a function of the added volume of NaOH.

^{1}H NMR (Bruker 400 MHz spectrometer) was used in order to detect any chemical shift in FITC-dextran as a result of changing the pH of the solution. For this experiment, 50 mg of FITC-dextran was added to 1 ml of D_2O at different pHs: 1, 4, 8 and 12.

5.3 Results and Discussion

5.3.1 Swelling of PMAA Hydrogel: Effect of Synthesis

As discussed in chapter 3, hydrogels can be defined by their equilibrium swelling degree. This swelling degree of hydrogels (the capability of absorbing water) can be controlled by many factors including the cross-link density and the volume fraction of the solvent used to prepare the hydrogel. Figure 5.5 shows the dependence of the equilibrium swelling ratio of PMAA hydrogel in pure water on the amount of the solvent used during the polymerization of MAA. The swelling ratio of PMAA hydrogel increases by a factor of 25 upon an increase in the solvent volume fraction from 0.5 to 0.83. The same trend can be seen for different cross-link densities. At low solvent volume fraction (0.5-0.75), different cross-linker concentrations show identical swelling ratios, whereas the swelling ratio increases with increasing the

cross-linker concentration at high solvent volume fraction. These results indicate that the number of cross-links per unit volume play a significant role in the swelling behaviour of PMAA hydrogels. This is due to the fact that introducing more cross-links in the matrix leads to the formation of shorter chains between cross-links, which is unfavourable for a large expansion. In other words, the elasticity of these networks decreases with increasing the cross-link concentration, which is unfavourable for mixing according to the thermodynamics described in Chapter 2, section 2.3.

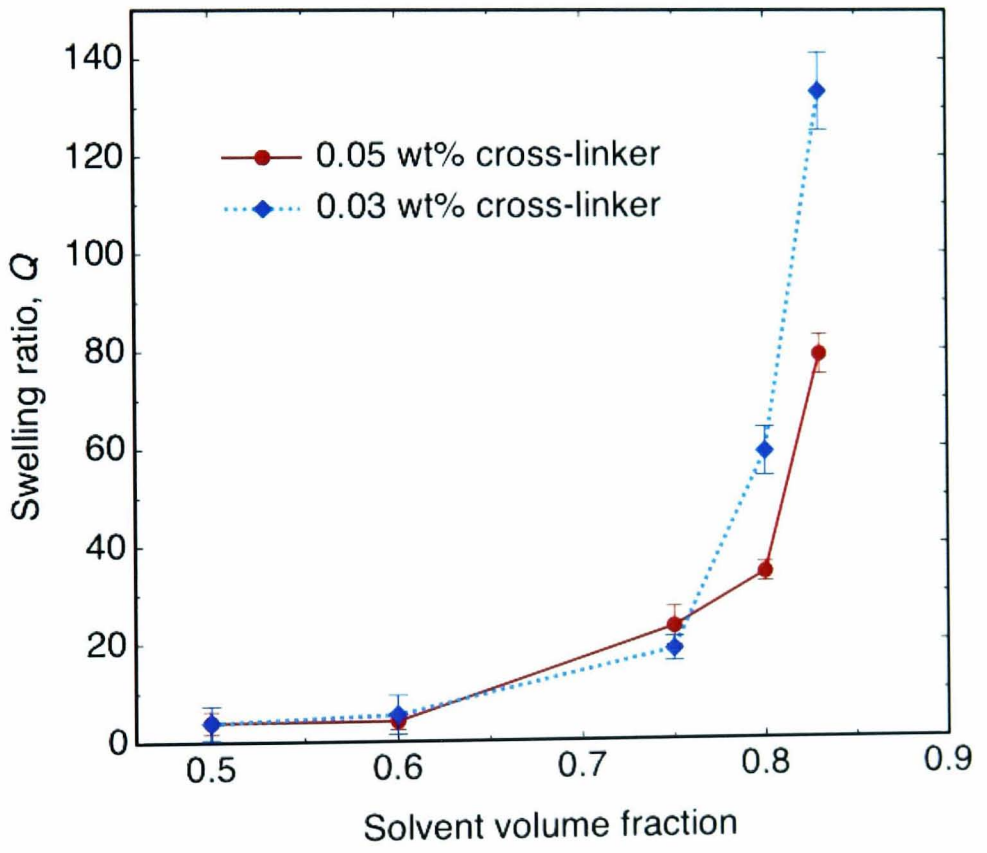

Figure 5.5: The effect of solvent volume fraction during preparation on the swelling of PMAA hydrogel at different cross-link densities in neutral water. The error bars are the statistical errors calculated from five measurements and the lines are guides for the eye.

5.3.2 Temperature Effect

The diffusion coefficient of FITC-dextran in pure water increases with temperature as expected from Zimm theory, described in Chapter 2. Figure 5.6 shows such a behaviour with the solid line being the fit to Zimm model (equation 2.51). This is due to a change in the viscosity of water at high temperature resulting from the disruption of hydrogen bonding leading to an increase in fluidity [195, 196]. The conformational behaviour of FITC-dextran chains with temperature might play a role in increasing the diffusion coefficient; however, this needs further study to be verified (see Chapter 9).

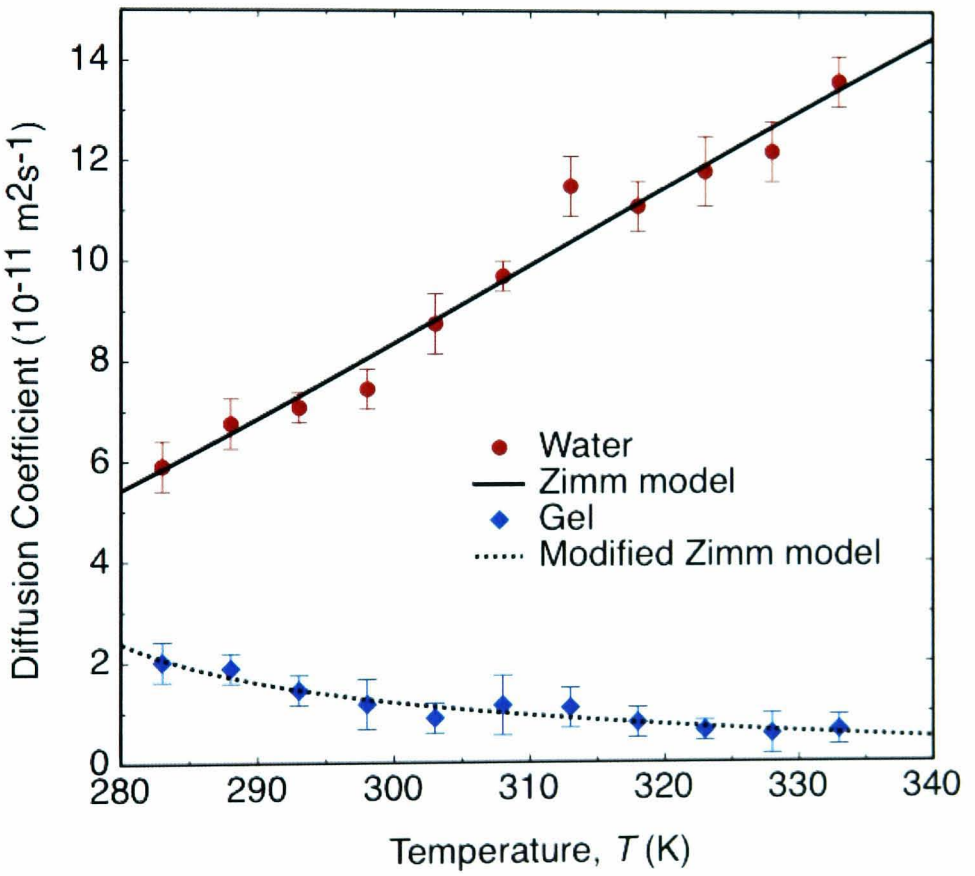

Figure 5.6: Temperature dependence of diffusion coefficient of FITC-dextran in pure water (circles) fitted to Zimm model (solid line) and in PMAA hydrogel (diamond) fitted to the modified Zimm model (dashed line). The latter model was developed by my colleague Matthew Mears.

The diffusion coefficient of FITC-dextran in PMAA hydrogel follows a negative trend from that seen in water (Figure 5.6). This can be attributed

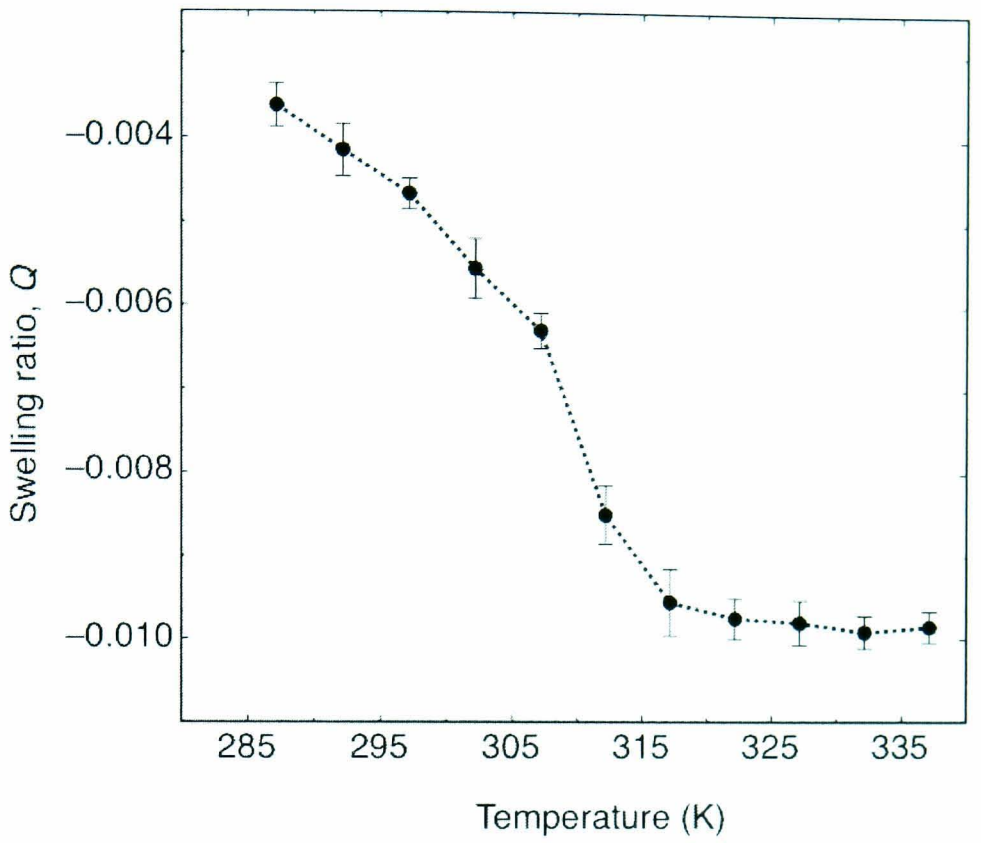

Figure 5.7: Temperature effect on the swelling of PMAA hydrogel. The negative values of Q mean that PMAA hydrogel collapses or shrinks with temperature, hence the final mass is smaller than the initial mass. The error bars are the statistical errors calculated from three measurements and the dashed line is a guide for the eye.

to the fact that the polymer network adds an effect that overtakes the normal thermal motion and decreases the diffusion coefficient with increasing temperature. Zimm theory suggests that in order to overwhelm any thermal effect the viscosity of the system must increase sufficiently. By studying the swelling behaviour of PMAA hydrogel as a function of temperature, it was found that the swelling ratio decreases with increasing tempreature (see Figure 5.7), although PMAA hydrogel is not among the class of materials that is considered to be highly sensitive to tempreature. This means that PMAA hydrogel shrinks in size upon an increase in temperature, with the solvent being drained out of the network. Assuming that no material is lost from the hydrogel during this collapse process, the decrease of solvent mass

per unit volume leads to an increase in the polymer mass concentration, c. In other words, removing some solvent from the hydrogel with temperature without any effect on the polymer network means the mass ratio of polymer to solvent increases per unit volume.

The viscosity in the Zimm model (equation 2.51) can be considered to be the viscosity of the whole system (the total viscosity $\eta = \eta_s + \eta_p$, where η_p is the viscosity of the viscoelastic polymer network), which can be determined from Huggins equation of intrinsic viscosity, $[\eta]$ [40]

$$\frac{\eta - \eta_s}{\eta_s c} = [\eta] + k_H [\eta]^2 c + ..., \tag{5.4}$$

where k_H is the Huggins coefficient. By substituting the Huggins equation into the Zimm model, the result is a diffusion model that shows a good fit to the data in Figure 5.6.

This modified Zimm model suggests that the change in hydrogel structure is due to the change in the net viscosity. However, there might be some other effects on the diffusion coefficient such as the change of the excluded volume of FITC-dextran molecules (chain conformation) with increasing temperature. Although the hydrodynamic radius of FITC-dextran can be determined from the diffusion in pure water, the latter effect was not taken into consideration in this work as further thermal characterization of FITC-dextran is required, in a similar manner to studies on other linear polymers such as polystyrene [197] and polyethylene [198], in order to be distinguished from the structural changes of the gel.

The mesh size of PMAA hydrogel was determined using equation 5.2 with the size of the diffusing molecule obtained from equation 5.1. Figure 5.8 shows an exponential decrease by almost a factor of 20 in the mesh size upon an increase in the temperature from 283 K to 333 K. In comparison to the swelling ratio change with temperature shown in Figure 5.7, which appears sigmoidal with a constant Q at high temperatures, the mesh size decays monotonically with temperature. The overall trends of the curves in Figures 5.7 and 5.8 are comparable, although the mesh size was obtained from the diffusion coefficient of FITC-dextran the interaction and conformation of

which was not taken into account (see the future work in Chapter 9).

If the hypothesis above that the only effect on the diffusion in PMAA hydrogel is the net viscosity is true, then the mesh size of the hydrogel can be correlated to the this viscosity. In reviewing the literature, little data were found on the association between the mesh size and temperature, although the mesh size of polymer networks after equilibrium swelling is well established [199, 200, 187]. The mesh size can be correlated to the equilibrium swelling ratio, ϕ, and the number of cross-links per chain, n, as [200]:

$$\xi = \phi^{1/3}\sqrt{C_n}\sqrt{n}l, \tag{5.5}$$

where C_n is a characteristic ratio of the polymer with a value of 14.6 for PMAA [200] and l is the C-C bond length (1.54 Å). The swelling ratio of the polymer network under temperature, $\phi(T)$, can be correlated to the viscosity of the medium by

$$\frac{\phi(T)}{\phi_0} = \frac{\eta\,(T)}{\eta_0}, \tag{5.6}$$

where ϕ_0 is the initial equilibrium swelling ratio. The viscosity of the medium can be written as a function of temperature using the Williams, Landel, and Ferry (WLF) equation [201, 202]:

$$\eta(T) = \eta_0 \exp\left(\frac{-C_1\,(T - T_0)}{C_2 + (T - T_0)}\right), \tag{5.7}$$

where C_1 and C_2 are quasi-universal constants with values of 17.4 and 51.6 K, repectively, and T_0 is a reference temperature, which is commonly taken to be the glass transition temperature T_g, at 273 K. By substituting equation 5.7 into equation 5.6 and then using the result in equation 5.5, the mesh size can be given as:

$$\xi = \phi_0^{1/3}\left[\exp\left(\frac{-C_1\,(T - T_0)}{C_2 + (T - T_0)}\right)\right]^{1/3}\sqrt{C_n}\sqrt{n}l. \tag{5.8}$$

This model shows a good fit to the data in Figure 5.8. The values of ϕ_0 were determined from the swelling measurements in section 5.3.1. n was not

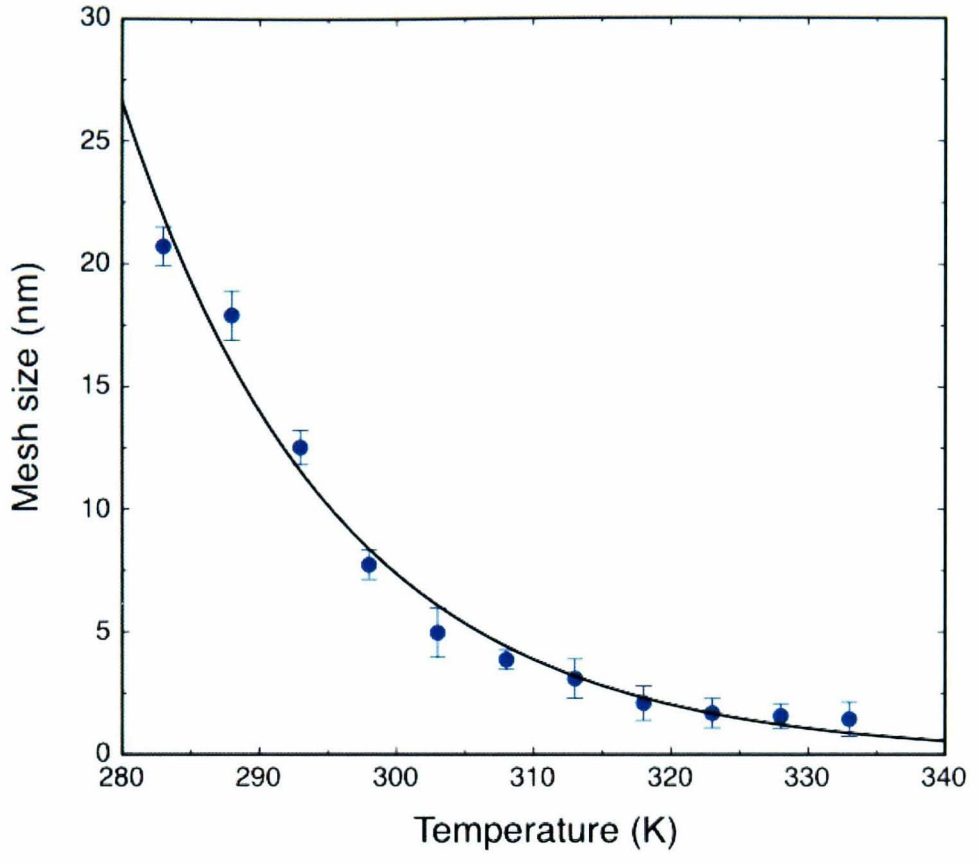

Figure 5.8: Mesh size of PMAA hydrogel as a function of temperature calculated using equation 5.2. The solid line is a fit to equation 5.8, a model developed to describe the effect of temperature on the mesh size. The error bars are the statistical errors originating from the errors of the diffusion coefficient (the data in Figure 5.6).

known previously and therefore it was let to vary during the fitting, giving a value of 47 cross-links per chain.

5.3.3 pH Effect

PMAA hydrogel is a weak polyacid that has a carboxylic acid group whose charge equilibrium is affected by the pH of the solution (as described in Chapter 3). In acid conditions, the carboxylic group is protonated (Figure 5.9) and therefore, due to the absence of repulsive forces between the charges, the polymer chains are in a "collapsed state". In basic conditions, the carboxylic group is more charged and therefore the polymer chains are in a "swollen state" due to the electrostatic repulsion between these charged groups and

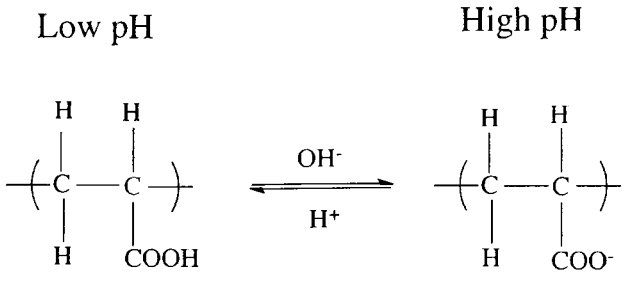

Figure 5.9: Effects of acid and basic conditions on the carboxylic acid in water.

the counterions. Polymer chains swell because they absorb the solvent to reduce or "screen" this electrostatic repulsion.

Therefore, any change in the pH results in structural changes in PMAA hydrogels which can be determined by measuring the equilibrium swelling ratio Q as shown in Figure 5.10. Compared to the small change in the swelling ratio as a function of temperature (Figure 5.7), the swelling ratio in the case of pH showed a significant increase at high pH. As expected and shown in previous studies [68, 203, 11], at low pH the swelling ratio is very low because PMAA chains tend to form very dense hydrophobic clusters connected by short polymer chains. This is due to the attractive forces caused by the carboxylic groups' acceptance of more protons. By increasing the pH, the swelling ratio increases due to the decrease in the hydrophobicity of these clusters, allowing polymer chains to extend (this occurs up to pH 6). As a polyelectrolyte, the swelling of PMAA hydrogel can be explained by the osmotic effect as the total osmotic swelling pressure is the sum of the mixing pressure, elastic pressure and ionic or Coulombic pressure, $\pi_{\text{swelling}} = \pi_{\text{mixing}} + \pi_{\text{elastic}} + \pi_{\text{ionic}}$ (see Chapter 2). At equilibrium, these three pressures must compensate each other and give $\pi_{\text{swelling}} = 0$ [72, 204, 11, 205]. Above pH 6, there is some conflict [68, 11] as to whether the swelling continues with increasing pH, or whether the increase of ionic strength causes a degree of charge shielding which allows the gel to collapse a little. The results presented here show the decrease of swelling ratio between pH 6 and pH 8, and this can be explained by the screening (or shielding) effect where an insoluble layer is formed which prevents further swelling. The swelling ratio then increases at

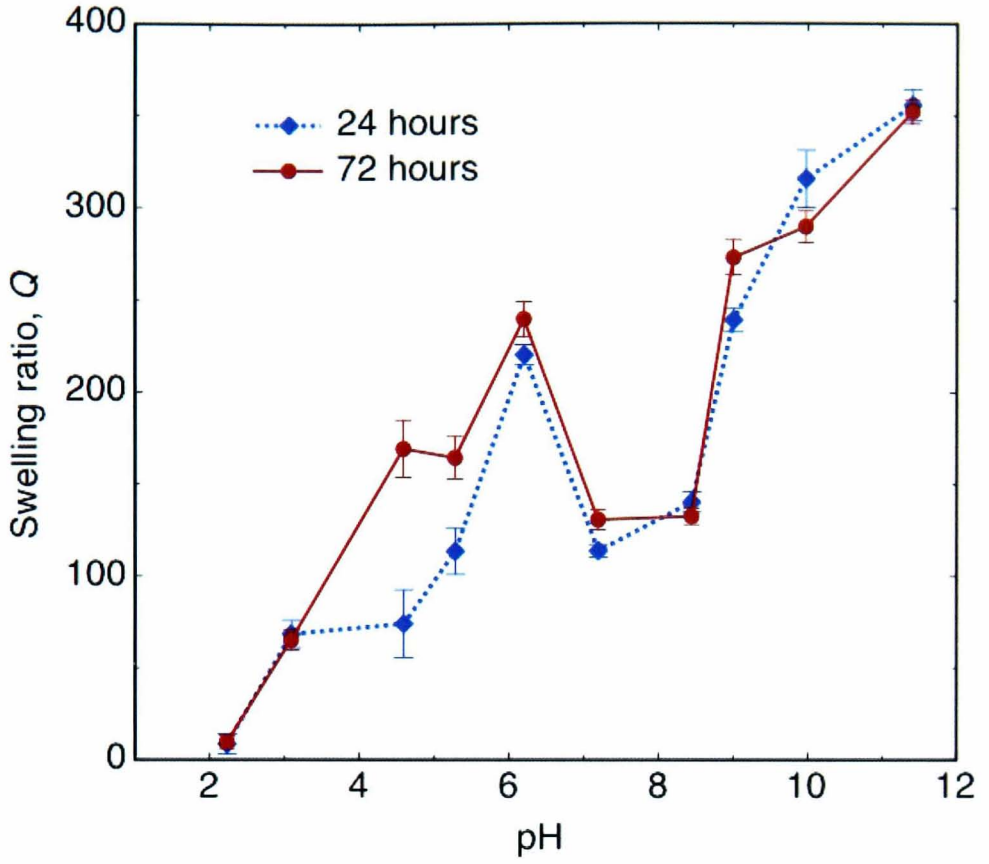

Figure 5.10: Swelling ratio of PMAA hydrogel as a function of pH. The two plots show the time of swelling before the measurement in order to test the time needed for equilibrium. The error bars are the statistical errors calculated from three measurements and the lines are guides for the eye.

higher pH after disengaging from the screening effect.

Testing the effect of cross-link density on the swelling of PMAA hydrogel in acid and basic conditions is shown in Figure 5.11. The swelling of different PMAA hydrogels with different cross-link densities showed identical trends in response to pH; however, in alkaline conditions, the swelling ratio reached higher values at low cross-link densities due to the fact that a low cross-link density leads to longer sub-chains between cross-links, increasing the elastic pressure π_{elastic} . In terms of the thermodynamics of mixing (Flory theory described in Chapter 2, equation 2.19), the decrease in cross-link density leads to an increase in the elastic energy term which is favorable for mixing.

The swelling results above can help with understanding the mechanism of FITC-dextran diffusion within PMAA hydrogel in acid and alkaline con-

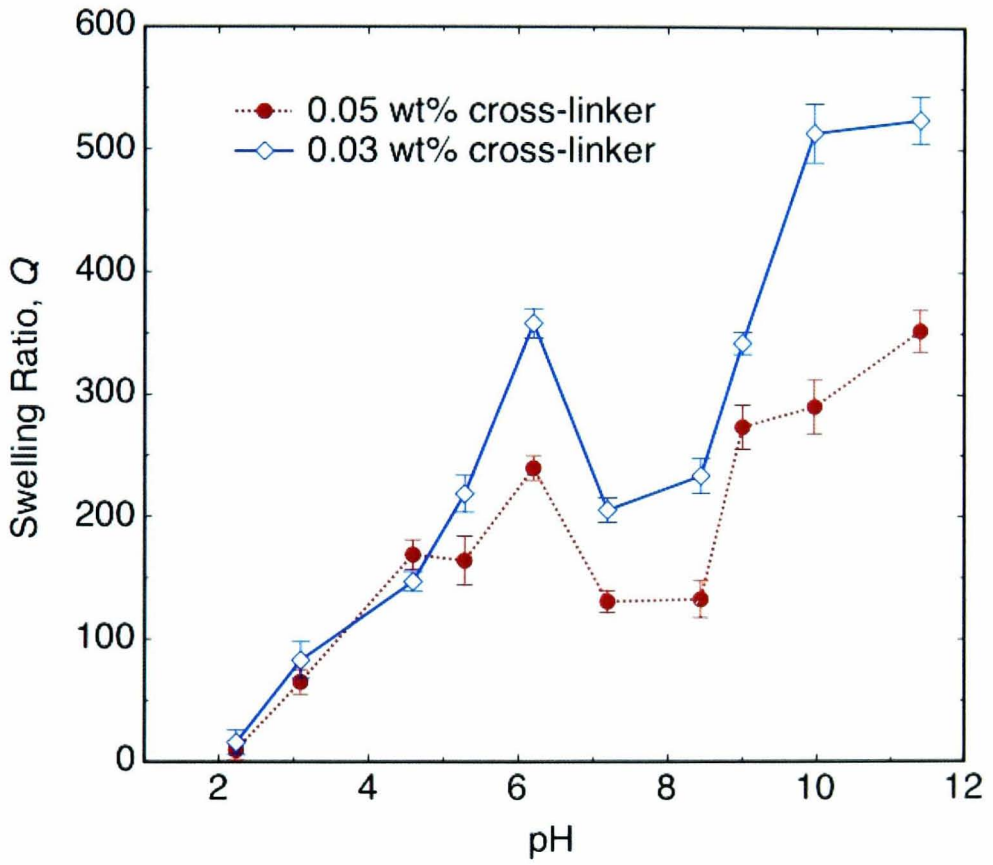

Figure 5.11: Swelling ratio of PMAA hydrogel as a function of pH at two different cross-link densities. The error bars are the statistical errors calculated from five measurements and the lines are guides for the eye.

ditions. The pH of the solution influences not only the structure of the hydrogel but also the conformation of FITC-dextran molecules which is in turn reflected in their diffusion coefficient. Figure 5.12 shows that the diffusion coefficient of FITC-dextran in pure water decreases with increasing the pH of the solution. This can be attributed to the change in the net charge of the solution, which therefore gives FITC-dextran molecules different conformations at different acid and basic conditions. For example, extending the FITC-dextran chain due to repulsive forces might delay the diffusion process at a certain pH value. However, previous studies have debated whether FITC-dextran is charged or neutral. For example, Ioan and co-workers [206] demonstrated that the radius of hydration of dextran in water is comparable to that in 0.5 mM NaOH. This study also showed a similar intrinsic viscosity of dextran in water and NaOH which is in agreement with the data in Figure 5.12 at high pH. Nevertheless, the titration results in Figure 5.13 provide evidence that FITC-dextran is a charged molecule (negatively charged) which seems to be consistent with other previous research [207, 208]. Yet, NMR spectra, shown in Figure 5.14, do not show any chemical shift with changing pH, which can be explained by the charges originating from the FITC, which was not the subject of the NMR investigation.

Moreover, the effect of pH on hydrogel structure (seen in Figure 5.10) plays a significant role in the diffusion process of FITC-dextran in these systems, taking into consideration the effect of pH on the FITC-dextran molecule itself. Figure 5.12 also shows that acidic conditions decrease the diffusion coefficient of FITC-dextran due to the collapse of the hydrogel. This collapse results in an increase in the polymer concentration (similar to the temperature case in section 5.3.2; however, further work would be required to be able to apply the same modeling procedure as for temperature), which hinders FITC-dextran molecules and reduces their diffusion coefficient. The repulsive force between the carboxylic group in PMAA hydrogel and the charges introduced in the solution at high pH causes the gel to swell and uptake a large amount of the solvent, which enhances the diffusion coefficient of the traversing molecules. It is noticeable from Figure 5.12 that at the highest pH point, within errors, the diffusion coefficient in the swollen hydrogel is

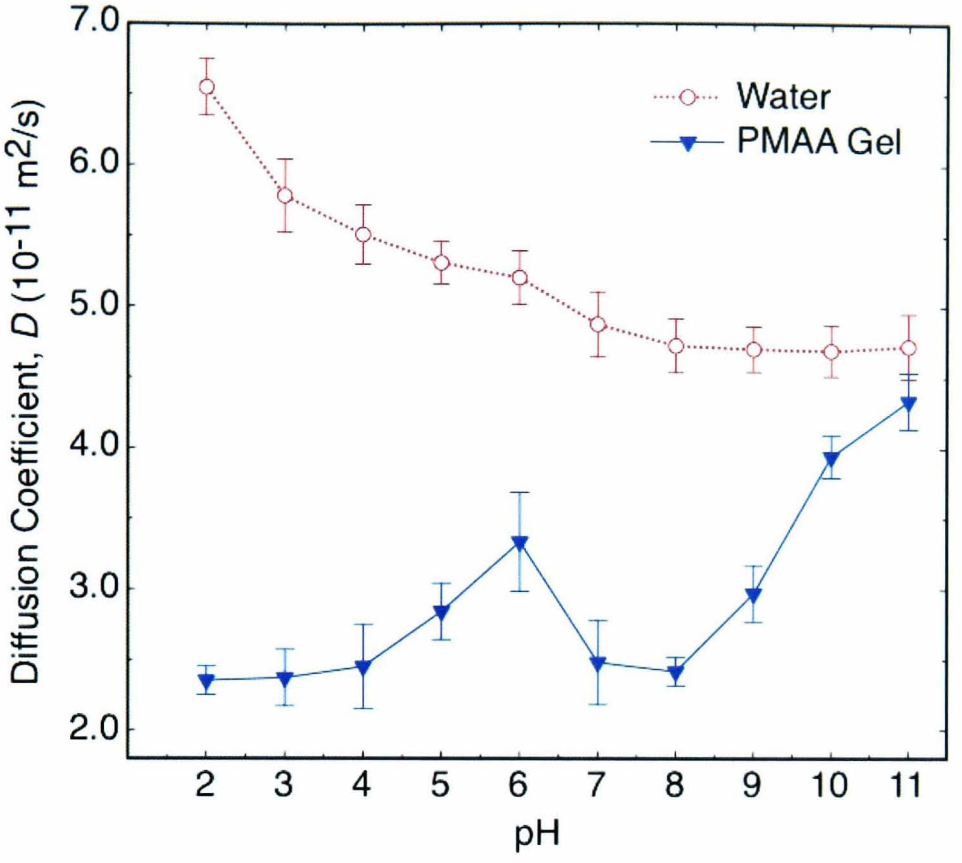

Figure 5.12: Diffusion coefficient of FITC-dextran in pure water and PMAA hydrogel as a function of pH. The diffusion coefficient of FITC-dextran in water decreases with increasing pH, while it increases with pH in PMAA hydrogel which follows the swelling ratio shown in Figure 5.10. Within errors, at the highest pH value, the diffusion coefficient in PMAA hydrogel reaches that in water, meaning that the effect of the gel network is negligible here. The error bars are the statistical errors calculated from three measurements and the lines are guides for the eye.

comparable to that in gel-free solution, which indicates that the hydrogel can be swollen upto a point where the concentration of the polymer network becomes negligible.

5.3.4 Salt Effect

The same approaches used in the previous sections (temperature and pH) can be used to analyze the effect of introducing salt ions on the structural behaviour of PMAA hydrogel and subsequently on the traversing molecules

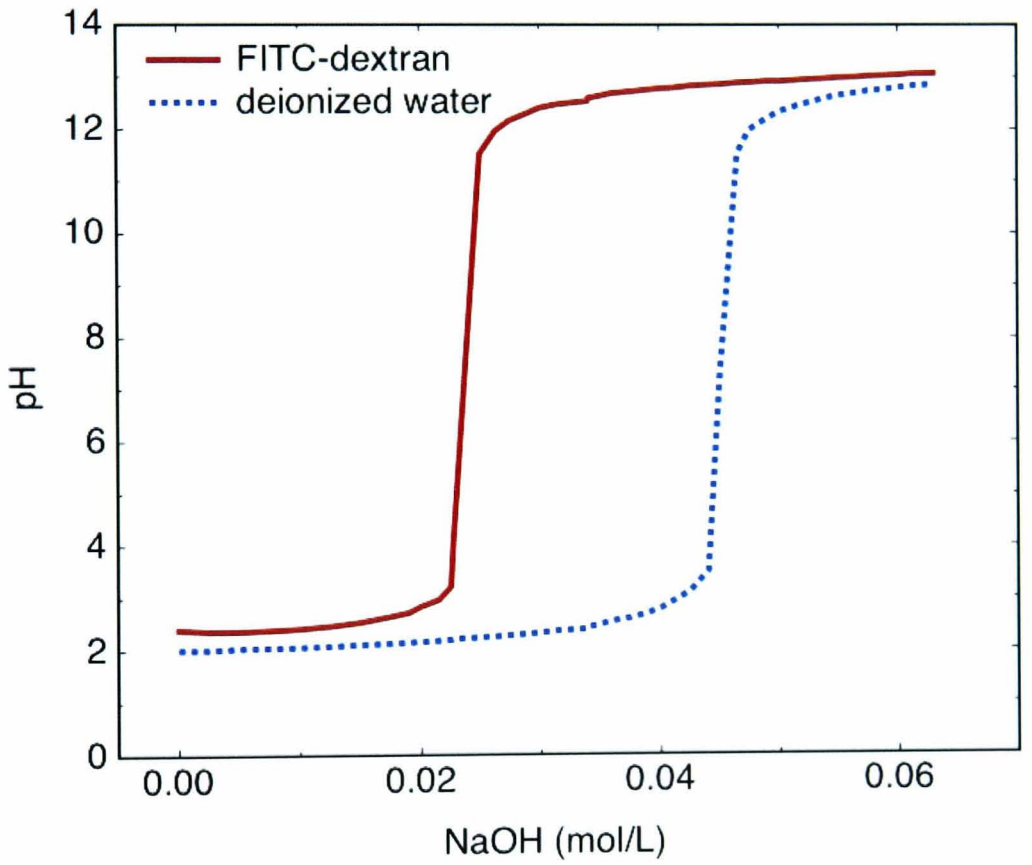

Figure 5.13: Titration curves for a solution of FITC-dextran at 0.011 M and deionized water. The shift between these two curves indicates that FITC-dextran is a polyelectrolyte.

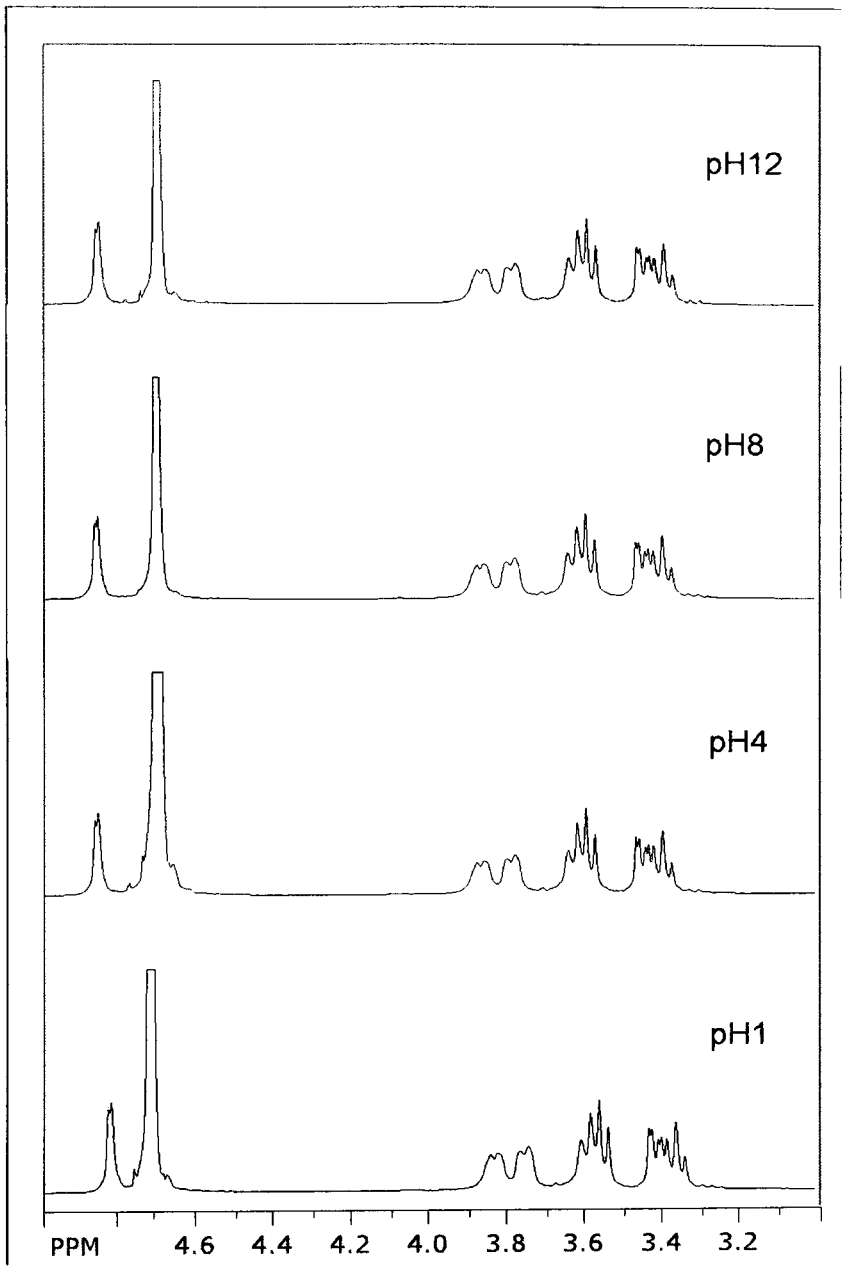

Figure 5.14: ^{1}H NMR spectra showing FITC-dextran at 0.1 M in D_2O as a function of pH. The spectra shows the identical chemical shifts at different pH which means that there is no structural change in the polymer chain with pH. This indicates that the charges on FITC-dextran are originating from the FITC (see text).

within it. There are similarities between the effect shown by pH and that by salt upon PMAA hydrogel in that the swelling ratio changes significantly with increasing ionic strength. PMAA hydrogel behaves differently in NaCl and $CaCl_2$ solutions. The swelling ratio varies non-monotonically with increasing the concentration of NaCl, first increasing and then decreasing; whereas Q decreases exponentially with increasing the concentration of $CaCl_2$ (Figure 5.15). Given that, according to the Hofmeister series [209, 210], the effect of Na^+ is larger than that of Ca^{2+}, the salting-in effect can take place at low NaCl concentrations then the hydrogel is salted-out with increasing NaCl concentration. By contrast, Ca^{2+} ions cause a charge condensation which makes the chains less charged. Nonetheless, at high salt concentration (> 0.1 mol/L), Q is almost independent of the salt concentration in both cases (NaCl and $CaCl_2$), but it is dependent on the nature and valency of the cations (Na^+or Ca^{2+}) present in the solution.

The dependent structural behaviour of PMAA hydrogel upon the ionic strength can also be investigated by tracing single molecules diffusing through the gel medium. Equation 2.32 and Figure 5.15 suggest that the diffusion coefficient of a molecule traversing through ionic hydrogels drops drastically with increasing ionic strength until it becomes independent of ionic stength at high salt concentrations. This behaviour was seen in the case of FITC-dextran diffusing through PMAA hydrogel (Figure 5.16). The reason behind this is the increase in the net viscosity of the gel, considering the viscosity term in the Zimm model (equation 2.51). Surprisingly, the increase of ionic strength has an effect not only on the diffusion of FITC-dextran in the hydrogel, but also in gel-free solutions, where the diffusion coefficient of FITC-dextran follows a similar trend. This can also be attributed to the change in the viscosity of the medium plus the change in the conformation (hydrodynamic radius) of FITC-dextran, due to its charge (section 5.3.3), via a change in the exponent ν in equation 2.51 depending on the quality of the solvent. This is in agreement with previous studies [211, 212] that demonstrated the dependence of viscosity on the ionic concentration in polyelectrolyte systems which was given by:

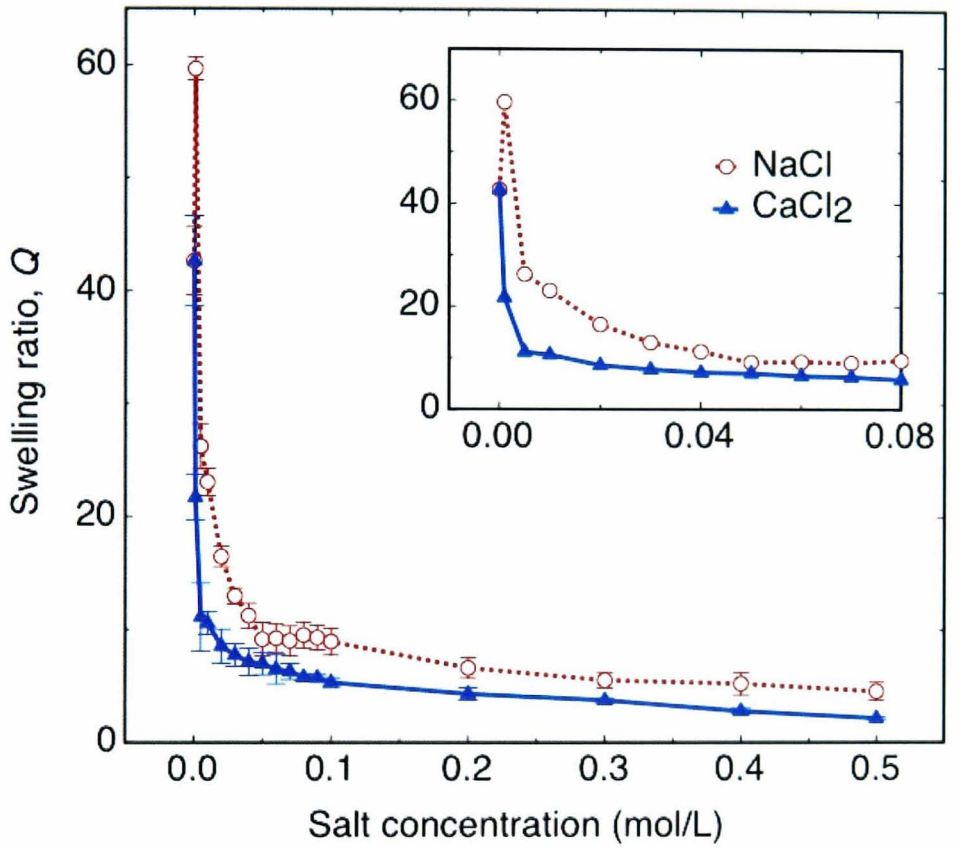

Figure 5.15: Swelling ratio of PMAA hydrogel in two different salt solutions (NaCl and $CaCl_2$) at different concentrations. Although the maximum swelling ratio is not as high as that in the case of pH (Figure 5.10), it can be seen that at low salt concentrations the ratio increases by a factor of 60. The plot in the inset is a magnification of the low concentration regime. The error bars are the statistical errors calculated from five measurements and the lines are guides for the eye.

Electrolytes	Debye length
NaCl (1:1 electrolytes)	$\kappa_D = \frac{0.304}{\sqrt{[NaCl]}}$ nm
$CaCl_2$ (2:1 or 1:2 electrolytes)	$\kappa_D = \frac{0.176}{\sqrt{[CaCl_2]}}$ nm

Table 5.2: The Debye screening length for some common electrolytes at room temperature in aqueous solution. For example, the Debye length for NaCl solution $\kappa_D = 30.4$ nm at 10^{-4} M, 4.6 nm at 10^{-3} M, 0.96 nm at 0.1 M. and 0.3 nm at 1 M, which is comparable to 960 nm in pure water [213] .

$$\eta(c) = \eta_0 + \frac{\kappa_D \zeta_0}{480\pi}, \tag{5.9}$$

where η_0 is the viscosity of pure solvent, ζ_0 is the friction coefficient of an ion in the soultion of an infinite concentration, and κ_D is Debye screening length, which can be defined as the critical distance over which the charge effect is screened (i.e. in 3D, the Debye length is the radius of a sphere of influence beyond which the charge effect is reduced). This lengthscale is given by [213]

$$\kappa_D = \left(\sum_{i=1}^{n} c_i z_i^2 \frac{e^2}{\varepsilon_r \varepsilon_0 k_B T} \right)^{-1/2}, \tag{5.10}$$

where ε_0 is the permittivity of free space, ε_r is the dielectric constant of the medium, e is the elementary charge. The two parameters related to the ionic strength I are c_i, the molar concentration of the ions, and z_i, the charge number. I can be written as

$$I = \frac{1}{2} \sum_{i=1}^{n} c_i z_i^2. \tag{5.11}$$

Table 5.2 lists the Debye length for NaCl and $CaCl_2$ based on equation 5.10.

By substituting the viscosity model above (equation 5.9) into the Zimm diffusion equation, the diffusion coefficient would be affected by the ion concentration in the solution via a change in viscosity. However. there are two limitations that would affect the diffusion of FITC-dextran when substituted into the Zimm equation; these are the high ionic concentration ($c_i \to \infty$) and low ionic concentration ($c_i \to 0$). At high ionic concentration, the Debye

length is negligible and the viscosity of the solvent will remain unchanged. Therefore, the diffusion coefficient would be expected to reach a plateau at high salt concentrations as the viscosity will become independent of ion concentration. In contrast, low salt concentrations will increase the Debye screening length which would increase the viscosity of the medium. This is because the sphere of influence of ions increases with decreasing ion concentration.

Diffusion measurements using FCS, shown in Figure 5.16, revealed the dependence of the diffusion coefficient of FITC-dextran on NaCl and $CaCl_2$ concentrations, both in water and PMAA hydrogel. The diffusion behaviour of FITC-dextran in NaCl and $CaCl_2$ solutions show a significant dependence on the ion concentration differing from the hypothesis of the viscosity model above, which might be due to charge driven conformational changes, in ionic environments (this must also be taken into account when studying the diffusion in the gel medium). However, at high ion concentration in both NaCl and $CaCl_2$ solutions, the diffusion coefficient reaches a plateau which is in agreement with the viscosity model above. This also suggests that the conformation of FITC-dextran molecules is independent of ionic strength at high ion concentration.

A similar behaviour was observed when investigating the diffusion of FITC-dextran in PMAA hydrogel as a function of NaCl and $CaCl_2$ concentrations but with a lower diffusion coefficient plateau at high salt concentrations (Figure 5.16). The decrease in diffusion coefficient may be attributed to change in the overall viscosity of the medium (the viscosity of the gel plus the solvent). Assuming the FITC-dextran size is independent of the type of ions (as seen in gel-free systems), the difference between the diffusion coefficient plateau in the two cases (NaCl and $CaCl_2$) suggests that PMAA hydrogel undergoes different degrees of swelling, which was observed when measuring the swelling ratio of PMAA hydrogel in salt solutions, Figure 5.15. To model the diffusion coefficient with the ion concentration, a further investigation on the effect of salt solutions on the conformation of FITC-dextran (see chapter 9). However, one can minimize the contribution from the effect of the ion concentration on FITC-dextran molecules by normalizing the diffusion

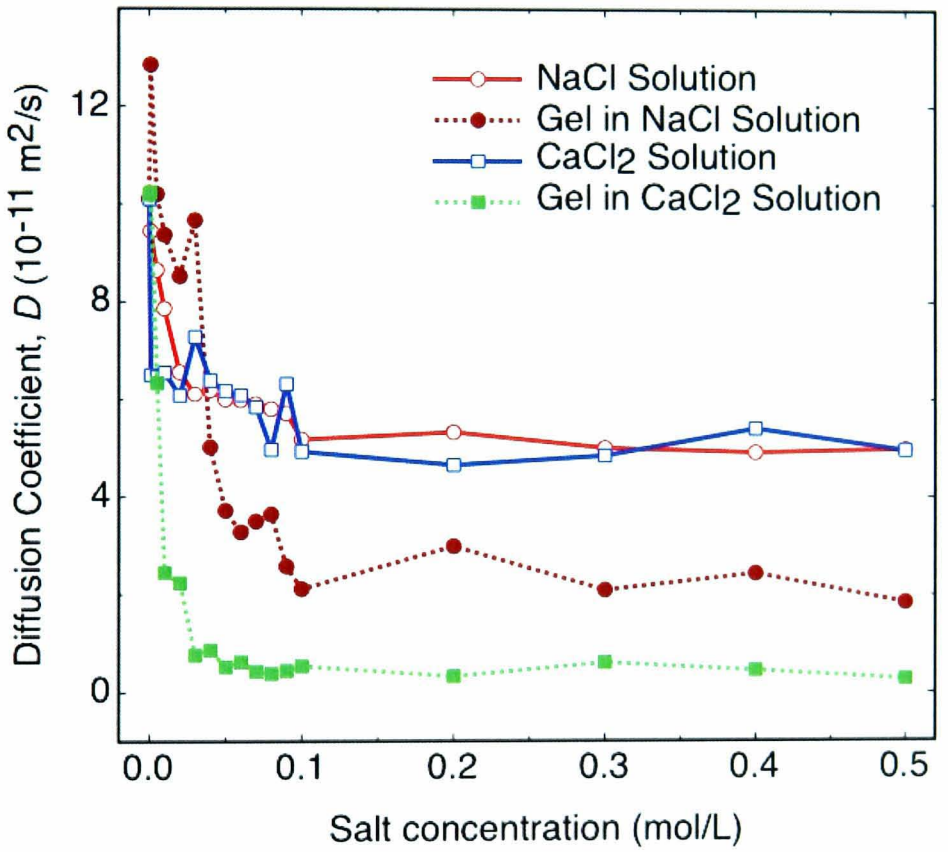

Figure 5.16: Diffusion coefficient of FITC-dextran in NaCl and $CaCl_2$ solutions compared to that in PMAA hydrogel immersed in the same solutions.

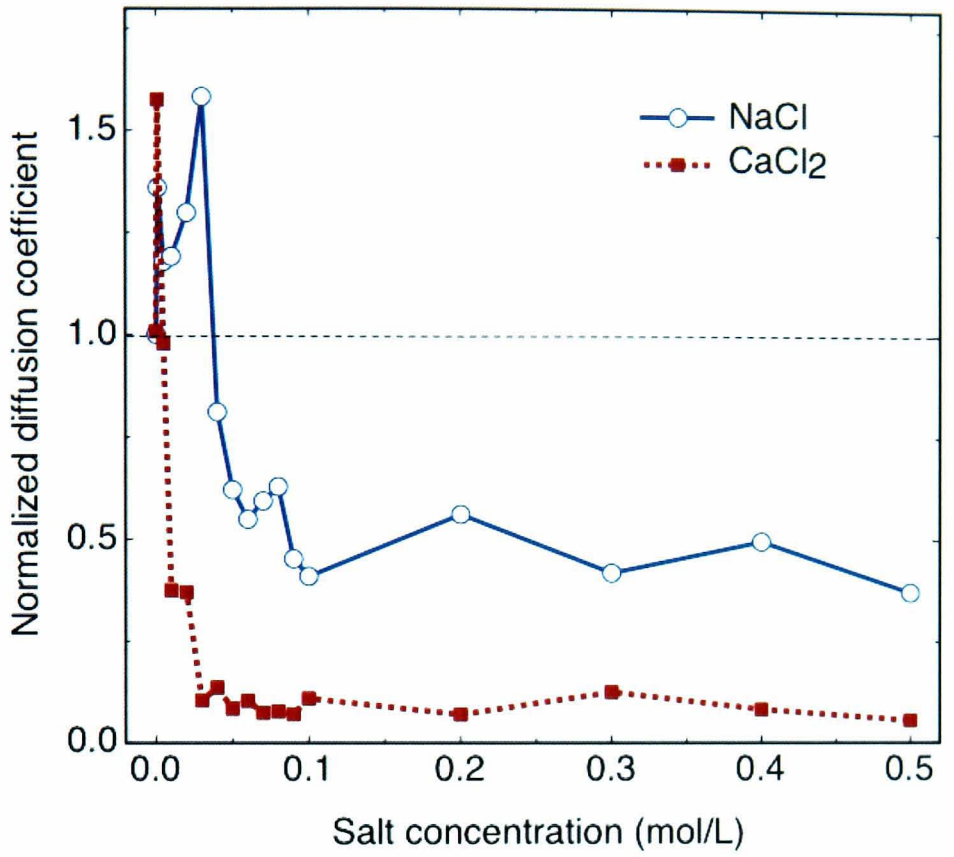

Figure 5.17: Normalized diffusion coefficient of FITC-dextran in NaCl and $CaCl_2$ obtained from the data in Figure 5.16. The horizontal dashed line corresponds to the equal value of the diffusion coefficients in water and the PMAA hydrogel.

coefficient in PMAA hydrogel to that in water, as shown in Figure 5.17. An interesting point that can be seen from the data in Figure 5.17 is that the normalized diffusion coefficient shows a value of unity, which corresponds to an equal diffusion coefficient in both water and gel and might indicate that the PMAA hydrogel has no effect of the conformation of FITC-dextran. It is also noticeable from this figure that at high diffusion coefficient values (> 1), the FITC-dextran diffuses faster than in gel-free salt solutions. This can be explained because PMAA hydrogel undergoes a swelling transition at low salt concentrations which is in agreement with the previously observed behaviour of PMAA hydrogel in salt solutions (Figure 5.15).

5.4 Conclusions

The purpose of this study was to use FCS to investigate the diffusion of a single molecule of FITC-dextran in water and PMAA hydrogels. This method was able to reveal the structural dependence of diffusion of FITC-dextran on temperature, pH and ionic strength. The success of this study was not limited to the fit of the data to well-known theoretical models (e.g. Zimm model) but rather it requires macroscopic measurements such as the swelling behaviour of the hydrogel.

This study has shown that the diffusion of FITC-dextran in water followed the Zimm model, as expected, showing an increase in the diffusion coefficient with increasing temperature. Whereas the diffusion in PMAA hydrogel was found to decrease with temperature, which was modelled by using Huggins relation for viscosity. These results suggested that the swelling and collapse transition of PMAA hydrogel can be explained in terms of the change of viscosity by increasing or decreasing the distance between cross-links, with the limitation that there is no effect from the gel matrix on the diffusing molecule. The obtained mesh size from diffusion measurements has been found to decrease exponentially with temperature for which a model has been developed by using Williams, Landel, and Ferry (WLF) equation for viscosity.

The diffusion coefficient of FITC-dextran in water was, surprisingly, found to decrease with increasing solution pH, which indicated a charge effect on the molecule itself. Titration measurements revealed that FITC-dextran was a charged molecule but NMR spectra showed that the charges originate from the FITC. The diffusion coefficient of FITC-dextran increased with increasing pH in the case of PMAA hydrogel. However, there was a discontinuity between pH6 and pH8 which was attributed to the shielding effect of charges. The same trends have been observed for the swelling behaviour of PMAA hydrogel.

The final investigation of this chapter was to determine the effect of salt solutions on the behaviour of PMAA hydrogel and single molecules diffusing within it. In both NaCl and $CaCl_2$ solutions, the diffusion coefficient was

found to decrease and then reach a constant value at high ion concentrations, which was in agreement with a previously proposed viscosity model. Similarly, the diffusion of FITC-dextran in PMAA immersed in salt solutions followed the same trends except that the gel behaves differently in response to different ions, depending on their valency. Normalization of the diffusion coefficient in the gel and water has shown an unexpected increase of the diffusion coefficient in PMAA hydrogel at low salt concentrations, which was explained by the gel having undergone swelling transition at these concentrations, allowing the probe to diffuse faster than in salt solutions. These findings coupled with the swelling behaviour of PMAA hydrogel in salt solutions remain an open question.

Chapter 6

Controlled Diffusion in Magnetic Fields

6.1 Introduction

In recent years there has been increasing interest in stimuli-responsive polymeric materials. Polymeric gels, for example, can be made into devices responsive to temperature [69, 214], pH [68, 71], and electric [215, 216] and magnetic fields [217, 7] depending on the polymer and any other components added to the system. A way to make gels responsive to magnetic fields is by introducing magnetic nanoparticles ($\sim$ 10 nm) either before or after cross-linking to form so-called "ferrogels". These magnetic nanoparticles are bound to the polymer network and are fixed in place, with no translational diffusion within the gel medium [218, 81].

The magnetic properties of ferrogels are similar to those of ferrofluids [217, 219]. Each magnetic nanoparticle can be considered as a monodomain with its own magnetic moment. In a magnetic field, these moments align in the direction of the applied magnetic field, so the magnetic force f_{m} on a ferrogel can be given as [80]:

$$f_{\mathrm{m}} = \mu_0 \int_V (M \cdot \nabla) H \mathrm{d}V, \tag{6.1}$$

where μ_0 is the magnetic permeability of vacuum, M is the magnetization, H is the magnetic field strength, and V is the ferrogel volume. The saturation magnetization M_s and magnetic susceptibility χ_m depend strongly on the nanoparticle size (radius r_0), and their volume fraction in the gel ϕ, and can be written as follows [17, 16]:

$$M_s = \phi M_\mathrm{f}\left(1 - \frac{3k_\mathrm{B}T}{4\mu_0\pi M_\mathrm{f} r_0^3 H}\right), \tag{6.2}$$

$$\chi_m = \phi M_\mathrm{f}^2 \frac{4\pi r_0^3 \mu_0}{9k_\mathrm{B}T}, \tag{6.3}$$

where M_f is the magnetization of the pure ferromagnetic material, k_B is the Boltzmann constant, and T is the absolute temperature.

Since Zrínyi and co-workers [17] introduced the concept of ferrogels in 1995, useful applications in biotechnology, membrane technology, artificial muscles and drug delivery and release have been suggested [18, 19]. A number of achievements have been reported particularly in terms of magnetically controlled drug release. For instance, direct current magnetic fields have been used to restrict the amount of drug released from ferrogels [220]. In addition, controlled drug release rate through an on-off magnetic field switch has also been demonstrated [91], with recent results demonstrating both *in vitro* and *in vivo* release of cells [86].

Nevertheless, the physical properties of molecular transport within ferrogels (i.e. Brownian motion or intradiffusion) and from these systems to the surrounding environment (interdiffusion) in an applied magnetic field remain poorly understood. The work in this chapter considers single molecular diffusion measurements within ferrogels in an applied magnetic field. Herein, the diffusion process of dextran molecules labeled with fluorescein isothiocyanate (FITC) within ferrogels based on poly(methacrylic acid) hydrogels (PMAA) under applied magnetic fields will be discussed. The synthetic method used in this study results in ferrogels with no cluster formation, even under the applied magnetic field, as confirmed by small-angle X-ray scattering (SAXS) and superconducting quantum interface device (SQUID) magnetometry measurements. However, these ferrogels are observed to undergo structural defor-

mation when exposed to magnetic fields, and it is this that can be controlled for molecular release applications. The work described in this chapter has been published [221].

6.2 Experimental

6.2.1 Ferrogel Synthesis

Three different ferrofluid solutions were prepared by dissolving 0.012 g, 0.053 g and 0.13 g of magnetite (Fe_3O_4) nanoparticles (of density 5.1 g/cc and purchased from Sigma-Aldrich) in 10 ml of distilled water. To prevent magnetic nanoparticle aggregation, 0.01 g of the surfactant dodecyl sulfate sodium (SDS) salt was added to the mixtures. The resulting mixtures were also sonicated for 5 minutes. This process was observed, using an optical microscope, to keep the aggregation of the magnetite to a minimum.

The ferrofluids were added dropwise to three mixtures of 2 ml of methacrylic acid (MAA), 0.002 g of 2,2'-azobis (2-methylpropionamidine) dihydrochloride (AMPA) and 0.008 g of methyl-bisacrylamide (MBA) (all materials were used as received from Sigma-Aldrich) in a sealed container and exposed to a nitrogen flow for 30 min. The polymerization of MAA took place by placing the solution (in its sealed container) in an oven at 65°C for 8 h. Samples studied immediately after this preparation are denoted as "unswollen" in the text. We also studied these ferrogels (with 0.1 wt%, 0.5 wt% and 1 wt% of Fe_3O_4 nanoparticles) after immersion in distilled water to ensure complete swelling. When equilibrium was reached (constant mass), small pieces of ferrogel were taken for examination. These ferrogels are denoted as "swollen" in what follows. For measurements of the swelling of ferrogels under an applied magnetic field, the ferrogel pieces were first dried under vacuum at 40°C for 5 h before being immersed in water and allowed to reach an equilibrium swelling under different applied magnetic fields for 24 h.

For diffusion experiments, fluorescein end-labeled dextran (FITC-dextran) with molecular mass of 70 kDa (Sigma-Aldrich) was introduced into the ferrogels in a nanomolar concentration to ensure single molecule detection in

the confocal volume in the FCS experiments.

6.2.2 FCS Measurements in a Magnetic Field

FCS principles and setup were described in Chapter 4, while the procedure of FCS experiemnts is similar to that described in Chapter 5, section 5.2.2. FCS measurements were carried out using a ConfoCor2 FCS module fitted to an LSM510 inverted confocal microscope (Zeiss) (pectured in Figure 5.3). The FITC was excited using a 488 nm Ar laser. A Linkam heating stage (Linkam Scientific Instruments Ltd, Surrey, UK) with TMS94 heat controller and LNP-1 nitrogen flow control was used to control the temperature. Magnetic fields were introduced using a homemade electromagnetic solenoid mounted on the FCS to produce a magnetic field strength of between 0.1 and 1 T. The obtained autocorrelation curves were fitted to the Widengren FCS autocorrelation function for diffusion in three dimensions (equation 4.19).

From fitting to equation 4.19, shown in Figures 6.1 and 6.2, one can determine the diffusion time τ_D. This diffusion time can then be converted to a diffusion coefficient using equation 4.15 as described in Chapter 4, section 4.2.4 and Chapter 5, section 5.2.2.

6.2.3 Magnetisation Measurements

The magnetization measurements were carried out in a Quantum Design RF SQUID magnetometer (model MPMS- 5), which enabled magnetic fields up to 5 T and temperatures from 2 to 400 K to be attained. All of the hysteresis loops in this study were acquired at room temperature. Any linear, diamagnetic contribution was subtracted off from the hysteresis loop, and each hysteresis loop was normalized to the corresponding sample weight. Zero field cooled/field cooled (ZFC/FC) measurements were made by cooling the sample to 5 K in zero magnetic field, and then a small magnetic field of 8.0 kA m (100 Oe) was applied, and the magnetization measured as a function of temperature whilst heating the sample to 300 K. While maintaining the field constant, the magnetization was again measured during cooling back down

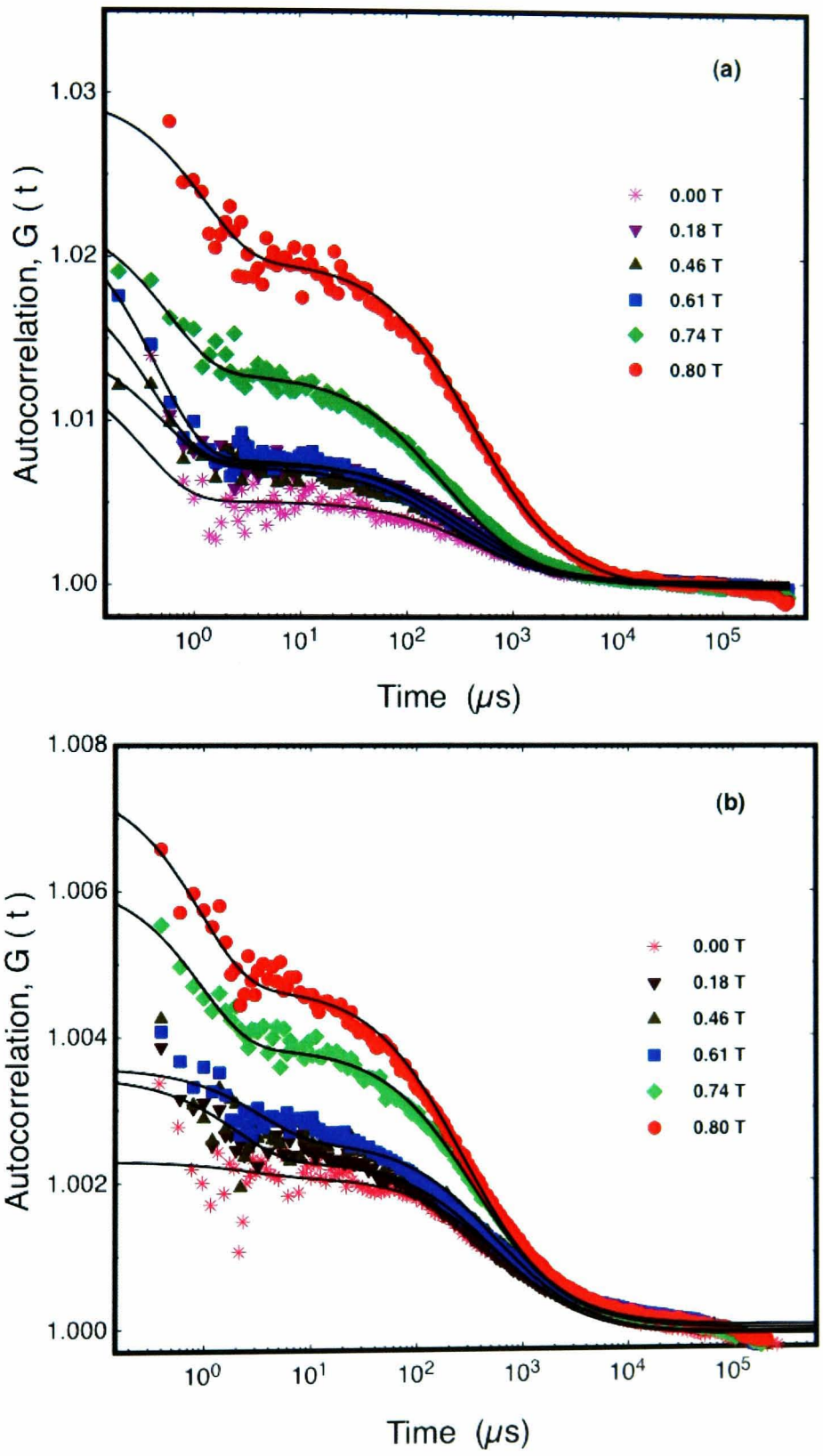

Figure 6.1: Experimental FCS autocorrelation curves for 5 nM FITC-dextran probe in ferrogels with (a) 1 wt%, (b) 0.5 wt% and (c) 0.1 wt% magnettite nanoparticles; and in a hydrogel (d). The solid lines are the corresponding fits to equation 4.19. Plots (c) and (d) are continued over the page.

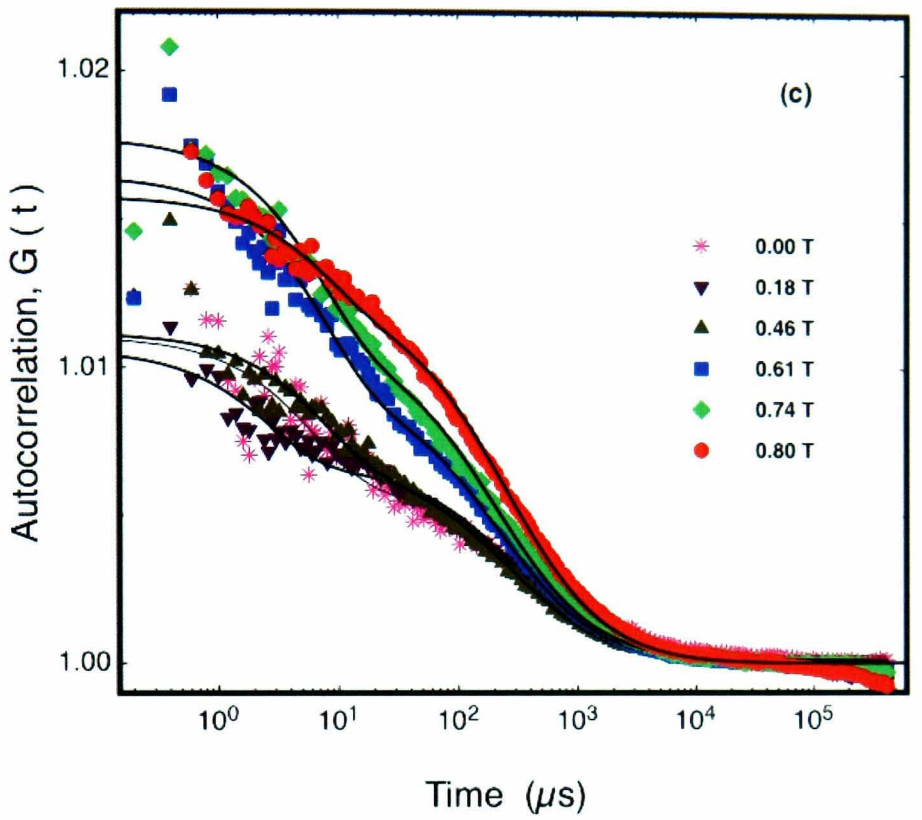

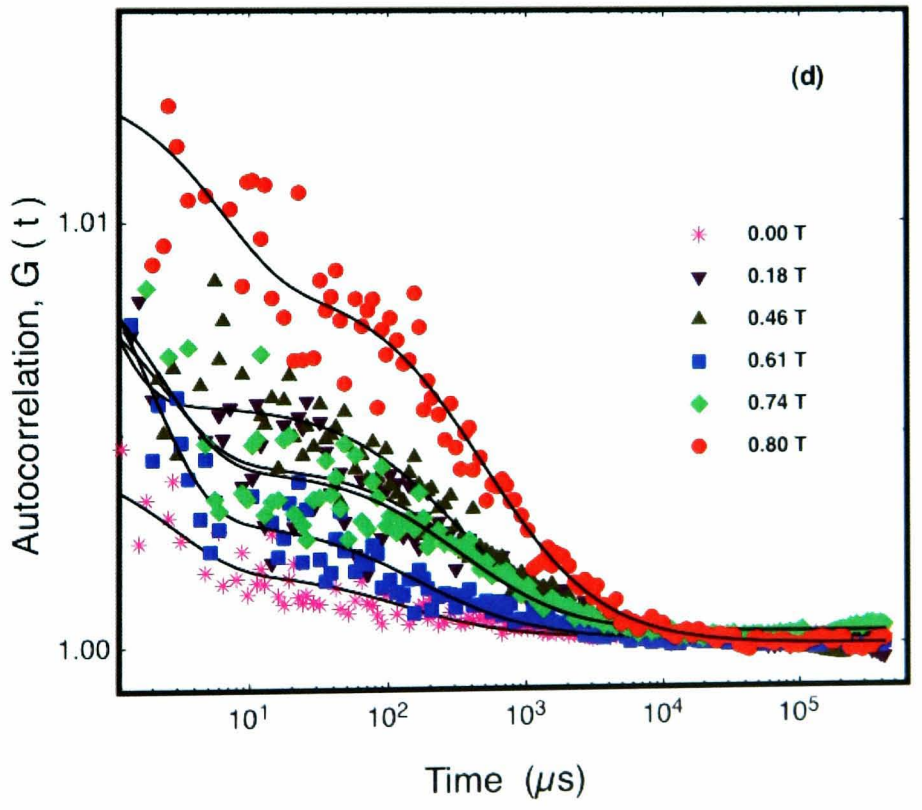

Figure 6.2: Continued Figure 6.1.

to 5 K. These ZFC/FC measurements permit a determination of particle size, as well as other properties not pertinent to the present study.

The resulting data are presented as the magnetisation versus magnetic field with the magnetisation being the contributions from the ferromagnetic and paramagnetic components in the sample. Typical raw SQUID data are shown in Figure 6.3(a) for an unswollen ferrogel with 1 wt% Fe_3O_4. Here, we are interested in characterizing the ferromagnetic materials (Fe_3O_4 nanoparticles); therefore, the contribution from the paramagnetic materials is subtracted from the data Figure 6.3(b) by calculating the slope of the line and subtracting this from each point to leave the ferromagnetic contribution.

6.2.4 SAXS measurements

Swollen and unswollen ferrogel (with 0.5 and 1 wt% of magnettite nanoparticles) and hydrogel were loaded on a sample holder with holes of 2.5 mm in diameter and 2 mm in thickness. The samples were held between two sides of a capton tape. Pure Fe_3O_4 nanopowder was compressed in a washer with 2.5 mm in diameter and 0.42 mm in thickness.

Small-angle X-ray scattering measurements for this study were carried out at room temperature using a Bruker AXS Nanostar (Figure 4.9) instrument (CuKα radiation) at zero magnatic field. The scattered intensities were recorded on a two-dimensional multiwire gas proportional detector (Hi-Star, Siemens AXS). The sample-detector distance was about 1.045 m giving a wave vector with a magnitude 0.01 $\text{Å}^{-1} < q < 0.10\ \text{Å}^{-1}$, where $q = (4\pi/\lambda)\sin\theta$, with 2θ being the scattering angle, and λ the radiation wavelength. The obtained two-dimensional scattering patterns, shown in Figure 6.4, were then normalized (the instrument is equipped with a semi-transparent beamstop) and integrated using Bruker AXS software.

Nanostar was also used to perform wide-angle X-ray scattering (WAXS) for pure Fe_3O_4 with increasing the scattering angle up to 20 degrees in order to investigate the crystalline structure of these nanoparticles.

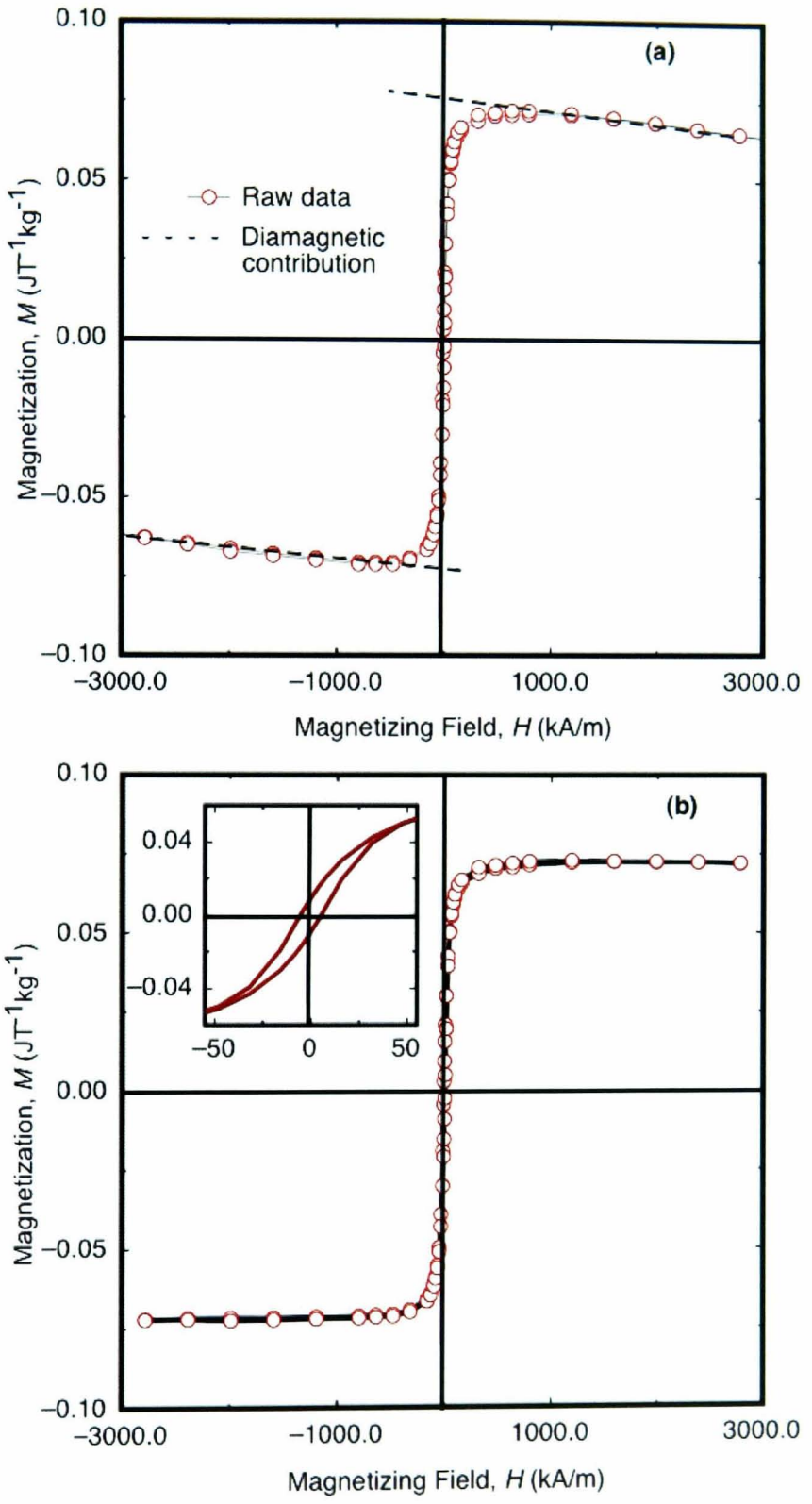

Figure 6.3: Room temperature untreated raw SQUID data for ferrogel 1 wt% unswollen sample (a), and with subtracting the diamagnetic contribution (b). The inset in Figure (b) shows the opening around the origin (i.e. the coercivity).

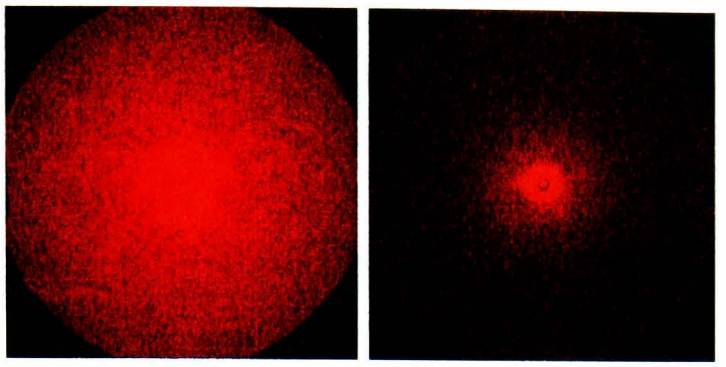

Unswollen (left) and swollen (right) 1 wt% ferrogel

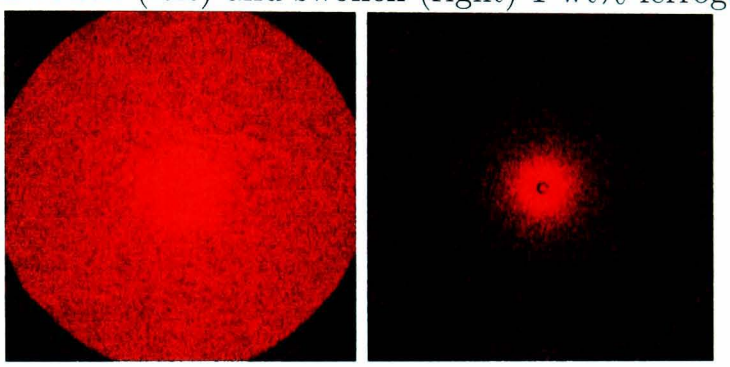

Unswollen (left) and swollen (right) 0.5 wt% ferrogel

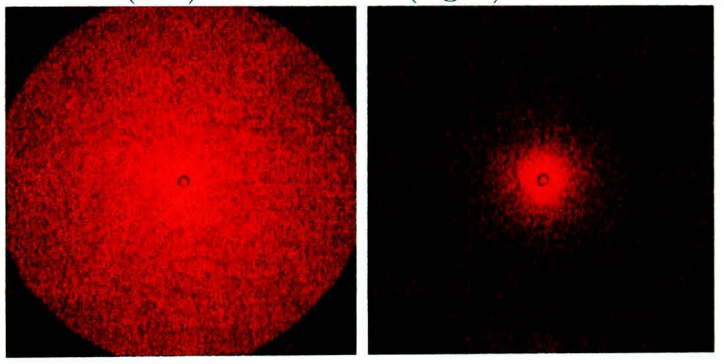

Unswollen (left) and swollen (right) hydrogel

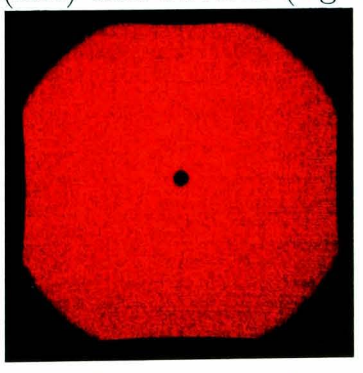

Fe_3O_4 nanopowder

Figure 6.4: SAXS 2D patterns for swollen and unswollen ferrogels and hydrogels and for pure Fe_3O_4 nanopowder.

6.3 Results and Discussion

6.3.1 Nanoparticle Size Distribution

Small-angle X-ray scattering (SAXS) by two-phase systems with sharp boundaries was studied by Porod in 1951 [222, 223]. This study predicted that, at large values of q, the scattering intensity decreases proportionally to the reciprocal fourth power of q:

$$\lim_{q\to\infty}[I_{\mathrm{P}}(q)] = \frac{K_{\mathrm{P}}}{q^4}, \tag{6.4}$$

where K_{P} is Porod's constant. This means that the scattering intensity reaches a constant value, K_{P}, when $Iq^4 \to \infty$ (the Porod regime). Porod's constant is of importance in that it can be used to determine other parameters such as the specific surface area, Σ/V, of nanoparticles, which can be given by Porod's equation,

$$\frac{\Sigma}{V} = \frac{\pi\phi_s(1-\phi_s)K_{\mathrm{P}}}{\int_0^\infty I(q)q^2\mathrm{dq}}, \tag{6.5}$$

where Σ is the total area of interface in a scattering volume V, ϕ_s is the volume fraction of the component from which scattering occurs, and V is the volume of a single nanoparticle assuming it is spherical. From equation 6.5, and with the assumption that the nanoparticles are spherical, one can calculate the sphere radius, r, from $\Sigma/V = 3\phi_s/r$.

SAXS plots from the ferrogels (Figure 6.5) demonstrate an increase in scattering intensity with increasing magnetic nanoparticle concentration. In addition, and for comparison, the scattering intensity by pure Fe_3O_4 nanopowder is shown in Figure 6.6. The data in this figure (with slope of -4) indicate the Porod behaviour of the scattering by this magnetite nanopowder. However, the tail of this plot is not continuing as Porod behaviour but rather there is an increase in the scattering intensity at high q values suggesting that there might be a crystalline structure within these nanoparticles. Therefore, WAXS was used to investigate the possibility of crystallinity in these systems, and the data from this method are shown in Figure 6.7. It is apparent

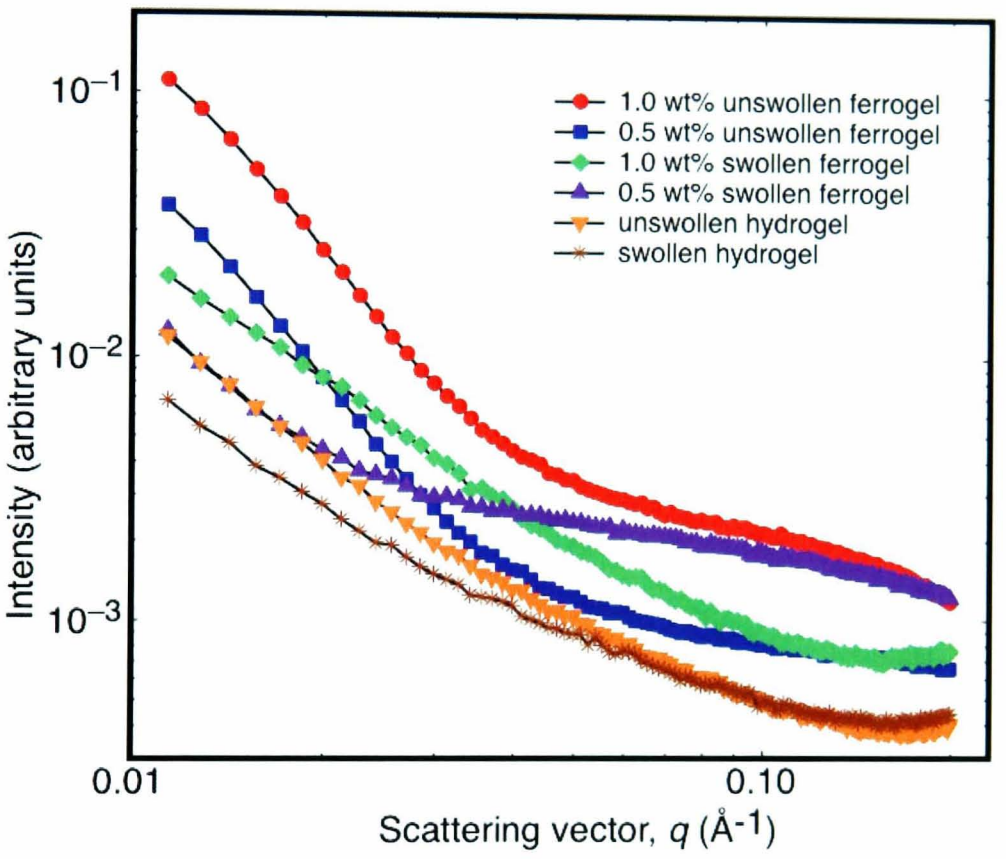

Figure 6.5: SAXS plot showing scattering intensity as a function of the scattering vector for hydrogel and ferrogels with different magnetic nanoparticle concentrations. This plot shows the increase in the intensity at higher nanoparticle concentration and the collapsed state of the ferrogels.

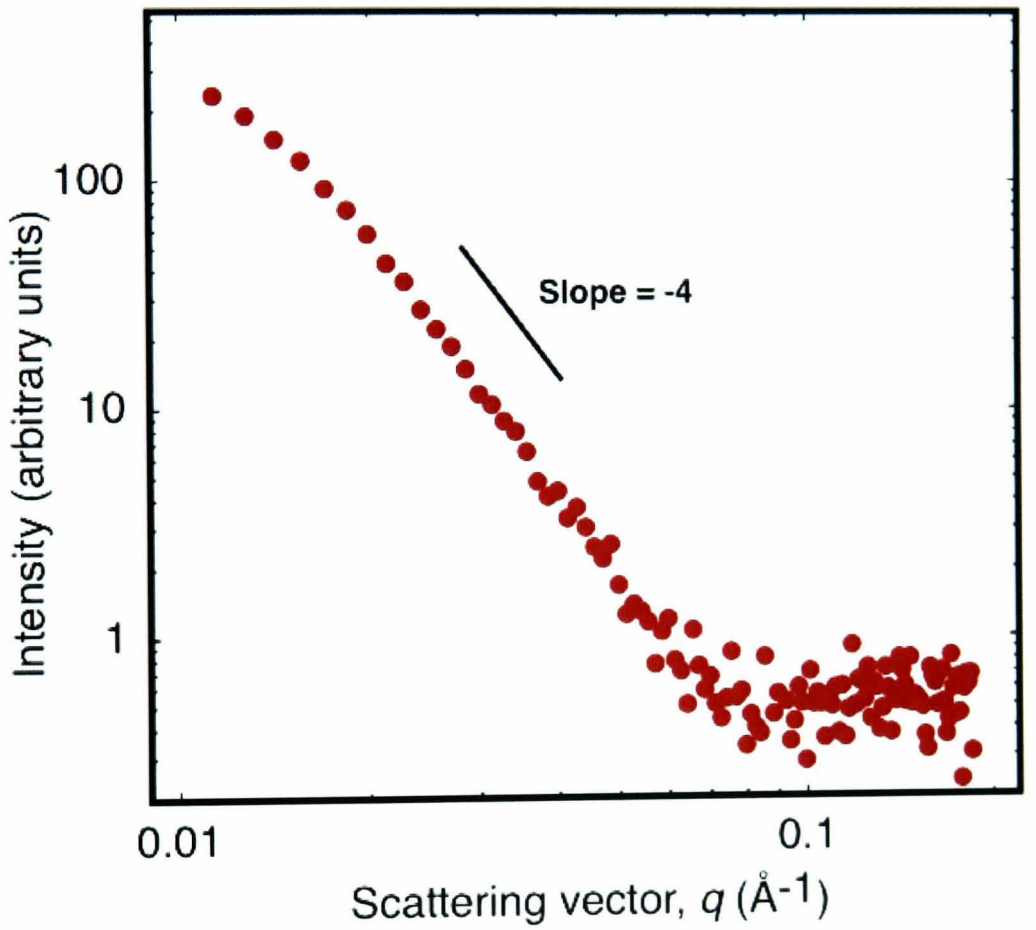

Figure 6.6: SAXS plot showing scattering intensity as a function of the scattering vector for pure Fe_3O_4 nanopowder. This plot shows the Porod's behaviour of scattering (slope = -4).

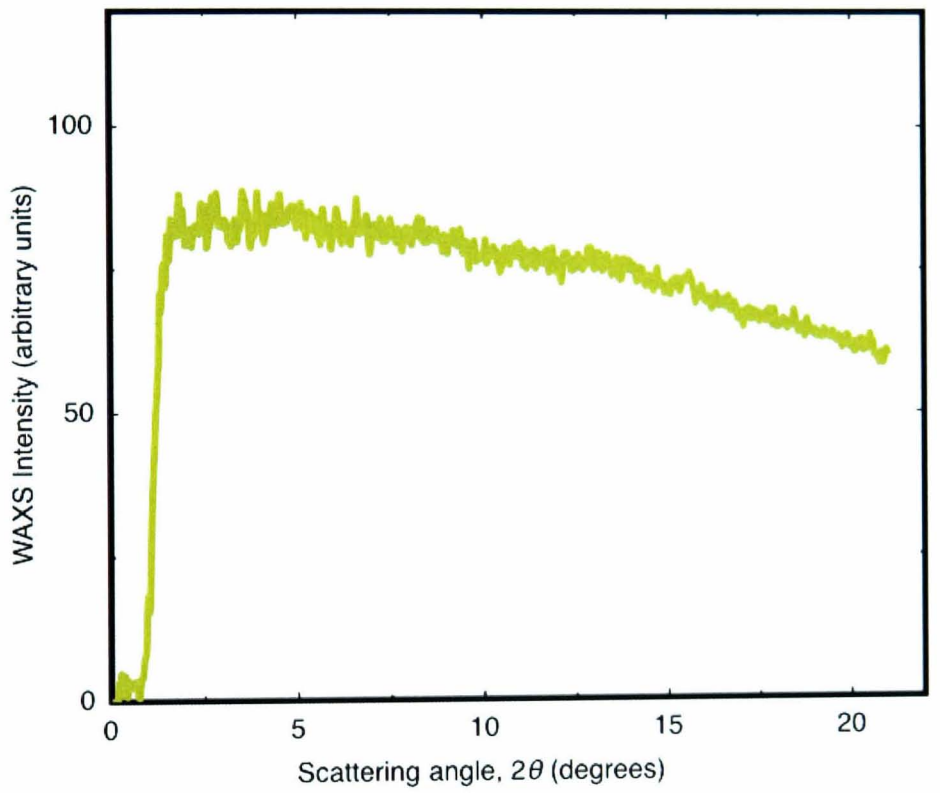

Figure 6.7: WAXS plot of pure Fe_3O_4 nanopowder showing no scattering peaks (flat intensity as a function of the scattering angle) meaning that there is no crystalline structure within these nanoparticles.

that the intensity is constant with increasing scattering angle (no scattering peaks), which indicates a dominant single structure. The tail in SAXS plots can then be ignored, especially since it appears only at low scattering intensities (below 1).

The difference between the swollen and unswollen states can be distinguished at different nanoparticle concentrations from Porod plots of the SAXS data (Figure 6.8). These plots correspond to the scattering intensity originating from the magnetite nanoparticles, and are obtained by subtraction of the scattering signal of a hydrogel sample containing no magnetite from the ferrogel SAXS patterns. The intensity for all of the ferrogels studied has the q^{-4} dependence indicative of Porod behavior at large q values, which indicates that the dominant scattering mechanism is that from smooth spherical particles [173, 160].

Porod's constant, K_{P} , can be determined from the data in Figure 6.8, which is the value of Iq^4 at the shoulder of each plot. By using Equation 6.5, one can obtain the specific surface area from which the size of the nanoparticle can be calculated. It can be seen from these results that $r \approx r_0$, and the calculated values for the studied systems are listed in Table 6.1. The absence of fringes in these data indicates that the nanoparticles do not have a monodisperse distribution of sizes.

The values in Table 6.1 indicate that the size of these nanoparticles is in reasonable agreement with their original size in feed ($\leq$ 30 nm in diameter from the manufacturer). In addition, the size of these particles is shown to be independent of whether or not the ferrogel was measured in the swollen or unswollen states.

6.3.2 Magnetic Properties

The magnetic hysteresis loops in Figure 6.9 show the concentration dependence of the saturation magnetization for unswollen (a) and swollen (b) ferrogels at room temperature. It is noticeable that by increasing the nanoparticle concentration the saturation magnetization increases because the density of magnetic moments increases. From these hysteresis loops, it is clear that

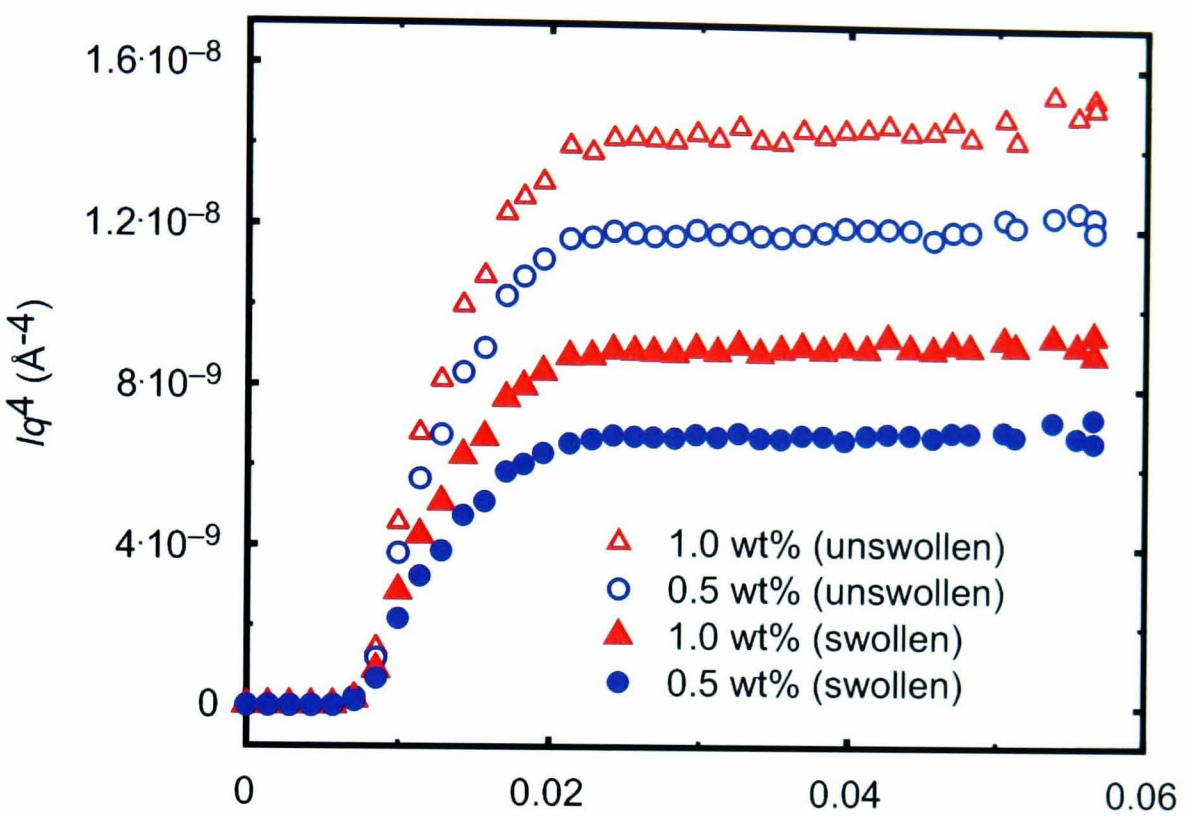

Figure 6.8: Background-subtracted scattering SAXS Porod plots for swollen and unswollen ferrogels containing 0.5 and 1 wt% magnetite nanoparticles.

Nanoparticles (wt.%)	Ferrogel	SAXS (r) (nm)	ZFC/FC (r) (nm)
0.1	Unswollen	.....	12.4 ± 1.1
0.1	Swollen	.....	12.0 ± 1.2
0.5	Unswollen	12.0 ± 1.1	12.4 ± 1.0
0.5	Swollen	12.5 ± 0.5	12.1 ± 1.2
1.0	Unswollen	14.3 ± 0.4	12.3 ± 1.1
1.0	Swollen	13.6 ± 0.7	12.0 ± 1.3
100	Pure	12.5 ± 1.0	.....

Table 6.1: Calculated nanoparticle size from SAXS measurements using Porod's theory for scattering from spherical particles and ZFC/FC SQUID magnetometry measurements under an applied magnetic field of 8.0 kA/m. The errors in SAXS measurements are the statistical errors associated with determination of Porod's constant, K_P, while the errors in ZFC/FC measurements arise from the determination of the blocking temperature, T_B .

these systems show ferromagnetic behavior at room temperature. Figure 6.9 also shows the similarity in the coercivity H_C at different nanoparticle concentrations and in different ferrogel states (4.9 kA/m for unswollen ferrogels and 5.1 kA/m for swollen ferrogels). From the relationship between coercivity and magnetic domain size [224, 225], the agreement between these values of the coercive fields indicate the similarity in the magnetic domains and therefore in the magnetic nanoparticle size.

According to the Néel theory of superparamagnetism [226], in an applied magnetic field there are two stable orientations for the magnetic moments of the nanoparticles (due to the magnetic anisotropy) which are antiparallel to each other and usually called the "easy axes". The magnetization can flip between these two orientations and the average time between these flips is called the Néel relaxation time, τ_N, and is given by an Arrhenius relation,

$$\tau_N = \tau_0 \exp\left(\frac{KV_p}{k_B T}\right), \tag{6.6}$$

where V_p is the magnetic particle volume, K ($= 1.35 \times 104$ J/m^3) is the magnetic anisotropy constant and τ_0 is a constant known as the attempt time and is usually taken as 10^{-9} s. If we were able to measure the magnetization of nanoparticles and let the measurement time be τ_m, the magnetization would flip to the other orientation only if $\tau_m \geq \tau_N$. This measuring time is usually taken to be $\tau_m = 100$ s for a typical set-up (such as ours). When $\tau_m = \tau_N$ and the applied magnetic field is much lower than the anisotropy field, then a maximum blocking temperature T_B is reached at which a transition between superparamagnetic and blocked states occurs. The peaks in the ZFC curves in Figure 6.10 denote the absolute T_B for different ferrogels from which one can obtain the magnetic particle size by the Bean-Livingstone equation [30]

$$KV_p = 25 k_B T_B, \tag{6.7}$$

where the factor $25 \approx \ln(\tau_m/\tau_0)$ is calculated from the values in the discussion above (equation 6.6). From the data in Figure 6.10, it is apparent that the peaks of the ZFC curves are displaced from the separation point between ZFC and FC curves (this is usually referred to as a bifurcation) indicating a

distribution of particle size. The calculated average nanoparticle sizes from these measurements are included in Table 6.1, and are in good agreement with those obtained from SAXS measurements, further confirming that there is no aggregation in these systems even under an applied magnetic field.

6.3.3 Swelling in a Magnetic Field

The swelling and collapse of PMAA ferrogels in pure water has been measured as a function of the magnetic nanoparticle concentration and the applied magnetic field. This was obtained by measuring the change in equilibrium swelling (swelling ratio), which can be defined as

$$Q = \frac{m_s - m_d}{m_d}, \tag{6.8}$$

where m_s and m_d are the mass of swollen and collapsed gels, respectively. Figure 6.11 demonstrates the swelling dependence on the concentration of magnetic nanoparticles and the applied magnetic field. It is noticeable that the swelling ratio remains constant with magnetic field when the magnetic nanoparticles are absent (i.e. swollen hydrogel). However, the swelling behavior of ferrogels is very dependent upon the applied magnetic field. For instance, from Figure 6.11, the swelling ratio of the ferrogel with 0.1 wt.% nanoparticles decreases by a factor of two upon an increase of magnetic field strength from 0.1 to 0.8 T. Likewise, ferrogels with the other two nanoparticle concentrations (0.5 and 1 wt.%) contract by almost the same factor in the same magnetic field. This can be understood by these single-domain magnetic nanoparticles being adhesively attached to the polymer chains and having no translational diffusion [81]. During the magnetic alignment of these nanoparticles under the applied magnetic field, the adhered nanoparticles disrupt the polymer network from further swelling. It is also reasonable to suggest that the nanoparticles might form magnetic clusters under the magnetic field, and this can affect the swelling behavior of the whole system. However, from the ZFC data above it can be shown that this latter effect is not taking place in these systems, as the particle size under the applied magnetic field is similar to that in the feed.

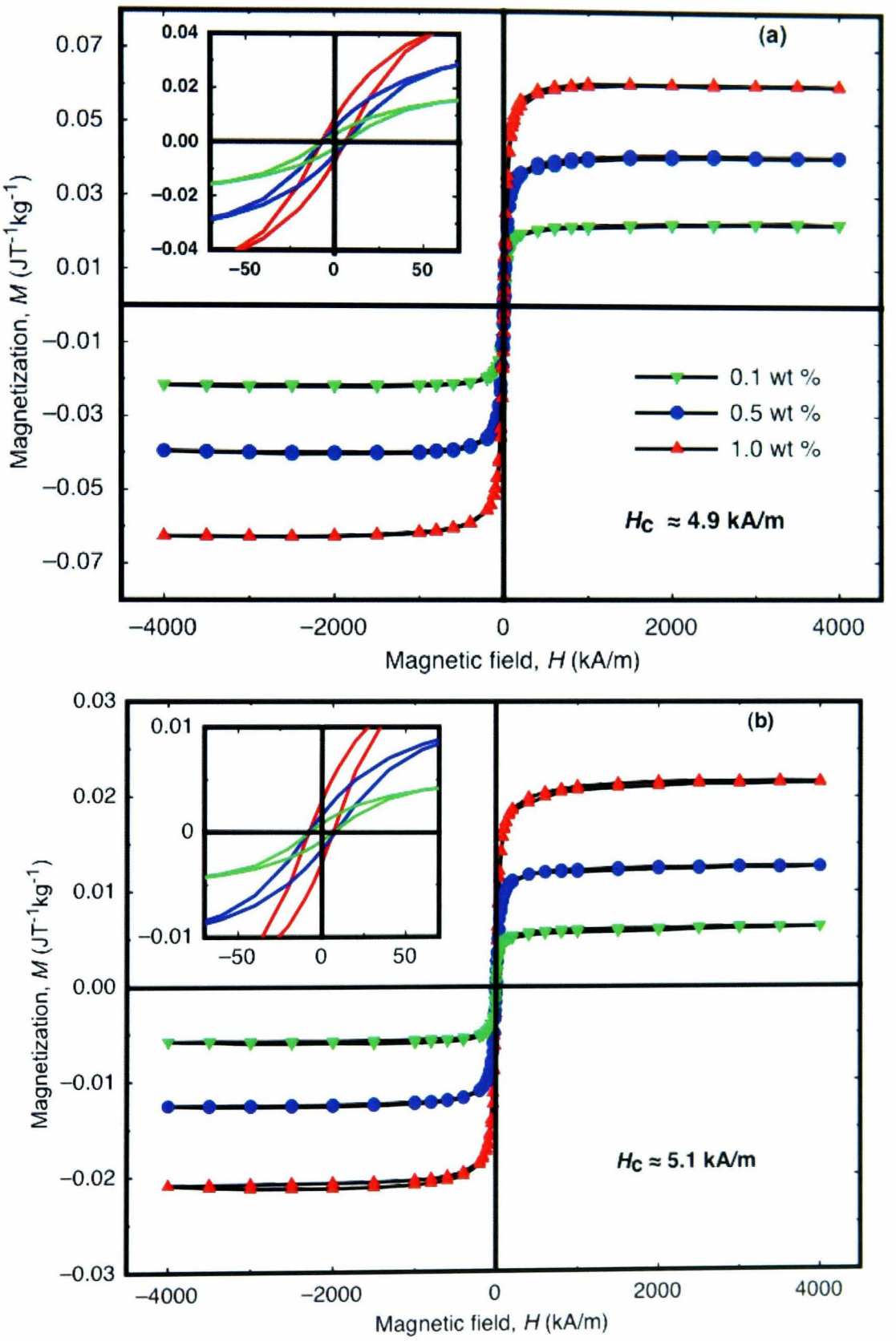

Figure 6.9: Magnetic hysteresis loops for unswollen (a) and swollen (b) ferrogels at T = 300 K. The inset of each Figure is a magnification of the plots showing the coercive fields, H_C which are independent of the nanoparticle concentration and the gel state.

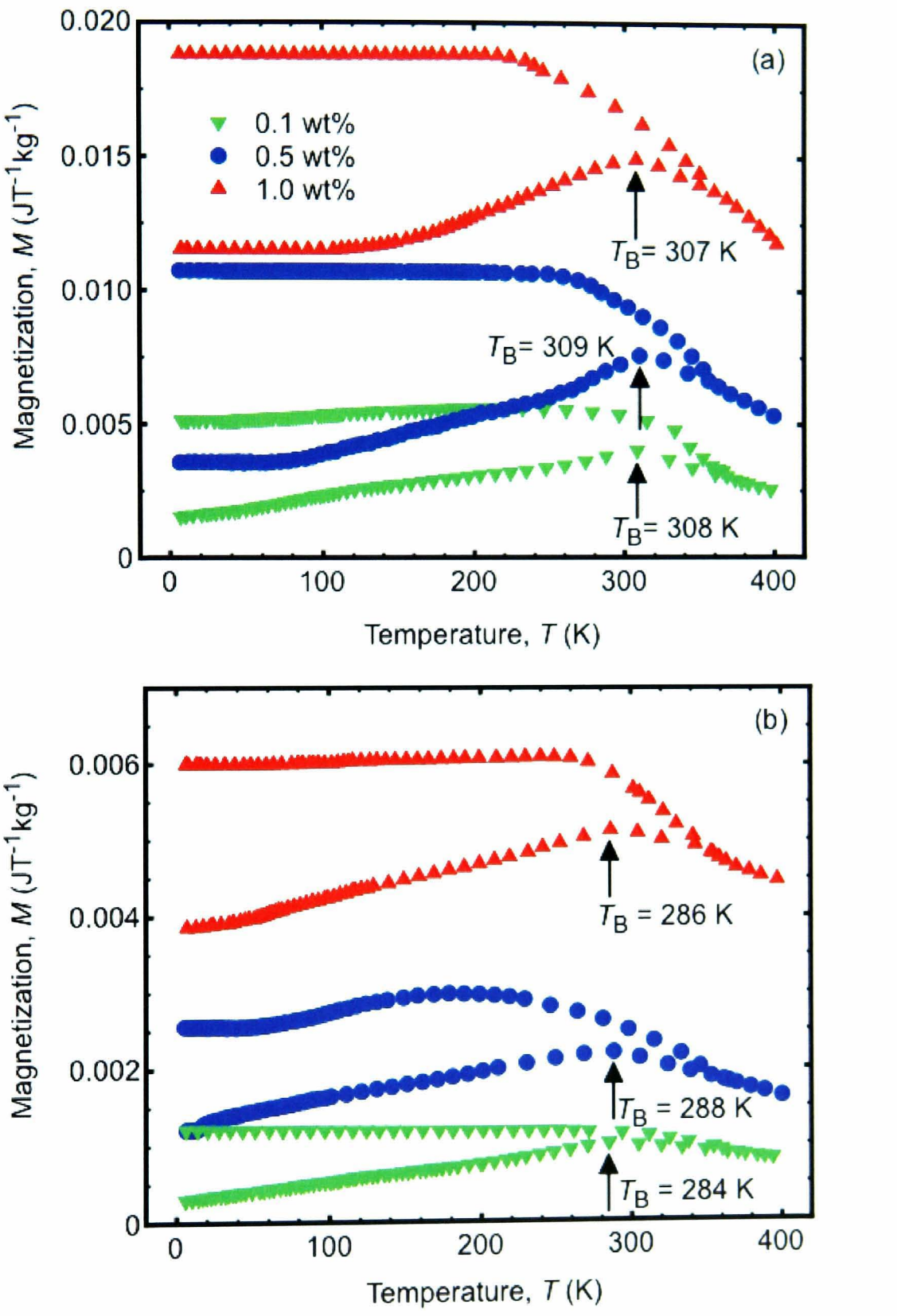

Figure 6.10: Zero field cooled/field cooled (ZFC/FC) plots showing the blocking temperatures for unswollen (a) and swollen (b) ferrogels as a function of the nanoparticle concentration. The arrows indicate the blocking temperatures T_B at each concentration. These data indicate that there is no cluster formation under the applied magnetic field for different concentrations and gel states (see text).

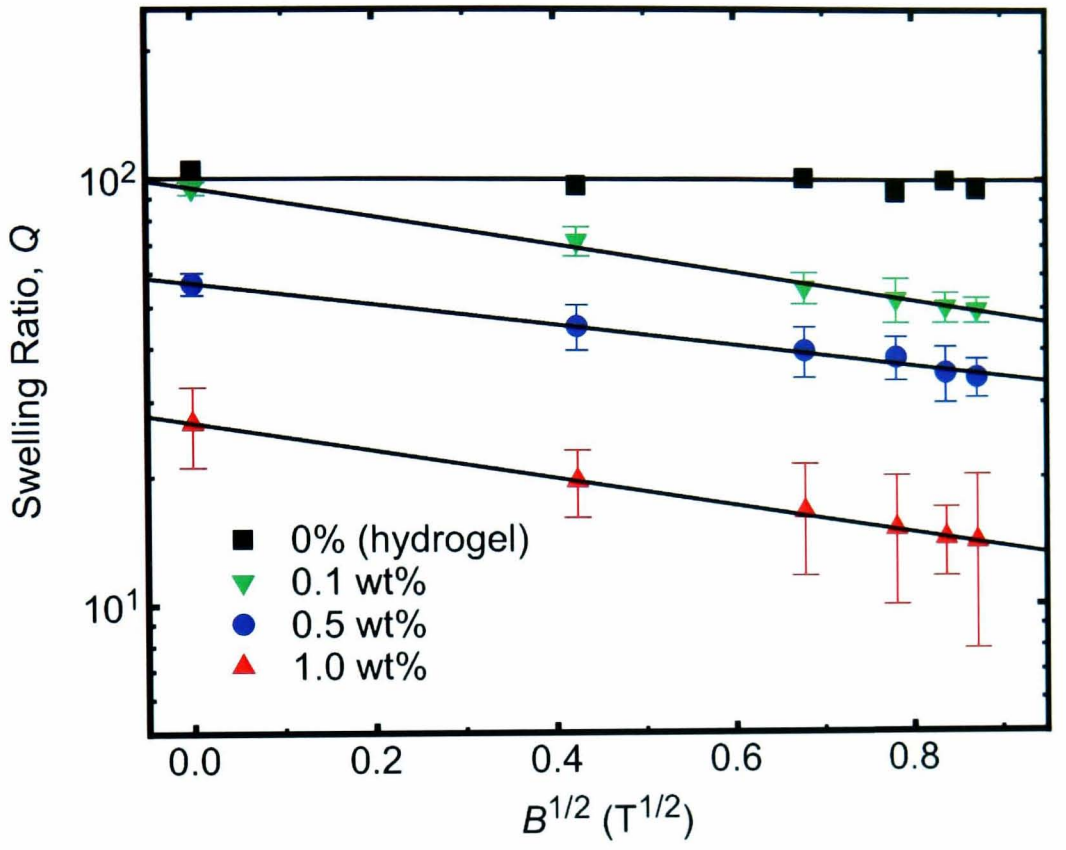

Figure 6.11: A plot showing the linear relationship between the logarithm of the swelling ratio and the square root of magnetic field for a hydrogel and different ferrogels. The solid lines are the least square fits to the data. The error bars are the statistical errors calculated from five measurements.

Figure 6.11 also shows the linear relationship between the logarithm of the swelling ratio and the square root of the applied magnetic field, which can be rewritten in terms of the magnetic-field energy density, $B^2/2\mu_0$ as follows:

$$Q = A \exp\left(-\left(\frac{\xi^3 B^2}{2\mu_0 k_B T}\right)^{1/4}\right), \tag{6.9}$$

where A is a constant and ξ is a correlation length in the gel. The calculated correlation lengths obtained from fitting to equation 6.9 are shown in Table 6.2. The values in this table indicate no discernable change in the correlation length with increasing magnetite concentration.

Nanoparticles (wt%)	Swelling (ξ) (nm)	Diffusion (ξ) (nm)	Relase (ξ) (nm)	η_0 (mPa s)
0.1	1.8 ± 0.1	2.2 ± 0.1	2.2 ± 0.2	0.9 ± 0.1
0.5	1.3 ± 0.3	2.3 ± 0.2	2.1 ± 0.2	1.3 ± 0.2
1.0	1.9 ± 0.1	2.2 ± 0.1	2.9 ± 0.1	1.4 ± 0.3

Table 6.2: Calculated correlation lengths from swelling [fits to equation (6.9)], diffusion [fits to equation (6.12)], and release [fits to equation (6.14)] measurements. The values of viscosity obtained from the fits to the diffusion data (Figure 6.12) are also tabulated.

6.3.4 Diffusion of Dextran in Ferrogels

In order to understand the structural behavior of ferrogels as well as transport properties in these materials, the diffusion of labeled dextran was investigated using FCS. Diffusion coefficients so obtained are plotted as a function of magnetic field in Figure 6.12. Three different (swollen) samples with different magnetic nanoparticle concentrations demonstrate the same trend, with different magnitudes, that the diffusion coefficient decreases exponentially upon an increase in magnetic field strength. In order to explain these data, we consider a model based on a Stokes-Einstein relationship for diffusion [227, 228]

$$D = \frac{k_{\mathrm{B}}T}{6\pi\eta R}, \tag{6.10}$$

where η is the viscosity of the medium and R is the size of the diffusing molecule. In this relation, the only parameter that can be affected by adding magnetite nanoparticles and applying a magnetic field is the viscosity within the ferrogel. From the swelling measurements in section 5.3.3, we observed the effect of the added magnetite nanoparticles and the applied magnetic field on the mesh size, which can be related to the viscosity of the ferrogel by

$$\eta = \eta_0 \exp\left(\left(\frac{\xi^3 B^2}{2\mu_0 k_{\mathrm{B}} T}\right)^{1/4}\right), \tag{6.11}$$

where η_0 is the viscosity of the solvent. By substituting equation (6.11) into equation (6.10), the Stokes-Einstein diffusion becomes

$$D = \frac{k_B T}{6\pi\eta_0 R} \exp\left(-\left(\frac{\xi^3 B^2}{2\mu_0 k_B T}\right)^{1/4}\right), \tag{6.12}$$

which is fitted to the data shown in Figure 6.12. The results obtained are presented in Table 6.2, with the size of dextran taken as $R = 9$ nm; R was obtained from measurements of the diffusion coefficient of dextran in water using the Stokes-Einstein relation for diffusion at $T = 298$ K. From the diffusion results in Table 6.2, it is clear that the viscosity obtained is the viscosity of water at or close to room temperature and the correlation lengths are comparable to those obtained from the swelling measurements. The data shown in Figure 6.12 demonstrate that there is no effect of the magnetic field on dextran diffusion when no magnetite particles are present, which shows that the dextran does not interact with the magnetic field. Our results are incapable of testing for any anisotropy in the diffusion, i.e. whether or not the diffusion increases or decreases in the direction of the magnetic field compared with directions orthogonal to it.

6.3.5 Controlled Molecular Release

The concentration gradient method [151, 150] was used to determine the concentration of dextran molecules released from swollen hydrogels and ferrogels into the surrounding solvent. A certain amount of dried hydrogels and ferrogels were swollen in 10 nM FITC-dextran solution. The swollen gels were then placed in 5 ml of water and exposed to a magnetic field. 1 ml of the resulting solution was taken for each measurement and replaced with 1 ml of distilled water. FCS was used to study the diffusion of FITC-dextran in these solutions to determine the number of molecules N, which can be obtained from the fits to equation 4.19. The concentration of the released molecules (in mol L) can be calculated from

$$C = N/V_{\text{eff}}, \tag{6.13}$$

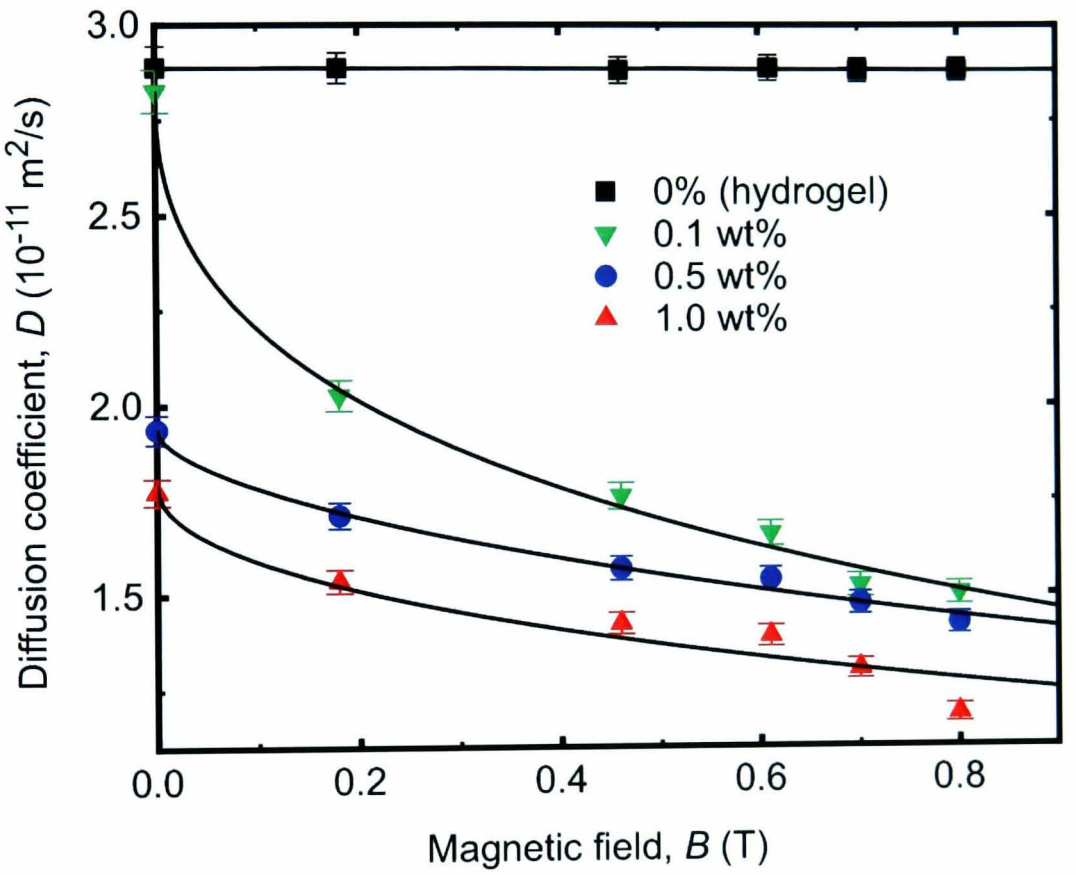

Figure 6.12: Magnetic field effect on diffusion of FITC-dextran in ferrogels with different volume fraction of magnetic nanoparticles. The solid lines are fits to the Stokes-Einstein model (equation 6.12).

where V_{eff} is an instrumental parameter, the effective confocal volume, given by $V_{\text{eff}} = \pi^{3/2} r_c^2 z_c$, where r_c and z_c are, respectively, the confocal radius and height. (For our experiments V_{eff}= 1.25 fL.) Molecular release from the ferrogel matrix to the surrounding solvent is strongly controlled by magnetic field (Figure 6.13). In general, increasing magnetic field strength causes some disruption in the polymer network during magnetic alignments, leading to less freedom for the diffusing molecules. This disruption increases with increasing concentration of the magnetic nanoparticles. The concentration of the FITC-dextran released under the applied magnetic field is reduced by almost a factor of two at 0.8 T for the highest magnetite concentration (1 wt%). This can be understood from the release mechanisms which were explained in Chapter 3, section 3.2.2.2 (see Figure 3.3). The increase of magnetic nanoparticle concentration leads to a smaller mesh size under applied magnetic fields which causes the macromolecular probe to be trapped inside the ferrogel. This explains the decrease in the release fraction in Figure 6.13 with increasing magnetite concentration. From the application point of view, ferrogels with higher magnetite concentrations work better in trapping macromolecules under applied magnetic fields to be delivered to the desired place according to the second mechanism in Figure 3.3. It is also noticeable from Figure 6.13 that the magnetic field has no effect on the molecular release from hydrogels (i.e. PMAA but without magnetite), which is to be expected for a paramagnetic material, and is in keeping with the diffusion results shown in Figure 6.12. Figure 6.13 also indicates that the concentration of expelled dextran molecules depends on the applied magnetic field by the same scaling behavior as the swelling of the ferrogels,

$$C = \alpha \exp\left(-\left(\frac{\xi^3 B^2}{2\mu_0 k_{\text{B}} T}\right)^{1/4}\right), \tag{6.14}$$

where α is a proportionality constant. This means that the volume phase transition of the ferrogel is the controlling factor for the molecular release and other influences such as physical or chemical interactions are not significant.

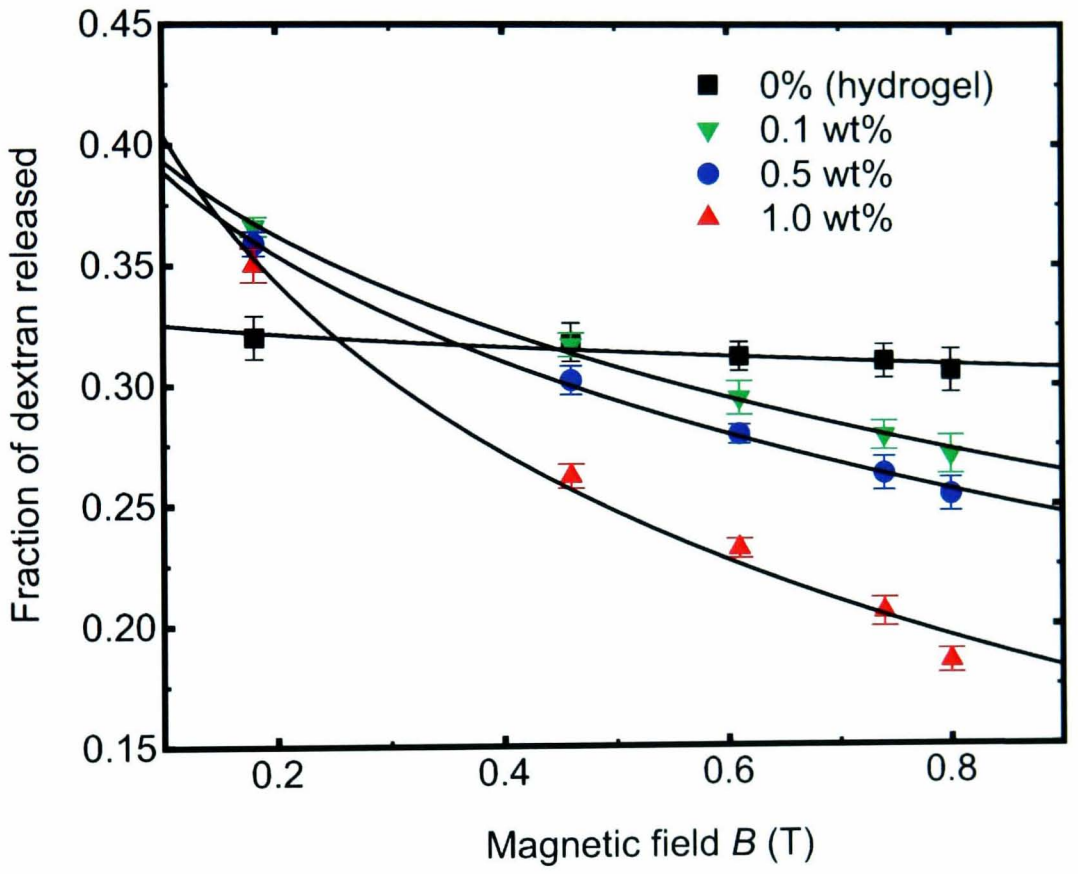

Figure 6.13: Controlled molecular release of FITC-dextran from different ferrogels to the surrounding medium as a function of magnetic field. The solid lines are fits to equation 6.14. The error bars are the statistical errors calculated from three measurements.

6.4 Conclusions

Introducing magnetite nanoparticles controls the structural and magnetic behaviour of hydrogels under applied magnetic fields. These properties make this class of materials good candidates for many applications, especially in the fields of bionanotechnology and drug delivery.

The work presented in this chapter considered the effect of applied magnetic fields on the diffusion of single dextran molecules labeled with fluorescein isothiocyanate within a ferrogel [a composite of magnetite nanoparticles in a poly(methacrylic acid) hydrogel (PMAA)] using fluorescence correlation spectroscopy (FCS). FCS studies of single molecule diffusion within these systems revealed the relationship between the applied magnetic field and the viscosity of ferrogels based on Stokes- Einstein diffusion. It has been found that the mesh size of the ferrogel is controlled by the applied magnetic field, B, and scales as $\exp\left(-\sqrt[4]{\xi^3 B^2/2\mu_0 k_B T}\right)$. The diffusion coefficient of the dextran can be modeled with a simple Stokes-Einstein law, containing the same scaling behavior with magnetic field as the swelling of the hydrogel. Furthermore, the magnetically controlled molecular release from ferrogels to the surrounding solvent was found to decrease considerably with increasing magnetic field induction from 0.2 to 0.8 T, especially at higher magnetic nanoparticle concentrations. The results suggest that the concentration of the released molecules is controlled only by the volume phase transition of the ferrogel under the applied magnetic field without any contributions from other physical or chemical interactions. The magnetic field-dependent release of dextran from these ferrogels is also controlled by the same relationship as the diffusion and swelling of these systems.

The samples were characterized by small angle x-ray scattering (SAXS) and magnetometry experiments. Magnetic hysteresis loops from these ferrogels and zero field cooled/field cooled measurements reveal single domain ferromagnetic behavior at room temperature with a similar coercivity for both as-prepared and fully swollen ferrogels, and for increasing magnetic nanoparticle concentration. SAXS experiments, such as the hysteresis loops, show that magnetite does not aggregate in these gels.

Part II

Hyperbranched Polymers

Chapter 7

Structure of Hyperbranched PNIPAM

7.1 Introduction

Poly(N-isopropyl acrylamide) (PNIPAM) is a reasonably biocompatible and popular polymer due to its temperature-induced collapse transition at a physiologically useful temperature of 32 °C. Therefore, PNIPAM has been a good candidate for many possible applications (see Chapter 3). It has been a challenge to increase the collapse transition temperature (LCST) of this polymer to the body temperature for which many attempts have been reported using different synthetic methods, such as copolymerizing PNIPAM with hydrophilic chain-end functionalized polymers. For example, Rimmer and co-workers [21, 114] have been able to synthesize hyperbranched PNIPAM (HB-PNIPAM) with no cyclization or microgelation. They have utilized the self-considering vinyl polymerization (SCVP) principles by using the Reversible Addition Chain Transfer Polymerization (RAFT) method to produce HB-PNIPAM with imidazole-chain ends. These end groups can be replaced with COOH acid groups or can be used for binding with other polymers or biological species [29].

However, a complete understanding of the structural behaviour of these hyperbranched polymers as a function of temperature is still lacking. Knowl-

edge about the internal structure of HB-PNIPAM is necessary so that the improvement and development of such materials into useful applications can rely on a logical design. How these polymers behave as they approach their LCST and whether they entangle or not are important questions that need to be answered. SANS is a powerful tool which is able to provide qualitative and quantitative answers to these questions.

The work presented in this chapter is extending the physical characterization of the previously synthesized HB-PNIPAM by Rimmer and co-workers. The temperature dependent behaviour of HB-PNIPAM as a function of the degree of branching will be explored and compared to a linear PNIPAM. UV-visible spectroscopy will be used to determine the macroscopic LCST of such polymers and SANS will be used to study the structural behaviour of HB-PNIPAM. Also, HB-PNIPAM has has been labelled with fluorescent species and will be visualized by a confocal laser scanning microscope (CLSM).

7.2 Experimental

7.2.1 RAFT Polymerisation

Reversible Addition-Fragmentation chain Transfer (RAFT) polymerisation is a type of controlled radical polymerisation which was introduced by Thang *et al.* in 1998 [229, 230]. RAFT polymerisation is advantageous over other controlled radical polymerisations in that it can be used with a variety of monomers and reactions, producing controlled molecular weight polymers with narrow polydispersities using thiocarbonylthio compounds, such as dithio-ester. RAFT polymerisation has been successfully used to synthesize polymers with well-defined architectures, such as linear block copolymers, polymer brushes and branched polymers. Figure 7.1 shows the currently accepted mechanism of RAFT polymerisation. The process starts with a reaction between an initiator ($I^{\bullet}$) and a monomer unit, producing a radical species ($P_n^{\bullet}$) which can start a polymerizing chain. The created active chain ($P_n^{\bullet}$) reacts with the dithioester giving a radical adduct which fragments into a polymeric dithioate product and a new radical species ($R^{\bullet}$). The latter

radical reinitiates a polymerisation creating a new propagating radical ($P_m^\bullet$). The last step of the RAFT process is the equilibration between the propagating radicals $P_n^\bullet$ and $P_m^\bullet$ and the dormant dithioate compound in which these radicals are trapped, forming an intermediate radical. In a reversible way, one polymer chain exists in the dormant stage (bound to the dithioate species), while the other is active to proceed in further polymerisation. The use of a variety of R and Z groups has been reported to produce desirable polymer chain-end functionality.

7.2.2 Synthesis

The work in chapter is concerned with the preparation and analysis of highly-branched poly(N-isopropylacrlamide) (HB-PNIPAM) (Figures 7.2 and 7.3) using a branching RAFT agent which had previously been developed by Rimmer and co-workers [21]. The resultant highly branched polymers, which contained the residual RAFT groups N-pyrrole dithioate at their chain-ends, could be converted to carboxylic acid chain-end functionalised polymers using previously developed methodology [115]. Three HB-PNIPAM samples with different degrees of branching (number of monomers between branch points 25, 60 and 90) were synthesized as follows:

Synthesis of hyperbranched N-pyrrole chain-end functionalized poly-Nisopropylacrylamide:

As shown in Figure 7.4, N-isopropylacrylamide (NIPAM), 4-vinylbenzylpyrrolecarbodithioate (RAFT agent) and azobis(isobutyronitrile) (AIBN) were dissolved in dioxane (quantities are given in table 7.1). The mixture was then transferred to a glass ampoule. The ampoule was sealed and freeze-pump-thaw cycles were carried out three times at 10^{-4} mbar. It was then heated at 60°C for 48 hours and quenched with liquid nitrogen. The polymer solution was precipitated by dropwise addition to diethylether (600 ml). The ether was decanted off, the solids further washed with ether then vacuum-oven dried at room temperature for 16 hours. The procedure was repeated twice

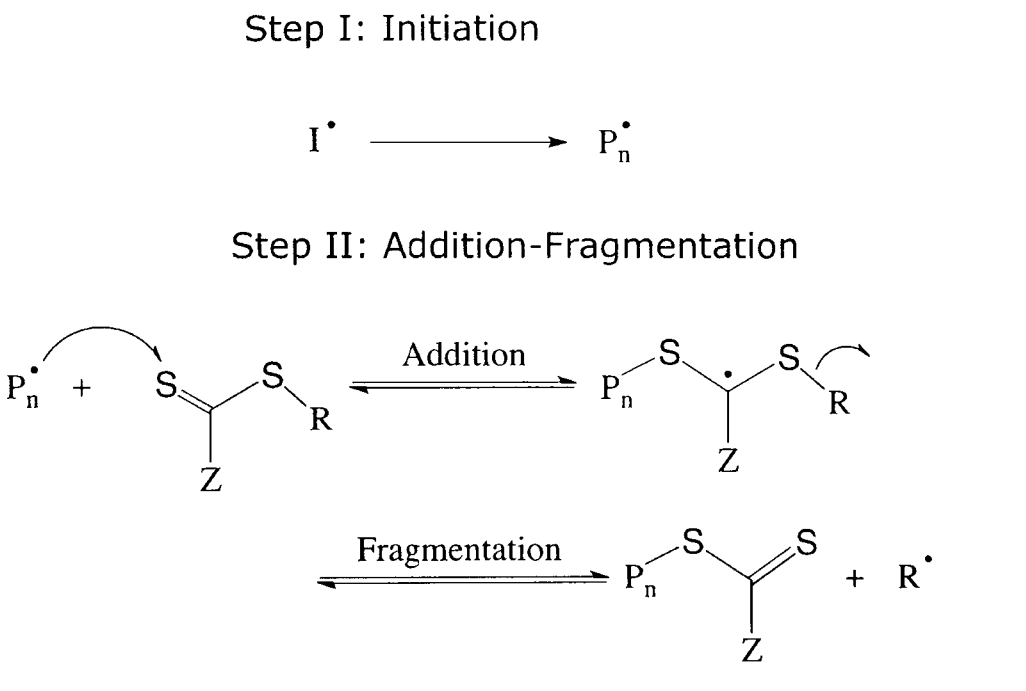

Figure 7.1: A general mechanism for RAFT polymerization.

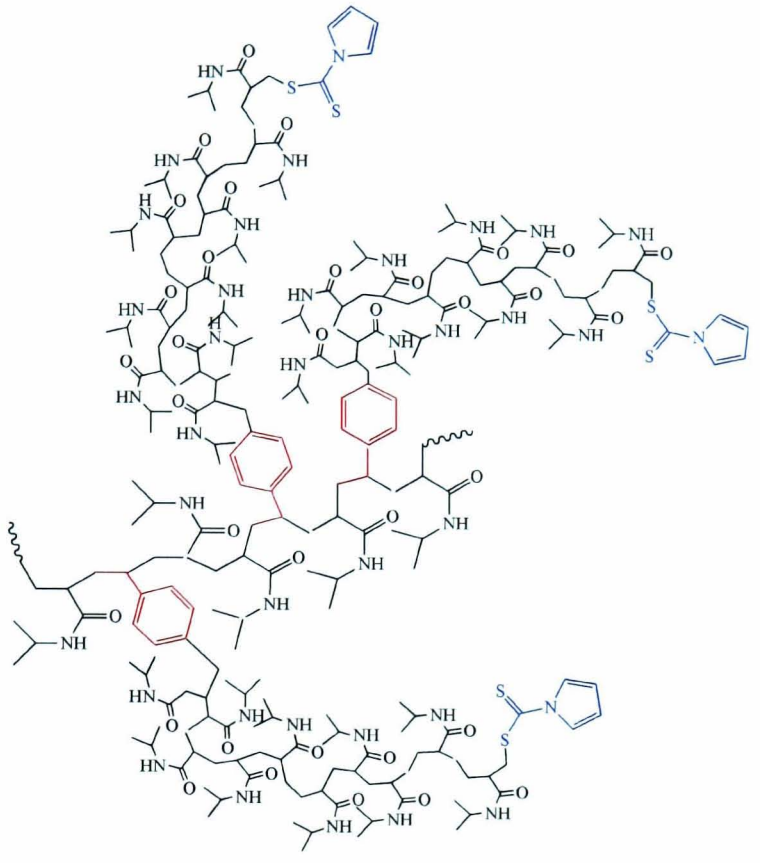

Figure 7.2: Structure of HB-PNIPAM showing links to polymer backbone via xylyl residues and residual N-pyrrole dithioate groups at branch chain-ends.

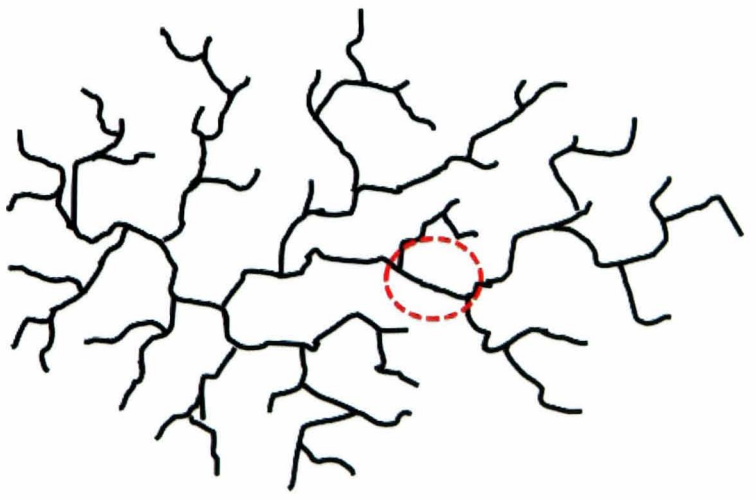

Figure 7.3: Schematic diagram showing HB-PNIPAM. The ringed area indicates the distance beyween two cross-links which is, in this study, 25, 60 or 90 monomers.

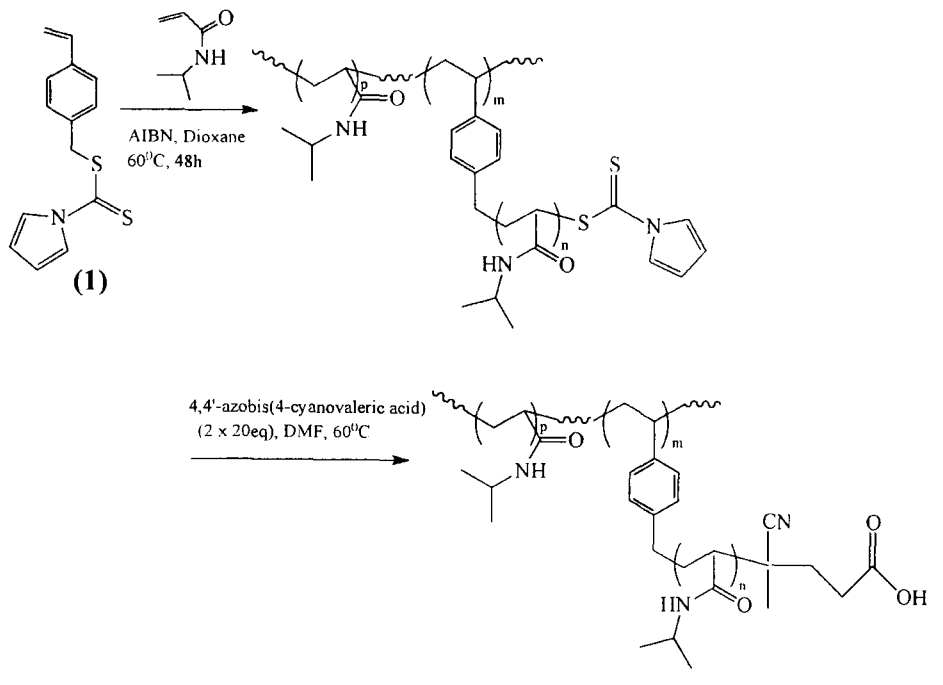

Figure 7.4: Synthesis of HB-PNIPAM *via* RAFT polymerisation and conversion to carboxylic acid chain-end functionalised HB-PNIPAM.

more to give a yellow solid (yields are shown in table 7.1).

Synthesis of hyperbranched carboxylic-acid chain-end functionalized Poly-Nisopropylacrylamides:

The highly-branched N-pyrroledithioate chain-ended polymers above were dissolved in DMF (degassed with nitrogen/30min) and stirred at 60°C under a nitrogen atmosphere. The 4,4'-azobis-(4-cyanopentanoic acid), 20 equivalents relative to the number of pyrrole chain-end groups, was added to the reaction mixture as a solution in DMF and heated at 60°C for 16 hours. This procedure was repeated twice more so that a total of 60 equivalents of the reagent were added. The DMF was removed under high vacuum at 40-50°C and the resultant oil was ultrafiltered using a blend of acetone/ethanol (10:1, vol:vol) through a 3,000 MWCO cellulose filter. The resultant concentrate was evaporated under reduced pressure and vacuum-oven dried at room temperature to give a buff coloured solid. The quantities and yield of this reaction are shown in table 7.2.

NIPAM/ RAFT Ratio	NIPAM/g	RAFT agent/g	AIBN/g	Dioxane /ml	Yield
(25:1)	2.5 g 22.1 mmol	0.229 g 0.882 mmol	0.1450 g 0.894 mmol	8.75 ml	84% 2.424 g
(60:1)	2.5 g 22.1 mmol	0.095 g 0.367 mmol	0.0598 g 0.369 mmol	9.24 ml	88% 2.2903 g
(90:1)	2.5 g 22.1 mmol	0.0636 g 0.246 mmol	0.0398 g 0.245 mmol	8.54 ml	71% 1.8283 g

Table 7.1: Quantities used to synthesize HB-PNIPAM.

NIPAM/RAFT Ratio	DMF to dissolve the polymer	4,4'-azobis-(4-cyanopen-tanoic acid)	DMF to dissolve the acid	Yield
HB-PNIPAm (25:1)	123 ml	8.582 g	22 ml	73% 2.121 g
HB-PNIPAm (60:1)	110 ml	7.659 g	20 ml	75% 1.987 g
HB-PNIPAm (90:1)	88 ml	6.097 g	18 ml	79% 2.132 g

Table 7.2: Quantities used to convert N-pyrrole dithioate chain end groups to carboxylic acid in HB-PNIPAM.

Ratio NIPAM/RAFT (in Feed)	Ratio NIPAM RAFT (NMR)	
(25:1)	(48:1)	δ 6-8.5 end-groups evident
(60:1)	(82:1)	δ 6-8.5 end-groups evident
(90:1)	(94:1)	δ 6-8.5 end-groups evident

Table 7.3: Branching degrees after conversion of N-pyrroledithioate chain-ended highly-branched polymers (HB-PNIPAM) to carboxylic-acid chain-end functionalized polymers.

7.2.3 NMR Characterisation

A Bruker 400 MHz NMR spectrometer was used to obtain NMR spectra (see Appendix C) for HB-PNIPAM at room temperature. 70 mg of each polymer was dissolved in 1 ml of deuterated chloroform and then transferred to an NMR tube. NMR spectra were used to calculate the actual branching degrees, as shown in table 7.3, which is the ratio of NIPAM to imidazole obtained from the integration of NMR spectra (Appendix C). The following are examples of the NMR analysis of a highly branched PNIPAM (25:1) with N-pyrrole and acid chain-end functionalities.

N-pyrrole chain-end functionalized PNIPAM:

1H NMR ($CDCl_3$, ca. 5% CD_3OD, RT, 400MHz): δ/ppm 1.0 (s, br, -$N(CH_3)_2$), 1.45-1.60 (m, br, 2H, -CH_2-CH-C_6H_4-) and (m, br, 1H, -CH_2-CH-C_6H_4-), 1.75-2.05 (m, br, 1H, -CH_2- CH-CO-NH-) and (m, br, 1H, -CH_2-CH-CO-NH-), 3.32 (s, br, H_2O-polymer bound), 3.98 (s, br, 1H, $(CH_3)_2CH$-), 4.50 (m, br, 1H, CH_2CH-S-C(=S)-N-pyrrole), 6.30 (s, br, 2H, N-pyrrole-Hb), 7.62 (d, br, 2H, N-pyrrole-Ha).

Carboxylic-acid chain-end functionalized PNIPAM:

1H NMR (CDCl3, ca. 5% CD_3OD, RT, 400MHz): δ/ppm 1.0 (s, br, -$N(CH_3)_2$), 1.45-1.60 (m, br, 2H, -CH_2-CH-C_6H_4-) and (m, br, 1H, -CH_2-CH-C_6H_4-), 1.75-2.05 (m, br, 1H,-CH_2-CH-CO-NH-) and (m, br, 1H, -CH_2-CH-CO-NH-), 3.32 (s, br, H_2O-polymer bound), 4.05 (s, br, 1H, $(CH_3)_2$CH-), 6.60-7.40 (m, br, 4H, -C_6H_4-), 7.65 (s, br, -NHCO-).

7.2.4 Gel Permeation Chromatography (GPC)

The average molecular weight, molecular weight distributions and polydispersity were measured by GPC relative to a poly(ethylene oxide) reference standard. Two different GPC techniques were used with single and triple detection features. For the single detection technique, 200 mg of ammonium acetate was dissolved in 1 litre of DMF. 2.5 ml of this solution was added to 5 mg of each polymer and all solutions were filtered before injecting them into the GPC. The solutions were then run through PL gel (mixed B, 950 mm) columns at 70°C with flow rate of 1.0 ml/min. For the triple detection GPC, the same polymer quantities were used as for the single detection, but 0.1% of tetrabutyl-ammonium bromide (TBAB) in tetrahydrofuran (THF) was used as eluent. Then the solutions were run through PL gel (2 x mixed-C) columns with flow rate of 1.0 ml/min. Figures 7.5 and 7.6 illustrate typical size exclusion chromatography (SEC) molecular weight distributions using the two techniques mentioned above. It is noticeable from these plots that, as expected, by introducing branching monomers the molecular weight distributions become broad and have multiple peaks compared to their analogous linear PNIPAms [21]. Table 7.4 show the obtained values of Mw, Mn and PD for linear and hyperbranched PNIPAM.

7.2.5 Fluorescently labelled Linear and HB-PNIPAM

The RAFT polymerisation procedure described in section 7.2.2 was also used to synthesize linear and hyperbranched PNIPAM with a chemically attached fluorescein to the polymer backbone. The same quantities shown in table 7.1

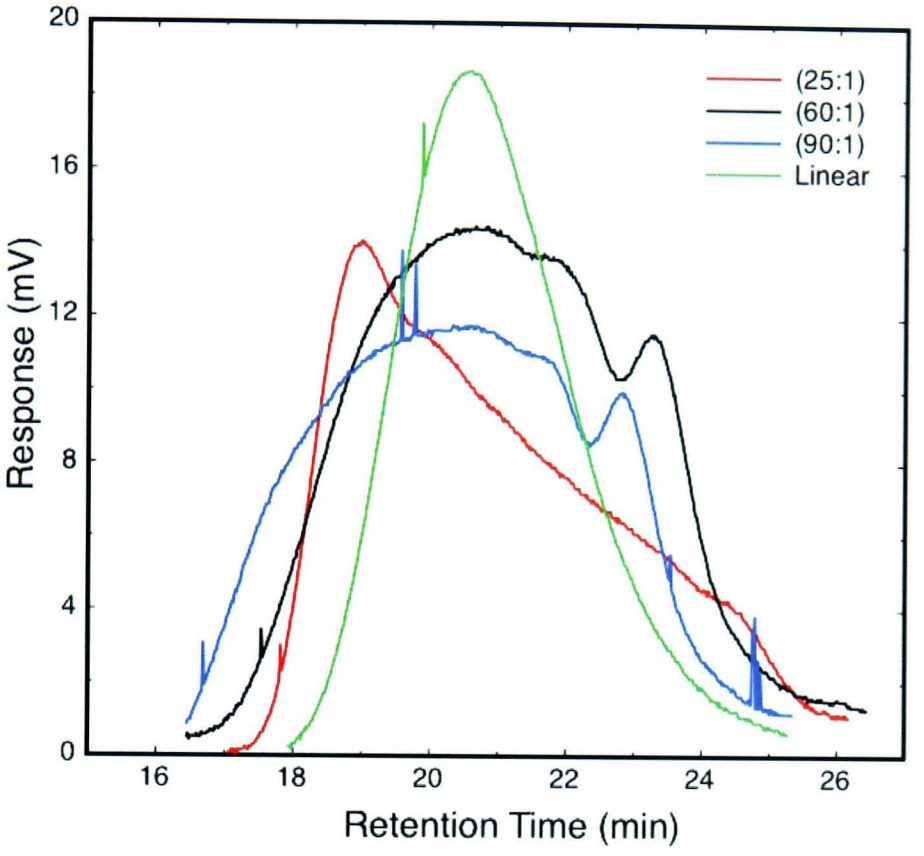

Figure 7.5: Typical SEC chromatograms for linear and hyperbranched PNIPAM with different branching degrees (25:1, 60:1 and 90:1) using a single detection GPC system. This figure shows a single peak for linear PNIPAM and broad and multiple peaks for HB-PNIPAMs. It is clear that single detection GPC is not appropriate for the highest degree of branching (25:1) as only a single peak is observed from which the average molecular weight is underestimated as shown in table 7.4.

Description	DMF (0.1% ammonium acetone)			THF (0.1% TBAB)			
	Mw	Mn	PD	Mw	Mn	PD	Rgw
(25:1)	48291	3911	12.3	316187	18551	17.0	10.74
(60:1)	46634	3706	12.6	168579	31831	5.3	8.86
(90:1)	82073	7180	11.43	357442	37399	9.6	11.4
Linear	28689	8513	3.37	135584	63452	2.14	8.63

Table 7.4: GPC data for linear and HB-PNIPAM using single (DMF (0.1% ammonium acetone)) and triple (THF (0.1%TBAB)) detection GPC systems at 70°C.

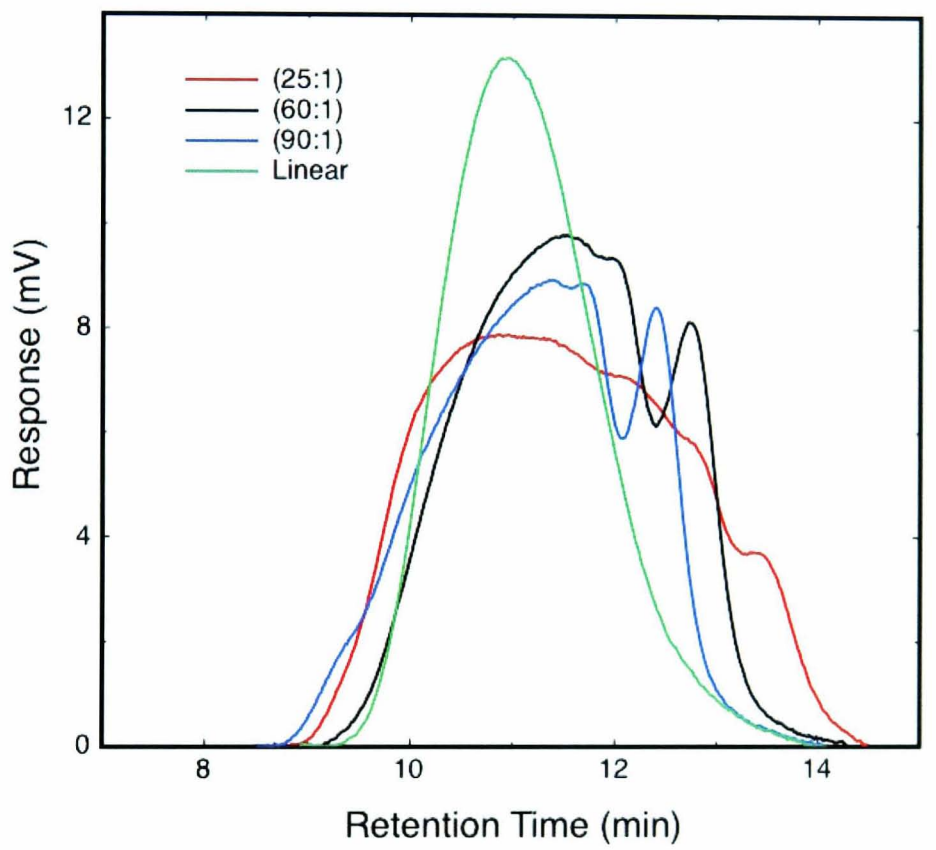

Figure 7.6: Typical SEC chromatograms for linear and hyperbranched PNIPAM with different branching degrees (25:1, 60:1 and 90:1) using a triple detection GPC system. This figure shows broad and multiple peaks for all HB-PNIPAMs and a single peak for the linear PNIPAM. The average molecular weights from these measurements are listed in table 7.4.

were used to prepare fluorescently labeled linear and hyperbranched PNIPAMs, but with the addition of 25 mg (i.e. 1% of the NIPAM quantity) of fluorescein o-acrylate (97% from Sigma-Aldrich). The N-pyrroledithioate chain-end groups were also converted to carboxylic-acid chain-end groups using the conversion method described in section 7.2.2 with the same quantities in table 7.2. To test the existence of the fluorescent labels, a UV-visible spectrometer (U-2010 spectrometer) was used to obtain the absorption spectra show in Figure 7.7 for 1% wt/wt of fluorescently labeled PNIPAM in pure water. These labelled linear and HB-PNIPAMs will also be used to study the dynamics of these polymers as a function of temperature and concentration.

7.2.6 LCST Determination

A Cary 3Bio UV-visible spectrophotometer, fitted with a Cary temperature controller, was used to determine the cloud point (LCST) of different concentrations (5 mg/ml and 10 mg/ml) of HB-PNIPAMs in D_2O (Figure 7.8). A Varian Cary temperature controller was utilized to an accuracy of $\pm 0.1°C$ to control the temperature of the cell holder and the condensation of the sample cell holder was avoided by a flow of nitrogen gas. All samples were heated from 15°C up to 60°C and the cloud points were obtained using a wavelength of 500 nm. The LCST of the polymer was determined as the point of inflexion of the increased absorbance with raising the temperature and the results are summarized in table 7.5.

It is clear from table 7.4 that the polydispersity (PD) of HB-PNIPAM is larger than that of linear PNIPAM due to an increase in the heterogeneity in the composition of the highly branched polymers. This increase in PD has been observed to affect the transition temperature (LCST) of HB-PNIPAM leading to a more gradual increase in the turbidity of the sample. The reason behind this is that some molecules or some parts of a molecule nucleate at lower temperatures forming intermolecular aggregates before the onset of the bulk sample. This effect can be seen in Figure 7.8 from the change in absorption with temperature. This figure shows a gradual increase of the absorption with a significant slope instead of a sharp change as in homo-

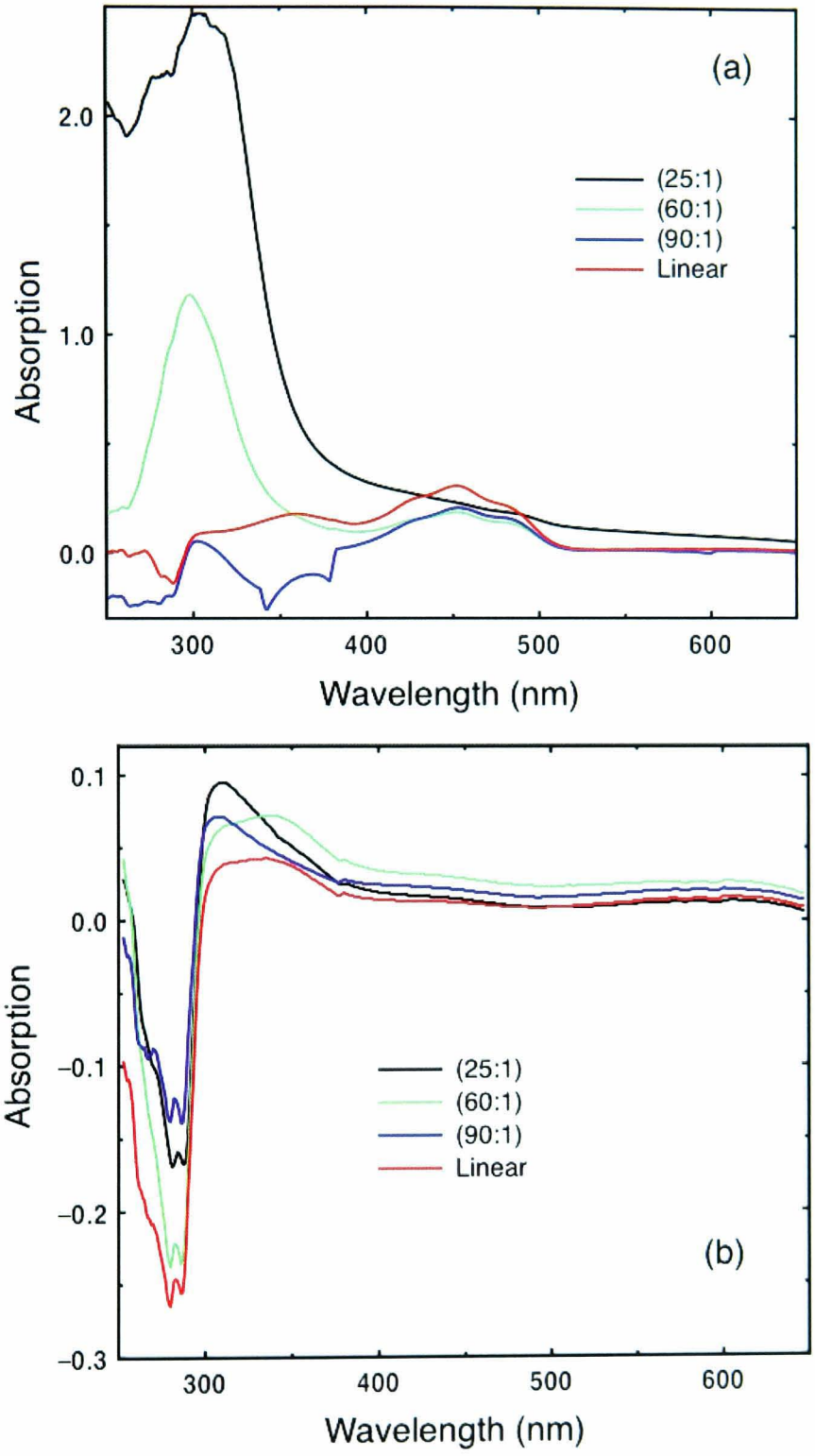

Figure 7.7: UV-visible spectra for fluorescently labeled linear and hyperbranched PNIPAM with (a) N-pyrroledithioate and (b) carboxylic-acid chain-end groups.

Sample	Cloud point in D_2O, 10% polymer/ °C	Cloud point in D_2O, 5% polymer/ °C
HB-PNIPAM (25:1)	25	26
HB-PNIPAM (60:1)	24	24
HB-PNIPAM (90:1)	18	30
Linear PNIPAM*	32	32

Table 7.5: Cloud points (LCST) of linear and hyperbranched PNIPAMs in D_2O at different concentrations. * The LCST of linear PNIPAM has been taken from reference [21].

PNIPAM which occurs over 1°C. The data in Figure 7.8 also indicate that the slope of the transition increases with decreasing the number of branches; in this case HB-PNIPAM (90:1) has the largest slope especially at higher polymer concentration (7.8 (b)).

7.2.7 Confocal Laser Scanning Microscopy (CLSM)

A confocal laser scanning microscope was used to visualize the microstructures of fluorescently labelled PNIPAMs prepared as described in section 7.2.5. The CLSM used in this study was an LSM510 inverted confocal microscope (Zeiss), which was discussed in Chapter 5, and pictured in Figure 5.3. Solutions containing 5% of linear and HB-PNIPAMs were prepared by dissolving 100 mg of each polymer in 2 ml of D_2O. The temperature of the sample was controlled using a Linkam heating stage (Linkam Scientific Instruments Ltd, Surrey, UK) with TMS94 heat controller and LNP-1 nitrogen flow control. The samples were excited by an argon laser with wavelength of 488 nm to obtain images in 2D with scan depth of 8 bit in a single direction, resulting in 512×512 pixel images. In order to measure the particle concentration and distribution from the resulting images as a function of temperature, ImageJ software was utilized which allows the number of particles per unit area to be counted.

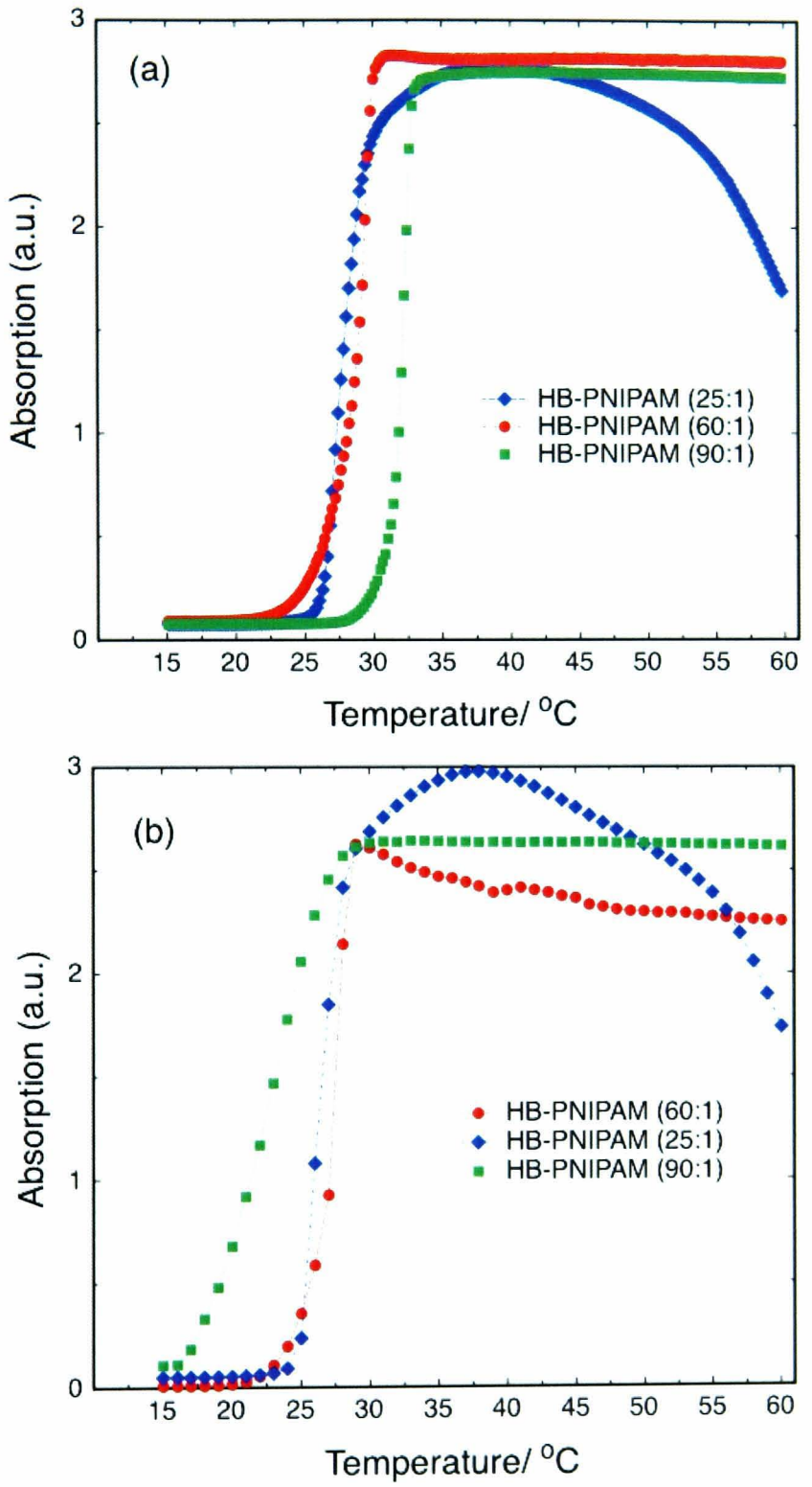

Figure 7.8: Optical density of (a) 5 wt% and (b) 10 wt% HB-PNIPAm in D_2O as a function of temperature for three different branching degrees (25, 60 and 90 monomers between branch points).

7.2.8 SANS Measurements

SANS measurements presented in this work were performed at the Rutherford Appleton Laboratory (ISIS Spallation Neutron Source, Didcot, UK) using the fixed-geometry, time-of-flight LOQ spectrometer. SANS experiments were also partially carried out at Laboratoire Leon Brillouin CEA-Saclay using the PAXY instrument. At ISIS, the LOQ instrument uses incident neutron wavelengths from 2.2 to 10.0 Å, which covers a scattering wavevector, Q, range of 0.009 to $\sim$1.3 $Å^{-1}$ at a sample-detector distance of 4.1 m. 5 and 10 wt% solutions of each polymer ((25:1), (60:1) and (90:1) HB-PNIPAM and linear PNIPAM) were prepared by dissolving 150 and 300 mg, respectively, in 2.8 ml of D_2O. All samples were transfered to 2 mm path-length quartz Hellma cells. The temperature was controlled by using circulating fluid baths giving a temperature range from -20 to 100 °C. A similar procedure was used on the PAXY instrument which covers almost the same Q-range from 0.003 to 1 $Å^{-1}$ at a sample-detector distance of 1 to 7 m. Scattering intensities were reduced and normalized as described in reference [156], using the standard procedures on the allocated softwares at each facility to obtain the differential scattering cross section, $d\Sigma/d\Omega$, in absolute units (cm^{-1}), which is referred to here as $I(Q)$. Two-dimensional (2D) SANS patterns of linear and HB-PNIPAM are shown in Appendix D.1 at temperatures below and around the LCST of each polymer.

As mentioned in Chapter 4, section 4.3.2.2, the differential scattering cross section or $I(Q)$ can expressed in terms of the form (shape) and structure factors of the sample (equation 4.36). However, the structure factor in the systems invistigated in this work can be considered as unity ($S(Q) = 1$), because the studied polymer solutions are diluted and therefore there is no interference between neutrons scattered by different scattering centres. In other words, there is no long-range local ordering in the samples which minimizes the possibility of the interactions between scattered neutrons [156].

7.3 Results and Discussion

7.3.1 Temperature-Dependent Microstructure of Linear and HB-PNIPAM

As discussed in Chapter 3, section 3.3, PNIPAM molecules in general undergo conformational transitions from swollen polymer coils to collapsed or globular structures above their transition temperatures (or the LCST). It has been found [115] that this conformational behaviour depends on the architecture of PNIPAM molecules and the chain end groups. In this section, a comparison between the microstructure of fluorescently labelled linear and hyperbranched PNIPAMs with different branching degrees is investigated using a confocal laser scanning microscope as a function of temperature. Figures 7.9, 7.10 and 7.11 show CLSM images for HB-PNIPAM with branching degrees of (25:1), (60:1) and (90:1). These polymers have different LCST transition points, 26°C, 24°C and 30°C, respectively, at a concentration of 5 wt% in D_2O (as shown in table 7.5). It can be seen clearly from these images that, at temperatures (e.g. 15°C) much lower than the LCST of all HB-PNIPAMs, polymer chains are swollen with no aggregate formation confirmed by the very low bright regions in the images at this temperature. Increasing the temperature leads to a collapse of HB-PNIPAMs which then interact with their neighbours and form aggregates. Surprisingly, the formation of these aggregates starts below the LCST of each polymer and the size of these aggregates increases with increasing temperature until they form stable and uniform closely packed colloidal dispersions. At and above the LCST of HB-PNIPAMs, these aggregates are spheres (the clearest case is the HB-PNIPAM (60:1) shown in Figure 7.10). Although gelation is not expected to take place in these systems at temperatures that much higher than the LCST of HB-PNIPAMs, for example 40°C as shown in Figure 7.14, gel regions as well as some spherical aggregates have been seen. By analysing these images (see Figure 7.13), it is clear that the aggregate concentration increases with temperature then remains constant above the LCST of each HB-PNIPAM. It is noticeable from Figure 7.13 that the aggregate concen-

tration increases with increasing the number of branches per molecule (i.e. the highest aggregate concentration was observed for HB-PNIPAM with 25 monomers between branch points).

Linear PNIPAM also follows the same trend as HB-PNIPAMs and forms aggregates with increasing temperature, as shown in Figure 7.12. However, linear PNIPAM seems to form undefined structures with increasing temperature. Furthermore, these linear PNIPAM aggregates form physical cross-links around the LCST (32°C) resulting in a network-like structure as shown in Figure 7.12 (f, g and h). In terms of the aggregate concentration as a function of temperature (Figure 7.13), linear PNIPAM shows an increase in aggregate concentration with temperature; however, this concentration was observed to level off even below its transition temperature.

7.3.2 SANS Study of The Structural Behaviour of Linear and HB-PNIPAM

7.3.2.1 Temperature-Dependent Shape and Size of Linear and HB-PNIPAM

Figures 7.15, 7.16 and 7.17 show log-log scale plots of SANS data from HB-PNIPAM with different branching degrees, while Figure 7.18 shows a similar plot for linear PNIPAM. It is apparent from these figures that scattering from linear and branched PNIPAMs follow the same Gaussian behaviour below their LCSTs where all polymers are swollen in good solvent environments. The scattering intensity increases with increasing temperature in both cases at low Q, which is an indication of contribution of scattering from the whole particles. However, SANS intensity is significantly higher in the case of HB-PNIPAM compared to the linear counterparts, increasing as the number of branches per molecule is increased (see Figure 7.19(a)) due to the increase of particle size. Tanaka and co-workers [231] obtained a similar SANS plot for linear PNIPAM in solution below and above the LCST when they compared it with the scattering from cross-linked PNIPAM.

SANS data shown in Figure 7.19 (b) indicates that linear and HB-PNIPAMs change conformation when collapsing and forming aggregates above their

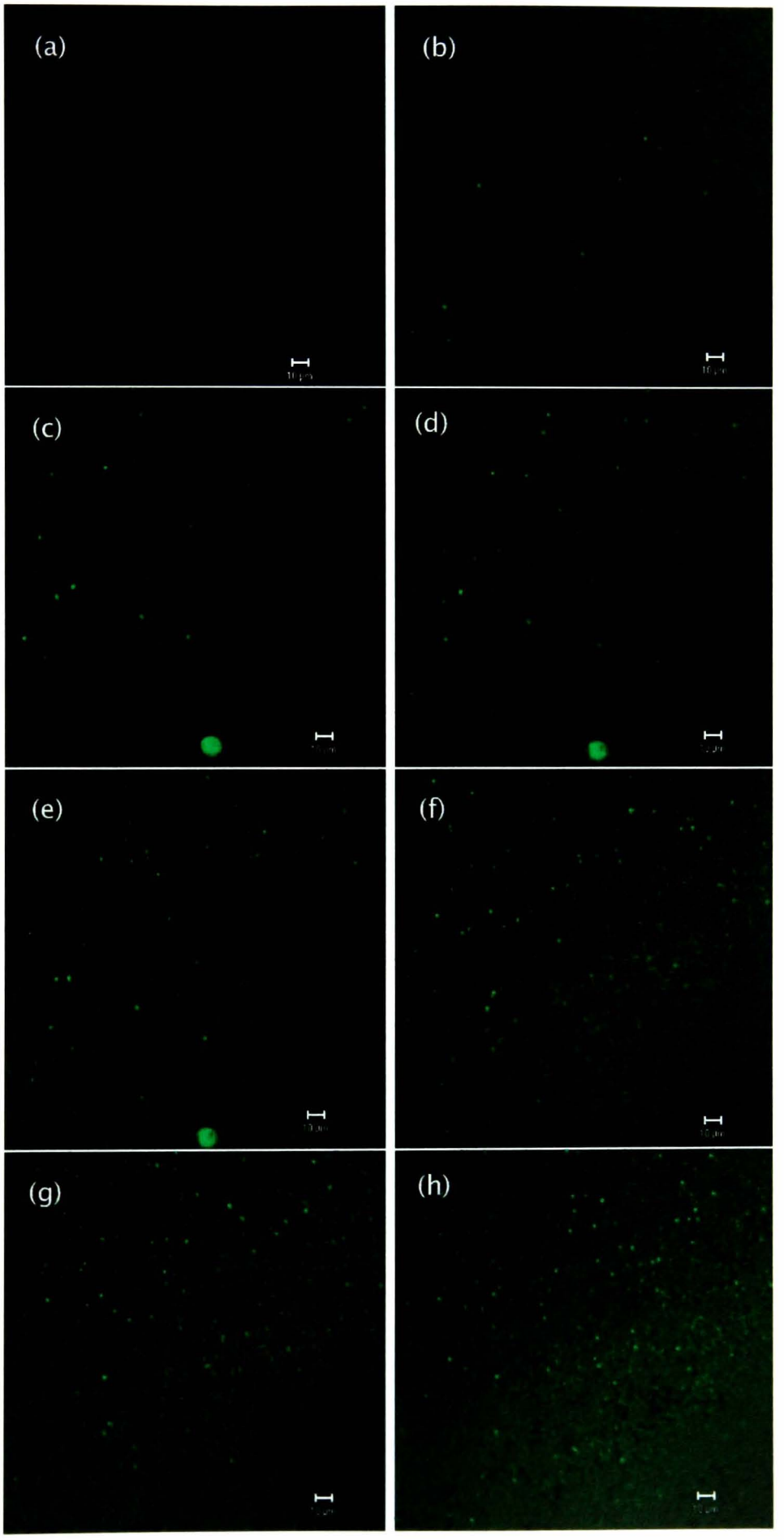

Figure 7.9: CLSM micrographs of 5 wt% of HB-PNIPAM (25:1). The temperature range is as follows: (a) 15°C, (b) 18°C, (c) 21°C, (d) 24°C, (e) 27°C,

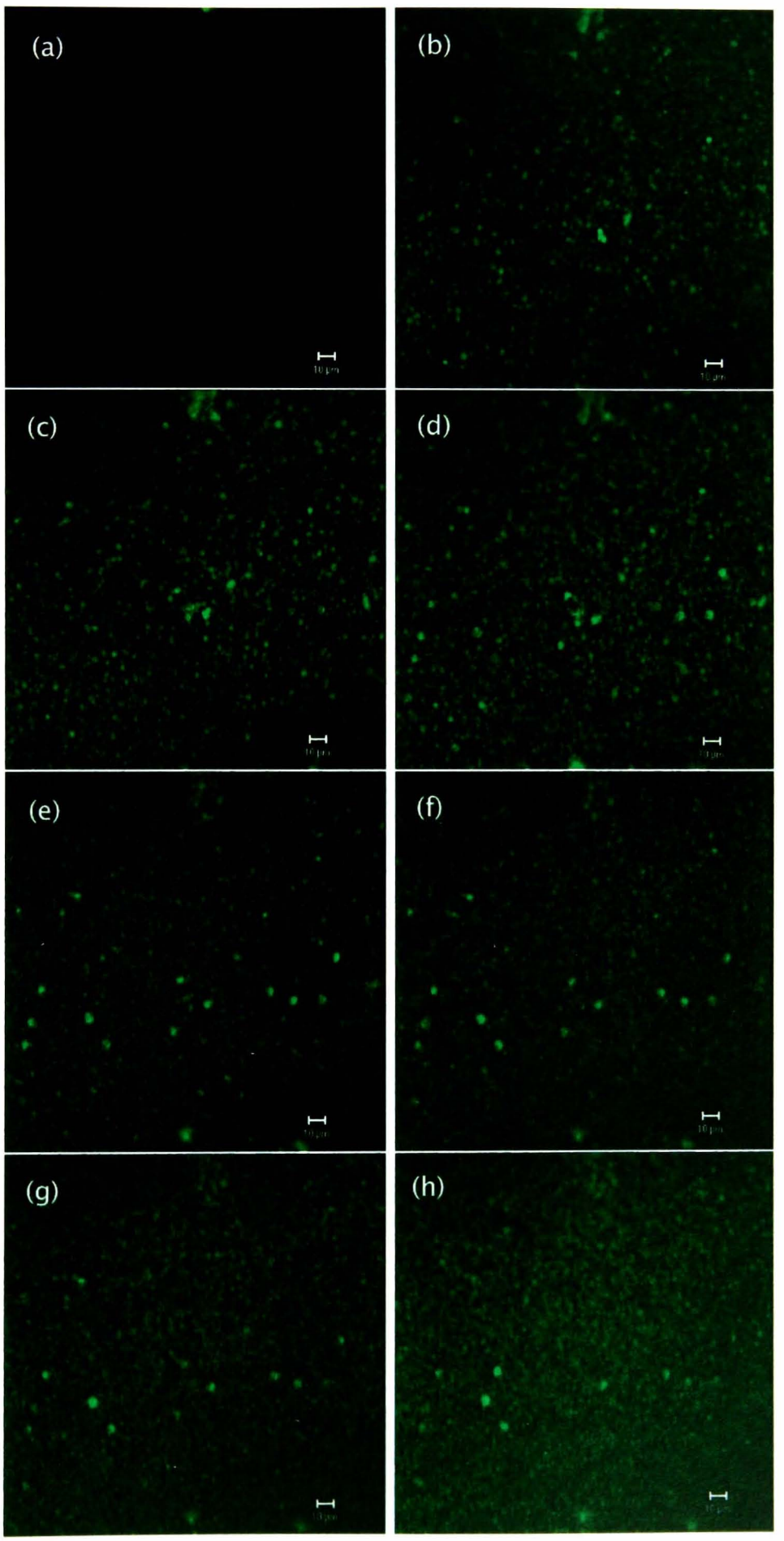

Figure 7.10: CLSM micrographs of 5 wt% HB-PNIPAM (60:1). The temperature range is as follows: (a) 15°C, (b) 18°C, (c) 21°C, (d) 24°C, (e) 27°C,

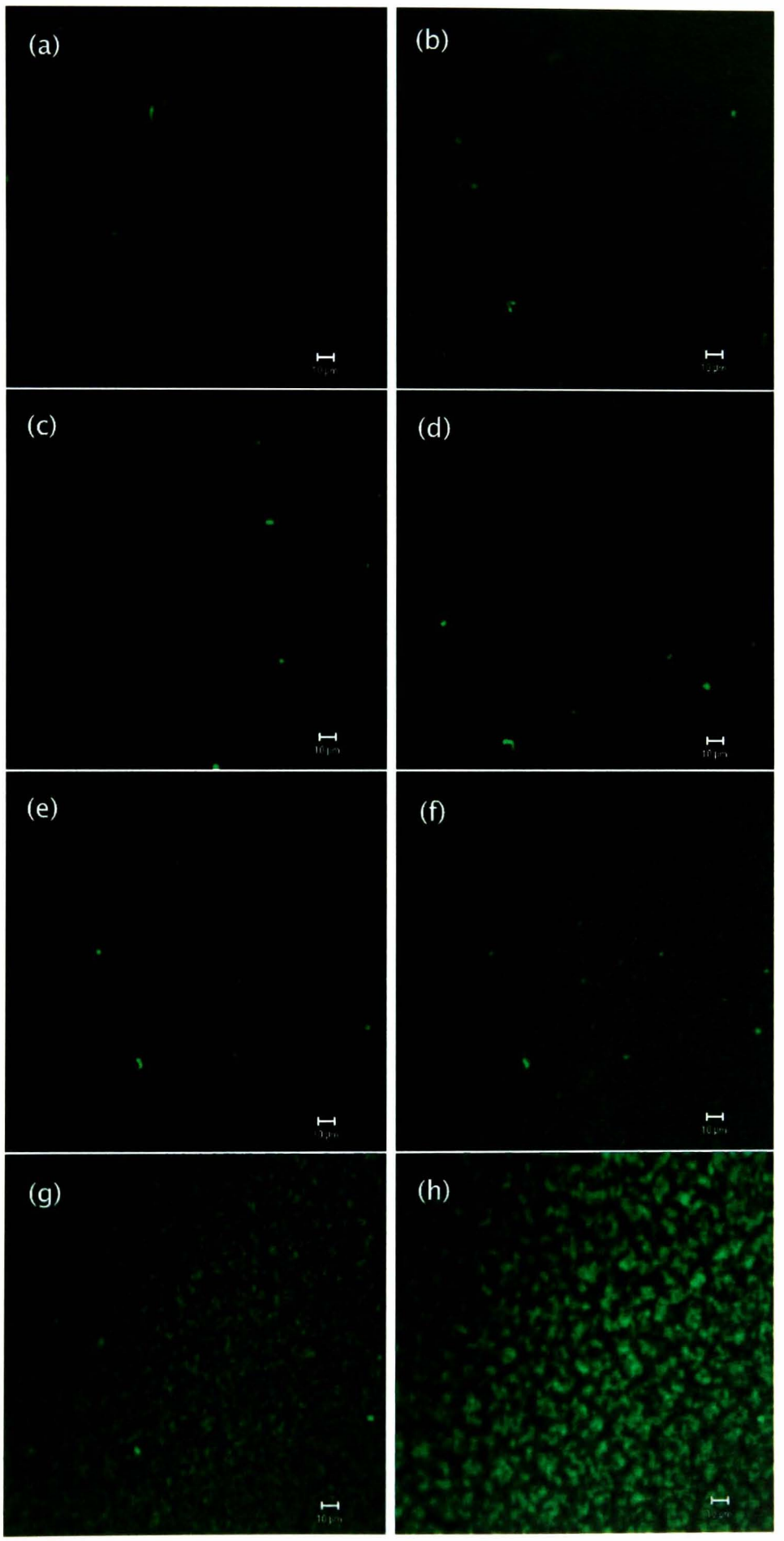

Figure 7.11: CLSM micrographs of 5 wt% HB-PNIPAM (90:1). The temperature range is as follows: (a) 15°C, (b) 18°C, (c) 21°C, (d) 24°C, (e) 27°C,

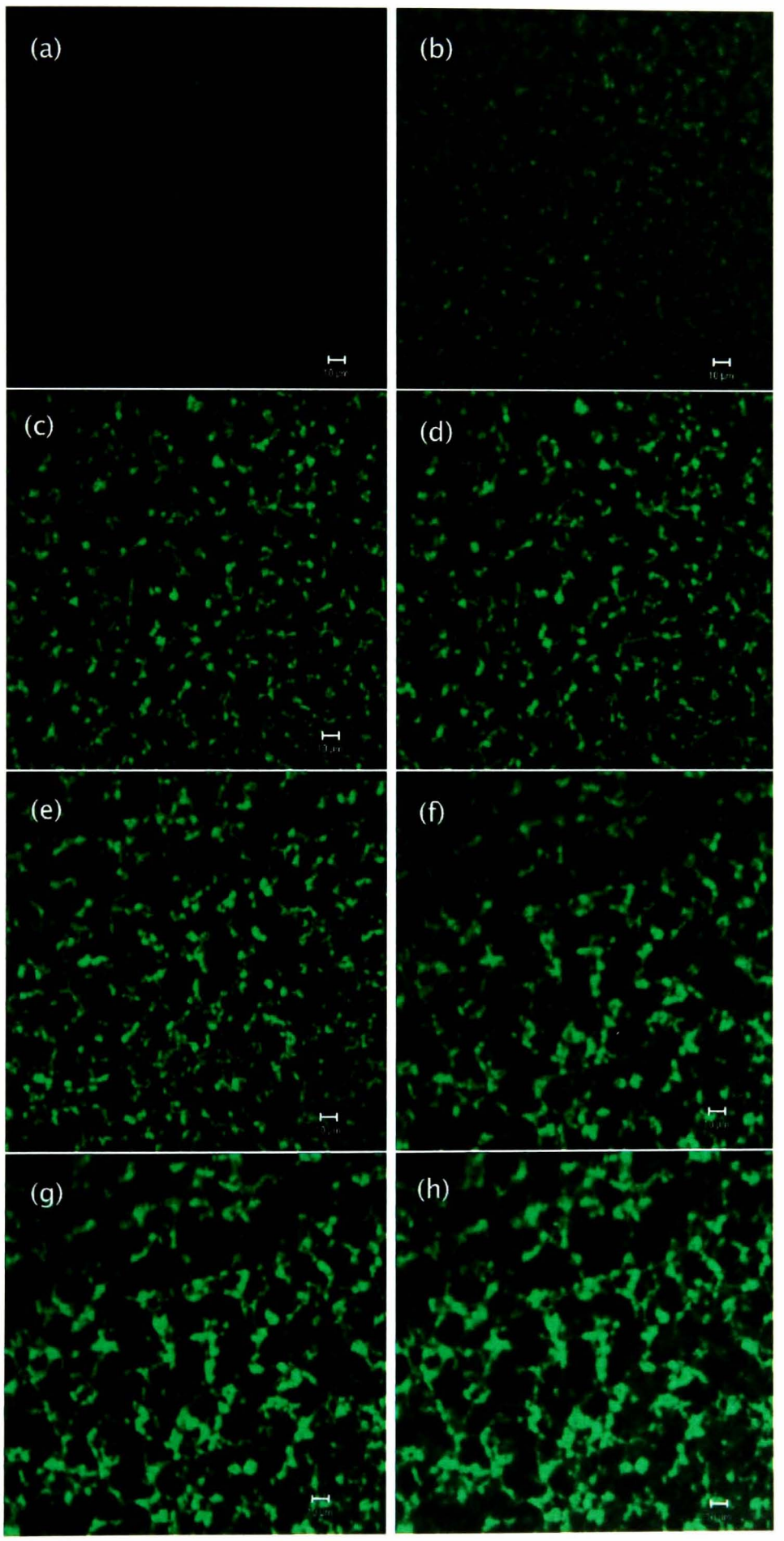

Figure 7.12: CLSM micrographs of 5 wt% of linear PNIPAM. The temperature range is as follows: (a) 15°C, (b) 18°C, (c) 21°C, (d) 24°C, (e) 27°C,

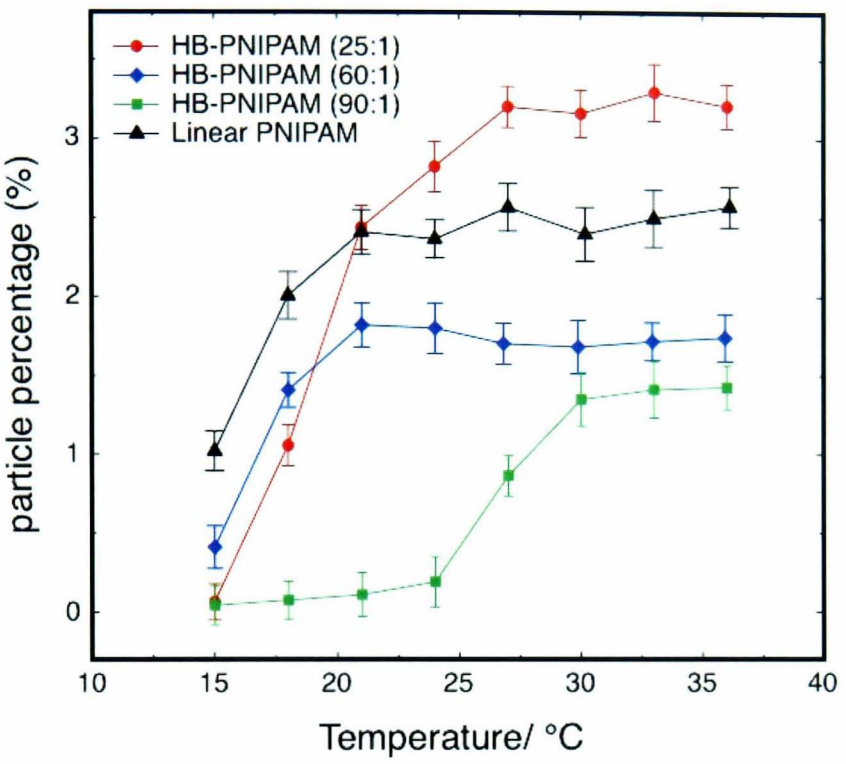

Figure 7.13: Percentage of PNIPAM particles as a function of temperature calculated from CLSM images (Figures 7.9, 7.10, 7.11 and 7.12).

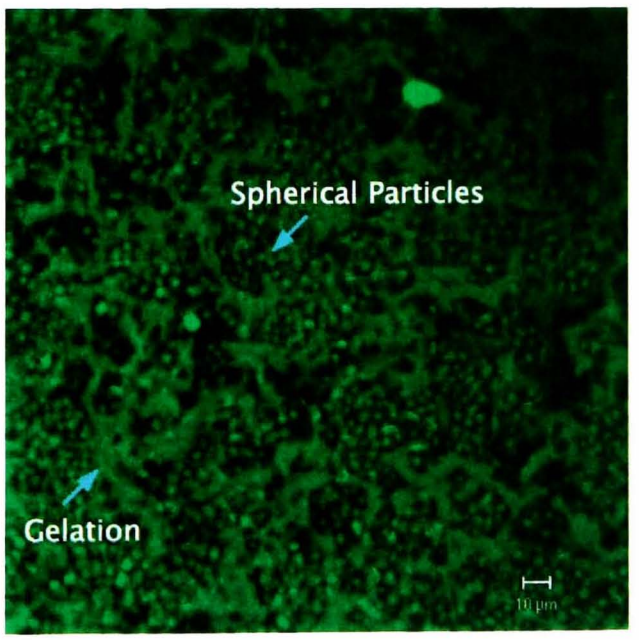

Figure 7.14: CLSM micrograph of 5 wt% of HB-PNIPAM (60:1) at a temperature (40°C) much higher than its LCST (24°C). This figure shows different regions of gels and spherical particles, indicated by the arrows.

LCSTs, showing a Porod scattering behaviour attributed to 3D spherical objects with sharp boundaries (slope of -4). However, scattering from linear PNIPAM slightly deviates from the slope of -4 due to the contribution to the scattering from entangled chains (network-like as seen in CLSM images, Figure 7.12). Interestingly, the change of conformation in HB-PNIPAMs starts immediately at the macroscopic LCST shown in Table 7.5; whereas the change to the Porod scattering behaviour was reached at a temperature much higher than the LCST of linear PNIPAM. This might be understood as the HB-PNIPAMs being more sensitive to temperature than their linear counterparts, due to the COOH end-groups in HB-PNIPAMs. This phenomenon was not observed in the work by Tanaka *et al.* [231] as the the highest temperature they used was only 1°C above the LCST of linear PNIPAM. However, the SANS intensity in Figure 7.19 (b) above the LCST continues to decay with a slope of -1 independently of temperature at high Q-values, indicating a one dimensional rod-like scattering behaviour from the internal structure of both linear and HB-PNIPAMs. This might be corresponding to the scattering from the backbone between branches in the case of HB-PNIPAM. This means that the branches and their COOH end-groups play a significant role in controlling the overall shape and size of HB-PNIPAMs, whereas the internal structure is similar to that of linear PNIPAM.

Another useful representation of scattering data can be obtained by plotting $I(Q)Q^2$ versus Q, which is known as a Kratky plot. A typical Kratky plot should asymptotically reach a plateau at high Q values. Figure 7.20 shows a typical Kratky plot of linear PNIPAM at different temperatures. Below the LCST of linear PNIPAM (32°C), the polymer is swollen (good solvent) forming a Gaussian chain, indicated by the plateau at high Q values of the Kratky plot. However, a deviation from the asymptotic behaviour can be seen at 36°C (above the LCST) when the D_2O becomes a poor solvent and the polymer collapses. The tail of the curve in this case follows an ascending line which if extrapolated towards $Q = 0$ passes through the origin. This is a characteristic of rod-like behaviour at the local structure or a local ordering of the polymer units at short ranges.

On the other hand, scattering from branched polymers is quite different

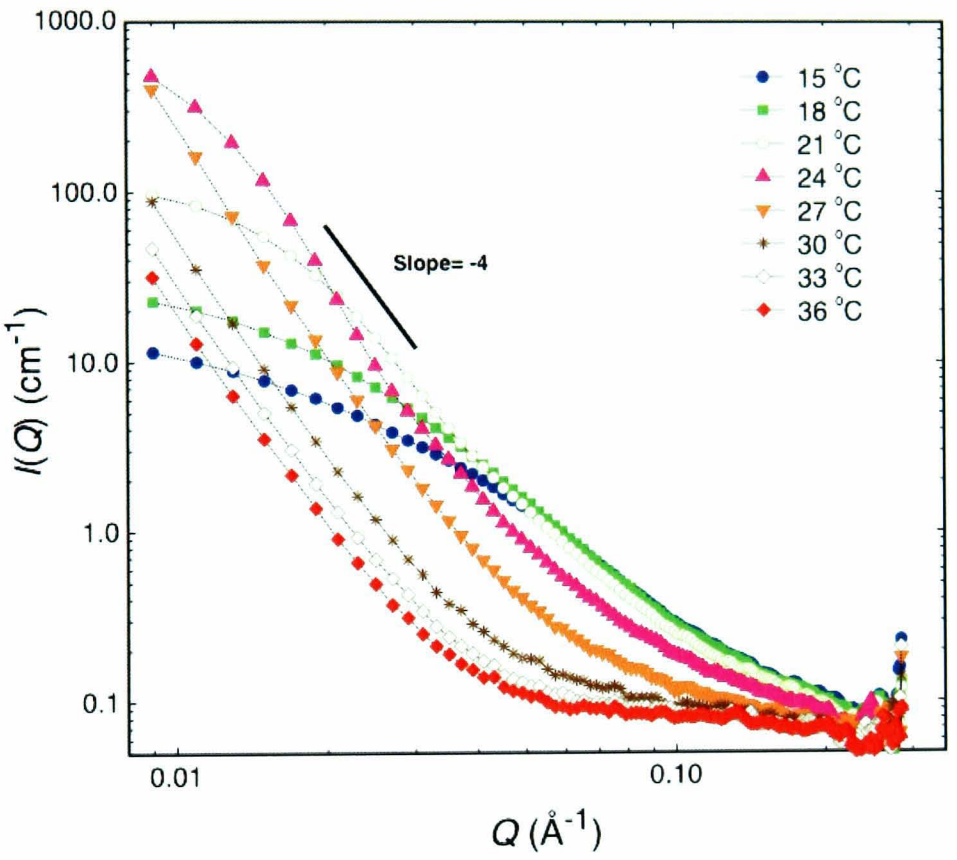

Figure 7.15: Log-log plot of SANS intensity versus the scattering vector for 5 wt% of HB-PNIPAM (25:1) in D_2O at temperatures below and above its LCST. The dashed lines are guides for the eye. This figure shows the transition from a swollen chain (Lorentzian scattering behaviour) to a shperical particle above the LCST (26°C) indicated by the slope of -4 (Porod scattering behaviour).

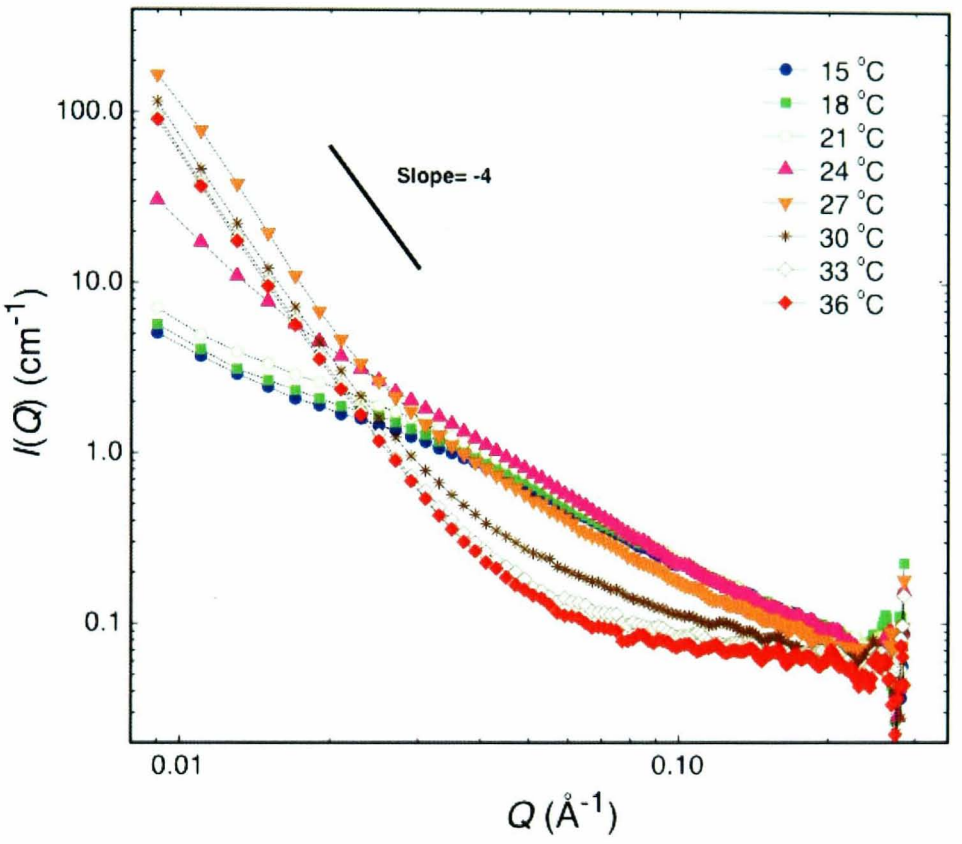

Figure 7.16: Log-log plot of SANS intensity versus the scattering vector for 5 wt% of HB-PNIPAM (60:1) in D_2O at temperatures below and above its LCST. The dashed lines are guides for the eye. This figure shows the transition from a swollen chain (Lorentzian scattering behaviour) to a shperical particle above the LCST (24°C) indicated by the slope of -4 (Porod scattering behaviour).

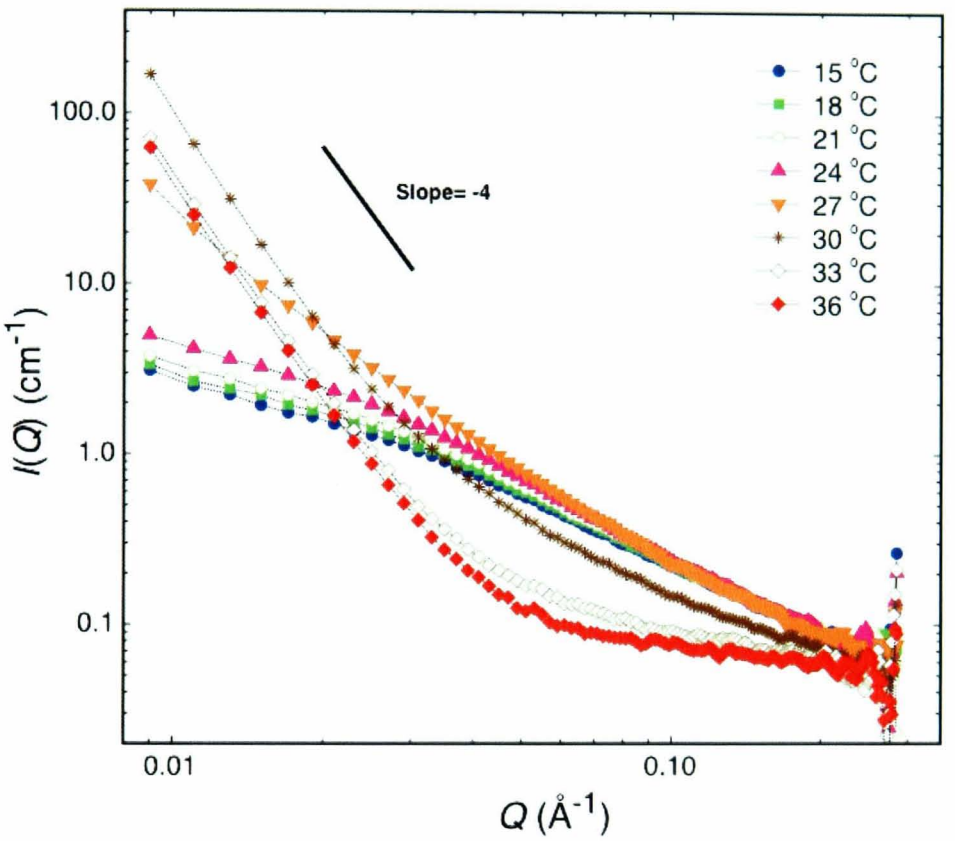

Figure 7.17: Log-log plot of SANS intensity versus the scattering vector for 5 wt% of HB-PNIPAM (90:1) in D_2O at temperatures below and above its LCST. The dashed lines are guides for the eye. This figure shows the transition from a swollen chain (Lorentzian scattering behaviour) to a shperical particle above the LCST (30°C) indicated by the slope of -4 (Porod scattering behaviour).

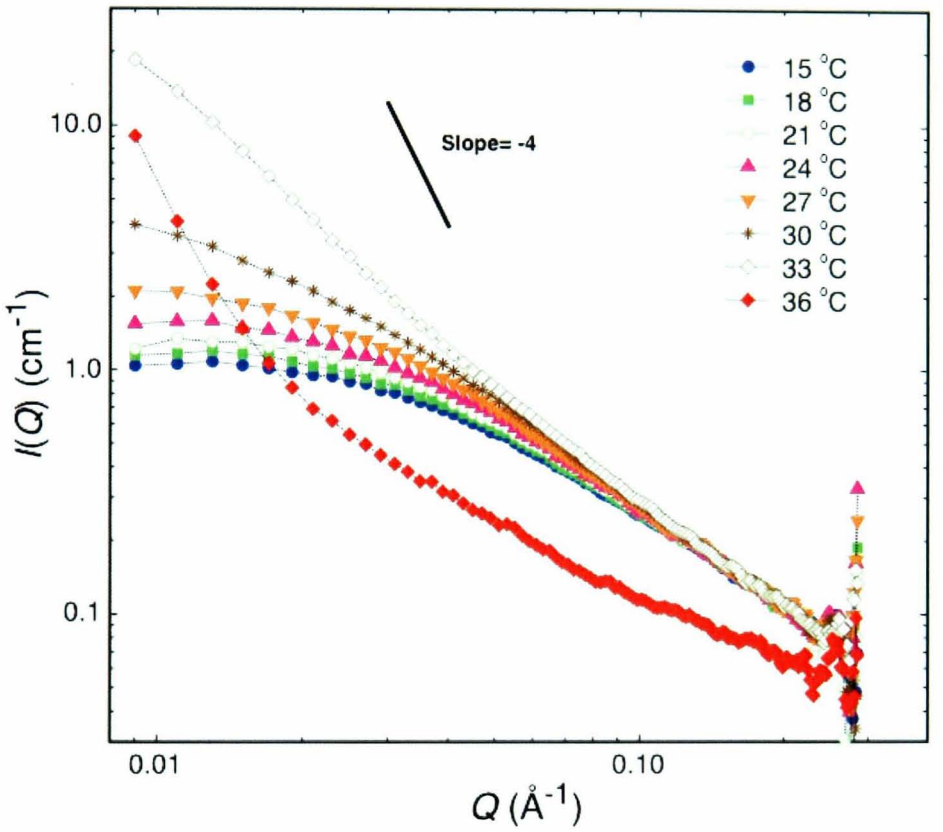

Figure 7.18: Log-log plot of SANS intensity versus the scattering vector for 5 wt% of linear PNIPAM in D_2O at temperatures below and above its LCST. The dashed lines are guides for the eye. This figure shows that linear PNIPAM is swollen below its LCST (32°C) (Lorentzian scattering behaviour) and does not form spherical particles above it, indicated by the slight deviation from Porod behaviour (slope of -4). It is rather a combination of Porod and Lorentzian scattering behaviour (see text).

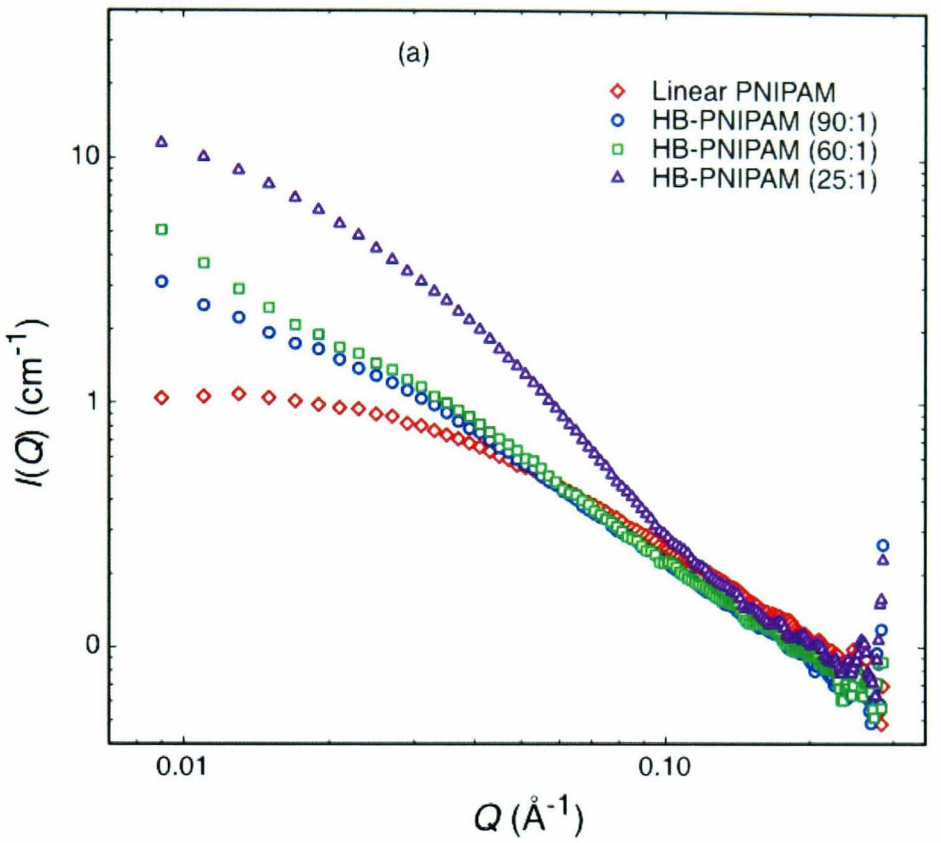

Figure 7.19: Log-log plot of SANS data showing a comparison between linear and HB-PNIPAM with different branching degrees at temperatures (a) below their LCSTs, 15 °C, and (b) above their LCSTs shown in table 7.5.

from that obtained from linear polymers. Figure 7.21 is a typical example of scattering from a branched polymer, which shows a Kratky plot of HB-PNIPAM (25:1), the highest branching degree in this study. These curves are different from that of linear PNIPAM in that, below the LCST, a peak is formed at low Q values which precedes the asymptote. These maxima in the Kratky plots indicate nonrandomly branched polymers in solution [232]. The magnitude of these peaks increases with increasing temperature with a shift towards low Q-region. These maxima disappear at temperatures above the LCST because the scattering at this low Q-range is representing the overall globular structure of the collapsed HB-PNIPAM. The behaviour of the tail of the curves at high Q values (local structural behaviour) in this case is similar to that of linear PNIPAM which shows a rod-like characteristic of the local structure (in this case the backbone between branches) above the LCST. A similar scattering behaviour was observed from lightly branched PNIPAM (60:1) and (90:1), shown in Figures 7.22 and 7.23, respectively, above their LCSTs. However, no peaks were observed below the LCST of these samples, which can be attributed to the dominated scattering by the backbone of the polymers given that there are considerable distances between branches.

7.3.2.2 Scattering Behaviour Below The LCST

Elastic scattering from polymer solutions in the semidilute regime can be described by a Lorentzian equation, Ornstein-Zrnike (OZ) equation, of the type:

$$I(Q) = \frac{I(0)}{(1 + \xi^2 Q^2)}, \tag{7.1}$$

where ξ is the blob size or the correlation length. This length scale is very important in the case of semidilute solutions, which is a distance at which neighbouring chains start to interact. Equation 7.1 allows the correlation length, ξ, to be determined from SANS in the case of semidilute theta solutions. From the discussion in the previous sections it is apparent that the scattering from linear and HB-PNIPAM below the LCST, when they are completely swollen in D_2O, is different from that above it, when they are col-

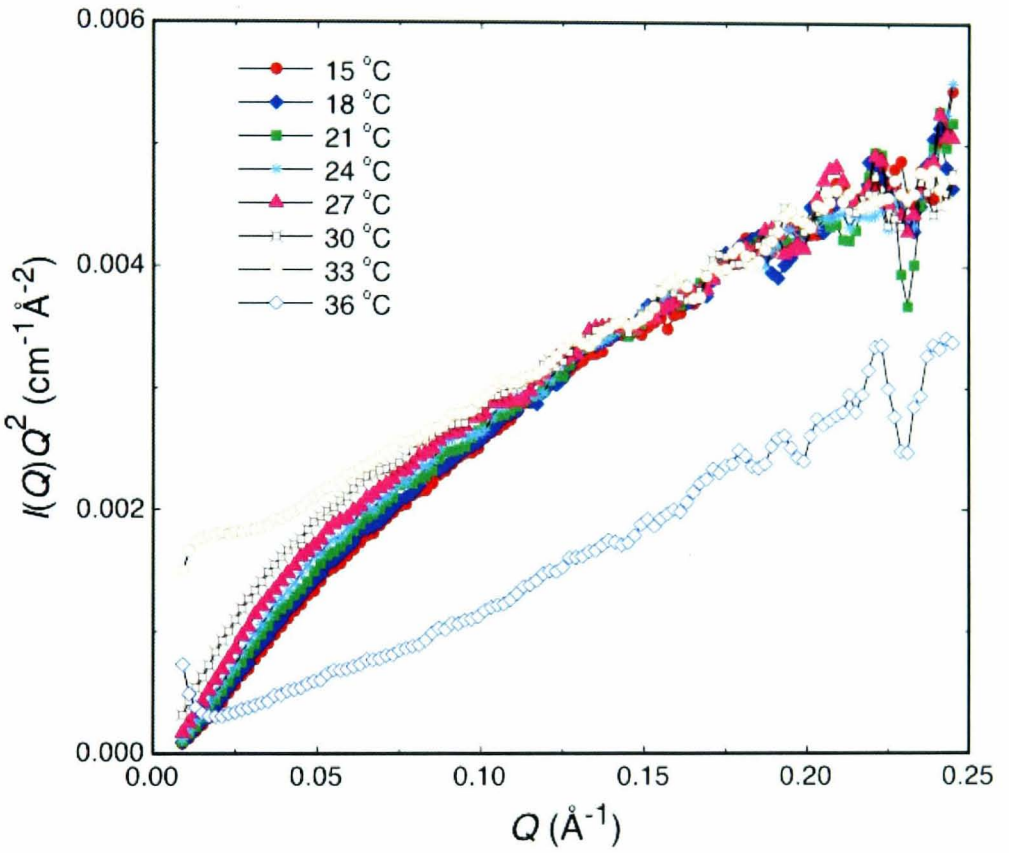

Figure 7.20: SANS scattering profiles represented as Kratky plots of 5 wt% Linear PNIPAM in D_2O. The solid lines are guides for the eye. This figure shows the linear increase of $I(Q)Q^2$ with Q until the LCST is reached above which a different structure is observed. This structure is a network-like structure (see sections 7.3.2.2 and 7.3.2.3).

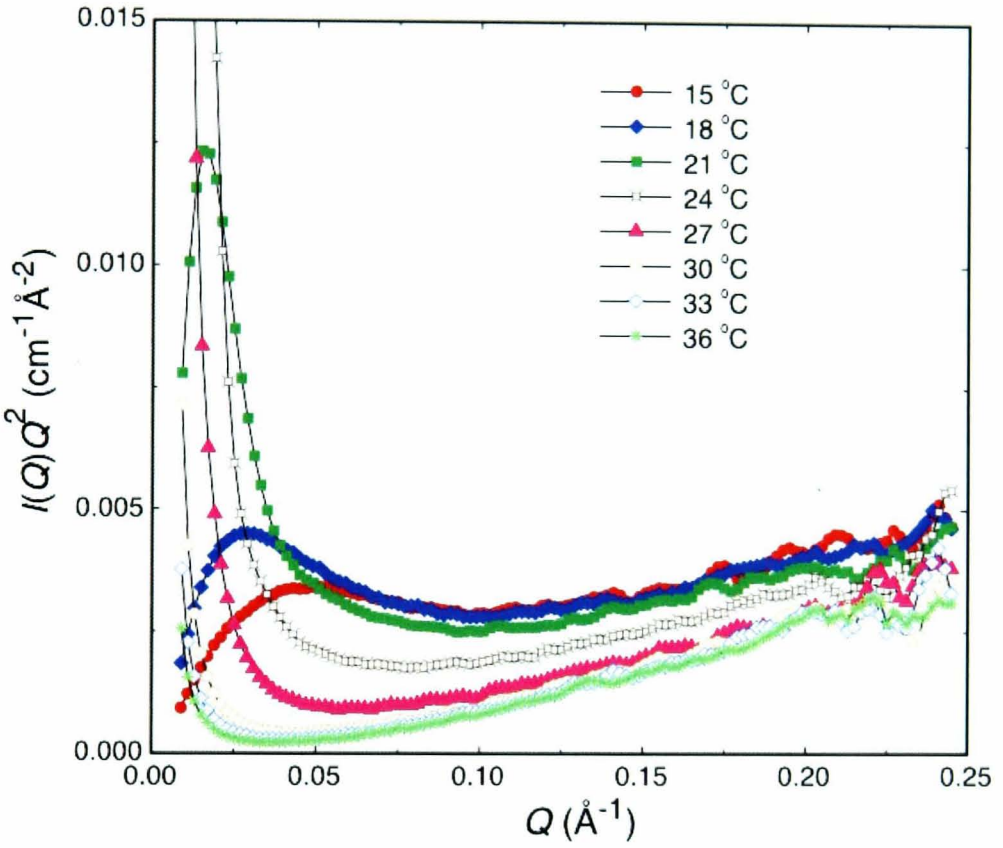

Figure 7.21: SANS scattering profiles represented as Kratky plots of 5 wt% HB-PNIPAM (25:1) in D_2O. The solid lines are guides for the eye. The peaks in this figure indicate a highly branched PNIPAM. These peaks increase with increasing temperature, because the number of branches increases per unit volume once the polymer collapses. Around the LCST of this polymer (26°C) the peaks disappear, indicating the scattering from the whole particle.

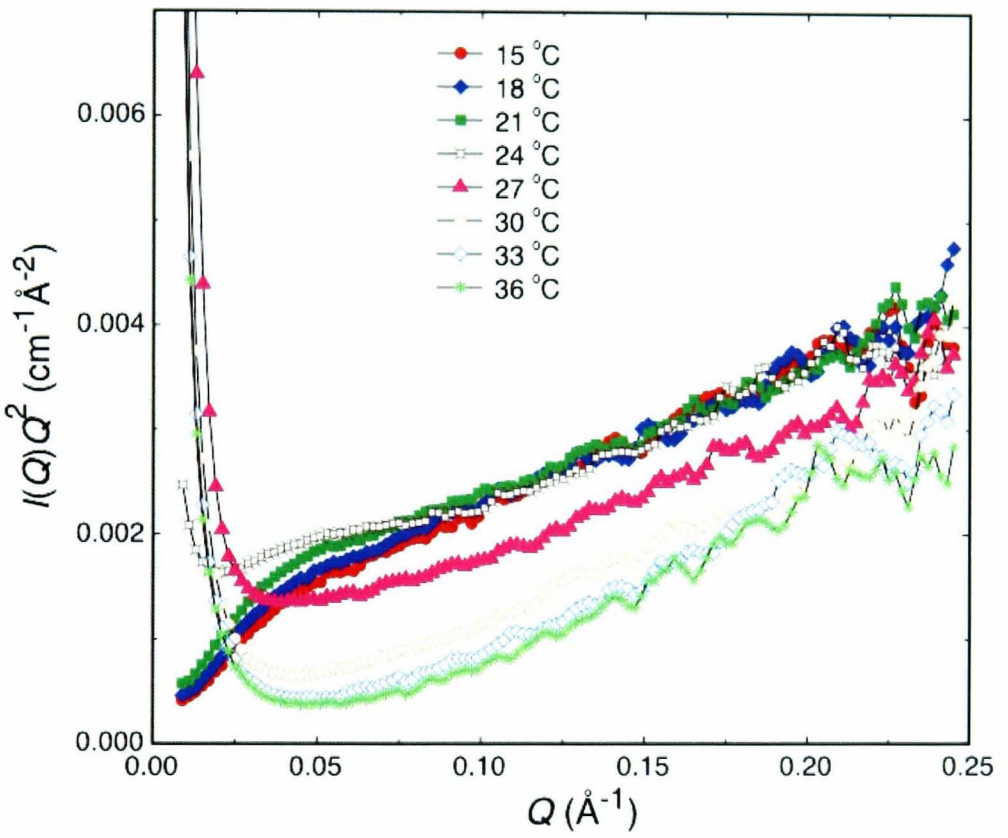

Figure 7.22: SANS scattering profiles represented as Kratky plots of 5 wt% HB-PNIPAM (60:1) in D_2O. The solid lines are guides for the eye. Although no peaks are present in this plot at low temperatures (similar to linear PNIPAM), the plot shows a scattering from the whole particle above the LCST. The reason why the peaks disappeared is because the length scale probed here is lower than the distance between branch points.

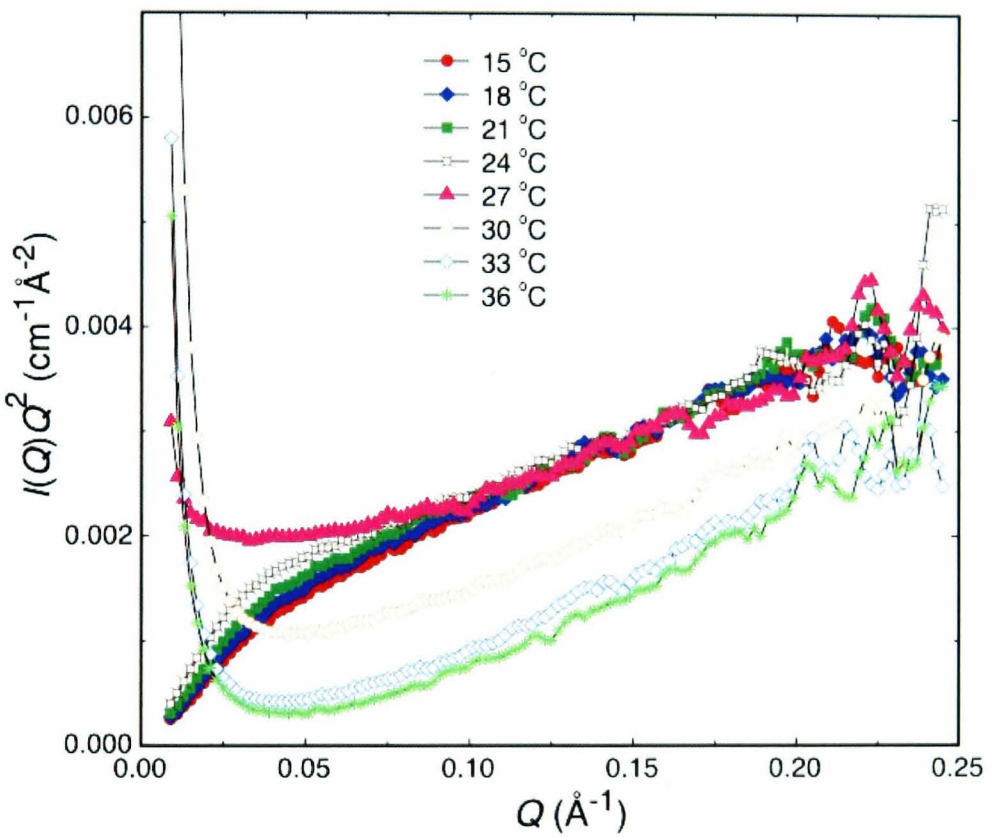

Figure 7.23: SANS scattering profiles represented as Kratky plots of 5 wt% HB-PNIPAM (90:1) in D_2O. The solid lines are guides for the eye. This plot shows a similar scattering behaviour as for HB-PNIPAM (60:1) in Figure 7.22 where the increase of the distance between branch point led to a scattering behaviour which, below the LCST, is similar to that of linear PNIPAM.

lapsed. The change of gradient of the scattering curves suggests scattering from molecules with different fractal dimensions, D_f, due to the change of polymer conformation as the temperature increases. In other words, the scattering intensity decays as a power law that is related to Q by $I(Q) \sim Q^{-D_f}$, where D_f is an exponent that correlates mass and size $M = R^{D_f}$, which according to Flory's theory is 5/3 for linear polymers and 2 for branched polymers in a good solvent [233, 40, 156]. In this case, polymer chains are represented as closely packed separated regimes of size ξ that are correlated to other regimes on different chains by the fractal dimension D_f. The scattering function in this case can be given as,

$$I(Q) = \frac{I(0)}{\left[1 + \frac{(1+D_f)(Q\xi)^2}{3}\right]^{D_f/2}}. \tag{7.2}$$

This equation is known as the generalized Ornstein-Zernike (OZ) equation which reduces to equation 7.1 if $D_f = 2$ in equation 7.2.

As shown in Figure 7.24, the scattering from linear PNIPAM below the LCST is described well by the general OZ equation with a fractal dimension $D_f = 5/3$ which does not change with increasing temperature until the LCST is reached. This fractal dimension is known to be valid for the case of extended linear polymer chains in a good solvent with excluded volume, according to Flory's theory. The correlation length (ξ) increases with increasing temperature which is an indication of the increase in swelling degree of the linear PNIPAM. In this case PNIPAM monomers are interacting only with neighbouring monomers on the same chain and the surrounding solvent molecules. Table 7.6 summerizes the obtained ξ values from fitting to the generalized OZ equation. Surprisingly, even above the LCST of linear PNIPAM, SANS data are described by the general OZ equation, but the fractal dimension increases to 1.9 and the correlation length increases significantly as well. This fractal dimension is known to be for a 2D network [156] and the correlation length in this case is the mesh size between the entangled PNIPAM linear chains. Therefore, it can be concluded that, at its transition temperature, linear PNIPAM forms a network-like structure which is

in agreement with the microscope images in Figure 7.12, despite the low resolution of CLSM.

Scattering from HB-PNIPAMs below their LCSTs can also be described by the generalized OZ model. Figures 7.25 (a), 7.26 (a) and 7.27 (a) show the fits to equation 7.2. Unlike the case of linear PNIPAM, the contribution of Lorentzian scattering disappears exactly at the macroscopic LCST of each polymer and the general OZ equation is no longer valid beyond these points. The fitting parameters of OZ equation for HB-PNIPAMs are shown in table 7.6. The fractal dimension, D_f, of the scattering from these hyperbranched polymers starts with a value of 2 at temperatures much below their LCSTs (15°C) which is in agreement with theoretical predictions for branched polymers in the semidilute regime in a good solvent [233]. Increasing the temperature leads to an increase in D_f, depending on the branching degree; the highly branched polymer showed a significant increase in D_f value at temperatures far below the LCST of this polymer. This can be explained by that D_2O is becoming a poor solvent with increasing temperature even below the macroscopic LCST. It can be noticed from table 7.6 that D_f reached a value of 4 at temperatures below the LCSTs of HB-PNIPAM (25:1) and (60:1), which means a change of conformation of the polymers to separated 3D spherical aggregates with no sharp boundries because the scattering here is still showing the Guinier regime described by a Lorentzian function. Again, CLSM images, in section 7.3.1, showed a similar transition from a randomly swollen chains to a spherical structures. However, this effect was not seen in the case of the lightly branched PNIPAM (90:1) below its LCST (below 30°C) and D_2O remains a good solvent up to a temperature close to the LCST. The correlation length values in table 7.6 show a decrese in ξ with temperature for all HB-PNIPAMs, confirming the gradual collapse of these polymers below their LCSTs.

7.3.2.3 Scattering Behaviour Above The LCST

Scattering from linear PNIPAM at 36°C (far above its LCST) in Figure 7.24 shows a different behaviour from that below its LCST, as described in the

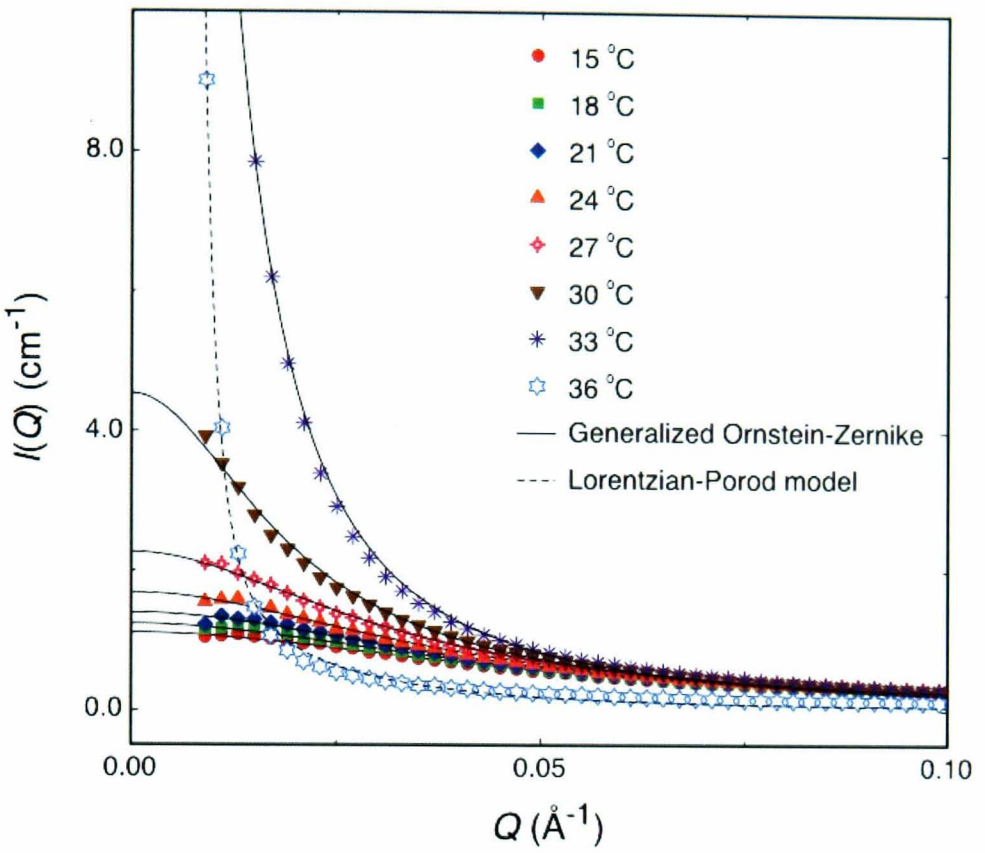

Figure 7.24: SANS intensity profiles of 5 wt% linear PNIPAM as a function of temperature. The data were fitted to the generalized OZ scattering function (equation 7.2) below the LCST (solid lines) and the combined Porod-Lorentzian scattering function (equation 7.3 above the LCST (dashed line).

	Linear		HB-(25:1)		HB-(60:1)		HB-(90:1)	
T /°C	D_f	ξ /Å	D_f	ξ /Å	D_f	ξ /Å	D_f	ξ /Å
15	1.66	23.3±2	2	63.9±1	2	110.4±2	2	108.5±3
18	1.66	24.9±3	2.7	48.4±2	2.5	103.8±1	2	94.3±5
21	1.66	26.9±1	4	45.9±1	2.7	100.4±1	2	88.6±2
24	1.66	30.4±2	4	25.1±5	4	80.5±3	2	86.7±4
27	1.66	37.0±4	...	...	...	...	2.5	76.1±6
30	1.66	59.9±3	...	...	...	...	...	...
33	1.9	256.1±2	...	...	...	...	...	...

Table 7.6: A summary of the parameters obtained by fitting SANS data for 5 wt% linear and HB-PNIPAMs to the generalized OZ (equation 7.2) below the LCST of these polymers.

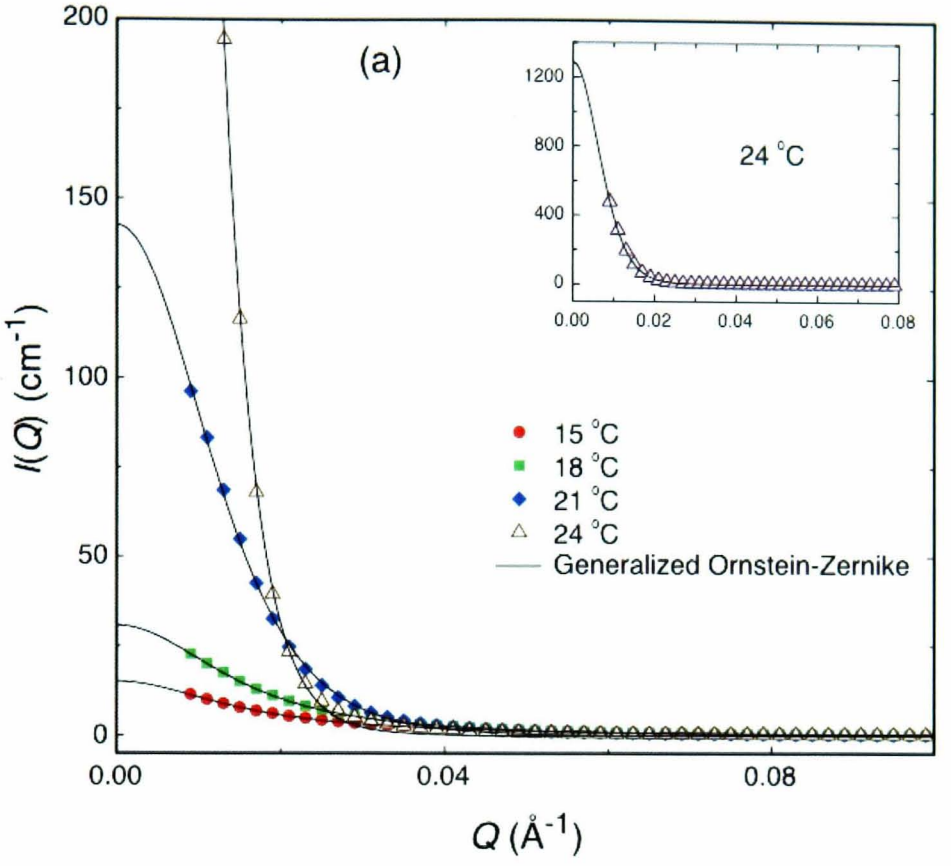

Figure 7.25: SANS intensity profiles of 5 wt% HB-PNIPAM (25:1) as a function of temperature. The data in figure (a), below the LCST, were fitted to the generalized OZ scattering function (equation 7.2); whereas figure (b) shows the fit to the Porod scattering function (equation 7.4) above the LCST.

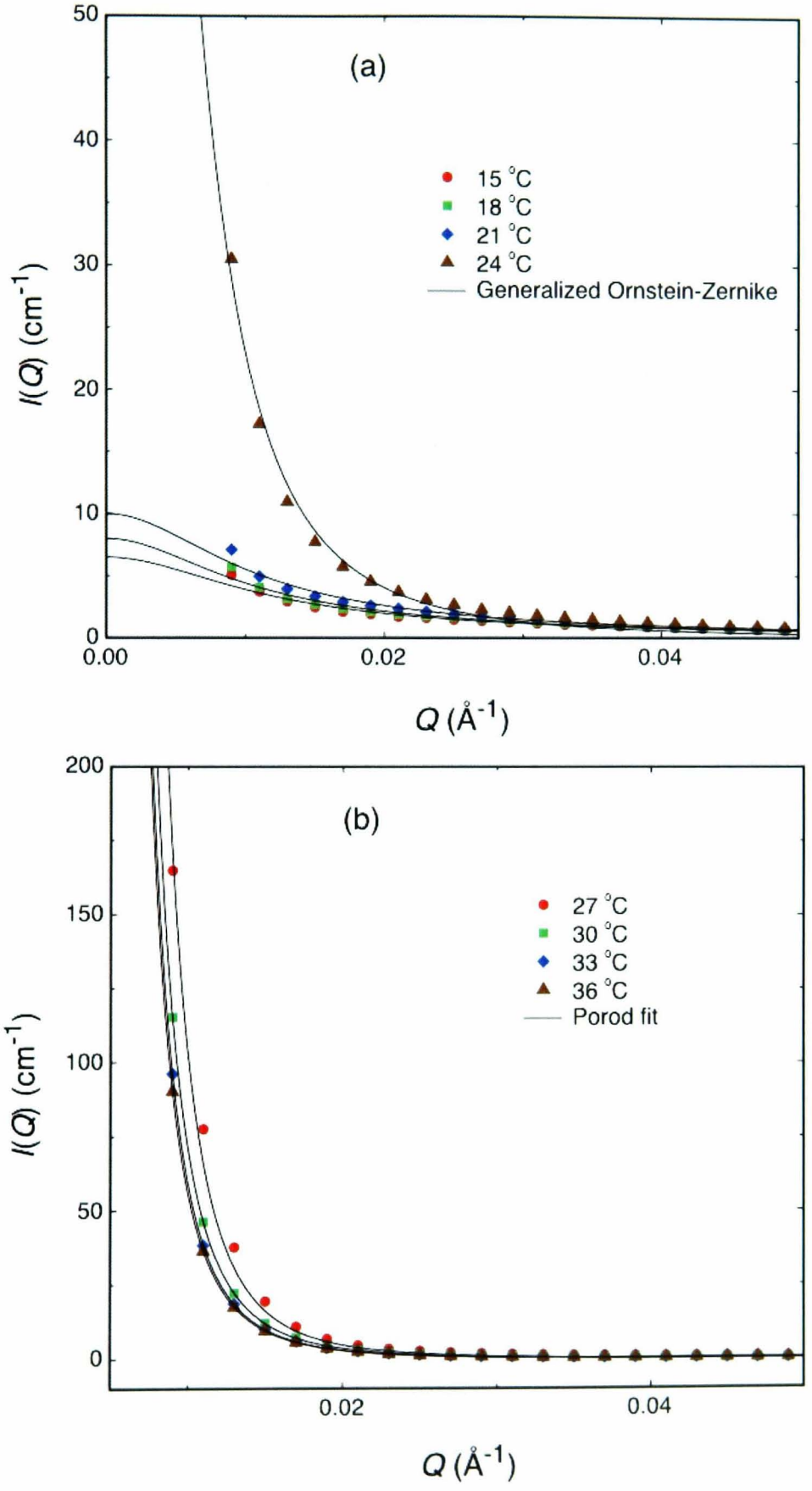

Figure 7.26: SANS intensity profiles of 5 wt% HB-PNIPAM (60:1) as a function of temperature. The data in figure (a), below the LCST, were fitted to the generalized OZ scattering function (equation 7.2); whereas figure (b) shows the fit to the Porod scattering function (equation 7.4) above the LCST.

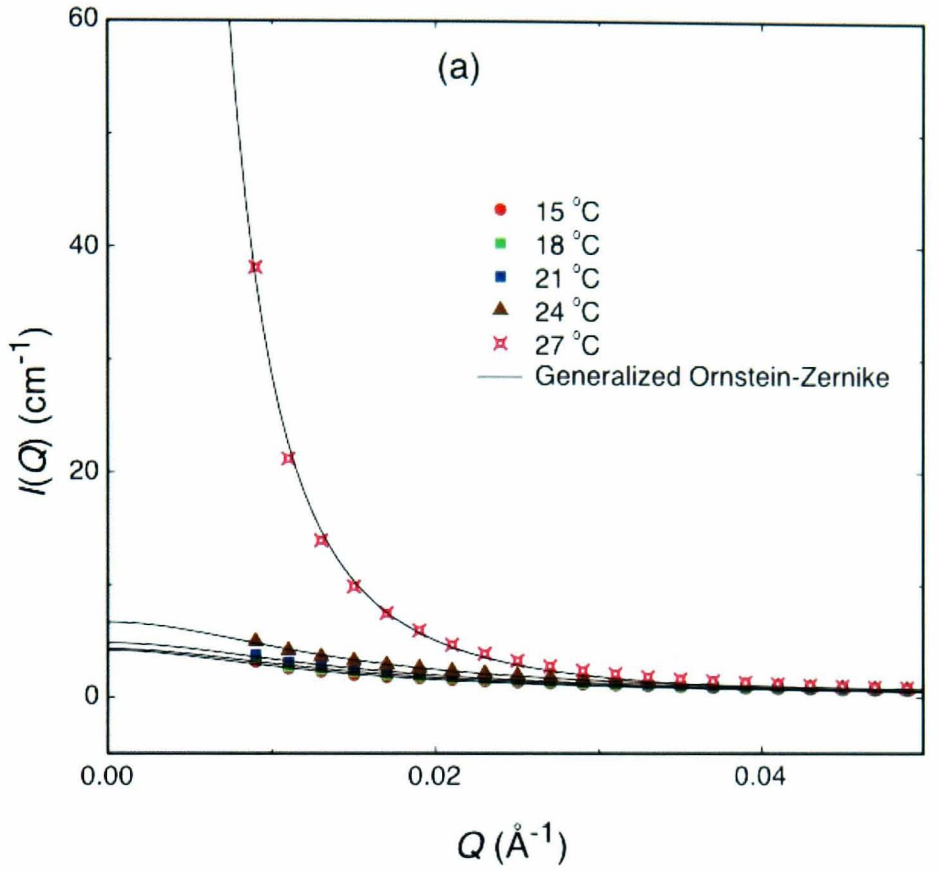

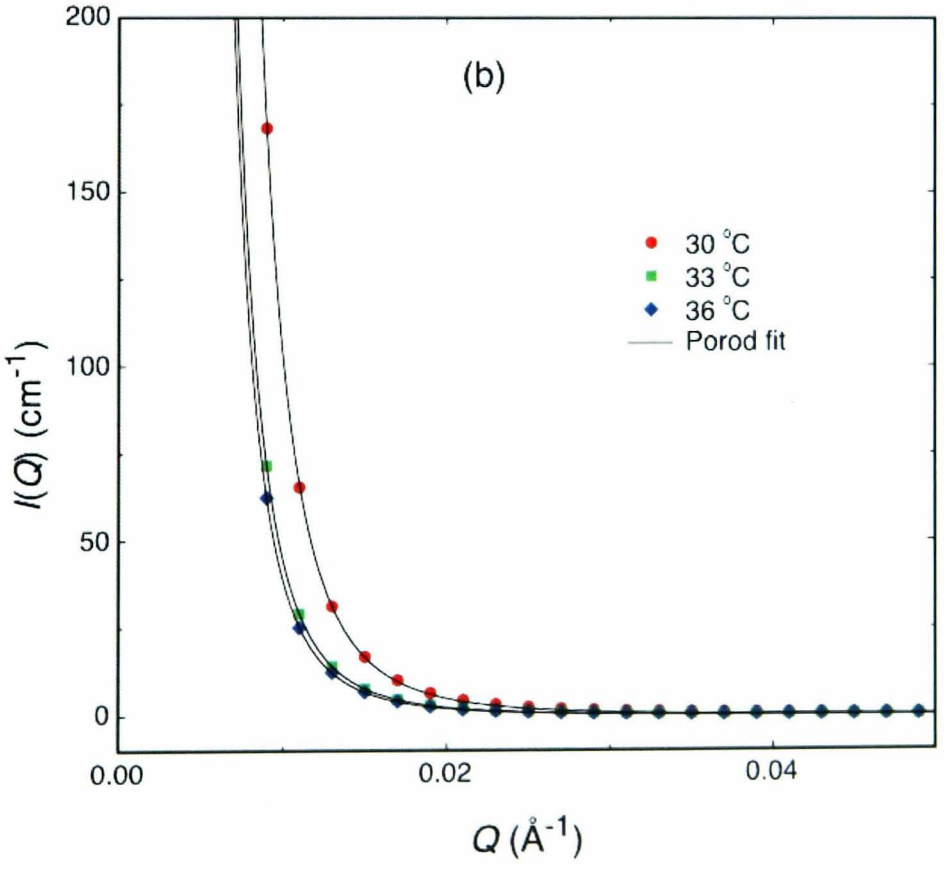

Figure 7.27: SANS intensity profiles of 5 wt% HB-PNIPAM (90:1) as a function of temperature. The data in figure (a), below the LCST, were fitted to the generalized OZ scattering function (equation 7.2); whereas figure (b) shows the fit to the Porod scattering function (equation 7.4) above the LCST.

	Linear	HB-(25:1)	HB-(60:1)	HB-(90:1)
T /°C	r_0 /nm	r_0 /nm	r_0 /nm	r_0 /nm
27	...	14.4±1.0	13.5±0.6	...
30	...	16.2±0.5	16.8±0.8	15.7±1.2
33	...	18.5±0.9	16.6±1.1	18.6±0.9
36	127±4.0	19.7±1.0	17.3±0.7	17.9±1.1

Table 7.7: A summary of the particle size obtained by fitting SANS data for 5 wt% linear and HB-PNIPAMs above their LCST to the (i) the combined Porod-Lorentzian function (equation 7.3) in the case of linear PNIPAM and (ii) the pure Porod scattering function (equation 7.4) in the case of HB-PNIPAMs.

previous section. The gradient of the intensity in this case, as shown in the log-log plot in Figure 7.18, indicates a behaviour close to Porod's regime (slope $\approx$ -4). The deviation from Porod's behaviour is attributed to the contribution of Lorentzian scattering resulting from the slightly solvated and entangled polymer chains. SANS data in this case can be described by a model that combines Porod and Lorentzian scattering, given by:

$$I(Q) = \frac{K}{Q^4 r_0}\left(1 + \frac{1}{Q^2 r_0^2}\right) + \frac{I(0)}{1 + \xi^2 Q^2}, \tag{7.3}$$

where r_0 is the particle radius and $K = 6\pi\phi_{\mathrm{p}} \left(\triangle\rho\right)^2$ is a constant with ϕ_{p} being the volume fraction of particles. The first term in equation 7.3 is corresponding to Porod scattering behaviour for the scattering from the whole particle, from which the shape and size of the polymer can be obtained. The second term in this equation is the Lorentzian scattering contribution from the internal structure of the polymer, from which the interactions with other chains can be determined (the correlation length). The fitted SANS data for linear PNIPAM at 36°C in Figure 7.24 shows that collapsed linear PNIPAM can be described well by the Porod-Lorentzian model (equation 7.3), giving a particle radius r_0 = 127 nm (see table 7.7). The correlation length from the fitting in this case droped from 256.1±2 Å at 33°C to 69±3 Å. A similar behaviour to the scattering from linear PNIPAM above 32°C was observed in the case of collapsed microgels, where cross-links are introduced between linear PNIPAM chains, for which SANS data were fitted to equation 7.3 [234].

This scattering behaviour of linear PNIPAM above its LCST is attributed to the entanglements formed when the polymer collapses with increasing temperature. CLSM images, shown in section 7.3.1, confirm the formation of a network-like structure above the LCST of linear PNIPAM.

On the other hand, scattering from HB-PNIPAMs at and above their LCSTs showed, on double logarithmic plots (Figures 7.15, 7.16 and 7.17). a gradient of exactly -4, indicating a pure Porod scattering behaviour from single spherical particles with sharp boundries. Therefore, the second term in equation 7.3 can be ignored and the scattering in this case can be described by Porod scattering function given as:

$$I(Q) = \frac{K}{Q^4 r_0} \left(1 + \frac{1}{Q^2 r_0^2}\right). \tag{7.4}$$

The fits in Figures 7.25 (b), 7.26 (b) and 7.27 (b) to equation 7.4 demonstrate that all HB-PNIPAMs are well described by a Porod scattering function above their LCSTs, with particle sizes that increase with increasing temperature (see table 7.7). This increase in particle size is expected for colloidal particles formed by aggregation. However, particle size seems to be independent of the degree of branching as all HB-PNIPAMs in this study showed, within errors, similar average particle radii (between 13.5 nm and 19.7 nm) depending on temperature. Again, this scattering behaviour agrees with CLMS images in section 7.3.1 where HB-PNIPAM showed a transition from a completely swollen to spherical structures, despite the lack of resolution in CLSM images.

7.3.2.4 Concentration Effect

Macroscopic measurements of the LCST shown in table 7.5 indicate a similarity of the cloud points at 5 wt% and 10 wt% (it is equal in the case of linear PNIPAM and there is a difference of 1°C for HB-PNIPAMs except for (90:1)). In this section, SANS measurements at 10 wt% of linear and HB-PNIPAMs are compared to the that at 5 wt% presented in the previous section. The scattering behaviour from linear PNIPAM is not affected by increasing the concentration from 5 wt% to 10 wt%. Figure 7.28 shows fits

	Linear		HB-(25:1)		HB-(60:1)		HB-(90:1)	
T /°C	D_f	ξ /Å	D_f	ξ /Å	D_f	ξ /Å	D_f	ξ Å
15	1.66	18.9±1	3.2	50.9±3	3.5	104.5±3	2	120±1
18	1.66	20±3	3.8	40.9±4	3.8	85.6±2	2	94.6±54
25	1.66	27±2	4	23.1±1	...	...	...	...
30	1.66	50±2	...	...	...	...	...	...

Table 7.8: A summary of the parameters obtained by fitting SANS data for 10 wt% linear and HB-PNIPAMs to the generalized OZ (equation 7.2) below their LCST of these polymers.

to the general OZ equation with a fractal dimension of 1.66 at all temperatures $\leq$ 30°C. It can be noticed from the fitting parameters in table 7.8 that the correlation length decreases with increasing concentration, which is expected as polymer chains become closer to each other. However, whether increasing concentration affects the entanglement of these linear polymers at higher temperatures needs further investigation (see Future Work in Chapter 9).

Likewise, scattering from 10 wt% HB-PNIPAM gives a similar behaviour to that at a lower concentration, as described in section 7.3.2.2. Figures 7.29, 7.30 and 7.31 show fitted SANS data of HB-PNIPAMs with different branching degrees at 10 wt%. These data are fitted to the generalized OZ model below the LCST and to Porod scattering function around the LCST. The fitting parameters are summarized in tables 7.8 and 7.9. It is clear from these values that both the correlation length and the particle size decrease with increasing concentration. The fractal dimension, D_f, increases with increasing concentration below the LCST of HB-PNIPAMs (25:1) and (60:1) indicating that the quality of D_2O as a solvent for HB-PNIPAMs changes with concentration, which might affect the internal structure of these polymers but not the overall shape and size. It is also worth mentioning that scattering from HB-PNIPAMs at high concentrations indicates scattering from separated spherical particles with sharp boundaries. Therefore, and despite the fact that there are few concentration data points, it can be concluded that HB-PNIPAM chains do not entangle with increasing temperature even at concentrations as high as 10 wt%.

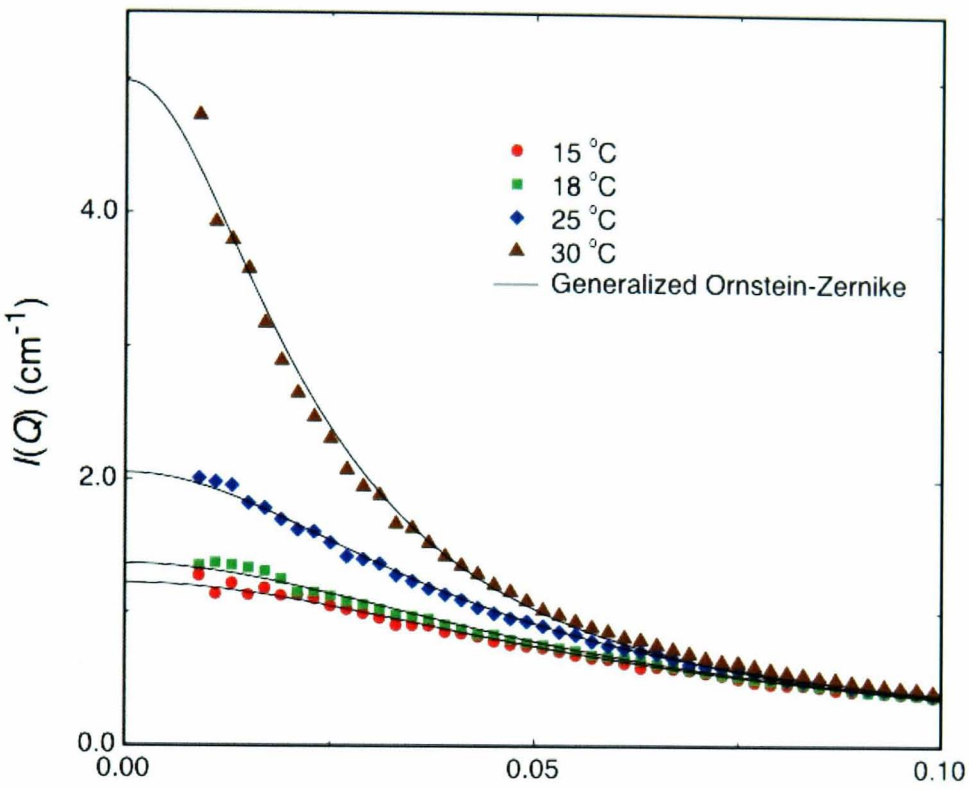

Figure 7.28: SANS intensity profiles of 10 wt% linear PNIPAM as a function of temperature. The data were fitted to the generalized OZ scattering function (equation 7.2) below the LCST (solid lines).

	HB-(25:1)	HB-(60:1)	HB-(90:1)
T /°C	r_0 /nm	r_0 /nm	r_0 /nm
25	...	12.3±0.6	13.5±0.8
30	14.3±0.5	13.1±0.8	14.1±1.0

Table 7.9: A summary of the particle size obtained by fitting SANS data for 10 wt% HB-PNIPAMs above their LCST to the (i) the combined Porod-Lorentzian function (equation 7.3) in the case of linear PNIPAM and (ii) the pure Porod scattering function (equation 7.4) in the case of HB-PNIPAMs.

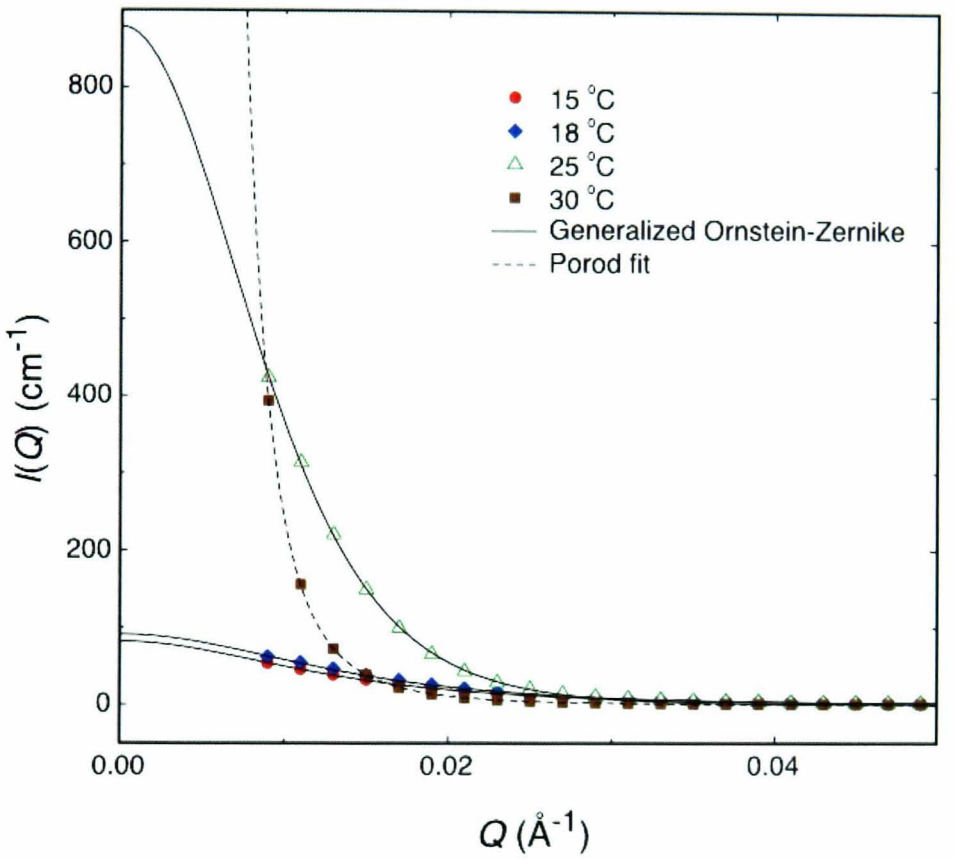

Figure 7.29: SANS intensity profiles of 10 wt% HB-PNIPAM (25:1) as a function of temperature. The data in this figure, below the LCST, were fitted to the generalized OZ scattering function (equation 7.2); whereas the dashed line is a fit to the Porod scattering function (equation 7.4) above the LCST.

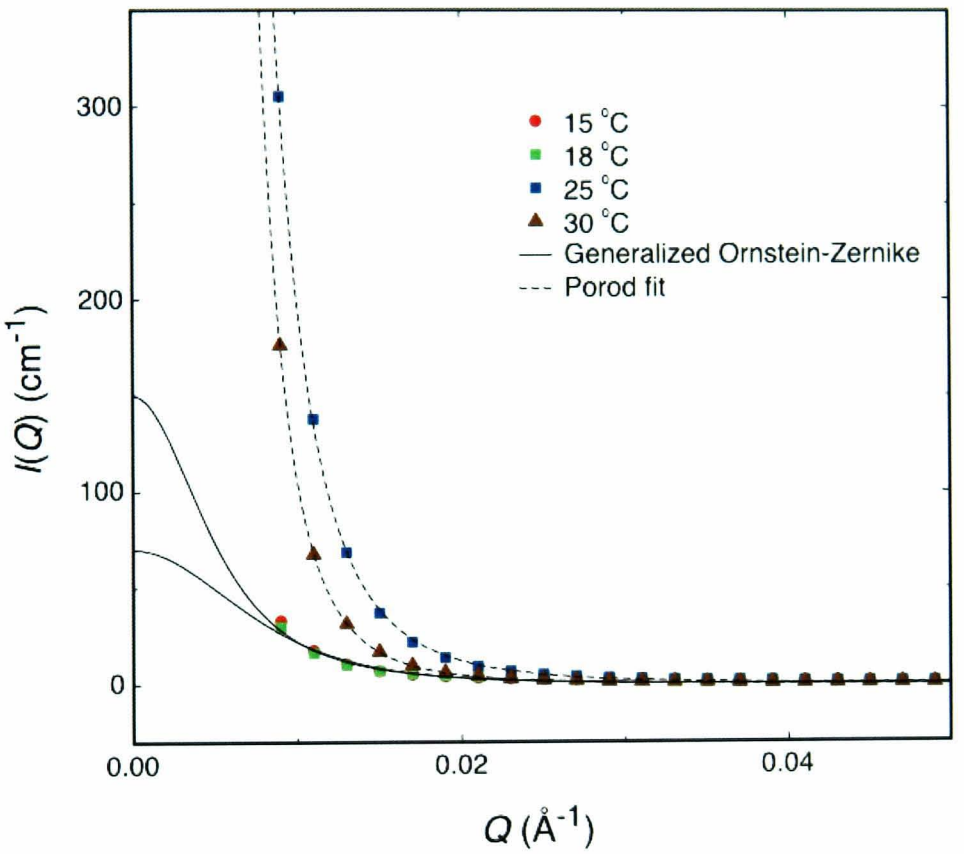

Figure 7.30: SANS intensity profiles of 10 wt% HB-PNIPAM (60:1) as a function of temperature. The data in this figure, below the LCST, were fitted to the generalized OZ scattering function (equation 7.2); whereas the dashed line is a fit to the Porod scattering function (equation 7.4) above the LCST.

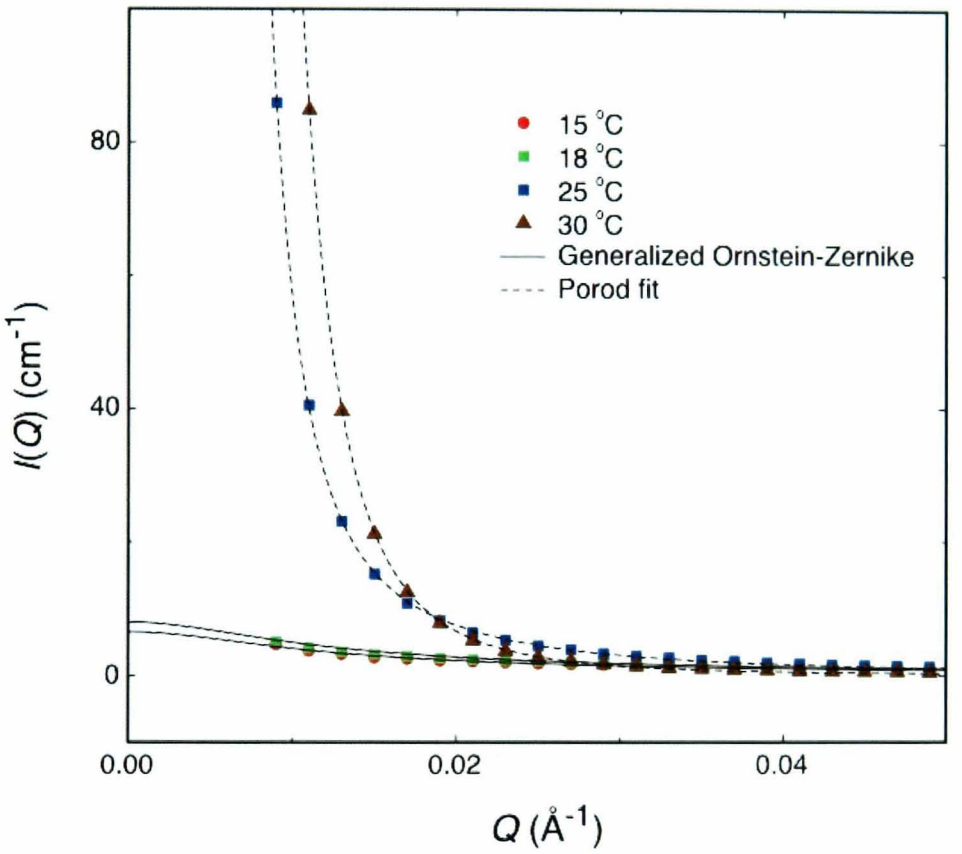

Figure 7.31: SANS intensity profiles of 10 wt% HB-PNIPAM (90:1) as a function of temperature. The data in this figure, below the LCST, were fitted to the generalized OZ scattering function (equation 7.2); whereas the dashed line is a fit to the Porod scattering function (equation 7.4) above the LCST.

7.4 Conclusions

The work presented in this chapter describes the structural behaviour of hyperbranched PNIPAM with different branching degrees: (25:1), (60:1) and (90:1) compared to their linear counterparts using small-angle neutron scattering (SANS). SANS results show that both linear and HB-PNIPAMs are completely swollen at very low temperatures (e.g. 15°C) and the scattering from these polymers in this case can be described by a Lorentzian scattering model known as the generalized Ornstein-Zernike (OZ). Both linear and HB-PNIPAMs showed a good fit to this model giving correlation lengths dependent on both temperature and concentration. The fractal dimension is also a parameter in this model, describing the conformational behaviour as a function of temperature. However, at temperatures above the LCST of each polymer, the OZ model failed to describe the scattering behaviour. Therefore, and according to the gradient of the scattering intensities (= -4), Porod scattering behaviour was applied, indicating the formation of separated spherical particles with sharp boundaries that are not entangled with other aggregated colloidal particles. In contrast, scattering from linear PNIPAM above the LCST is not purely Porod scattering and therefore an addition of a Lorentzian scattering was used to describe their behaviour above the LCST. This can be explained by linear PNIPAM forming a network-like structure at high temperatures due to entanglements between interacting PNIPAM chains.

These polymers were also studied by CLSM and the images obtained are in good agreement with SANS results. These images illustrated the transition from extended HB-PNIPAM chains at low temperatures to form spherical structures at and above the LCST. CLSM showed linear PNIPAM to have a network-like structure, compared to the spheres in the case of HB-PNIPAMs, despite the lack of resolution. Basic characterisations of such polymers using techniques like NMR and GPC were also considered. The macroscopic cloud point (LCST) was determined using UV-visible spectrometer.

Chapter 8

Dynamics of Hyperbranched PNIPAM

8.1 Introduction

The previous chapter covered the structural behaviour of HB-PNIPAM as a function of temperature compared to its linear counterpart using SANS. This study showed that HB-PNIPAM gradually collapses with increasing temperature until it forms spherical particles above the LCST. These spherical particles were observed to have sharp boundaries with a particle radius between 12.3 and 19.7 nm depending on branching degree. These findings indicate that HB-PNIPAM shows no entanglements at these length scales. However, the internal dynamics of these systems is worth testing in order to judge the behaviour of the entire system. In other words, self-entanglement is another point of interest, which is important for the stability and functionality of HB-PNIPAM in applications such as drug delivery systems.

Polymer dynamics in general is very complicated due to the fact that different molecular motions take place on different length scales governed by the general chain properties and the chemical structure of monomers [39, 44]. The first and simplest theoretical approach to address such dynamics was started by Langevin as an alternative to Brownian theory. However, the first successful model to describe molecular motion was developed by Rouse, who

introduced the entropic effect between monomers (beads). This was followed by the Zimm theory which takes into account the hydrodynamic interactions between monomers and the surrounding solvent [40, 39, 44]. These theories were described in detail in Chapter 2, section 2.5.

In this chapter, the internal dynamics of deuterated HB-PNIPAM (D_7-HB-PNIPAM) is investigated using neutron spin echo (NSE). These dynamical results complement the structural behaviour of these polymers as obtained by SANS in Chapter 7. In addition, self-diffusion of fluorescently labelled linear and HB-PNIPAM is studied using FCS.

8.2 Experimental

8.2.1 Synthesis of D_7-HB-PNIPAM

Deuterated NIPAM (D_7-NIPAM) was used to prepare three deuterated HB-PNIPAM samples with the same branching degree as the non-deuterated samples used in Chapter 7: these are (25:1), (60:1) and (90:1). The reason behind using deuterated monomers is to give a better contrast for neutron spin echo experiments to study the dynamics of these branched polymers. D_7-HB-PNIPAM was prepared in a similar way to that described in Chapter 7, section 7.2.2. The quantities used to prepare these polymers are shown in table 8.1. The conversion method to COOH acid end-groups that was used in Chapter 7, section 7.2.2, has been employed here as well, with the quantities shown in table 8.2.

8.2.2 NMR Characterisation

NMR spectra (see appendix C) of D_7-HB-PNIPAM were obtained using the method described in the previous chapter, section 7.2.3. NMR spectra were used to calculate the ratio of D_7-NIPAM to imidazole (the branching degree) and the calculated ratios are shown in table 8.3.

NIPAM/ RAFT Ratio	D7- NIPAM (g)	RAFT agent (g)	AIBN (g)	Dioxane (ml)	Yield
(25:1)	1.1085 g 9.222 mmol	0.0956 g 0.369 mmol	0.0597 g 0.369 mmol	3.9 ml	80% 1.0121 g
(60:1)	1.039 g 8.644 mmol	0.0373 g 0.144 mmol	0.0234 g 0.144 mmol	3.6 ml	84% 0.9080 g
(90:1)	1.1417 g 9.498 mmol	0.0273 g 0.106 mmol	0.0171 g 0.106 mmol	4.0 ml	82% 1.1021 g

Table 8.1: Quantities used to synthesize D_7-HB-PNIPAM.

NIPAM/RAFT Ratio	DMF to dissolve the polymer	4,4'-azobis-(4-cyanopen-tanoic acid)	DMF to dissolve the acid	Yield
D_7-HB-PNIPAm (25:1)	47 ml	3.204 g	9 ml	52% 0.658 g
D_7-HB-PNIPAm (60:1)	42 ml	2.892 g	8 ml	91% 1.002 g
D_7-HB-PNIPAm (90:1)	47 ml	3.232 g	9 ml	85% 1.013 g

Table 8.2: Quantities used to convert N-pyrrole dithioate chain end groups to carboxylic acid in D_7-HB-PNIPAM.

Ratio NIPAM/RAFT (in Feed)	Ratio NIPAM/RAFT (NMR)	
D_7-(25:1)	(21:1)	δ 6-8.5 end-groups evident
D_7-(60:1)	(57:1)	δ 6-8.5 end-groups evident
D_7-(90:1)	(75-80:1) Level of accuracy	δ 6-8.5 end-groups evident

Table 8.3: Branching degrees after conversion of N-pyrroledithioate chain-ended highly-branched polymers (D7-HB-PNIPAM) to carboxylic-acid chain-end functionalized polymers.

Description	DMF (0.1% ammonium acetone)			THF (0.1% TBAB)			
	Mw	Mn	PD	Mw	Mn	PD	Rgw
D_7-(25:1)	53460	3987	13.4	366630	21846	16.8	9.78
D_7-(60:1)	97556	7355	13.2	166171	57549	2.9	8.38
D_7-(90:1)	66566	7042	9.5	189837	47711	4.0	6.21

Table 8.4: GPC data for D_7-HB-PNIPAMs using single (DMF (0.1% ammonium acetone)) and triple (THF(0.1%TBAB)) detection GPC systems at 70°C.

8.2.3 Gel Permeation Chromatography (GPC)

Single and triple detection GPC methods like those described in Chapter 7, section 7.2.4 were used to obtain the average molecular weight, molecular weight distributions and polydispersity of D7-HB-PNIPAM. Figures 8.1 and 8.2 show size exclusion chromatography (SEC) molecular weight distributions of D7-HB-PNIPAM with different branching degrees, (25:1), (60:1) and (90:1). The obtained molecular weight and polydispersity values of these samples are listed in table 8.4.

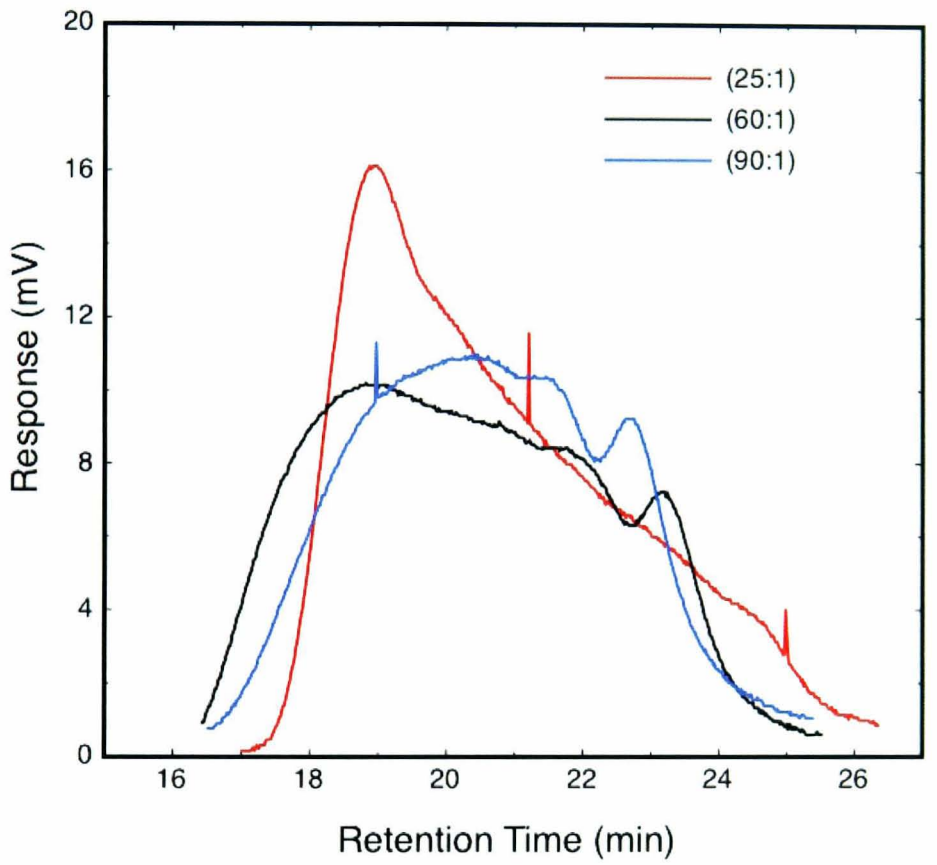

Figure 8.1: Typical SEC chromatograms for hyperbranched D_7-HB-PNIPAM with different branching degrees (25:1, 60:1 and 90:1) using a single detection GPC system. The broad and multiple peaks indicate branched polymers of PNIPAM. It is clear that the single detection GPC method underestimates the average molecular weight of the highest branched PNIPAM, where a single and narrow peak was observed. The average molecular weights are listed in table 8.4.

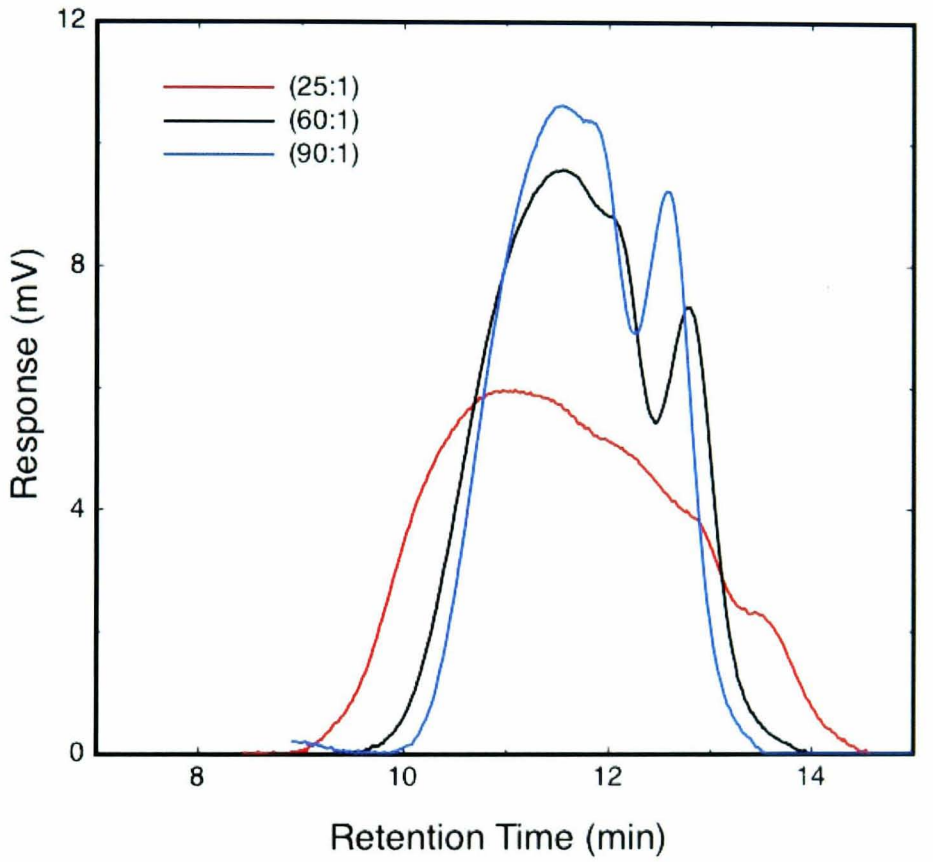

Figure 8.2: Typical SEC chromatograms for hyperbranched D_7-HB-PNIPAM with different branching degrees (25:1, 60:1 and 90:1) using a triple detection GPC system. This figure shows broad and multiple peaks for at all branching degrees. The average molecular weights are listed in table 8.4.

Sample	Cloud point in D_2O, 10% polymer/ °C	Cloud point in D_2O, 5% polymer/ °C
D_7-HB-PNIPAM (25:1)	28	28
D_7-HB-PNIPAM (60:1)	27	26
D_7-HB-PNIPAM (90:1)	23	30

Table 8.5: Cloud points (LCST) of 5 and 10 wt% of D_7-HB-PNIPAM with different branching degrees in D_2O.

8.2.4 LCST of D_7-HB-PNIPAMs

The cloud points (LCST) of D_7-HB-PNIPAM were determined by using a UV-visible spectrophotometer as described in Chapter 7, section 7.2.6. Figure 8.3 shows the optical density of 5 and 10 wt% of D_7-HB-PNIPAM with different branching degrees as a function of temperature. The obtained LCST values of each polymer at these two concentrations are listed in table 8.5.

8.2.5 NSE Measurements

NSE measurements were carried out using IN11 at Institut Laue-Langevin (ILL) in Grenoble, France, with incident neutron beam wavelength of 5.5 Å and $\triangle\lambda/\lambda = 10\%$ at a scattering angles $2\theta = 20°$ and 45° resulting in a range of Q between 0.0438 and 0.1734 $Å^{-1}$. The obtained time window was between 0 and 50.5 ns. 5 wt% solutions of two different D_7-HB-PNIPAM, (25:1) and (90:1), were prepared by dissolving 150 mg of each polymer in 3 ml D_2O. The samples were held in a 2 mm pathlength aluminum cell (4×3 mm). NSE measurements were conducted at 15°C and 25.4°C for D_7-HB-PNIPAM (25:1), and at 24°C and 31.1°C for D_7-HB-PNIPAM (90:1). These are temperatures far below and around the LCST of each polymer, respectively (see table 8.5). All NSE spectra were corrected and background subtracted from the scattering of the pure solvent and the sample holder at the ILL.

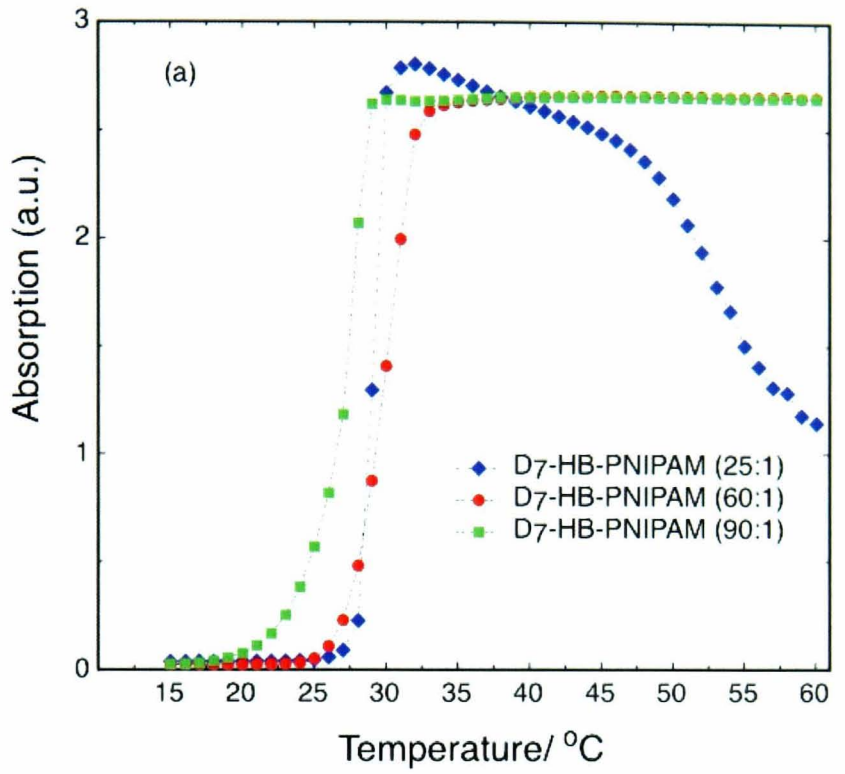

Figure 8.3: Optical density of (a) 10 wt% and (b) 5 wt% D_7-HB-PNIPAm in D_2O as a function of temperature for three different branching degrees ((25:1), (60:1) and (90:1)).

		τ (ns)			
Q(Å^{-1})	$d = 2\pi/Q$ (Å)	(25:1), 15 °C	(25:1), 25.4 °C	(90:1), 24 °C	(90:1), 31.1 °C
0.0438	143.5	249.6	48.5	1018.9	31.6
0.0543	115.7	71.9	23.5	51.0	35.4
0.0647	97.4	44.5	26.1	32.7	36.3
0.0980	64.1	23.7	14.2	16.0	12.1
0.1086	57.9	17.7	7.6	12.6	6.7
0.1191	52.8	14.2	7.0	10.1	4.6
0.1524	41.2	9.63	4.8	6.0	3.3

Table 8.6: Relaxation times for D_7-HB-PNIPAM (25:1) and (90:1) at different temperatures obtained by fitting the NSE data to a single decay function (equation 8.1) in the Q range shown in the table. The table also shows the length scales ($d = 2\pi/Q$) being probed by the NSE.

8.2.5.1 NSE Data Analysis

The obtained NSE data are normaly in the form of the normalized intermediate scattering function, $S(Q,t)/S(Q,0)$, as a function of Fourier time, t (see Chapter 4, section 4.4). Preliminary NSE data were fitted to a single exponential decay in the form:

$$\frac{S(Q,t)}{S(Q,0)} = A\exp\left(-\frac{t}{\tau}\right) + S_0, \tag{8.1}$$

where A and $S_0 = 1 - A$ are constants while τ is the relaxation time. Figure 8.4 shows typical NSE data for D_7-HB-PNIPAM (25:1) at 15°C fitted to equation 8.1. All of the obtained NSE data showed the same behaviour and the values of the relaxation times from this fitting for the studied polymers are listed in table 8.6. This indicates that simple dynamics theories, such as Rouse and Zimm, can be applied to these systems (see results section 8.3.1).

8.2.6 FCS Measurements

The fluorescently labelled linear and HB-PNIPAM samples described in Chapter 7, section 7.2.5 were used to study the dynamics of these polymers. Self-diffusion of linear and HB-PNIPAMs were studied in their own solutions

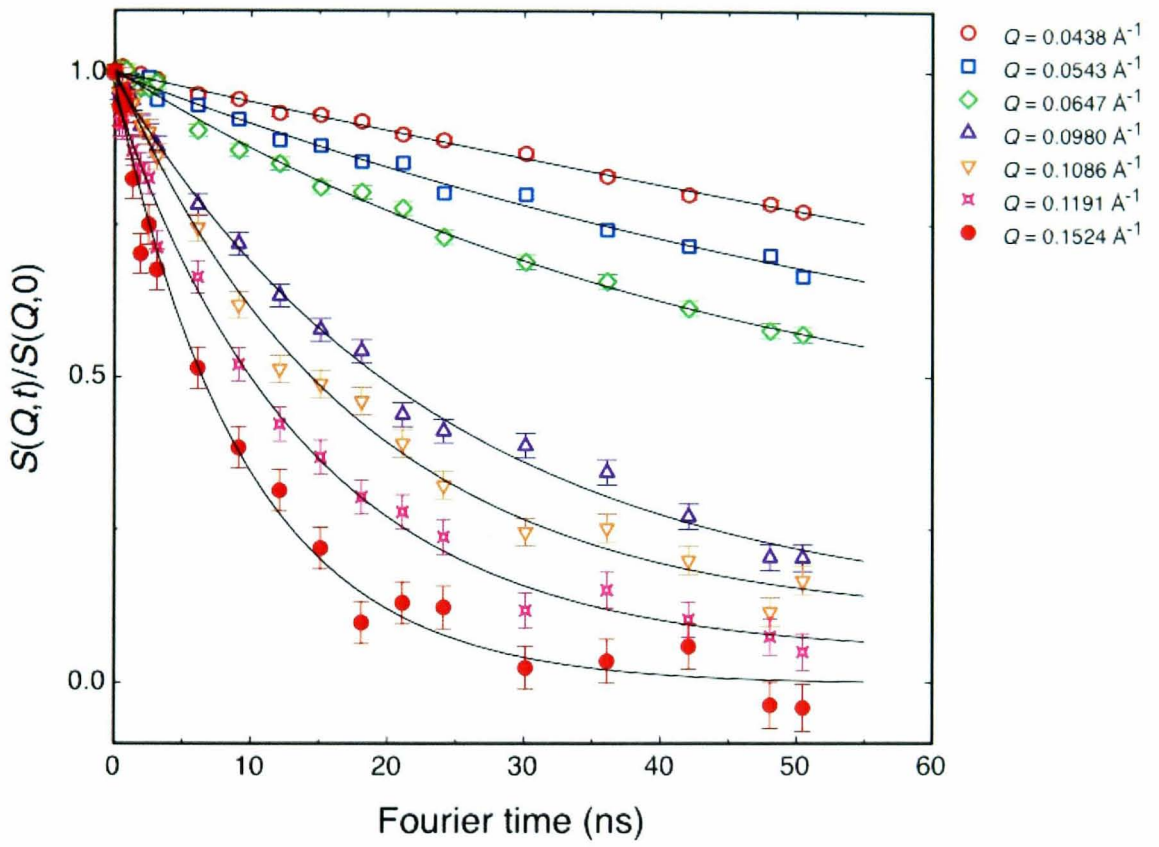

Figure 8.4: A typical NSE plot of dynamic structure factor as a function of Fourier time for D_7-HB-PNIPAM (25:1) at 15 °C. This figure shows that the obtained NSE data from these HB-PNIPAM can be described by a single exponential decay. The solid lines are fits to a single exponential decay (equation 8.1).

as a function of temperature and concentration. 1 nM solutions of the labeled linear and HB-PNIPAMs were prepared in their coresponding linear and HB-PNIPAM solutions with different concentrations (1.0, 1.2 and 1.5 wt%) as described in Chapter 5, section 5.2.1.3. FCS was used to investigate the self-diffusion behaviour of linear and HB-PNIPAM in their solutions in a similar way to that described in Chapter 5, section 5.2.2. A ConfoCor2 FCS module fitted to an LSM510 inverted confocal microscope (Zeiss) was used to carry out these experiments. The fluorescently labelled linear and HB-PNIPAMs were excited using a 488 nm Ar laser. The temperature was controlled by a Linkam heating stage (Linkam Scientific Instruments Ltd, Surrey, UK) with TMS94 heat controller and LNP-1 nitrogen flow control. FCS data were fitted to equation 4.19 to obtain the diffusion times which were then be converted to diffusion coefficients using equation 4.15.

8.3 Results and Discussion

8.3.1 Internal Dynamics of HB-PNIPAM

The obtained NSE data are presented in Figures 8.5, 8.6 and 8.7. These figures show the dynamic structure factor of D_7-HB-PNIPAM with different branching degrees at temperatures below and around the LCST of each polymer. The data analysis described in section 8.2.5.1 indicated that the dynamics of D_7-HB-PNIPAM follows a single exponential decay. The single exponential decay given by equation 8.1 can also be written in the form of the stretched exponential equation introduced by Zilman and Granek [119, 178, 40] as:

$$\frac{S(Q,t)}{S(Q,0)} = \exp\left(-\Gamma t\right)^{\beta}, \tag{8.2}$$

where β is the stretching parameter which has values of $1/2$ and $2/3$ for Rouse and Zimm dynamics, respectively, and $\Gamma = D_{\text{eff}}\, Q^2$ is the relaxation rate with D_{eff} being the effective diffusion coefficient. The characteristic relaxation rate in the case of Rouse dynamics can be given by [178]:

$$\Gamma = \frac{k_B T b^2}{12\xi} Q^4, \tag{8.3}$$

where b is the segment length. The data in Figure 8.5 show the fitting to Zimm dynamics with $\beta = 2/3$. The relaxation behaviour of hyperbranched PNIPAM at this length sacle cannot be described by the hydrodynamic interactions in the Zimm model. This can be attributed to the small length scale that is probed by NSE. This length scale, as shown in table 8.6, is between 41.2 Å and 143.5 Å corresponding to 0.0438 $Å^{-1} \leq Q \leq$ 0.1524 $Å^{-1}$. Below the LCST of HB-PNIPAM (25:1) and (90:1) these length scales start from distances smaller than the correlation lengths for each polymer (63.9 Å and 86.7 Å at 15°C for HB-PNIPAM (25:1) and 24°C for HB-PNIPAM (90:1)) to distances that are larger than the interaction distance with neighbouring chains. Above the LCST of each polymer, where the correlation length is no more valid because the polymer is in a poor solvent, the probed length scale is mush smaller than the polymer size (diameter) measured by SANS at these temperatures (288 Å for HB-PNIPAM (25:1) and 314 Å HB-PNIPAM (90:1)). In this case, the observed motion is not corresponding to the centre of mass diffusion but rather it is the motion of a trapped linear PNIPAM between the cross-links (i.e. the motion of the backbone between branch points). Therefore, the dynamic structure factor of hyperbranched PNIPAMs shown in Figures 8.6 and 8.7 is described well by the Rouse dynamics behaviour ($\beta = 1/2$) for relaxation of unentangled short chains ($\leq$ 100 monomers). This confirms that these systems are not entangled, at least at the length scales probed and the temperatures studied. Figure 8.8 shows the double logarithmic plot of the relaxation rate of D_7-HB-PNIPAM (25:1) and (90:1) as a function of Q at different temperatures. It is clear from this figure that the relaxation rate dependence of Q is linear following the Rouse behaviour (the slope of 4 in equation 8.3). The calculated effective diffusion coefficient (D_{eff}) is shown in Figure 8.9 as a function of Q. This figure illustrates the linear increase in D_{eff} with Q and with increasing temperature for both D_7-HB-PNIPAM systems. An interesting point which can be observed in Figure 8.9 is that the D_{eff} increases as the number of branches

per backbone is decreased. This confirms that the length scale probed is the backbone between two branch points. Hence, the more monomers between branch points, the more flexible the chain and the more effectively it diffuses. These results show that the length scale probed is not that of the branches of the polymers, because these polymers have identical branches and therefore should have similar relaxation behaviour in these two systems.

8.3.2 Self-Diffusion of linear and HB-PNIPAMs

Self-diffusion coefficients of linear and HB-PNIPAMs were determined as a function of temperature and concentration. Figure 8.10 shows the dependence of the self-diffusion coefficient on temperature in HB-PNIPAM (25:1). In this figure, the self-diffusion coefficient increases linearly with temperature for all of the studied concentrations, although the diffusion coefficient drops with increasing concentration. This linear relationship was found to follow the Zimm diffusion behaviour of a freely diffusing molecule in a solution (equation 2.51). These results suggest that these polymers, despite being large and branched, show a temperature-induced fast diffusion as they collapse and form spheres (confirmed previously by SANS measurements in Chapter 7). Likewise, the data in Figures 8.11 and 8.12 illustrate similar findings where the self-diffusion of both HB-PNIPAM (60:1) and (90:1) showed a linear increasing behaviour as a function of temperature with a good fit to the Zimm model for diffusion of hydrodynamically coupled polymer chains. Also, the increase of the concentration of these solutions was found to slow down the self-diffusion process. By comparing the self-diffusion of these three HB-PNIPAMs in Figures 8.10, 8.11 and 8.12, it is clear that, as expected, increasing the number of branches per molecule reduces the diffusion of HB-PNIPAM. However, these results also indicate and confirm the unentanglement of such systems. This behaviour has also been observed by NSE for the internal dynamics, as described in section 8.3.1. The particle size, $R_{\cdot}$ of these HB-PNIPAMs was determined from the fit to the Zimm model and the values are listed in table 8.7. The size range of these particles, 7.9-21.3 nm, is lower than the values obtained by SANS (table 7.7), 24-40 nm. Given that the

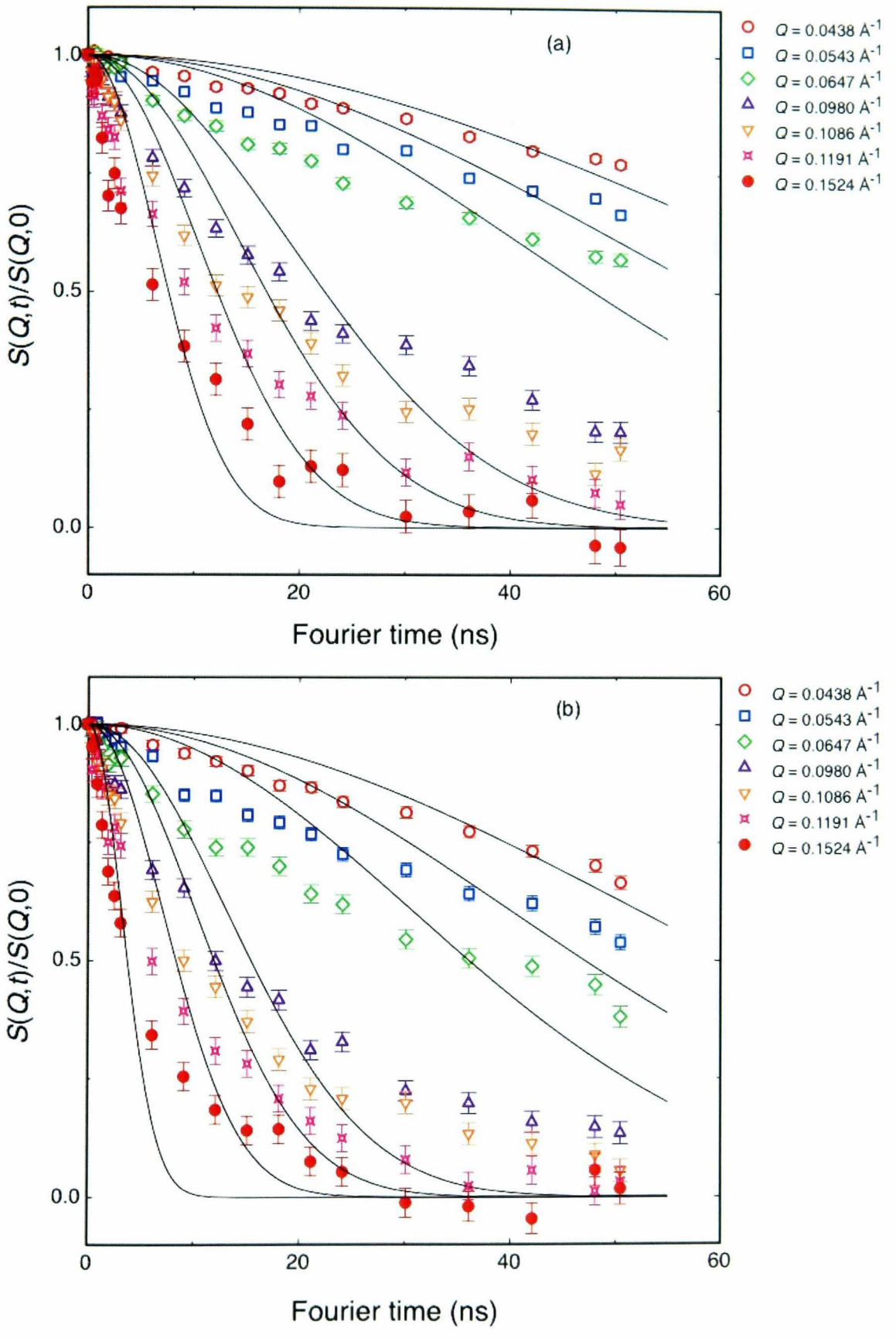

Figure 8.5: Dynamic structure factor for: (a) D_7-HB-PNIPAM (25:1) at 15°C and (b) D_7-HB-PNIPAM (90:1) at 24°C, at the indicated Q values. The solid lines are fits to Zimm dynamics (equation 8.2 with $\beta = 2/3$) behaviour, showing the discrepancy between the obtained results and the predicted Zimm-type hydrodynamic interactions.

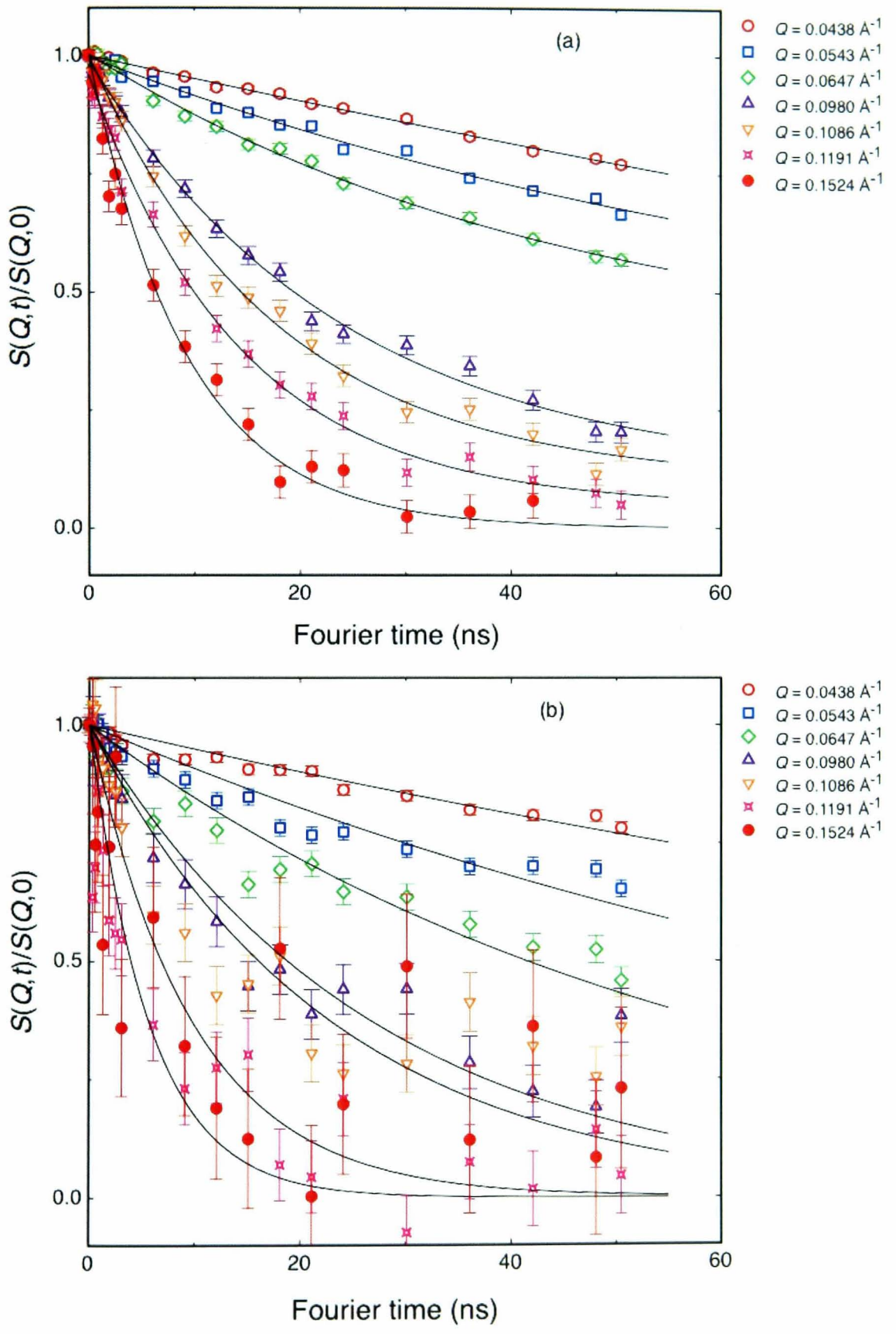

Figure 8.6: Dynamic structure factor for D_7-HB-PNIPAM (25:1) at: (a) 15°C and (b) 25.4°C, at the indicated Q values. The LCST of this polymer at the studied concentration is 28°C (table 8.5). The solid lines show a good fit to the Rouse model (equation 8.2 with $\beta = 1/2$) of unentangled chains.

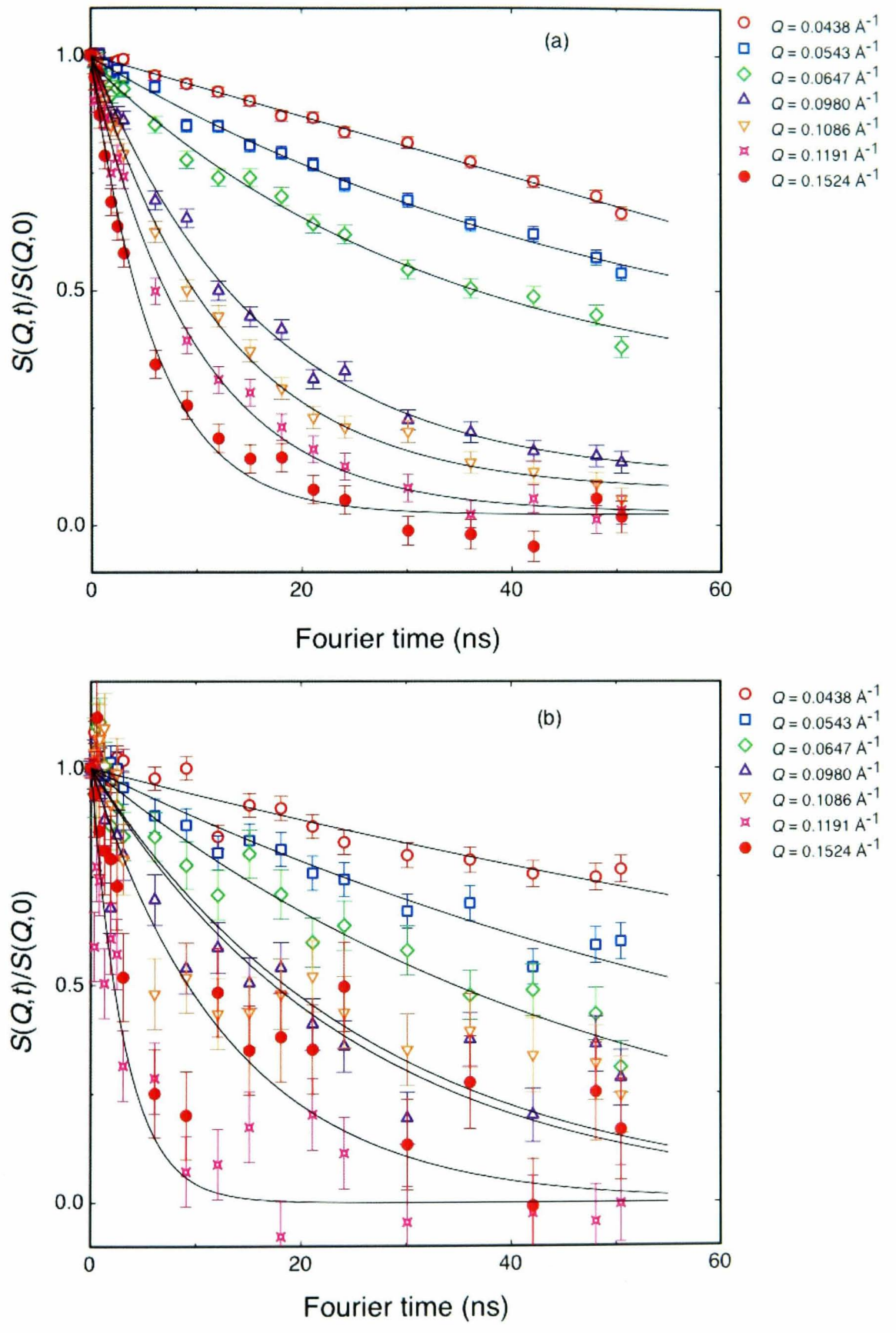

Figure 8.7: Dynamic structure factor for D_7-HB-PNIPAM (90:1) at: (a) 24°C and (b) 31.1°C, at the indicated Q values. The LCST of this polymer at the studied concentration is 30°C (table 8.5). The solid lines show a good fit to the Rouse model (equation 8.2 with $\beta = 1/2$) of unentangled chains.

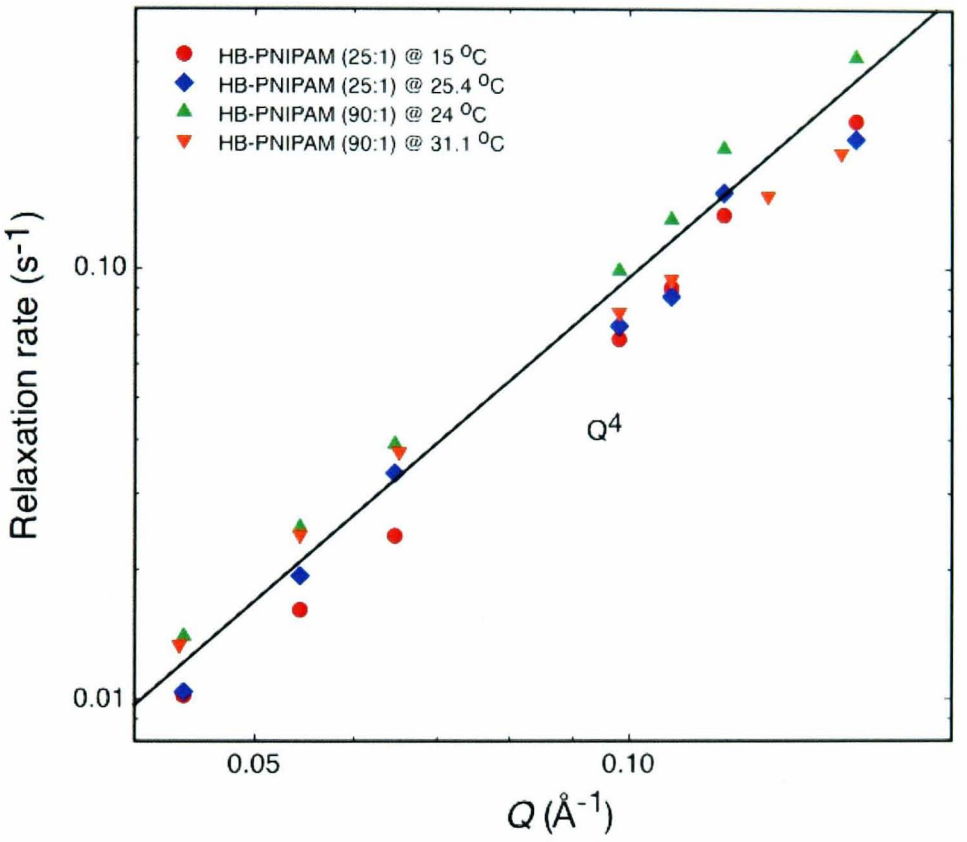

Figure 8.8: Double logarthmic plot of the relaxation rate of D_7-HB-PNIPAM (25:1) and (90:1) as a function of Q. The solid line represents a slope of 4 that corresponds to Rouse relaxation behaviour equation 8.3.

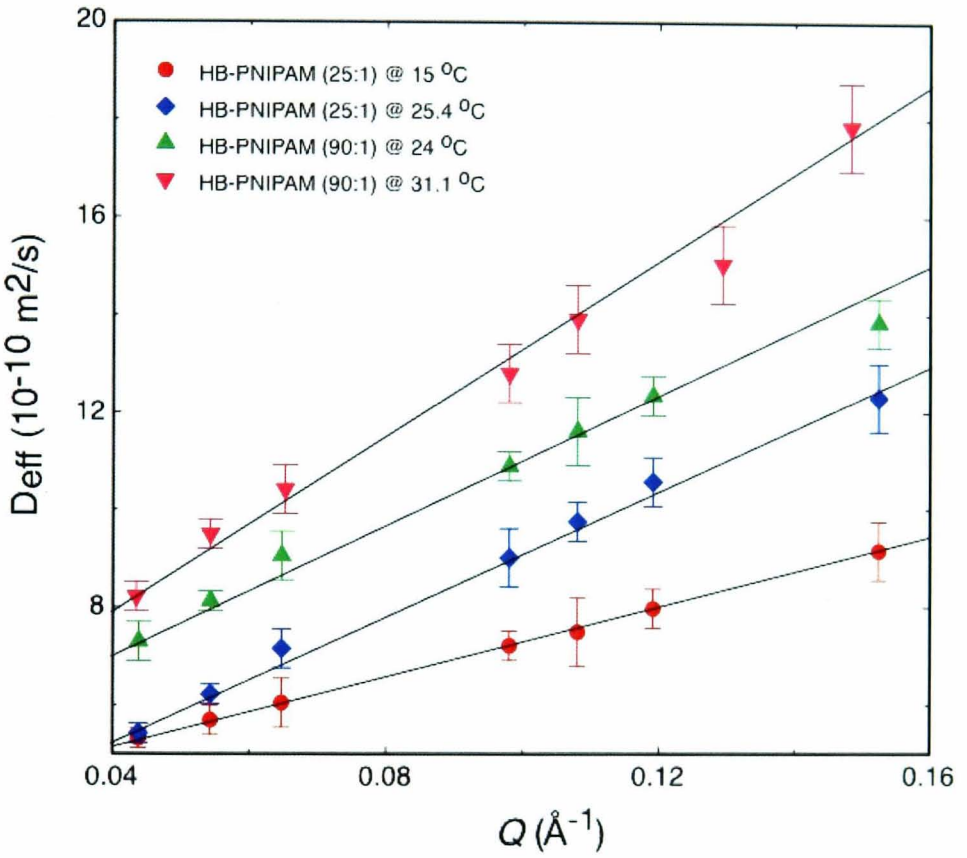

Figure 8.9: Effective diffusion coefficient of D_7-HB-PNIPAM (25:1) and (90:1) as a function of Q. The solid lines are the linear least square fit to the data. This figure shows the increase of the effective diffusion coefficient with increasing temperature and the decrease of D_{eff} as the number of branches per backbone is increased.

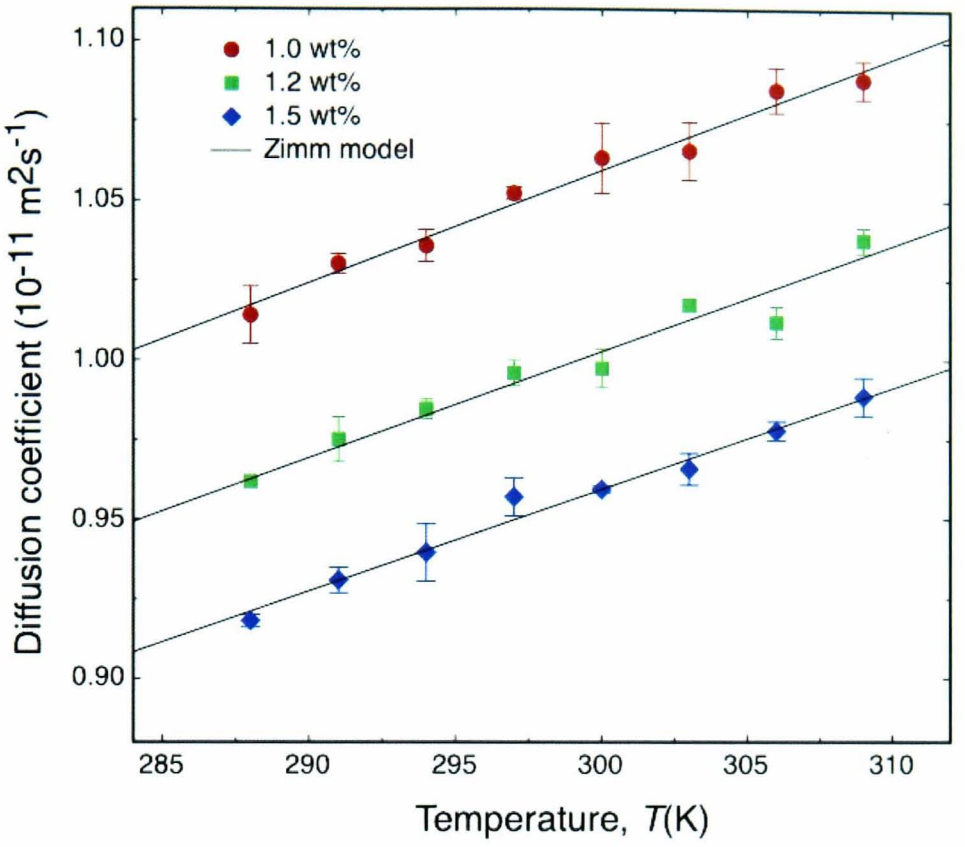

Figure 8.10: Temperature dependence of the diffusion coefficient of HB-PNIPAM (25:1) in its own solution as a function of concentration. This figure shows the linear increase of the diffusion coefficient with temperature, as opposed to its drop with increasing concentration. The solid lines are fits to the Zimm diffusion model (equation 2.51).

investigated concentrations here are much lower than those used for SANS experiments, these polymers do not form large aggregates. Another reason behind this discrepancy in size is that R is independent of temperature in the Zimm model.

On the other hand, linear PNIPAM self-diffusion, shown in Figure 8.13, was found to decay exponentially with increasing temperature, depending on concentration. The Arrhenius diffusion model that correlates the diffusion coefficient with temperature requires an activation energy, E_a, given as:

$$D = D_0 \exp\left(-\frac{E_a}{\bar{R}T}\right). \tag{8.4}$$

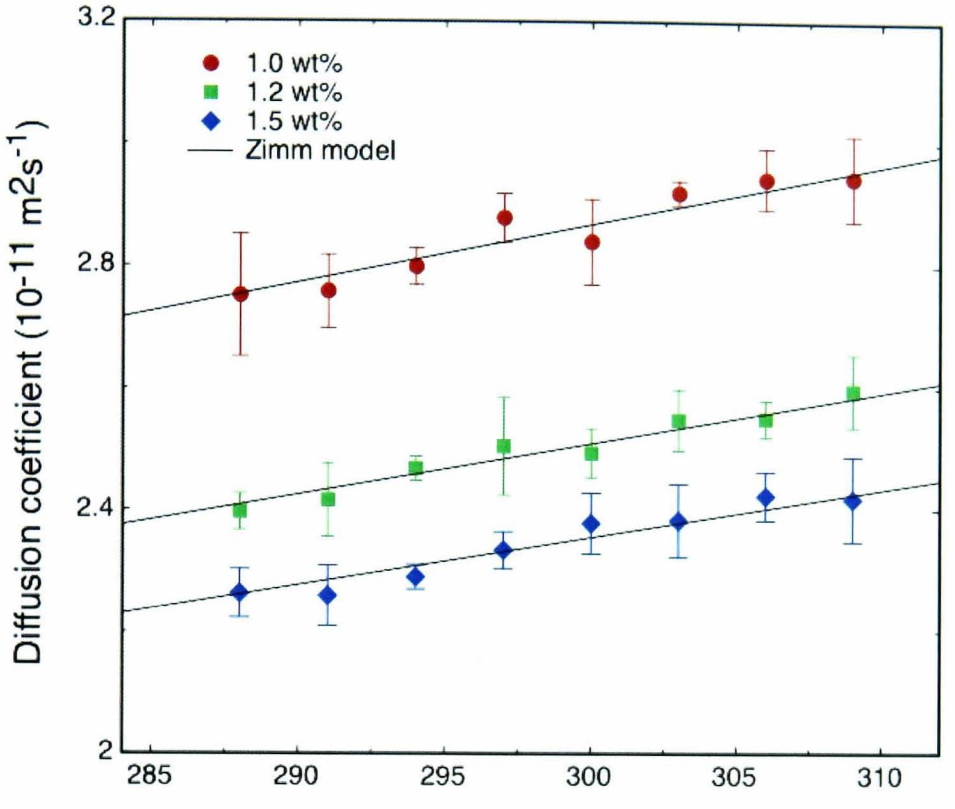

Figure 8.11: Temperature dependence of the diffusion coefficient of HB-PNIPAM (60:1) in its own solution as a function of concentration. This figure shows the linear increase of the diffusion coefficient with temperature, as opposed to its drop with increasing concentration. The solid lines are fits to the Zimm diffusion model (equation 2.51).

	R (nm)		
	(25:1)	(60:1)	(90:1)
1.0 wt%	20.1±0.4	10.5±0.2	7.9±0.4
1.2 wt%	21.3±0.5	11.0±0.5	8.1±0.2
1.5 wt%	20.5±0.2	10.9±0.3	8.2±0.4

Table 8.7: Particle size for HB-PNIPAMs as obtained from the fit to the Zimm diffusion model in Figures 8.10, 8.11 and 8.12.

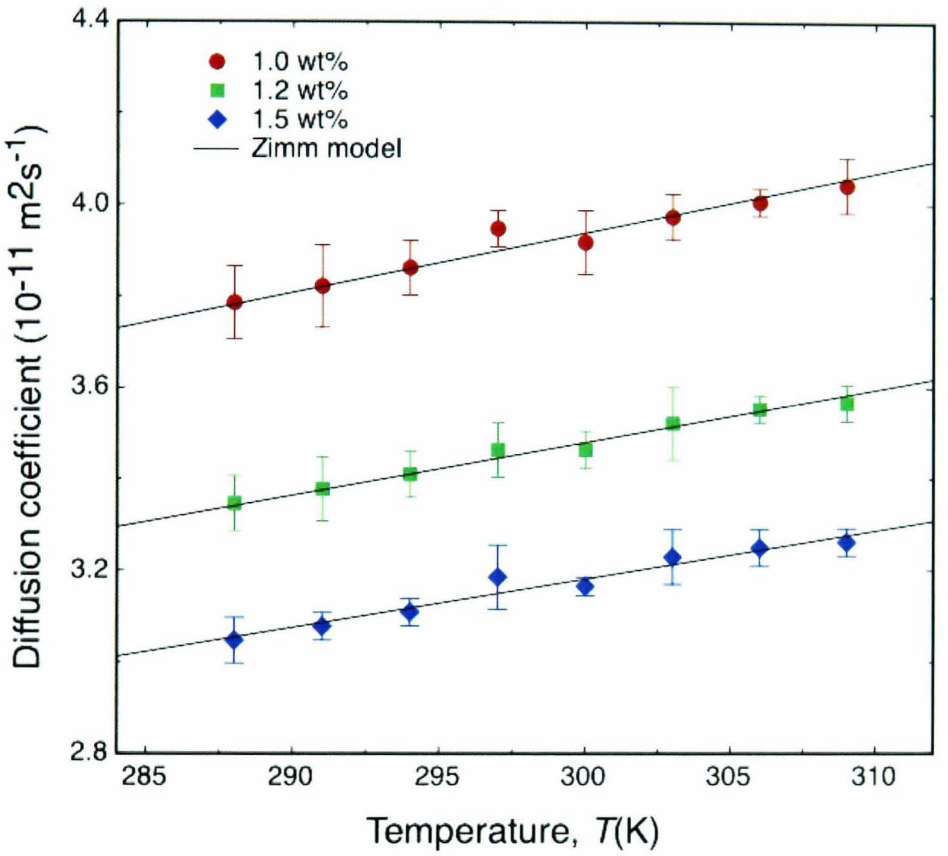

Figure 8.12: Temperature dependence of the diffusion coefficient of HB-PNIPAM (90:1) in its own solution as a function of concentration. This figure shows the linear increase of the diffusion coefficient with temperature, as opposed to its drop with increasing concentration. The solid lines are fits to the Zimm diffusion model (equation 2.51).

	E_a (KJ/mol)
1.0 wt%	-19±0.5
1.2 wt%	-17±0.7
1.5 wt%	-14±0.6

Table 8.8: Activation energy of linear PNIPAM obtained from the fit to the Arrhenius diffusion model in Figure 8.13.

This equation was used to describe the self-diffusion of linear PNIPAM. In equation 8.4, D_0 denotes the diffusion coefficient of linear PNIPAM in the solvent (water) and $\bar{R}$=8.3115 J/molK is the gas constant. The deviation from Zimm behaviour in this case indicates that linear PNIPAM molecules are not freely diffusing in the solution, but rather they entangle and minimize their mobility. These findings are in good agreement with the previously presented results in Chapter 7 from CLSM microscopy and SANS measurements. Another point of interest is that the activation energy of linear PNIPAM obtained from fitting to the Arrhenius diffusion model in table 8.8 is negative. This indicates that the interactions between linear PNIPAM molecules decrease with increasing temperature which is due to the netwok-like structure formed by the entangled chains.

8.4 Conclusions

The aim of this chapter was to investigate the dynamics of HB-PNIPAM. Two different techniques have been employed: NSE has been used to probe the internal dynamics of HB-PNIPAM and FCS to study self-diffusion of such a polymer, in comparison to their linear counterparts. NSE results have shown that the internal dynamics of these hyperbranched PNIPAMs can be described well be the Rouse relaxation behaviour of unentangled short chains. The length scale studied by NSE is lower than the correlation length obtained by SANS measurements in the previous chapter. Therefore, no hydrodynamic interactions were observed, as confirmed by the inability to fit the NSE data to the Zimm model. However, the NSE data were described well by the Rouse model for unentangled short chains. By studying the effective diffusion

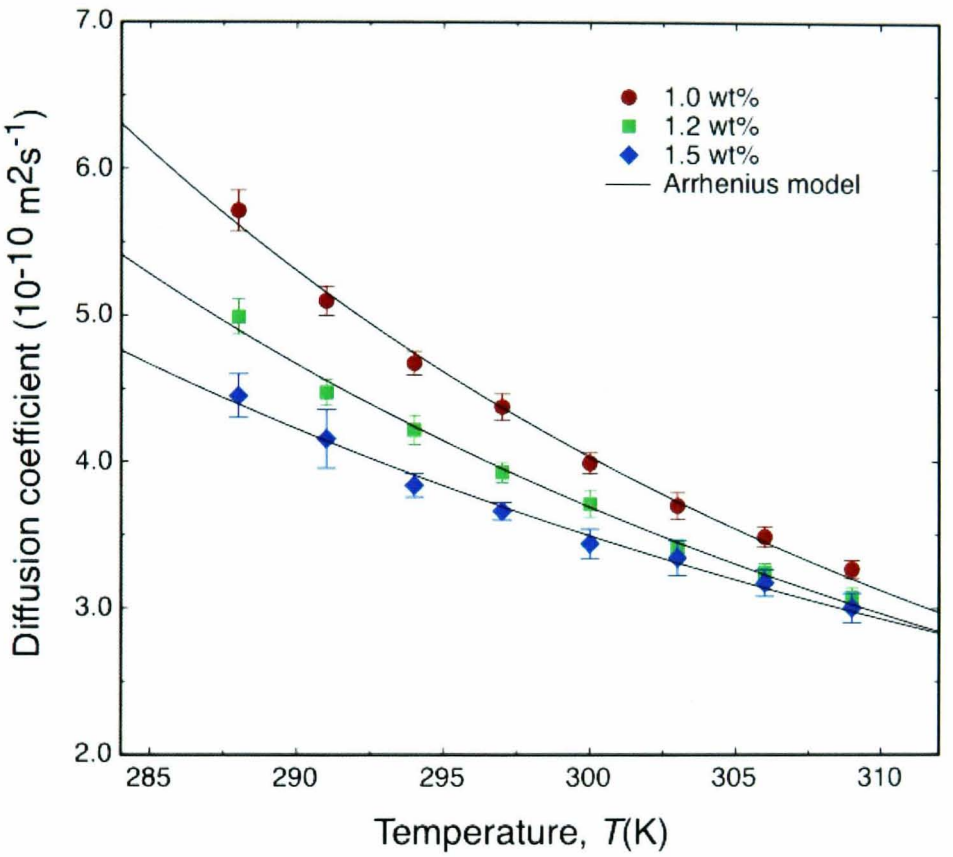

Figure 8.13: Temperature dependence of the diffusion coefficient of linear PNIPAM in its own solution as a function of concentration. The diffusion coefficient in this case decreases exponentially with increasing temperature and concentration. The solid lines are fits to the Arrhenius diffusion model (equation 8.4).

coefficient, it was found that the length scale probed is the backbone between branch points. Hence, the backbone of the hyperbranched polymer with more monomers between branch points was observed to effectively diffuse more than a similar polymer with a higher branching degree.

The FCS study of HB-PNIPAMs revealed the center of mass diffusion behaviour of the polymers as a function of temperature and concentration. The measured diffusion coefficients of the polymers were found to follow the Zimm diffusion behaviour of hydrodynamically interacting chains for different polymer concentrations. The diffusion coefficient was found to increase with increasing temperature as the size of the particles decreased, indicating that these polymers do not entangle. It was also observed that the increase of the branching degree leads to a decrease in the diffusion coefficient, which is expected because this corresponds to an increase in the molecular weight of the polymer. In contrast, linear PNIPAM was also investigated by FCS showing that the the centre of mass diffusion coefficient decreased exponentially with increasing temperature and concentration. This was well described by the Arrhenius diffusion model and can be explained by the linear polymes forming a network-like structure as a result of their entanglements. This was also seen by CLSM images and SANS experiments described in Chapter 7.

Chapter 9

Summary and Further Work

9.1 Summary

The work conducted in this thesis has described the structural behaviour and dynamics of different smart polymeric systems at the molecular level. Powerful techniques, such as fluorescence correlation spectroscopy (FCS), small angle X-ray and neutron scattering (SAXS and SANS) and neutron spin echo (NSE) allowed quantitative and qualitative analysis of stimuli responsive PMAA hydrogels, ferrogels and HB-PNIPAM.

FCS has been used to study the structural dependence of diffusion of a single molecule of FITC-dextran on temperature, pH and salt. This study has shown an unusual diffusion of FITC-dextran in PMAA hydrogels as a function of temperature, while in contrast, the diffusion of FITC-dextran in pure water has been found to follow Zimm diffusion behaviour. This strange diffusion behaviour in the case of PMAA hydrogel has been modelled by inserting the Huggins relation for viscosity into the Zimm model. This suggests that the observed macroscopic swelling and collapse transition can be understood in terms of the change in viscosity. The obtained mesh size from the diffusion measurements using de Gennes equation has been found to decrease exponentially with temperature. To the best knowledge of the author there is no existing theory that correlates the change in the mesh size to temperature. For this reason, a model has been developed by using the

Williams, Landel, and Ferry (WLF) equation for viscosity in a well-known equation for determining the mesh size from swelling measurements. The diffusion coefficient of FITC-dextran in water was found to decrease with increasing the pH of the solution, indicating a diffusing charged molecule. This was confirmed by titration measurements, but NMR spectra showed no chemical shift from dextran suggesting that the charges are originating from the FITC part of the molecule. The effect of NaCl and $CaCl_2$ on the swelling of PMAA hydrogel and the diffusion of FITC-dextran within it has also been studied. The diffusion coefficient of FITC-dextran in PMAA hydrogel showed an increase at low salt concentrations suggesting a swelling of PMAA hydrogel at these concentrations.

PMAA ferrogels have been prepared by introducing magnetic nanoparticles (Fe_3O_4) to PMAA hydrogels during polymerisation. This resulted in these magnetic nanoparticles being attached to the polymer network which in turn affects the structural behaviour of this network under applied magnetic fields. Controlling these polymer networks under applied magnetic fields is a key feature of these systems, making them possible candidates for delivery and release applications. The effect of the applied magnetic field on the diffusion of FITC-dextran within these ferrogels has been investigated using FCS. These experiments have shown that the diffusion coefficient of FITC-dextran depends strongly on the applied magnetic field, from which a relationship between the applied magnetic field and the viscosity of ferrogels based on Stokes-Einstein diffusion has been developed. The model developed has shown that the mesh size of the ferrogel is controlled by the applied magnetic field, B, and scales as $\exp\left(-\sqrt[4]{\xi^3 B^2/2\mu_0 k_B T}\right)$. The diffusion of FITC-dextran was found to follow a simple Stokes-Einstein law containing this scaling behaviour. In addition, the release of FITC-dextran molecules from PMAA ferrogels to the surrounding environment has been studied by FCS showing a considerable decrease of the molecular release with increasing magnetic field induction from 0.2 to 0.8 T. This effect was observed to increase with increasing the magnetic nanoparticle concentration in the gel. The scaling relationship mentioned above has also been found to be appropriate for describing molecular release from ferrogels as a function of magnetic

field. Small angle X-ray scattering has been used to characterize these ferrogels, finding that the size of magnetic nanoparticles does not change before (as a powder) and after (within the gel medium) polymerisation. This indicates that no particle aggregation is taking place in these gels. This has also been confirmed by magnetic hysteresis loops from these ferrogels and zero field cooled/field cooled measurements using SQUID where single domain ferromagnetic behavior at room temperature with a similar coercivity has been observed for both as-prepared and fully swollen ferrogels, and for increasing magnetic nanoparticle concentration.

HB-PNIPAM has been investigated by SANS, NSE and FCS. SANS experiments have revealed the structural behaviour of HB-PNIPAM as a function of temperature compared to its linear counterpart. These results have shown that D_2O is a good solvent for linear and HB-PNIPAM at low temperature, while increasing the temperature leads to a gradual collapse of these polymers. Data for both linear and HB-PNIPAM could be fitted well to the generalized Ornstein-Zernike equation for scattering giving a correlation length that is dependent on temperature. Increasing the temperature caused a change in the fractal dimension in the generalized OZ equation until the spherical behaviour is reached around the LCST of each polymer ($D_f = 4$). Above the LCST of HB-PNIPAMs, the scattering showed Porod behaviour for scattering from spherical particles. The measured sphere radius is between 12.3 and 19.7 nm depending on the temperature and degree of branching. These findings indicate that HB-PNIPAM does not entangle, which has also been observed in CLSM images in all studied HB-PNIPAM. In contrast, linear PNIPAM at temperatures above its LCST (above 32°C) shows a network-like structure (entanglements) where Porod's scattering law alone did not describe the scattering in this case and a Lorentzian contribution was included. Increasing the concentration of HB-PNIPAM from 5 wt% to 10 wt% did not change the scattering behaviour (no change in the structural behaviour) except, as expected, that the particle size decreases with increasing concentration. NSE measurements show that the relaxation of HB-PNIPAM at length scales below the correlation length can be described by Rouse model for unentangled polymer chains. FCS results show that.

despite being branched, HB-PNIPAM diffuses faster with increasing temperature. However, the increase of branching degree leads to a decrease in the center of mass diffusivity of HB-PNIPAM. The diffusion coefficient of these polymers has been found to increase linearly with temperature, which can be described by the simple Zimm theory. On the other hand, a deviation from Zimm theory has been observed at high concentrations of linear PNIPAM. This is in good agreement with SANS findings that HB-PNIPAM with different branching degrees and with increasing temperature are not entangled while their linear counterparts show entanglements at high temperatures above their LCST.

9.2 Further Work

The obtained results summarized in Section 9.1 suggest many future experiments and investigations. Although most of the results shown in this thesis are coupled with theories that described them well, more experimental and theoretical work is still needed. The purpose of this section is to give an overview on the possible work that can improve or lead to a better understanding of the systems under investigation.

9.2.1 Responsive Hydrogels

FCS experiments on PMAA hydrogels showed interesting diffusion behaviour of FITC-dextran within the gel. However, it is not clear if this is mainly due to the swelling behaviour of the hydrogel or if there is a contribution from the FITC-dextran molecule itself. Therefore, experimental techniques such as dynamic light scattering might reveal the structural behaviour of FITC-dextran as a function of temperature, pH and ionic strength. Moreover, in this work the FITC-dextran used has a fixed molecular weight throughout the whole study, therefore varying the molcular weight might be a point of interest. The mesh size of PMAA hydrogel has been obtained based on diffusion measurements and it is worthwhile investigating the effect of temperature on the mesh size of chemical hydrogels using imaging techniques. The diffusion

of FITC-dextran in PMAA hydrogels in the presence of salt ions showed a strange behaviour which could not be described by known diffusion models. Hence, more experimental and theoretical work needs to be conducted for a complete understanding of the diffusion under these conditions.

9.2.2 Ferrogels

Regarding the described work on PMAA ferrogels there are a number of suggestions to obtain a better understanding of such systems in magnetic fiels. The results shown in Chapter 6 included the measurement of the release from PMAA ferrogels to the surrounding solvent. However, the only measured parameter here is the number of molecules as a function of the applied magnetic field. The time parameter in these systems is significant, i.e. how fast these systems can release or restrict the diffusing molecules is of great importance. Therefore, an experiment that would measure the time of release from these ferrogels might be worth doing. An important issue with these ferrogels in general is their toxicity. Although Fe_3O_4 has been proved to be a safe material for biological and medical applications, the toxicity originating from cross-linking materials is not so clear. As a solution to this problem one might think of synthesizing ferrogels without using cross-linkers. This can be obtained if one successfully coats Fe_3O_4 nanoparticles with a monolayer that can form covalent bonds with MAA monomers.

9.2.3 Hyperbranched PNIPAM

The SANS results showed that HB-PNIPAM does not entangle at the measured temperatures, concentrations and branching degrees. Although the SANS measurements included some in excess of the LCST of each polymer, whether these HB-PNIPAM molecules are entangled at high temperatures for concentrated systems remains an open question. The studied HB-PNIPAM has COOH end groups which might be appropriate for investigation as a function of pH or salt concentration. Previous studies showed that these hyperbranched polymers exhibit interesting behaviour under shear which decreases their collapsing temperature. Thus, a rheology investigation using a

technique such as Rheo-SANS on these systems might reveal the structural behaviour of these polymers under shear.

The study of the dynamics of D_7-HB-PNIPAM using NSE, shown in Chapter 8, looked at the internal dynamics of these polymers at quite high Q values. According to SANS measurements, the probed length scales are in the order of below the correlation length, above which most of polymer interactions occur. Hence, performing NSE experiments at a lower Q range would allow us to probe larger length scales of more interest. Also, the molecular dynamics of these polymers in different environments is important, and can be investigated using FCS.

Bibliography

[1] N.A. Peppas. Hydrogels and drug delivery. *Current Opinion in Colloid and Interface Science*, 2(5):531–537, 1997.

[2] R. Barbucci. *Hydrogels: biological properties and applications*. Springer Verlag, 2009.

[3] Y Qiu and K Park. Environment-sensitive hydrogels for drug delivery. *Advanced Drug Delivery Reviews*, 53(3):321–339, December 2001.

[4] J. Jagur-Grodzinski. Polymeric gels and hydrogels for biomedical and pharmaceutical applications. *Polymers for Advanced Technologies*, 21(1):27–47, 2010.

[5] S. Hopkins, S. R. Carter, J. W. Haycock, N. J. Fullwood, S. MacNeil, and S. Rimmer. Sub-micron poly(n-isopropylacrylamide) particles as temperature responsive vehicles for the detachment and delivery of human cells. *Soft Matter*, 5(24):4928–4937, 2009.

[6] L.E. Bromberg and E.S. Ron. Temperature-responsive gels and thermogelling polymer matrices for protein and peptide delivery. *Advanced drug delivery reviews*, 31(3):197–221, 1998.

[7] M. Zrínyi. Intelligent polymer gels controlled by magnetic fields. *Colloid & Polymer Science*, 278(2):98–103, 2000.

[8] T.Y. Liu, S.H. Hu, K.H. Liu, D.M. Liu, and S.Y. Chen. Preparation and characterization of smart magnetic hydrogels and its use for drug

release. *Journal of Magnetism and Magnetic Materials*, 304(1):E397–E399, SEP 2006.

[9] G. Filipcsei, J. Feher, and M. Zrínyi. Electric field sensitive neutral polymer gels. *Journal of Molecular Structure*, 554(1):109–117, 2000.

[10] R. J. Hill. Electric-field-enhanced transport in polyacrylamide hydrogel nanocomposites. *Journal of Colloid and Interface Science*, 316(2):635–644, December 2007.

[11] J. Ostroha, M. Pong, A. Lowman, and N. Dan. Controlling the collapse/swelling transition in charged hydrogels. *Biomaterials*, 25(18):4345–4353, August 2004.

[12] F. Horkay and P. J. Basser. Ionic and ph effects on the osmotic properties and structure of polyelectrolyte gels. *Journal of Polymer Science Part B-Polymer Physics*, 46(24):2803–2810, December 2008.

[13] T. Okano. *Biorelated Polymers and Gels: Controlled Release and Applications in Biomedical Engineering.* Academic Press, 1998.

[14] S.V. Madihally. *Principles of Biomedical Engineering.* Artech House Publishers, 2010.

[15] R. La Spina, M. R. Tomlinson, L. Ruiz-Perez, A. Chiche, S. Langridge, and M. Geoghegan. Controlling network-brush interactions to achieve switchable adhesion. *Angewandte Chemie International Edition*, 46(34):6460–6463, 2007.

[16] Y. Osada and A. R. Khokhlov. *Polymer gels and networks.* CRC, 2002.

[17] M. Zrínyi and L. Barsi. Ferrogel: a new magneto-controlled elastic medium. *Polymer Gels and Networks*, 5(5):415–427, 1997.

[18] S.H. Hu, T.-Y. Liu, D.M. Liu, and S.-Y. Chen. Nano-ferrosponges for controlled drug release. *Journal of Controlled Release*, 121(3):181–189, August 2007.

[19] A. Kumar, A. Srivastava, I.Y. Galaev, and B. Mattiasson. Smart polymers: physical forms and bioengineering applications. *Progress in Polymer Science*, 32(10):1205–1237. 2007.

[20] H. G. SCHILD. Poly(n-isopropylacrylamide)-experiment, theory and application. *Progress In Polymer Science*, 17(2):163–249, 1992.

[21] S. Carter, B. Hunt, and S. Rimmer. Highly branched poly(n-isopropylacrylamide)s with imidazole end groups prepared by radical polymerization in the presence of a styryl monomer containing a dithioester group. *Macromolecules*, 38(11):4595–4603, May 2005.

[22] C.K. Chee, B.J. Hunt, S. Rimmer, R. Rutkaite, I. Soutar, and L. Swanson. Manipulating the thermoresponsive behaviour of poly (n-isopropylacrylamide) 3. on the conformational behaviour of n-isopropylacrylamide graft copolymers. *Soft Matter*, 5(19):3701–3712, 2009.

[23] R. Pelton. Temperature-sensitive aqueous microgels. *Advances In Colloid and Interface Science*, 85(1):1–33, February 2000.

[24] J.X. Zhang, L.Y. Qiu, K.J. Zhu, and Y. Jin. Thermosensitive micelles self-assembled by novel n-isopropylacrylamide oligomer grafted polyphosphazene. *Macromolecular rapid communications*, 25(17):1563–1567, 2004.

[25] S. Carter, S. Rimmer, A. Sturdy, and M. Webb. Highly branched stimuli responsive poly [(n-isopropyl acrylamide)-co-(1,2-propandiol-3-methacrylate)]s with protein binding functionality. *Macromolecular Bioscience*, 5(5):373–378, May 2005.

[26] S.R. Carter, S. Rimmer, R. Rutkaite, L. Swanson, and J. Haycock. Highly branched polymers via raft: Chain-end functionalization with peptides. volume 230. American Chemical Society, August 2005.

[27] S. R. Carter, S. Rimmer, M. Webb, and A. Sturdy. Highly-branched smart polymers using styryl dithioate esters. In *Abstracts of Papers*

of the American Chemical Society, volume 230, pages U4247–U4248. American Chemical Society, August 2005.

[28] J. M. J. Frechet, M. Henmi, I. Gitsov, S. Aoshima, M. R. Leduc, and R. B. Grubbs. Self-condensing vinyl polymerization - an approach to dendritic materials. *Science*, 269(5227):1080–1083, August 1995.

[29] S. Carter, S. Rimmer, R. Rutkaite, L. Swanson, J. Fairclough, A. Sturdy, and M. Webb. Highly branched poly(n-isopropylacrylamide) for use in protein purification. *Biomacromolecules*, 7(4):1124–1130, April 2006.

[30] S. Rimmer. Branched poly(n-ispropyl acrylamide)s: Synthesis critical behavior and biological properties. In *Abstracts of Papers of the American Chemical Society*, volume 231, 1155 16TH ST, NW, WASHINGTON, DC 20036 USA, March 2006. AMER CHEMICAL SOC.

[31] B.R. Twaites, C.D. Alarcon, D. Cunliffe, M. Lavigne, S. Pennadam, J.R. Smith, D.C. Gorecki, and C. Alexander. Thermo and ph responsive polymers as gene delivery vectors: effect of polymer architecture on dna complexation in vitro. *Journal of Controlled Release*, 97(3):551–566, July 2004.

[32] S. Hopkins, S. Carter, S. MacNeil, and S. Rimmer. Temperature-dependent phagocytosis of highly branched poly(n-isopropyl acrylamide-co-1,2 propandiol-3-methacrylate)s prepared by raft polymerization. *Journal of Materials Chemistry*, 17(38):4022–4027, 2007.

[33] K. Lubyphelps, D.L. Taylor, and F. Lanni. Probing the structure of cytoplasm. *Journal of cell biology*, 102(6):2015–2022, JUN 1986.

[34] T. Russ, R. Brenn, and M. Geoghegan. Equilibrium swelling of polystyrene networks by linear polystyrene. *Macromolecules*, 36(1):127–141, January 2003.

[35] L. Masaro and XX Zhu. Physical models of diffusion for polymer solutions, gels and solids. *Progress in polymer science*, 24(5):731–775. 1999.

[36] B. Amsden. An obstruction-scaling model for diffusion in homogeneous hydrogels. *Macromolecules*, 32(3):874–879, February 1999.

[37] S.R. Aragon and R. Pecora. Fluorescence correlation spectroscopy as a probe of molecular dynamics. *Journal of Chemical Physics*, 64(4):1791–1803, 1976.

[38] P.J. Flory. *Principles of polymer chemistry.* Cornell Univ Press, 1953.

[39] P.G. de Gennes. *Scaling concepts in polymer physics.* Cornell Univ Press, 1979.

[40] M. Rubinstein and R.H. Colby. *Polymer physics.* Oxford University Press, USA, 2003.

[41] M. Doi. *Introduction to polymer physics.* Oxford University Press, USA, 1996.

[42] U.W. Gedde. *Polymer physics.* Springer, 1995.

[43] I.I. Perepechko and A. Beknazarov. *An introduction to polymer physics.* Mir, 1981.

[44] M. Doi and S.F. Edwards. *The theory of polymer dynamics.* Oxford University Press, USA, 1988.

[45] N. Yui, R.J. Mrsny, and K. Park. *Reflexive polymers and hydrogels: understanding and designing fast responsive polymeric systems.* CRC, 2004.

[46] P.J. Flory and J. Rehner. Statistical mechanics of cross-linked polymer networks i rubberlike elasticity. *Journal of Chemical Physics*, 11(11):512–520, November 1943.

[47] A. Katchalsky, S. Lifson, and H. Exsenberg. Equation of swelling for polyelectrolyte gels. *Journal of Polymer Science*, 7(5):571–574, 1951.

[48] L. Brannon-Peppas and N.A. Peppas. Equilibrium swelling behavior of ph-sensitive hydrogels. *Chemical Engineering Science*, 46(3):715–722, 1991.

[49] J. Ricka and T. Tanaka. Swelling of ionic gels: quantitative performance of the donnan theory. *Macromolecules*, 17(12):2916–2921, 1984.

[50] N.A. Peppas and E.W. Merrill. Poly (vinyl alcohol) hydrogels: Reinforcement of radiation-crosslinked networks by crystallization. *Journal of Polymer Science: Polymer Chemistry Edition*, 14(2):441–457, 1976.

[51] J. Crank. *The mathematics of diffusion.* Oxford University Press, 1983.

[52] E.L. Cussler. *Diffusion: Mass transfer in fluid systems.* Cambridge Univ Pr, 1997.

[53] R.A.L. Jones. *Soft condensed matter.* Oxford University Press, USA, 2002.

[54] P.C. Hiemenz. *Polymer chemistry: the basic concepts.* CRC Press, 1984.

[55] J. Newman. *Physics of the life sciences.* Springer Verlag, 2008.

[56] R.A. Waggoner, F.D. Blum, and J.C. Lang. Diffusion in aqueous solutions of poly (ethylene glycol) at low concentrations. *Macromolecules*, 28(8):2658–2664, 1995.

[57] H.B. Bohidar. Dynamics in thermoreversible polymer gels. *Current Science*, 80(8):1008–1017, April 2001.

[58] P. Heitjans and J. Kärger. *Diffusion in condensed matter: methods, materials, models.* Springer Verlag, 2005.

[59] M. Geoghegan. Linear polymers in networks: Swelling, diffusion, and interdigitation. *Advances in Solid State Physics*, pages 29–44, 2006.

[60] P.G. de Gennes. *Introduction to polymer dynamics.* Cambridge Univ Pr, 1990.

[61] M. Doi and SF Edwards. The theory of polymer dynamics. 1986. *Clarendon: Oxford.*

[62] K. Okamoto, M. Terazima, and N. Hirota. Temperature dependence of diffusion of radical intermediates probed by the transient grating method. *Journal of Chemical Physics*, 103(24):10445–10452, 1995.

[63] Y. Osada and A. R. Khokhlov. *Polymer gels and networks.* Marcel Dekker, New York, 2002.

[64] K. Park. *Biomedical applications of hydrogels handbook.* Springer Verlag, 2010.

[65] I. Galaev and B. Mattiasson. *Smart polymers: applications in biotechnology and biomedicine.* CRC, 2007.

[66] J.F. Mano. Smart polymers: Applications in biotechnology and biomedicine. *Macromolecular Bioscience*, 9(6):622, 2009.

[67] L.B. Luo, M. Ranger, D.G. Lessard, D. Le Garrec, S. Gori, J.C. Leroux, S. Rimmer, and D. Smith. Novel amphiphilic diblock copolymer of low molecular weight poly(N-vinylpyrrolidone)-block-poly(D,L-lactide): Synthesis, characterization, and micellization. *MACROMOLECULES*, 37(11):4008–4013, JUN 1 2004.

[68] C.J. Crook, A. Smith, R.A.L. Jones, and A.J. Ryan. Chemically induced oscillations in a ph-responsive hydrogel. *Physical Chemistry Chemical Physics*, 4(8):1367–1369, 2002.

[69] G.R. Deen and LH Gan. Determination of reactivity ratios and swelling characteristics of "stimuli" responsive copolymers of n-acryloyl-n'-ethyl piperazine and mma. *Polymer*, 47(14):5025–5034, 2006.

[70] H.Y. He, L. Li, and L.J. Lee. Photopolymerization and structure formation of methacrylic acid based hydrogels in water/ethanol mixture. *Polymer*, 47(5):1612–1619, February 2006.

[71] E.S. Gil and S.M. Hudson. Stimuli-reponsive polymers and their bioconjugates. *Progress In Polymer Science*, 29(12):1173–1222, December 2004.

[72] M. J. Molina, M. R. Gómez-Antón, and I. F. Piérola. Determination of the parameters controlling swelling of chemically cross-linked phsensitive poly(n-vinylimidazole) hydrogels. *Journal of Physical Chemistry B*, 111(42):12066–74, Oct 2007.

[73] G. Nisato, F. Schosseler, and SJ Candau. Swelling equilibrium properties of partially charged gels: the effect of salt on the shear modulus. *Polymer Gels and Networks*, 4(5-6):481–498, 1996.

[74] T. Caykara, U. Bozkaya, and O. Kantoglu. Network structure and swelling behavior of poly(acrylamide/crotonic acid) hydrogels in aqueous salt solutions. *Journal of Polymer Science Part B-Polymer Physics*, 41(14):1656–1664, July 2003.

[75] F. Horkay, I. Tasaki, and P.J. Basser. Osmotic swelling of polyacrylate hydrogels in physiological salt solutions. *Biomacromolecules*, 1(1):84–90, 2000.

[76] F. Horkay, P.J. Basser, A.M. Hecht, and E. Geissler. Osmotic and sans observations on sodium polyacrylate hydrogels in physiological salt solutions. *Macromolecules*, 33(22):8329–8333, 2000.

[77] S.G. Starodoubtsev, E.V. Saenko, A.R. Khokhlov, V.V. Volkov, K.A. Dembo, V.V. Klechkovskaya, E.V. Shtykova, and I.S. Zanaveskina. Poly(acrylamide) gels with embedded magnetite nanoparticles. *Microelectronic Engineering*, 69(2-4):324–329, September 2003.

[78] C.S.S.R. Kumar and C. Hierold. *Nanomaterials for the Life Sciences*, volume 1. Wiley Online Library.

[79] G. Filipcsei, I. Csetneki, A. Szilágyi, and M. Zrínyi. Magnetic field-responsive smart polymer composites. *Oligomers Polymer Composites Molecular Imprinting*, pages 137–189, 2007.

[80] M. Zrínyi, L. Barsi, and A. Buki. Deformation of ferrogels induced by nonuniform magnetic fields. *Journal of Chemical Physics*, 104(21):8750, 1996.

[81] G. Torok, V.T. Lebedev, L. Cser, and M. Zrínyi. NSE-study of magnetic phase dynamics in poly(vinylalcohol) ferrogel. *PHYSICA B*, 276:396–397, MAR 2000. 2nd European Conference on Neutron Scattering (ECNS 99), BUDAPEST, HUNGARY, SEP 01-04. 1999.

[82] G. Torok, V.T. Lebedev, L. Cser, G. Kali, and M. Zrínyi. Dynamics of pva-gel with magnetic macrojunctions. *Physica B*, 297(1-4):40–44, March 2001.

[83] S.H. Hu, T.Y. Liu, D.M. Liu, and S.Y. Chen. Controlled pulsatile drug release from a ferrogel by a high-frequency magnetic field. *Macromolecules*, 40(19):6786–6788, 2007.

[84] J. Chatterjee, Y. Haik, and C. Jen Chen. Biodegradable magnetic gel: synthesis and characterization. *Colloid & Polymer Science*, 281(9):892–896, 2003.

[85] J. Qin, I. Asempah, S. Laurent, A. Fornara, R.N. Muller, and M. Muhammed. Injectable superparamagnetic ferrogels for controlled release of hydrophobic drugs. *Advanced Materials*, 21(13):1354–1357, 2009.

[86] X. Zhao, J. Kim, C.A. Cezar, N. Huebsch, K. Lee, K. Bouhadir, and D.J. Mooney. Active scaffolds for on-demand drug and cell delivery. *Proceedings of the National Academy of Sciences*, 108(1):67, 2011.

[87] P.J. Resendiz-Hernandez, O.S. Rodriguez-Fernandez, and L.A. Garcia-Cerda. Synthesis of poly (vinyl alcohol)-magnetite ferrogel obtained

by freezing-thawing technique. *Journal of Magnetism and Magnetic Materials*, 320(14):e373–e376, 2008.

[88] M. Czaun, L. Hevesi, M. Takafuji, and H. Ihara. A novel approach to magneto-responsive polymeric gels assisted by iron nanoparticles as nano cross-linkers. *Chemical Communications*, (18):2124–2126, May 2008.

[89] S. Monz, A. Tschöpe, and R. Birringer. Magnetic properties of isotropic and anisotropic cofe2o4-based ferrogels and their application as torsional and rotational actuators. *Physical Review E*, 78(2 Pt 1):021404. Aug 2008.

[90] T.Y. Liu, S.H. Hu, T.Y. Liu, D.M. Liu, and S.Y. Chen. Magnetic-sensitive behavior of intelligent ferrogels for controlled release of drug. *Langmuir*, 22(14):5974–5978, July 2006.

[91] T.Y. Liu, S.H. Hu, K.H. Liu, D.M. Liu, and S.Y. Chen. Preparation and characterization of smart magnetic hydrogels and its use for drug release. *Journal of Magnetism and Magnetic Materials*, 304(1):E397–E399, September 2006.

[92] N.S. Satarkar and J.Z. Hilt. Magnetic hydrogel nanocomposites for remote controlled pulsatile drug release. *Journal of Controlled Release*, 130(3):246–251, September 2008.

[93] S. Nitin, W. Zhang, R. Eitel, and Z. Hilt. Magnetic hydrogel nanocomposites as remote controlled microfluidic valves. *Lab Chip*, 2009.

[94] J. Sun, J. Wu, H. Li, and J. Chang. Macroporous poly (3-hydroxybutyrate-co-3-hydroxyvalerate) matrices for cartilage tissue engineering. *European polymer journal*, 41(10):2443–2449, 2005.

[95] X.Z. Zhang, P. Jo Lewis, and C.C. Chu. Fabrication and characterization of a smart drug delivery system: microsphere in hydrogel. *Biomaterials*, 26(16):3299–3309, 2005.

[96] F. Eeckman, A.J. Moes, and K. Amighi. Poly (n-isopropylacrylamide) copolymers for constant temperature controlled drug delivery. *International journal of pharmaceutics*, 273(1-2):109–119, 2004.

[97] J.S. Scarpa, D.D. Mueller, and I.M. Klotz. Slow hydrogen-deuterium exchange in a non-. alpha.-helical polyamide. *Journal of the American Chemical Society*, 89(24):6024–6030, 1967.

[98] H.G. SCHILD. Probes of the lower critical solution temperature of poly(n-isopropylacrylamide). *Acs Symposium Series*, 467:249–260, 1991.

[99] M. Heskins and J.E. Guillet. Solution properties of poly (n-isopropylacrylamide). *Journal of Macromolecular Science, Chemistry*, 2(8):1441–1455, 1968.

[100] M.M. Prange, H.H. Hooper, and J.M. Prausnitz. Thermodynamics of aqueous systems containing hydrophilic polymers or gels. *AIChE journal*, 35(5):803–813, 1989.

[101] A. Matsuyama and F. Tanaka. Theory of solvation-induced reentrant coil–globule transition of an isolated polymer chain. *The Journal of chemical physics*, 94:781, 1991.

[102] S. Fujishige, K. Kubota, and I. Ando. Phase transition of aqueous solutions of poly (n-isopropylacrylamide) and poly (n-isopropylmethacrylamide). *The Journal of Physical Chemistry*, 93(8):3311–3313, 1989.

[103] K. Kubota, S. Fujishige, and I. Ando. Single-chain transition of poly (n-isopropylacrylamide) in water. *Journal of Physical Chemistry*, 94(12):5154–5158, 1990.

[104] K. Otake, H. Inomata, M. Konno, and S. Saito. Thermal analysis of the volume phase transition with n-isopropylacrylamide gels. *Macromolecules*, 23(1):283–289, 1990.

[105] F.M. Winnik. Fluorescence studies of aqueous solutions of poly (n-isopropylacrylamide) below and above their lcst. *Macromolecules*, 23(1):233–242, 1990.

[106] B.A. Wolf and S. Enders. *Polymer Thermodynamics: Liquid Polymer-Containing Mixtures*, volume 238. Springer Verlag, 2010.

[107] C.K. Chee, S. Rimmer, D.A. Shaw, I. Soutar, and L. Swanson. Manipulating the thermoresponsive behavior of poly (n-isopropylacrylamide). 1. on the conformational behavior of a series of n-isopropylacrylamide-styrene statistical copolymers. *Macromolecules*, 34(21):7544–7549, 2001.

[108] S. Kim and K.E. Healy. Synthesis and characterization of injectable poly (n-isopropylacrylamide-co-acrylic acid) hydrogels with proteolytically degradable cross-links. *Biomacromolecules*, 4(5):1214–1223, 2003.

[109] V. Bulmus, S. Patir, S.A. Tuncel, and E. Piskin. Stimuli-responsive properties of conjugates of n-isopropylacrylamide-co-acrylic acid oligomers with alanine, glycine and serine mono-, di-and tri-peptides. *Journal of controlled release*, 76(3):265–274, 2001.

[110] H. Wei, X.Z. Zhang, Y. Zhou, S.X. Cheng, and R.X. Zhuo. Self-assembled thermoresponsive micelles of poly (n-isopropylacrylamide-b-methyl methacrylate). *Biomaterials*, 27(9):2028–2034, 2006.

[111] C. Yang and Y.L. Cheng. Raft synthesis of poly (n-isopropylacrylamide) and poly (methacrylic acid) homopolymers and block copolymers: Kinetics and characterization. *Journal of applied polymer science*, 102(2):1191–1201, 2006.

[112] C.K. Chee, S. Rimmer, I. Soutar, and L. Swanson. Synthesis and conformational behaviour of luminescently labelled poly[styrene-graft-(n-isopropyl acrylamide)] copolymers. *Polymer International*, 55(7):740–748, July 2006.

[113] J.E. Chung, M. Yokoyama, T. Aoyagi, Y. Sakurai, and T. Okano. Effect of molecular architecture of hydrophobically modified poly (n-isopropylacrylamide) on the formation of thermoresponsive core-shell micellar drug carriers. *Journal of controlled release*, 53(1-3):119–130, 1998.

[114] S.R. Carter, R. M. England, B. J. Hunt, and S. Rimmer. Functional graft poly(n-isopropyl acrylamide)s using reversible addition-fragmentation chain transfer (raft) polymerisation. *Macromolecular Bioscience*, 7(8):975–986, August 2007.

[115] S. Rimmer, S. Carter, R. Rutkaite, J.W. Haycock, and L. Swanson. Highly branched poly-(n-isopropylacrylamide)s with arginine-glycine-aspartic acid (rgd)- or cooh-chain ends that form sub-micron stimulus-responsive particles above the critical solution temperature. *Soft Matter*, 3(8):971–973, 2007.

[116] A.P. Vogt and B.S. Sumerlin. Tuning the temperature response of branched poly (n-isopropylacrylamide) prepared by raft polymerization. *Macromolecules*, 41(20):7368–7373, 2008.

[117] L.M. Geever, D.M. Devine, M.J.D. Nugent, J.E. Kennedy, J.G. Lyons, and C.L. Higginbotham. The synthesis, characterisation, phase behaviour and swelling of temperature sensitive physically crosslinked poly (1-vinyl-2-pyrrolidinone)/poly (n-isopropylacrylamide) hydrogels. *European polymer journal*, 42(1):69–80, 2006.

[118] W. Tao and L. Yan. Thermogelling of highly branched poly (n-isopropylacrylamide). *Journal of Applied Polymer Science*, 2010.

[119] D. Richter, M. Monkenbusch, A. Arbe, and J. Colmenero. Neutron spin echo in polymer systems. *Neutron Spin Echo In Polymer Systems*, 174:1–221, 2005.

[120] B. Ewen and D. Richter. Neutron spin echo investigations on the segmental dynamics of polymers in melts, networks and solutions. *Neutron Spin Echo Spectroscopy Viscoelasticity Rheology*. 134:1–129. 1997.

[121] M.S. Burns-Bellhorn, R.W. Bellhorn, and J.V. Benjamin. Anterior segment permeability to fluorescein-labeled dextrans in the rat. *Investigative Ophthalmology and Visual Science*, 17(9):857, 1978.

[122] Z. Feng, C. Gao, and J. Shen. Spontaneous deposition of fitc-labeled dextran into covalently assembled (pgma/pah) 4 microcapsules. *Macromolecular Chemistry and Physics*, 210(17):1387–1393. 2009.

[123] S.C. DeSmedt, T.K.L. Meyvis, J. Demeester, P. VanOostveldt, J.C.G. Blonk, and W.E. Hennink. Diffusion of macromolecules in dextran methacrylate solutions and gels as studied by confocal scanning laser microscopy. *Macromolecules*, 30(17):4863–4870, August 1997.

[124] D. Pristinski, V. Kozlovskaya, and S.A. Sukhishvili. Fluorescence correlation spectroscopy studies of diffusion of a weak polyelectrolyte in aqueous solutions. *Journal of Chemical Physics*, 122(1), January 2005.

[125] S. Seiffert and W. Oppermann. Diffusion of linear macromolecules and spherical particles in semidilute polymer solutions and polymer networks. *Polymer*, 49(19):4115–4126, September 2008.

[126] A. Michelman-Ribeiro, F. Horkay, R. Nossal, and H. Boukari. Probe diffusion in aqueous poly(vinyl alcohol) solutions studied by fluorescence correlation spectroscopy. *Biomacromolecules*, 8(5):1595–600, May 2007.

[127] R. Raccis, A. Nikoubashman, M. Retsch, U. Jonas, K. Koynov, H.J. Butt, C.N. Likos, and G. Fytas. Confined diffusion in periodic porous nanostructures. *ACS nano*.

[128] S.P. Zustiak, H. Boukari, and J.B. Leach. Solute diffusion and interactions in cross-linked poly(ethylene glycol) hydrogels studied by Fluorescence Correlation Spectroscopy. *Soft Matter*, 6(15):3609–3618. 2010.

[129] A. Michelman-Ribeiro, H. Boukari, R. Nossal, and F. Horkay. Structural changes in polymer gels probed by fluorescence correlation spectroscopy. *Macromolecules*, 37(26):10212–10214, 2004.

[130] M.D. Burke, J.O. Park, M. Srinivasarao, and S.A. Khan. Diffusion of macromolecules in polymer solutions and gels: a laser scanning confocal microscopy study. *Macromolecules*, 33(20):7500–7507, 2000.

[131] E. Haustein and P. Schwille. Fluorescence correlation spectroscopy: novel variations of an established technique. *Biophysics*, 36(1):151, 2007.

[132] H. Asai and T. Ando. Fluorescence correlation spectroscopy illuminated by standing exciting light waves. *Journal of the Physical Society of Japan*, 40:1527, 1976.

[133] Y. Chen, J.D. Muller, K.M. Berland, and E. Gratton. Fluorescence fluctuation spectroscopy. *Methods*, 19(2):234–252, 1999.

[134] O. Krichevsky and G. Bonnet. Fluorescence correlation spectroscopy: the technique and its applications. *Reports On Progress In Physics*, 65(2):251–297, February 2002.

[135] S. Maiti, U. Haupts, and W.W. Webb. Fluorescence correlation spectroscopy: Diagnostics for sparse molecules. *Proceedings of the National Academy of Sciences of the United States of America*, 94(22):11753–11757, OCT 28 1997.

[136] P. Schwille and E. Haustein. Fluorescence correlation spectroscopy. an introduction to its concepts and applications. *Biophysics Textbook Online*, 1(3), 2001.

[137] M. Hattori, H. Shimizu, and H. Yokoyama. Fluorescence correlation spectroscopy with traveling interference fringe excitation. *Review of Scientific Instruments*, 67(12):4064–4071, December 1996.

[138] R. Rigler, U. Mets, J. Widengren, and P. Kask. Fluorescence correlation spectroscopy with high count rate and low-background- analysis of translational diffusion. *European Biophysics Journal With Biophysics Letters*, 22(3):169–175, August 1993.

[139] E.L. Elson and D. Magde. Fluorescence correlation spectroscopy. i. conceptual basis and theory. *Biopolymers*, 13(1):1–27, 1974.

[140] K.M. Berland, PT So, and E. Gratton. Two-photon fluorescence correlation spectroscopy: method and application to the intracellular environment. *Biophysical journal*, 68(2):694–701, 1995.

[141] K.M. Berland, P.T. So, Y. Chen, W.W. Mantulin, and E. Gratton. Scanning two-photon fluctuation correlation spectroscopy: particle counting measurements for detection of molecular aggregation. *Biophysical journal*, 71(1):410–420, 1996.

[142] A. Benda, M. Benes, V. Marecek, A. Lhotsky, W.T. Hermens, and M. Hof. How to determine diffusion coefficients in planar phospholipid systems by confocal fluorescence correlation spectroscopy. *Langmuir*, 19(10):4120–4126, May 2003.

[143] Z. Burgos, P.and Zhang, R. Golestanian, G. J. Leggett, and M. Geoghegan. Directed single molecule diffusion triggered by surface energy gradients. *Acs Nano*, 3(10):3235–3243, October 2009.

[144] J. Ricka and T. Binkert. Direct measurement of a distinct correlation function by fluorescence cross correlation. *Physical Review A*, 39(5):2646–2652, 1989.

[145] J.R. Lakowicz. *Principles of fluorescence spectroscopy*. Springer, New York, 3rd ed edition, 2006.

[146] J.B. Pawley. *Handbook of biological confocal microscopy*. Springer Verlag, 2006.

[147] B.L. Sprague, F. Muller, R.L. Pego, P.M. Bungay, D.A. Stavreva, and J.G. McNally. Analysis of binding at a single spatially localized cluster of binding sites by fluorescence recovery after photobleaching. *Biophysical Journal*, 91(4):1169–1191, August 2006.

[148] U. Mets, J. Widengren, and R. Rigler. Application of the antibunching in dye fluorescence: measuringthe excitation rates in solution. *Chemical Physics*, 218(1-2):191–198, 1997.

[149] J. Enderlein and I. Gregor. Using fluorescence lifetime for discriminating detector afterpulsing in fluorescence-correlation spectroscopy. *Review of Scientific Instruments*, 76(3), March 2005.

[150] P. Schwille, F.J. MeyerAlmes, and R. Rigler. Dual-color fluorescence cross-correlation spectroscopy for multicomponent diffusional analysis in solution. *Biophysical Journal*, 72(4):1878–1886, April 1997.

[151] E. Haustein and P. Schwille. Ultrasensitive investigations of biological systems by fluorescence correlation spectroscopy. *Methods*, 29(2):153–166, 2003.

[152] B.K. Varma, Y. Fujita, M. Takahashi, and T. Nose. Hydrodynamic radius and intrinsic viscosity of polystyrene in the crossover region from theta- to good-solvent conditions. *Journal of Polymer Science: Polymer Physics Edition*, 22(10):1781–1797, 1984.

[153] A.G. PALMER and N.L. THOMPSON. Fluorescence correlation spectroscopy for detecting submicroscopic clusters of fluorescent molecules in membranes. *Chemistry and Physics of Lipids*, 50(3-4):253–270, June 1989.

[154] C. Eggeling, J. Widengren, R. Rigler, and C.A.M. Seidel. Photobleaching of fluorescent dyes under conditions used for single-molecule detection: Evidence of two-step photolysis. *Analytical Chemistry*, 70(13):2651–2659, July 1998.

[155] J. Widengren, U. Mets, and R. Rigler. Fluorescence correlation spectroscopy of triplet states in solution: a theoretical and experimental study. *Journal of Physical Chemistry*, 99(36):13368–13379, September 1995.

[156] R.A. Pethrick and JV Dawkins. *Modern Techniques for Polymer Characterisation.* Wiley, 1999.

[157] J. Fitter, T. Gutberlet, and J. Katsaras. *Neutron scattering in biology: techniques and applications.* Springer Verlag, 2006.

[158] J. Stellbrink, A. Niu, J. Allgaier, D. Richter, B.W. Koenig, R. Hartmann, G.W. Coates, and L.J. Fetters. Analysis of polymeric methylaluminoxane (mao) via small angle neutron scattering. *Macromolecules*, 40(14):4972–4981, July 2007.

[159] R.J. Roe and RJ Roe. *Methods of X-ray and neutron scattering in polymer science.* Oxford University Press New York, 2000.

[160] O. Glatter and O. Kratky. *Small angle X-ray scattering*, volume 69. Academic Press London, 1982.

[161] J. Lipfert and S. Doniach. Small-angle x-ray scattering from rna, proteins, and protein complexes. *Annual Review of Biophysics and Biomolecular Structure*, 36:307–327, 2007.

[162] K. Sinko, T. T., Viktoria, and A. Kovacs. Saxs investigation of porous nanostructures. *Journal of Non-Crystalline Solids*, 354(52-54):5466–5474, December 2008.

[163] M.H.J. Koch, P. Vachette, and D.I. Svergun. Small-angle scattering: a view on the properties, structures and structural changes of biological macromolecules in solution. *Quarterly reviews of Biophysics*, 36(02):147–227, 2003.

[164] J. Muller, P. Lothman, and D.C. Meyer. Small angle x-ray transmission characterisation of nanometersized pt-clusters in a ceramic thin film

on metal substrate. *Crystal Research and Technology*, 40(1-2):177–181, January 2005.

[165] D.I. Svergun and M.H.J. Koch. Small-angle scattering studies of biological macromolecules in solution. *Reports On Progress In Physics*, 66(10):1735–1782, October 2003.

[166] A.V. Teixeira, I. Morfin, F. Ehrburger-Dolle, C. Rochas, P. Panine, P. Licinio, and E. Geissler. Structure and magnetic properties of dilute ferrofluids suspended in gels. *Composites Science and Technology*, 63(8):1105–1111, June 2003.

[167] C. Hammond and C. Hammond. *Basics of Crystallography and Diffraction*. Oxford, 2001.

[168] M. Tomsic, M. Bester-Rogac, A. Jamnik, W. Kunz, D. Touraud, A. Bergmann, and O. Glatter. Ternary systems of nonionic surfactant brij 35, water and various simple alcohols: Structural investigations by small-angle x-ray scattering and dynamic light scattering. *Journal of Colloid and Interface Science*, 294(1):194–211, 2006.

[169] P. Lindner and T. Zemb. *Neutrons, X-rays, and light: scattering methods applied to soft condensed matter*. Elsevier Amsterdam, 2002.

[170] J. Daillant and A. Gibaud. *X-ray and neutron reflectivity: principles and applications*. Springer Verlag, 2009.

[171] M. Stieger, W. Richtering, J.S. Pedersen, and P. Lindner. Small-angle neutron scattering study of structural changes in temperature sensitive microgel colloids. *Journal of Chemical Physics*, 120(13):6197–6206, April 2004.

[172] M. Stieger and W. Richtering. Shear-induced phase separation in aqueous polymer solutions: Temperature-sensitive microgels and linear polymer chains. *Macromolecules*, 36(23):8811–8818, November 2003.

[173] J.S. Higgins and H. Benoît. *Polymers and Neutron Scattering*. Oxford University Press, USA, 1997.

[174] K. Mayumi, M. Nagao, H. Endo, N. Osaka, M. Shibayama, and K. Ito. Dynamics of polyrotaxane investigated by neutron spin echo. *Physica B: Condensed Matter*, 404(17):2600–2602, 2009.

[175] F.R. Trouw and D.L. Price. Chemical applications of neutron scattering. *Annual Review of Physical Chemistry*, 50:571–601, 1999.

[176] M. Geoghegan, R.A.L. Jones, M.G.D. van der Grinten, and A.S. Clough. Interdiffusion in blends of deuterated polystyrene and poly(alpha-methylstyrene). *Polymer*, 40(9):2323–2329, April 1999.

[177] R.B. Bird, R.C. Armstrong, and O. Hassager. Dynamics of polymeric liquids. vol. 1: Fluid mechanics. 1987.

[178] F. Mezei, C. Pappas, and T. Gutberlet. *Neutron spin echo spectroscopy: basics, trends, and applications.* Springer Verlag, 2003.

[179] J.K. Maranas. The effect of environment on local dynamics of macromolecules. *Current Opinion in Colloid and Interface Science*, 12(1):29–42, FEB 2007.

[180] F. Mezei. Neutron spin echo. In *Neutron Spin Echo*, volume 128, 1980.

[181] S.J. Swithenby. Squids and their applications in the measurement of weak magnetic-fields. *Journal of Physics E-Scientific Instruments*, 13(8):801–813, 1980.

[182] J.C. Gallop and B.W. Petley. Squids and their applications. *Journal of Physics E: Scientific Instruments*, 9:417, 1976.

[183] J. Clarke. Principles and applications of squids. *Proceedings of the IEEE*, 77(8):1208–1223, August 1989.

[184] J. Clarke. Superconductivity - squids in with applications. *Nature*, 352(6331):110–111, July 1991.

[185] B.D. Josephson. The discovery of tunnelling supercurrents. *Reviews of Modern Physics*, 46(2):251–254, 1974.

[186] B.S. Deaver and W.M. Fairbank. Experimental evidence for quantized flux in superconducting cylinders. *Physical Review Letters*, 7(2):43–&. 1961.

[187] V. Kozlovskaya, E. Kharlampieva, M.L. Mansfield, and S.A. Sukhishvili. Poly(methacrylic acid) hydrogel films and capsules: Response to ph and ionic strength, and encapsulation of macromolecules. *Chemistry of Materials*, 18(2):328–336, January 2006.

[188] D.L. Bernik, D. Zubiri, M.E. Monge, and R.M. Negri. New kinetic model of drug release from swollen gels under non-sink conditions. *Colloids and Surfaces A: Physicochemical and Engineering Aspects*, 273(1-3):165–173, 2006.

[189] S. Barbeiro and JA Ferreira. Coupled vehicle-skin models for drug release. *Computer Methods in Applied Mechanics and Engineering*, 198(27-29):2078–2086, 2009.

[190] G. Bose, P. Schwille, and T. Lamparter. The mobility of phytochrome within protonemal tip cells of the moss ceratodon purpureus, monitored by fluorescence correlation spectroscopy. *Biophysical Journal*, 87(3):2013–2021, September 2004.

[191] J.M.K.G. Cowie. *Polymers: chemistry and physics of modern materials*. CRC press, 1991.

[192] J. Wang and Y. Han. Tunable Multiresponsive Methacrylic Acid Based Inverse Opal Hydrogels Prepared by Controlling the Synthesis Conditions. *Langmuir*, 25(3):1855–1864, FEB 3 2009.

[193] C.F. Schmidt, M. Baermann, G. Isenberg, and E. Sackmann. Chain dynamics, mesh size, and diffusive transport in networks of polymerized actin: a quasielastic light scattering and microfluorescence study. *Macromolecules*, 22(9):3638–3649, 1989.

[194] D. Langevin and F. Rondelez. Sedimentation of large colloidal particles through semidilute polymer solutions. *Polymer*, 19(8):875–882, 1978.

[195] H.E. Stanley, J. Teixeira, A. Geiger, and RL Blumberg. Interpretation of the unusual behavior of h2o and d2o at low temperature: Are concepts of percolation relevant to the. *Physica A: Statistical and Theoretical Physics*, 106(1-2):260–277, 1981.

[196] J.R. Errington and P.G. Debenedetti. Relationship between structural order and the anomalies of liquid water. *Nature*, 409(6818):318–321, January 2001.

[197] G.C. Berry. Thermodynamic and conformational properties of polystyrene. i. light-scattering studies on dilute solutions of linear polystyrenes. *The Journal of Chemical Physics*, 44:4550, 1966.

[198] J.H. Sung, D.C. Lee, and H.J. Park. Conformational characteristics of poly (ethylene oxide)(peo) in methanol. *Polymer*, 48(14):4205–4212, 2007.

[199] T. Canal and N.A. Peppas. Correlation between mesh size and equilibrium degree of swelling of polymeric networks. *Journal of Biomedical Materials Research*, 23(10):1183–1193, 1989.

[200] C.L. Bell and N.A. Peppas. Modulation of drug permeation through interpolymer complexed hydrogels for drug delivery applications. *Journal of controlled release*, 39(2-3):201–207, 1996.

[201] M.L. Williams, R.F. Landel, and J.D. Ferry. The temperature dependence of relaxation mechanisms in amorphous polymers and other glass-forming liquids. *Journal of the American Chemical Society*, 77(14):3701–3707, 1955.

[202] J.E. Mark. *Physical properties of polymers handbook*. Springer, 2007.

[203] M. Seno, M.L. Lin, and K. Iwamoto. Swelling of poly(methacrylic acid) gels and adsorption of l-lysine and its polymer on the gels. *Colloid and Polymer Science*, 269(9):873–879, September 1991.

[204] K. Zhang and X.Y. Wu. Temperature and ph-responsive polymeric composite membranes for controlled delivery of proteins and peptides. *Biomaterials*, 25(22):5281–5291, 2004.

[205] B.o. Wang, X.D. Xu, Z.C. Wang, S.X. Cheng, X.Z. Zhang, and R.X. Zhu. Synthesis and properties of ph and temperature sensitive p(nipaam-co-dmaema) hydrogels. *Colloids and Surfaces B-Biointerfaces*, 64(1):34–41, June 2008.

[206] C.E. Ioan, T. Aberle, and W. Burchard. Structure properties of dextran. 2. dilute solution. *Macromolecules*, 33(15):5730–5739, 2000.

[207] M. S. Toprak, B. J. McKenna, J. H. Waite, and G. D. Stucky. Control of size and permeability of nanocomposite microspheres. *Chemistry of Materials*, 19(17):4263–4269, August 2007.

[208] P. Kurtzhals, C. Larsen, and M. Johansen. High-performance size-exclusion chromatographic procedure for the determination of fluoresceinyl isothiocyanate dextrans of various molecular masses in biological media. *Journal of Chromatography-Biomedical Applications*, 491(1):117–127, June 1989.

[209] Y. Koga. *Solution thermodynamics and its application to aqueous solutions: a differential approach.* Elsevier Science, 2007.

[210] T. Heimburg and Inc ebrary. *Thermal biophysics of membranes.* Wiley Online Library, 2007.

[211] H. Falkanhagen. The quantitative limiting law for the viscosity of strong binary electrolytes. *Physik. Z*, 32:745–764, 1931.

[212] L. Onsager and R.M. Fuoss. Irreversible processes in electrolytes. diffusion, conductance and viscous flow in arbitrary mixtures of strong electrolytes. *The Journal of Physical Chemistry*, 36(11):2689–2778, 1932.

[213] J.N. Israelachvili. *Intermolecular and surface forces*, volume 450. Academic press London, 1992.

[214] F. Ikkai and M. Shibayama. Gel-size dependence of temperature-induced microphase separation in weakly-charged polymer gels. *Polymer*, 48(8):2387–2394, 2007.

[215] M.R. Abidian, D.H. Kim, and D.C. Martin. Conducting-polymer nanotubes for controlled drug release. *Advanced Materials*, 18(4):405–+, February 2006.

[216] S. Murdan. Electro-responsive drug delivery from hydrogels. *Journal of Controlled Release*, 92(1-2):1–17, 2003.

[217] G. Wang, WJ Tian, and JP Huang. Response of ferrogels subjected to an ac magnetic field. *J. Phys. Chem. B*, 110(22):10738–10745, 2006.

[218] J.A. Galicia, F. Cousin, E. Dubois, O. Sandre, V. Cabuil, and R. Perzynski. Static and dynamic structural probing of swollen polyacrylamide ferrogels. *Soft Matter*, 5(13):2614–2624, 2009.

[219] E. Jarkova, H. Pleiner, H.W. Muller, and H.R. Brand. Hydrodynamics of isotropic ferrogels. *Physical Review E*, 68(4), October 2003.

[220] T.Y. Liu, S.H. Hu, T.Y. Liu, D.M. Liu, and S.Y. Chen. Magnetic-sensitive behavior of intelligent ferrogels for controlled release of drug. *Langmuir*, 22(14):5974–5978, 2006.

[221] A.M. Al-Baradi, O.O. Mykhaylyk, H.J. Blythe, and M. Geoghegan. Magnetic field dependence of the diffusion of single dextran molecules within a hydrogel containing magnetite nanoparticles. *The Journal of Chemical Physics*, 134:094901, 2011.

[222] G. Porod. Small angle x-ray scattering. In *Proceedings of the Syracuse Conference*, pages 1–15, 1967.

[223] J.T. Koberstein, B. Morra, and R.S. Stein. The determination of diffuse-boundary thicknesses of polymers by small-angle x-ray scattering. *Journal of applied crystallography*, 13(1):34–45, 1980.

[224] R.W. Chantrell, J. Popplewell, and S.W. Charles. Measurements of particle size distribution parameters in ferrofluids. *IEEE Transactions on Magnetics*, 14:975–977.

[225] F. Vereda, J. de Vicente, and R. Hidalgo-Alvarez. Physical properties of elongated magnetic particles: Magnetization and friction coefficient anisotropies. *Journal of Chemical Physics and Physical Chemistry*, 10(8):1165–1179, June 2009.

[226] L. Néel. *Annales Geophysicae*, 5(99), 1949.

[227] A.L. Kholodenko and J.F. Douglas. Generalized stokes-einstein equation for spherical particle suspensions. *Physical Review E*, 51(2):1081–1090, 1995.

[228] A. F. Kostko, M. A. Anisimov, and J. V. Sengers. Dynamics of critical fluctuations in polymer solutions. *Physical Review E*, 76(2), August 2007.

[229] J. Chiefari, YK (Bill) Chong, F. Ercole, J. Krstina, J. Jeffery, T.P.T. Le, R.T.A. Mayadunne, G.F. Meijs, C.L. Moad, G. Moad, et al. Living free-radical polymerization by reversible addition-fragmentation chain transfer: the raft process. *Macromolecules*, 31(16):5559–5562, 1998.

[230] R.T.A. Mayadunne, E. Rizzardo, J. Chiefari, Y.K. Chong, G. Moad, and S.H. Thang. Living radical polymerization with reversible addition-fragmentation chain transfer (raft polymerization) using dithiocarbamates as chain transfer agents. *Macromolecules*, 32(21):6977–6980, 1999.

[231] M. Shibayama, T. Tanaka, and C.C. Han. Small angle neutron scattering study on poly (n-isopropyl acrylamide) gels near their volume-phase transition temperature. *The Journal of chemical physics*, 97:6829, 1992.

[232] D.R. Vollet, D.A. Donatti, C.M. Awano, W. Chiappim, M.R. Vicelli, and A. Ibanez Ruiz. Structure and aggregation kinetics of

vinyltriethoxysilane-derived organic/silica hybrids. *Journal of Applied Crystallography*, 43(5):1005–1011, 2010.

[233] M. Delsanti, JP Munch, D. Durand, JP Busnel, and M. Adam. Conformation of monodisperse branched polymers in semi-dilute solutions. *EPL (Europhysics Letters)*, 13:697, 1990.

[234] H.M. Crowther, B.R. Saunders, S.J. Mears, T. Cosgrove, B. Vincent, S.M. King, and G.E. Yu. Poly (nipam) microgel particle de-swelling: a light scattering and small-angle neutron scattering study. *Colloids and Surfaces A: Physicochemical and Engineering Aspects*, 152(3):327–333, 1999.

List of Figures

List of Tables

Appendix A

Appendix A.1: Copyright License Agreements

License Number	2752550126800
License date	Sep 19, 2011
Licensed content publisher	Elsevier
Licensed content publication	Polymer
Licensed content title	Photopolymerization and structure formation of methacrylic acid based hydrogels in water/ethanol mixture
Licensed content author	Hongyan He,Ling Li,L. James Lee
Licensed content date	22 February 2006
Licensed content volume number	47
Licensed content issue number	5
Number of pages	8
Type of Use	reuse in a thesis/dissertation
Portion	figures/tables/illustrations
Number of figures/tables/illustrations	1
Format	both print and electronic
Are you the author of this Elsevier article?	Yes
Will you be translating?	No
Order reference number	1
Title of your thesis/dissertation	Nanoscale Structure and Single Molecule Diffusion in Smart Polymeric Systems
Expected completion date	Sep 2011
Estimated size (number of pages)	250
Elsevier VAT number	GB 494 6272 12
Permissions price	0.00 GBP
VAT/Local Sales Tax	0.0 USD / 0.0 GBP
Total	0.00 GBP

Appendix B

Appendix B.1: Acid and Base Properties

According to Bronsted Lowry theory, an acid is described as any substance that donates a proton to another substance, a process after which the acid is said to be dissociated. On the other hand, the same theory defines a base as any substance that accepts a proton from another substance. These definitions are generic for any substance in any condition. However, the common example is the dissociation of acids and bases in aqueous solutions. If an acid, for example, is represented by HA, the following formula can be written for the dissociation of this acid in water:

$$HA\ (aq) + H_2O\ (l) \rightleftharpoons H_3O^+(aq) + A^-(aq), \tag{B.1}$$

where A^- is the conjugate base of the acid and H_3O^+ is the hydronium ion, which is the protonated water molecule. A Hydronium ion is usually refered to as H^+ (hydrogen ion) or a proton. The equilibrium constant for the reaction of HA with H_2O (or acidity constant), K_a, is given by,

$$K_a = \frac{[A^-][H_3O^+]}{[HA]}, \tag{B.2}$$

where $[A^-]$, $[H_3O^+]$ and [HA] are the concentrations of the conjugate base, the hydronium and the acid, respectively. If HA is completely dissociated in

water, a high value of K_a (unity or greater) is obtained and the acid in this case is said to be a strong acid (e.g. $K_a = 10^7$ for HCl). On the other hand, if the acid is partially dissociated in water, the three species HA, H_3O^+, A^- will be present in the solution in significant amounts, leading to a range of K_a values depending on these concentrations. Organic acids (e.g. carboxylic acid) are known as weak acids. The common way to measure the strength of an acid is by taking the negative logarithm of K_a, which is refered to as pK_a:

$$pK_a = -\log K_a. \tag{B.3}$$

In this case, a high value of pK_a means a small value of K_a indicating a weak acid; while zero or less values of pK_a indicate a strong acid.

A similar reaction to that of an acid in water can be considered for a base in water, which can be given as,

$$B\ (aq) + H_2O\ (l) \rightleftharpoons HB^+(aq) + OH^-(aq), \tag{B.4}$$

where HB^+ is the conjugate acid of the base B. As for the acid case above, the basicity constant, K_b, can be given by,

$$K_b = \frac{[HB^+][OH^-]}{[B]}. \tag{B.5}$$

The strength of a base can be determined from its K_b as $pK_b = -\log K_b$. However, base strength can also be determined from its conjugate acid HB^+, which gives

$$HB^+(aq) + H_2O\ (l) \rightleftharpoons H_3O^+(aq) + B\ (aq). \tag{B.6}$$

in water. Therefore,

$$K_a = \frac{[B][H_3O^+]}{[HB^+]}. \tag{B.7}$$

The dissociation of water can be written in the following way:

$$H_2O\ (l) + H_2O\ (l) \rightleftharpoons H_3O^+(aq) + OH^-(aq). \tag{B.8}$$

The dissociation constant (or self-ionization constant) of water, K_w, is expressed as,

$$K_w=[H_3O^+]\cdot[OH^-], \tag{B.9}$$

which can be obtained by multiplying equations B.5 and B.7,

$$K_aK_b = [H_3O^+]\cdot[OH^-] = K_w. \tag{B.10}$$

For pure water at room temperature, $K_w = [H_3O^+]\cdot[OH^-] = 10^{-7}\times 10^{-7} = 1.0\times10^{-14}$ and $pK_w = -\log(1.0\times10^{-14}) = 14$. This means that if the solution has more H^+ ions it is more acidic and it is more basic if $[OH^-] > [H^+]$. A neutral solution has equal amounts of H^+ and OH^-. It is common to express the acidity and basicity of a solution just in terms of the concentration of H^+ as,

$$pH = -\log[H^+]. \tag{B.11}$$

In a neutral solution, at room temperature, $[H^+] = 10^{-7}$, which gives $pH = 7$.

Appendix C

Appendix C.1: NMR Spectra of PNIPAms

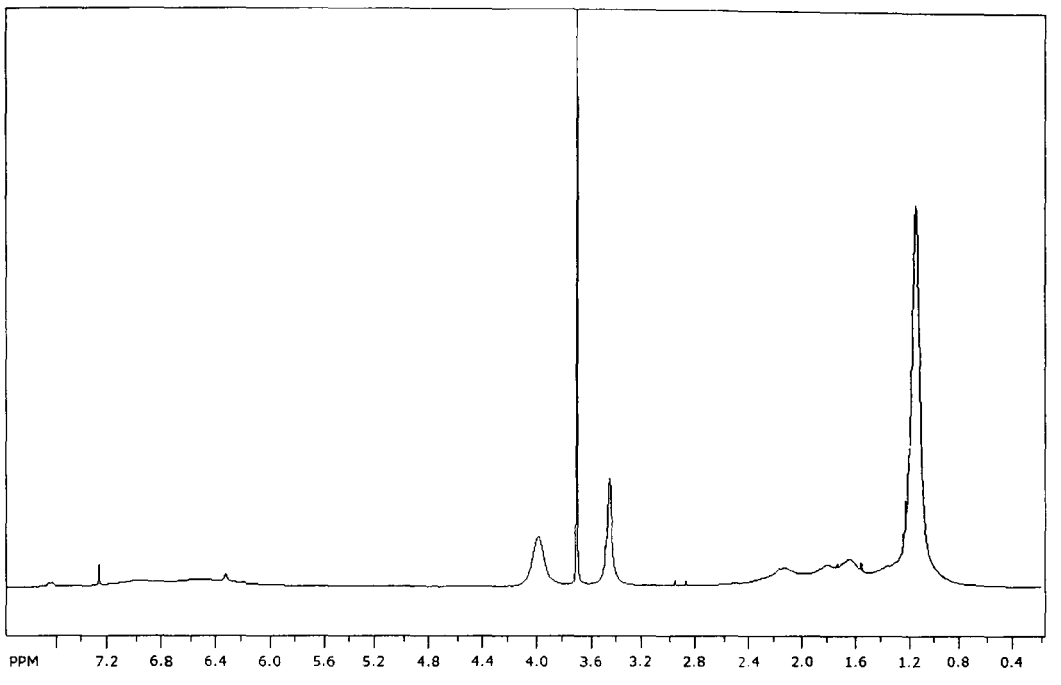

Figure C.1: ^{1}H NMR (400 MHz) spectrum of HB-PNIPAM (25:1).

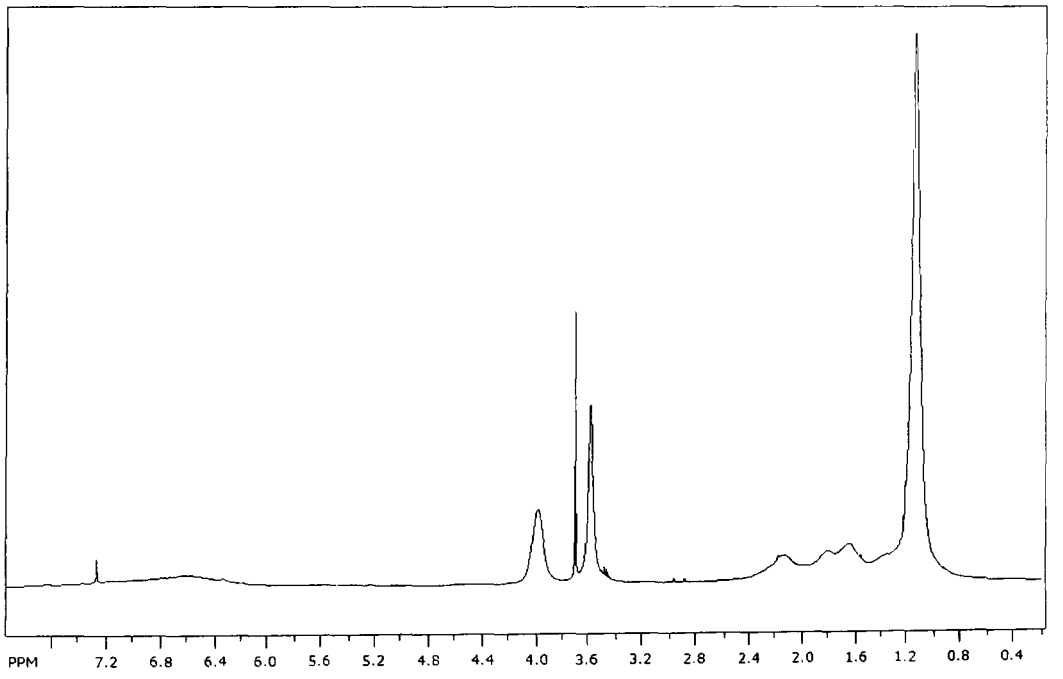

Figure C.2: ^{1}H NMR (400 MHz) spectrum of HB-PNIPAM (60:1).

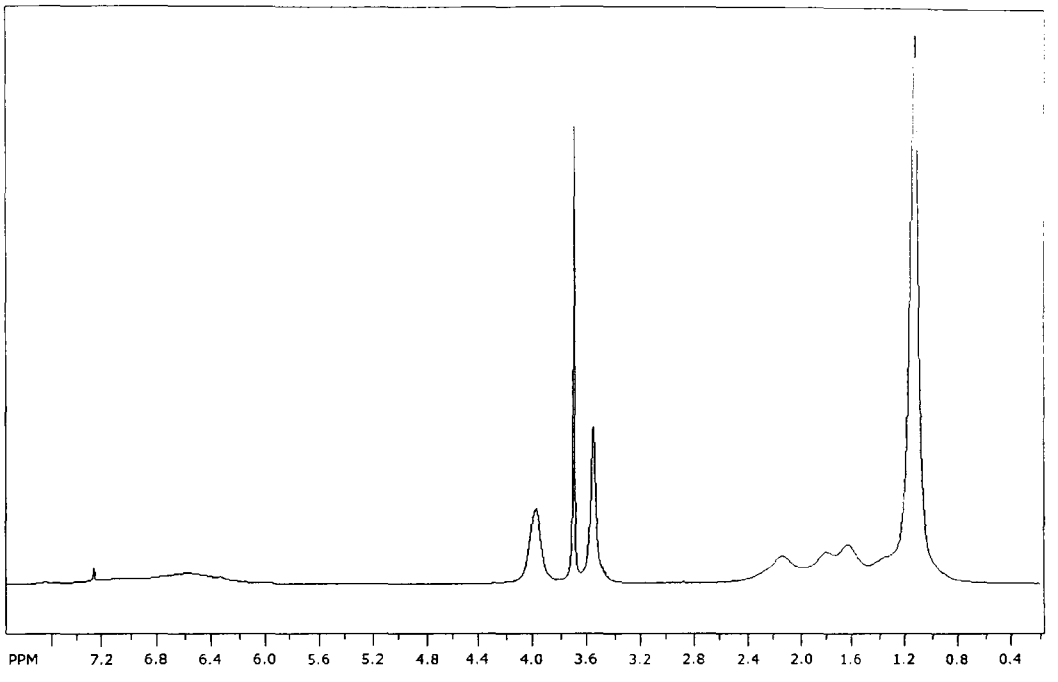

Figure C.3: ^{1}H NMR (400 MHz) spectrum of HB-PNIPAM (90:1).

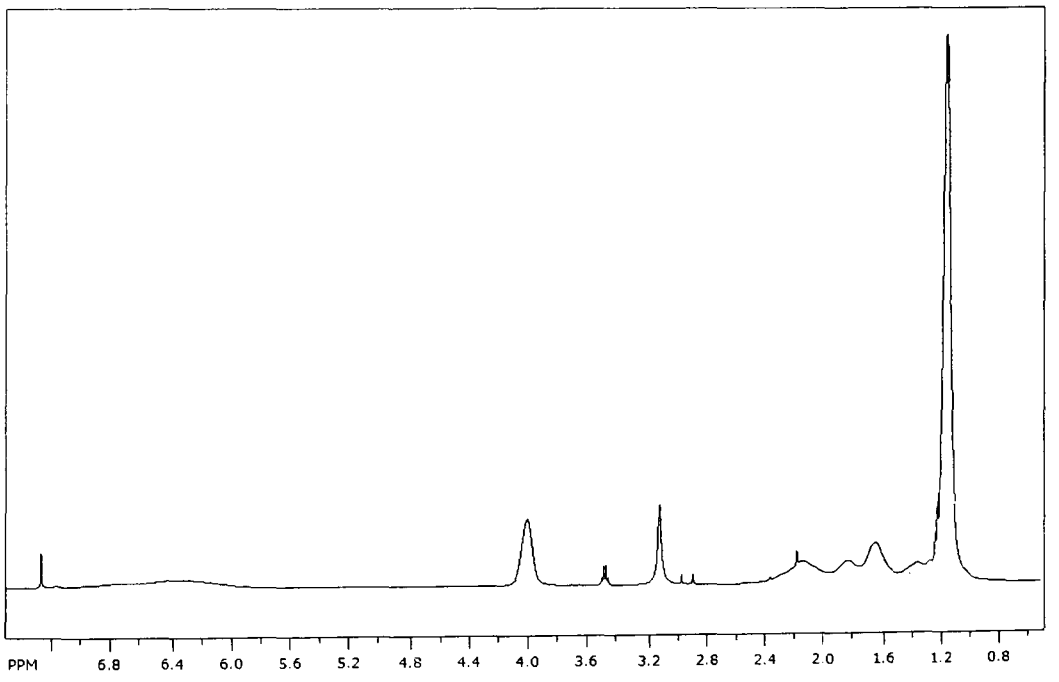

Figure C.4: ^{1}H NMR (400 MHz) spectrum of linear PNIPAM.

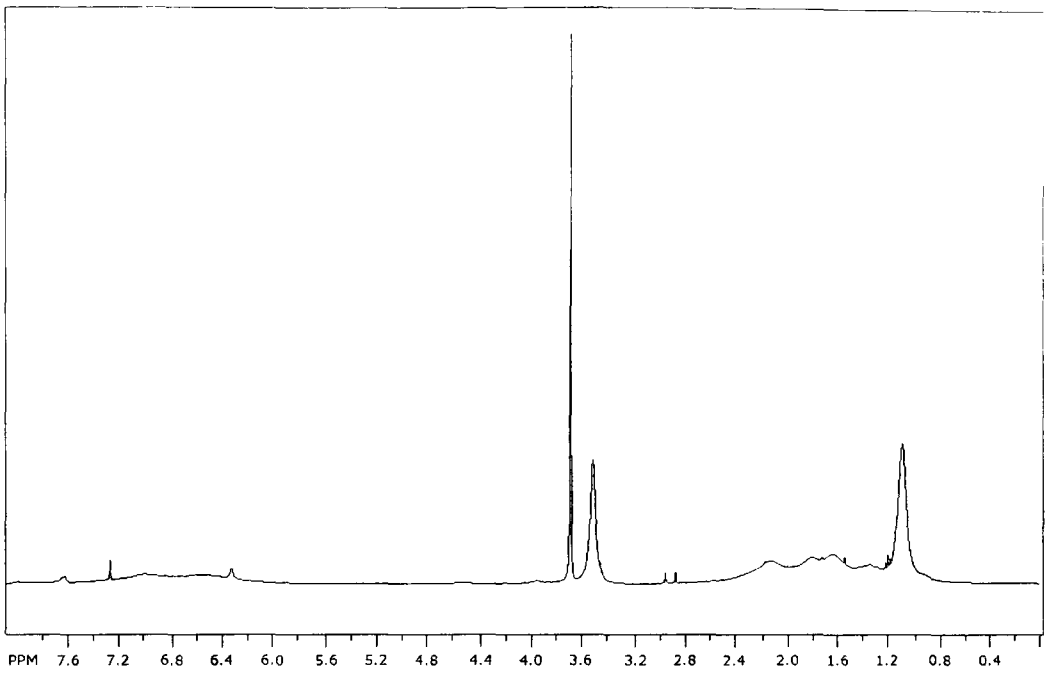

Figure C.5: ^{1}H NMR (400 MHz) spectrum of D_7-HB-PNIPAM (25:1).

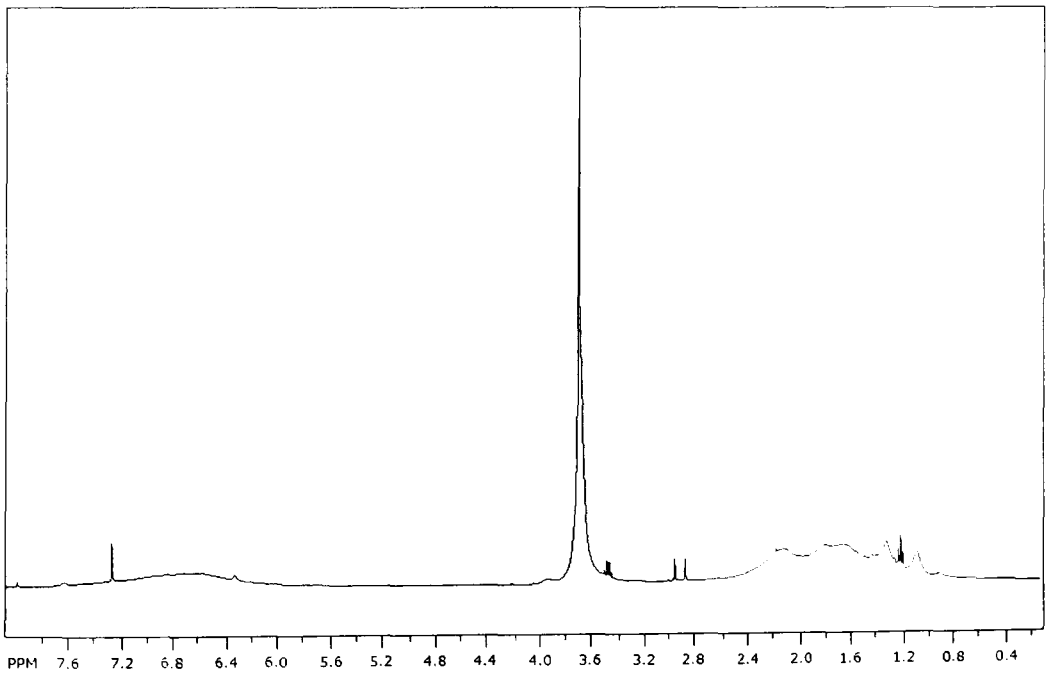

Figure C.6: ^{1}H NMR (400 MHz) spectrum of D_7-HB-PNIPAM (60:1).

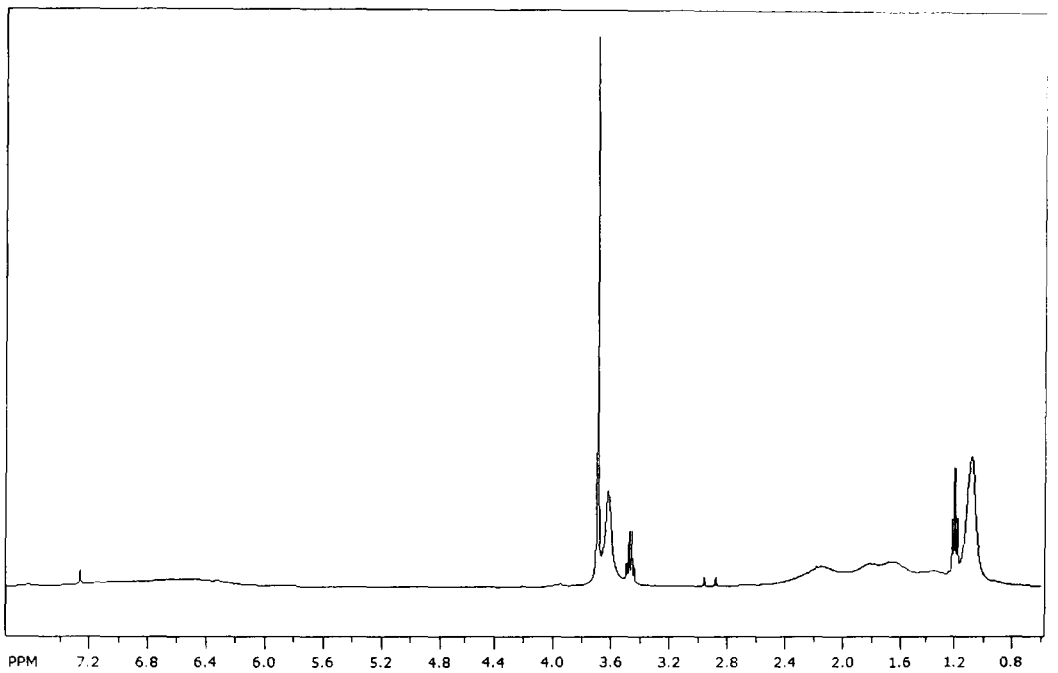

Figure C.7: ^{1}H NMR (400 MHz) spectrum of D_7-HB-PNIPAM (90:1).

Appendix D

Appendix D.1: SANS 2D Patterns

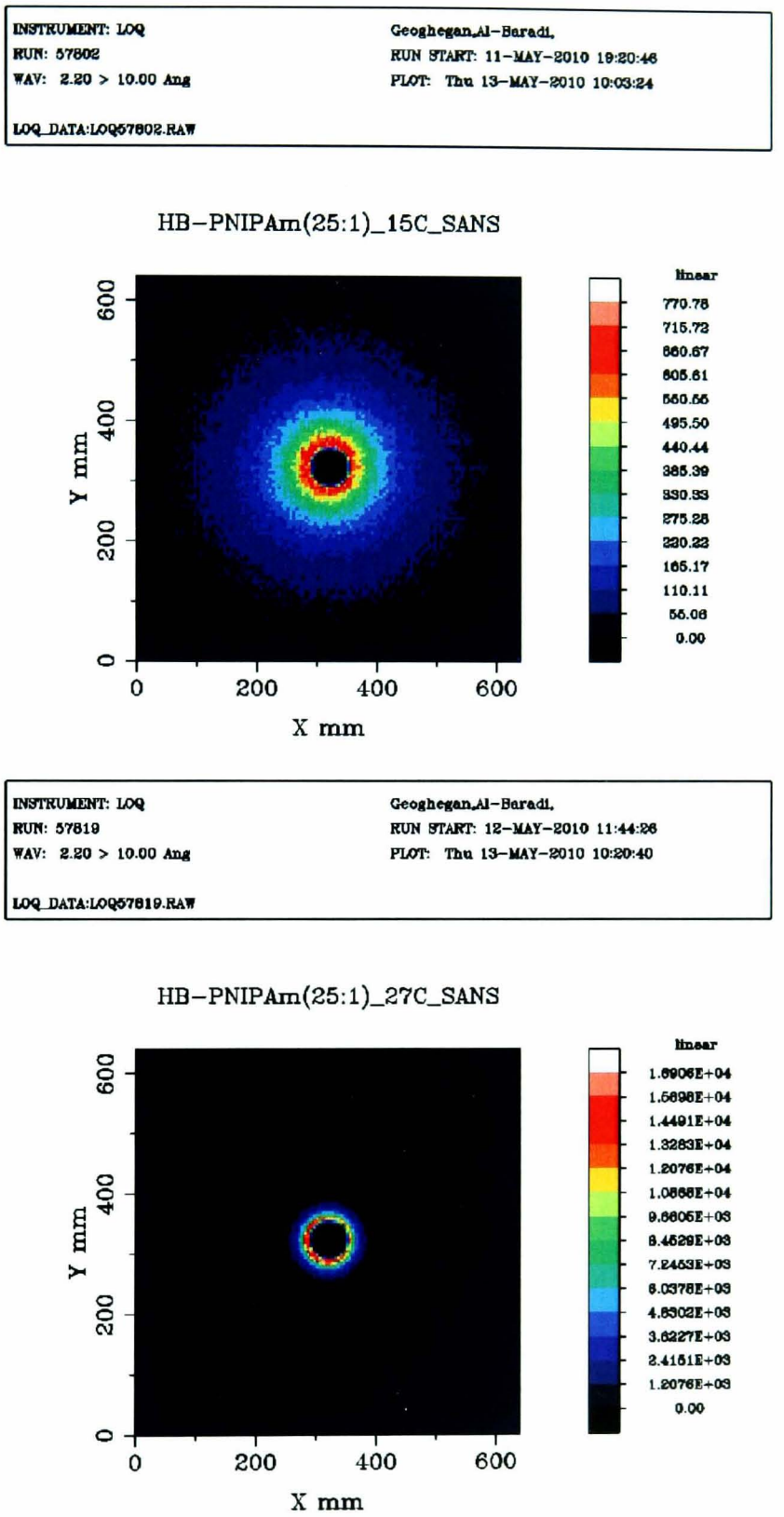

Figure D.1: SANS 2D scattering patterns for HB-PNIPAM (25:1) below (15°C, top) and around (27°C, bottom) its LCST.

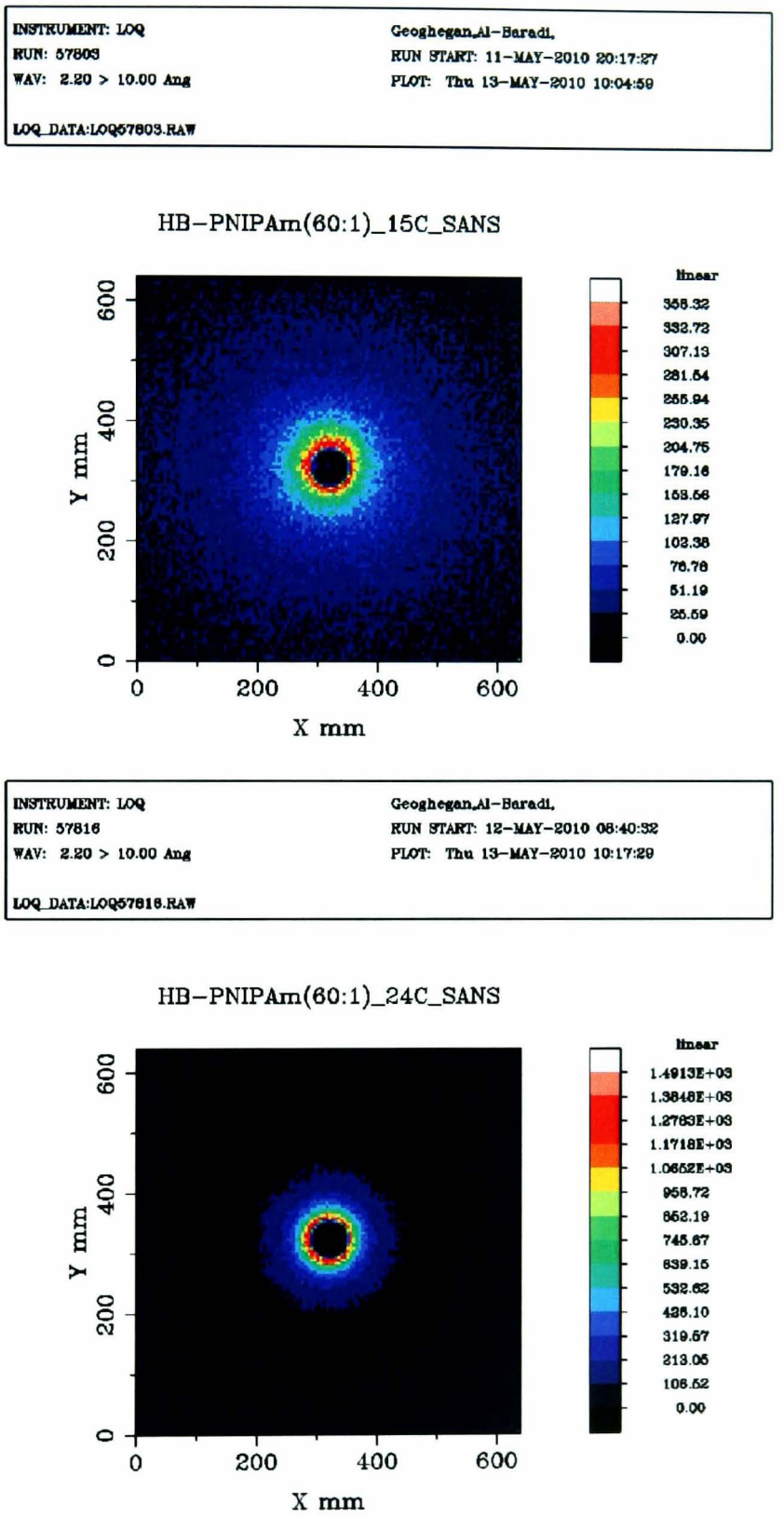

Figure D.2: SANS 2D scattering patterns for HB-PNIPAM (60:1) below (15°C, top) and around (24°C, bottom) its LCST.

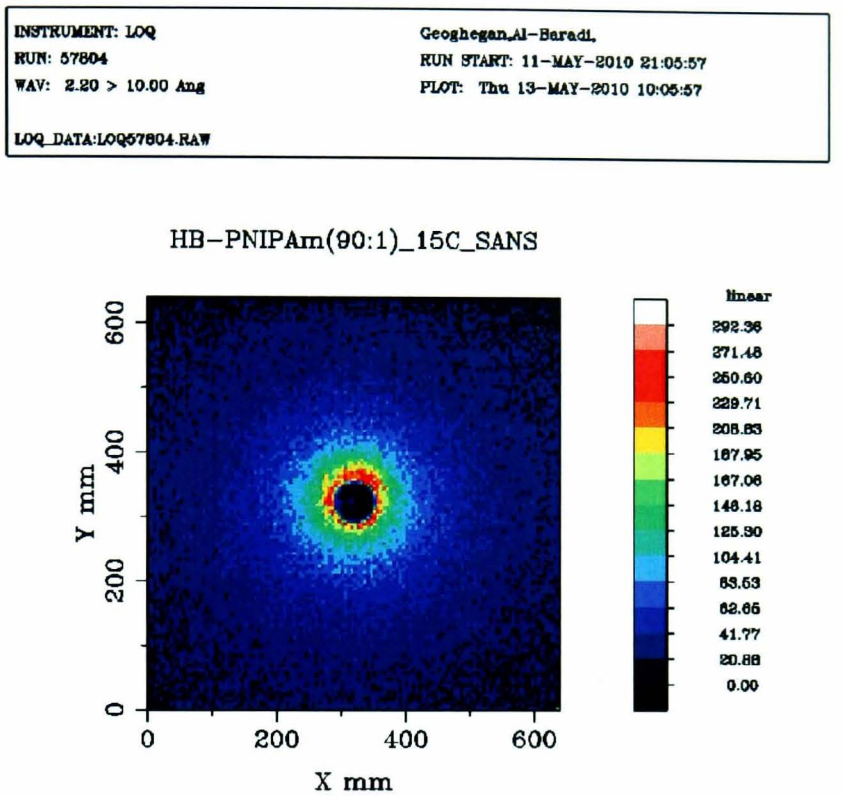

Figure D.3: SANS 2D scattering patterns for HB-PNIPAM (90:1) below (15°C, top) and around (27°C, bottom) its LCST.

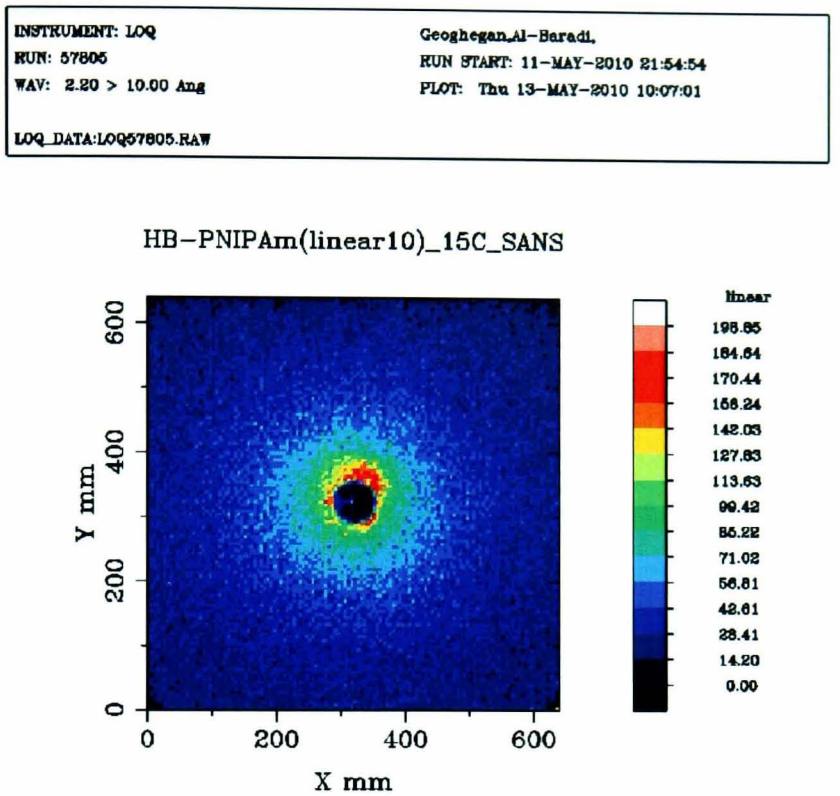

Figure D.4: SANS 2D scattering patterns for linear PNIPAM below (15°C, top) and around (33°C, bottom) its LCST.